

Preface

When planning to construct structures such as large dams, nuclear power plants, and tall buildings in seismically unstable regions, the activity of faults or fault systems in and around the sites must be assessed. This is to prevent the damage of structures due to ground shaking or displacement accompanying earthquakes caused by the motions of the faults or fault systems.

Taking into account the assessment, such construction sites must be carefully chosen and earthquake-proof designs must then be diligently devised for each structure. The earthquake-proof design and its construction must also sufficiently reflect outcomes of scientific research into the dynamic or static behavior of the faults, and groundwater circulations in the foundation rocks of the structure at all sites.

The largest magnitude inland earthquake (7.2) occurred at 0546JST on January 17, 1995, just beneath Kobe City in central Japan. Kobe City has approximately 1.5 million inhabitants. The earthquake seriously damaged the modern city and its adjacent areas. While this earthquake was formally named the “Hyogo-ken-nanbu (Southern Hyogo Prefecture) earthquake” by the Japan Meteorological Agency, it is popularly called the “Kobe earthquake” outside Japan.

The serious structural damage and high number of fatalities came as a great shock to some researchers and engineers. One reason for this shock was that the seriousness of the damage was beyond anyone’s expectation. The other reason was the ground motions generated by the event were far greater than the proposed seismic standard for earthquake-proof designs in Japan. It can be stated that the recent academic progress in the fields of geology and geophysics has not been sufficiently transferred to earthquake-proof designs that would help mitigate seismic disasters.

This book collects recent work and case history in engineering geology and highlights multidisciplinary aspects of engineering geology spanning science and technology. This book also emphasizes interdisciplinary studies that link the geological aspects of active faults with the seismological aspects of inland earthquakes, and transfers new knowledge to the earthquake-proof designs of large structures.

This book consists of 15 chapters. The first 11 chapters include all materials published in *Engineering Geology*, Vol. 43, No. 2–3 (1996), while the last four chapters (12 to 15) are original contributions to this book version.

The editor wishes to express sincere thanks to the authors who have contributed excellent papers to this book. Acknowledgment is also made to K. Watanabe and S-i. Kawakami for invaluable assistance and suggestion in editing the book.

YUJI KANAORI

Gifu University

@Seismicisolation

CHAPTER 1

Fault Activity and Earthquake Proof Design—Preface

Y. KANAORI and K. WATANABE

When planning to construct large structures such as large dams, nuclear power plants, and tall buildings in seismically unstable regions, the activity of faults or fault systems in and around the sites must be assessed. This is to prevent the damage of structures due to ground shaking or displacement accompanying earthquakes caused by the motions of the faults or fault systems. Taking into account the assessment, such construction sites must be carefully chosen and earthquake-proof designs must then be strictly performed for each structure. Also, the earthquake-proof design and practical construction, at any selected site, must sufficiently reflect the outcomes of scientific research concerning the dynamic or static behavior of the faults and groundwater circulation in the foundation rocks of the structure.

A large magnitude (7.2) inland earthquake occurred at 05:46 JST on January 17, 1995, just beneath Kobe City in central Japan. Kobe City has approximately 1.5 million inhabitants. The earthquake seriously damaged the modern city and its adjacent areas. While this earthquake was formally named the 'Hyogo-ken-nanbu (Southern Hyogo Prefecture) earthquake' by the Japan Meteorological Agency, it is popularly called the 'Kobe earthquake' outside Japan. Strong ground motion was induced by the earthquake, the maximum acceleration of 833 g (cm/s^2) being recorded at downtown Kobe City. Numerous houses, buildings, railroads and highway bridges were destroyed or seriously damaged, with fires occurring at about 300 locations. More than 5500 people were killed by this seismic disaster. The serious damage and large loss of life, came as a great shock to a number of researchers and engineers. One reason was that the seriousness of the damage was beyond anyone's expectation. Another was that the ground motions generated by the event were far greater than the proposed seismic standard for earthquake-proof designs in Japan. It can be stated that the recent academic progress in the fields of geology and geophysics has not been sufficiently transferred to earthquake-proof designs which would help mitigate seismic disasters.

The objectives of this special issue were to collect recent work and case histories in engineering geology and to highlight multidisciplinary aspects of engineering geology spanning science and technology. This issue also emphasizes interdisciplinary studies, which link the geological aspects of active faults with the seismological aspects of inland earthquakes and then transfer new knowledge to the earthquake-proof designs of large structures.

This special issue contains ten original papers, five of which include topics related

@Seismicisolation

to the 1995 Kobe earthquake: the first three papers are related to ground and fault motions or ground water circulation accompanying earthquakes, the next five papers attempt to evaluate fault activity and earthquake generations using various methods, and the last two papers characterize materials accompanying active faults.

Oka et al. overview a number of seismic records of strong ground motions, which were obtained at surface and borehole stations around seismic source regions, and conduct a seismic response analysis of grounds using two numerical methods. *Shimizu et al.* observe the attenuation characteristics of ground motions with varying depths from 0 to 600 m, trying to understand the effects of earthquake motions on deep groundwaters. Using linear elastic fracture mechanics theory, *Vallejo and Shettama* calculate stress concentration at the ends of active fault segments and the resulting deformations which develop around moving fault segments.

From the distribution of aftershocks and surface ruptures, together with calculations of seismic moments released by a fault system, *Kanaori and Kawakami* point out the probability that the movement of the Arima-Takatsuki tectonic line (fault system) produced the Kobe earthquake. *Toda et al.* describe surface faults and ruptures created by the Kobe earthquake and discuss problems of evaluating fault activity from surface faulting. On the basis of the block structure of central Japan, *Matsuaki et al.* simulate seismic sequences of destructive earthquakes using a rheology model made of springs and boxes and compare the results with the actual sequences of earthquakes which have damaged central Japan. They also interpret the generation of the Kobe earthquake using the rheology model and discuss fault systems having a high probability of producing coupling motions. *Kawakami et al.*, by analyzing drilled core samples of lacustrine sediments, examine the correlation between historical earthquake events and the density variation of the sediments, and propose a new sedimentological approach for reading past earthquake events from the density variation of the sediment cores. *C.F. Lee* describes the intraplate seismic setting of the Darlington nuclear power plant site, eastern Canada, as a case study. On the basis of the tectonic setting, he estimates input seismicity data for the design of the plant.

Using the ESR (electron spin resonance) method, *T. Fukuchi* estimates the fracturing ages of quartz within a fault gouge accompanying the Nojima fault at northern Awaji Island, along which surface ruptures were found just after the Kobe earthquake, and the Median Tectonic Line in Shikoku Island, with a discussion of the formation of both faults. *Lin* describes injection veins of crushing-originated pseudotachylite and fault gouges in granitic cataclasite and concludes that they were formed during seismic faulting by the rapid intrusion and fluidization.

This special issue benefited from discussion with Dr. B. Kerkhof (publishing editor with Elsevier) at Gifu University during her visit to Japan in the spring of 1994. The guest editors express thanks to Dr. S.-i. Kawakami of Gifu University for assistance and suggestion in editing the special issue. Special thanks are extended, for peer reviews of the papers contributed to this issue, to S. Hasegawa, R. Hataya, T. Ishida, I. Kawabe, K. Miki, M. Miyajima, M. Nagata, T. Otani, T. Ouchi, T. Sawada, H. Takayasu, T. Takeshita, K. Tanaka, M. Torii, and T. Yamabe.

Yuji Kanaori (Gifu University, Japan)
Kunio Watanabe (Saitama University, Japan)

@Seismicisolation

CHAPTER 2

Analysis of strong motion records from the Southern Hyogo earthquake of January 17, 1995¹

FUSAO OKA^{a,*}, MASATA SUGITO^a, ATSUSHI YASHIMA^a,
YOSUKE TAGUCHI^b and KOJI SEKIGUCHI^c

^a*Department of Civil Engineering, Gifu University, Gifu 501-11, Japan*, ^b*Civil Engineering Division, Taisei Corporation, Japan* and ^c*Applied Technology Research Center, NKK Corporation, Japan*

Abstract

Strong motion records from the Southern Hyogo earthquake of January 17, 1995, are overviewed. The discussion is focused on (1) the characteristic of near field records including the predominant direction of motion versus the fault strike and their spectral characteristic, and (2) the orientation error of seismometers and ground motion amplification at borehole array stations. Two numerical techniques for seismic response analysis of ground are applied for the array stations. The one is the frequency-dependent equi-linearized technique for the frequency domain analysis, and the other is the effective stress-based liquefaction analysis method. The numerical calculations are compared with the records at four borehole array stations.

1. Introduction

Strong motion records at over 400 stations from the Southern Hyogo earthquake of January 17, 1995, were obtained by various organizations, including the Japan Meteorological Agency (JMA), the Committee of Earthquake Motion Observation and Research in the Kansai Area (CEORKA), Port and Harbor Research Institute, Ministry of Transport, and some other public organizations and several private companies. The records were obtained at stations with various ground conditions including those at sites where soil liquefaction occurred. Several records exceeded 0.5 g in their peak acceleration and the maximum recorded acceleration was 0.818 g obtained at the Japan Marine Meteorological Observatory in Kobe City. The records from borehole and ground surface-array observation systems were also obtained.

* Corresponding author.

¹This earthquake has been officially named by the Japan Meteorological Agency as “the 1995 Hyogoken-Nanbu earthquake”.

Herein the strong ground motion records from the earthquake are overviewed using typical records from the epicentral region and those from borehole array stations. In Section 2, the near-field strong motion records are discussed focusing on the relation between directivity of faulting and ground-displacement orbit as well as the spectral characteristic of ground motions. In Section 3, the borehole array records at four stations are introduced and the correction of the orientation error of seismometers are discussed. Ground motion amplification is also demonstrated. In Section 4, the response analysis of the ground at four borehole array stations is carried out. The frequency-dependent equi-linearized technique for the response analysis of layered ground is applied for the array stations and the results are compared with the records. The effective stress-based 3D liquefaction analysis is carried out for one of the borehole array stations where severe soil liquefaction occurred.

2. Near field strong motion records

Fig. 1 shows the location of strong ground motion observation stations with horizontal peak acceleration or peak velocity (Committee of Earthquake Motion Observation and Research in Kansai Area, 1995, (CEORKA); Hanshin Public Expressway, 1995; Japan Meteorological Agency, 1995, (JMA); Kashima and Kitagawa, 1995; Kobe City Development Bureau, 1995; Osaka Gas Company, 1995; Technical Research Institute and Kansai Electric Power Company, 1995; The National Research Institute for Earth Science and Disaster Prevention, 1995). Most stations are located on alluvial sites around Osaka Bay and, unfortunately, no record was reported from Awaji Island. It is observed that the records which exceed 0.5 g were obtained in near fault zone and there exists a strong directivity in the direction of approximately N60E to S60W which is nearly the strike of the fault. It is also observed that the ground motion in the Osaka plain area was generally amplified by a soft soil deposit compared with those in other areas.

Fig. 2 shows the typical strong ground motion record in the epicentral region which was obtained at Kobe Marine Meteorological Observatory located in the west part of Kobe City. Fig. 2a shows the three components of acceleration time histories. The station stands on a small hill and the condition of the ground surface is relatively stiff soil. The two main phases can be observed in the strong motion part of the N-S component. The dominant frequency of the first half is lower than that of the second half. Fig. 2b shows the evolutionary power spectrum (Kameda, 1975) for these three components. Because of the short duration the nonstationary characteristic is not clear, however, it can be observed that, in the up-down (UD) component, the frequency content around 0.8 Hz is dominant 5 s after the strongest motion. Fig. 2c shows the pseudo-velocity response spectra for these three components. It can be observed that the velocity response of the natural period of around 1 s with 5% damping exceeds 200 cm/s.

Fig. 3 shows another example of records obtained at the station close to the fault.

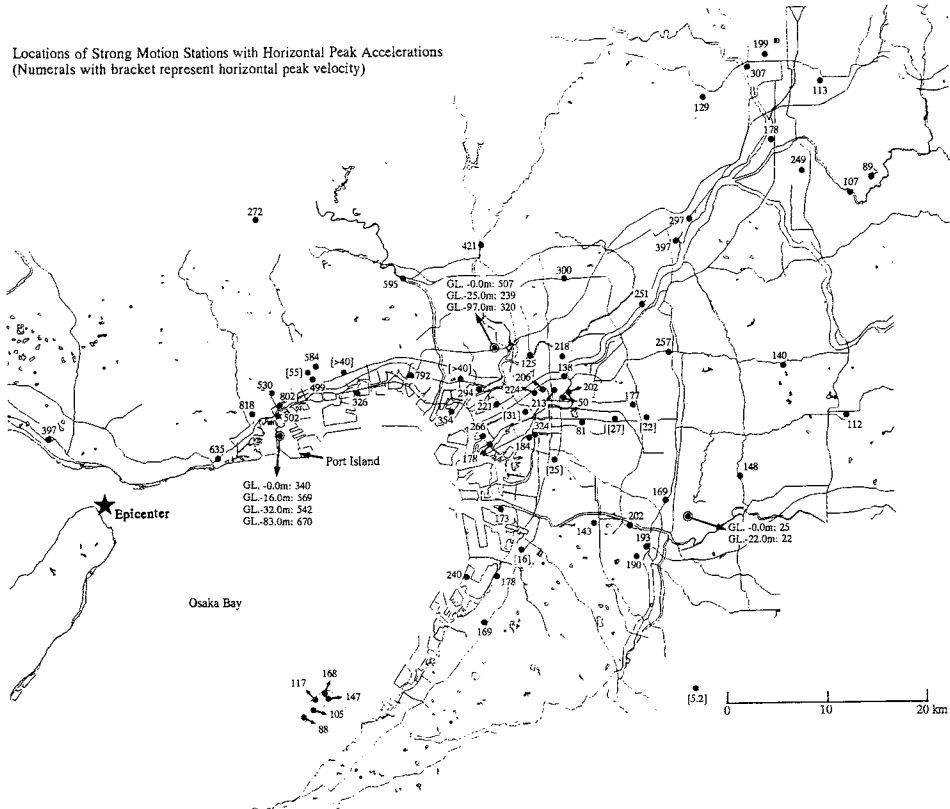
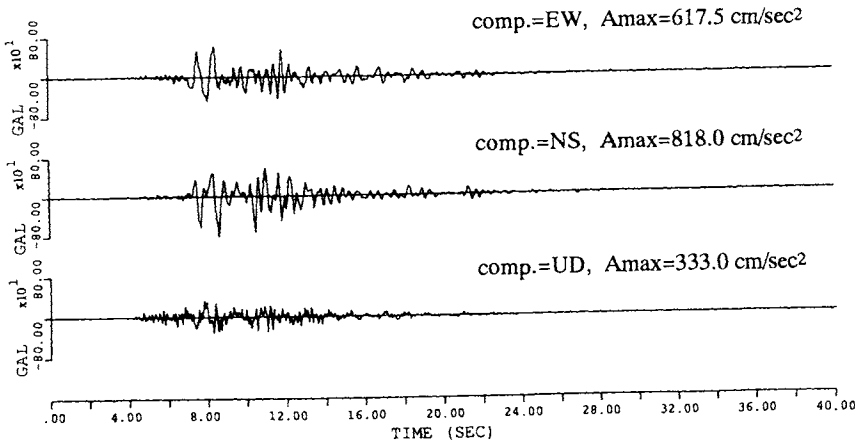


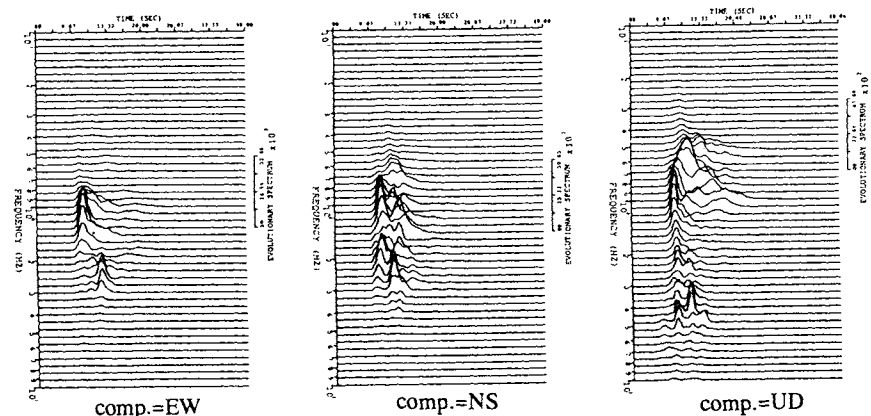
Fig. 1. Location of strong motion stations with horizontal peak acceleration.

Two horizontal components were obtained at Fukiai supply station of Osaka Gas Company in Kobe City. The peak value of the synthesized horizontal acceleration was reported as 0.833 g. The dominant period for the Y-component was about 1–2 s and the response spectrum with 5% damping on this period yields 300 cm/s. The component, N30W, is nearly the transverse direction of the fault. This could be one of the strongest acceleration records, regarding the spectral intensity in the range of 0.5–2.0 s, in Japan.

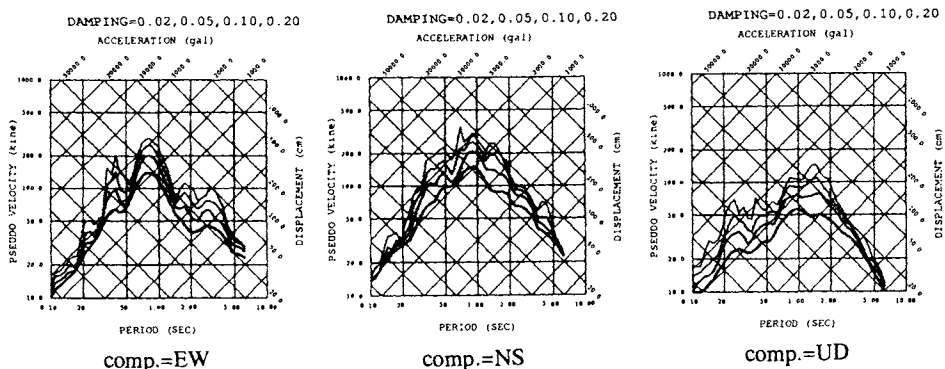
The records at several other sites in the near field region are reported. Fig. 4 shows the horizontal orbits of ground displacement in near field region. It is clearly observed that the ground motion in the direction of N30W to S30E is predominant. This direction is nearly the transverse of the fault, and the result is consistent with the simple double couple mechanism of faulting.



(a) acceleration time history (filtered between 0.1 and 20.0 Hz)



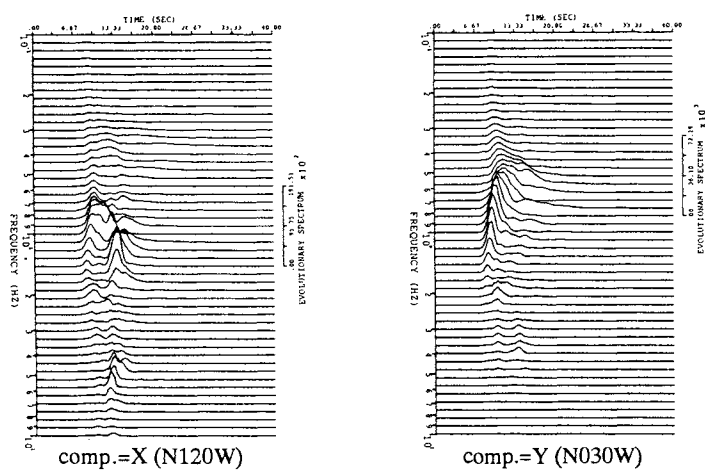
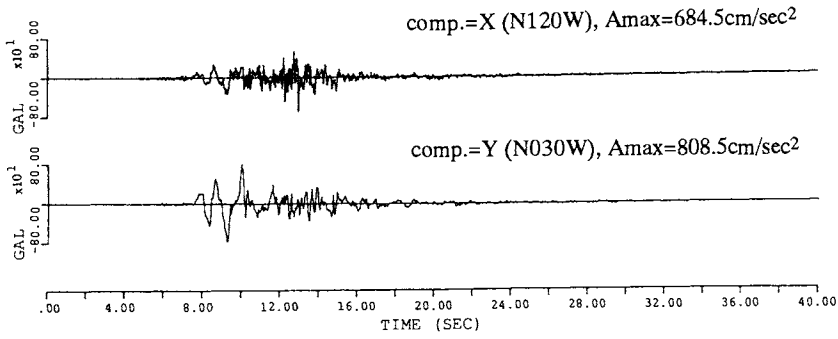
(b) evolutionary power spectrum



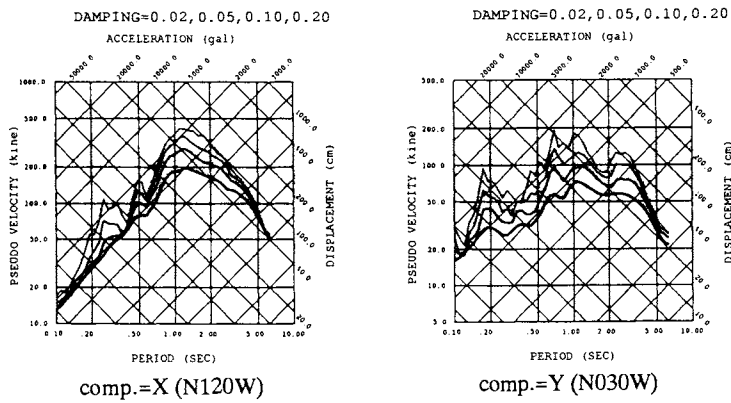
(c) pseudo velocity response spectrum

Fig. 2. Strong motion record observed at Kobe Marine Meteorological Observatory.

@Seismicisolation



(b) evolutionary power spectrum



(c) pseudo velocity response spectrum

Fig. 3. Strong motion record observed at Kobe Fukiai Supply Center of the Osaka Gas Company.

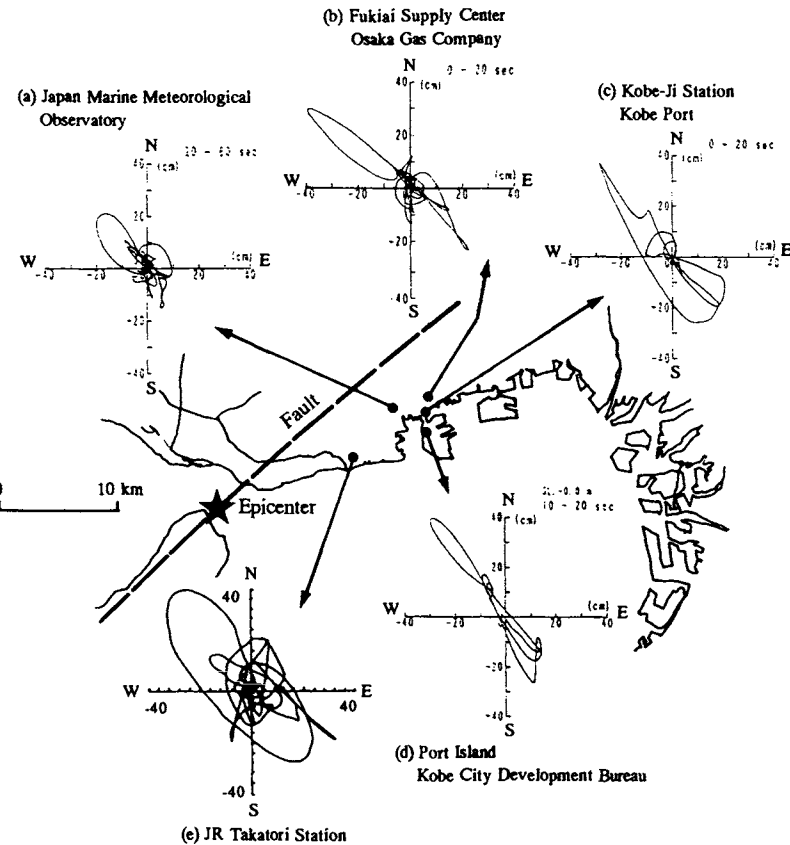


Fig. 4. Horizontal ground motion orbit in near field.

3. Strong motion amplification in borehole array records

3.1. Layout of array stations

Herein, the four sets of borehole array records obtained during the Southern Hyogo earthquake of January 17, 1995, are examined. Fig. 5 shows the locations of these array stations. The epicentral distances for these stations are, $\Delta = 21$ (PI), 43 (TRC), 53 (KPS), and 26 km (TPS). The stations belong to the following organizations: PI, Port Island Array Station, Kobe City Development Bureau; TRC, Technical Research Center, Kansai Electric Power Company; KPS, Kainan Port Sub-station, Kansai Electric Power Company; TPS, Takasago Power Station, Kansai Electric Power Company.

Fig. 6 shows the layout of the array observation systems. The Port Island station (PI), TPS, and KPS are located on reclaimed land. The severe soil liquefaction was reported at PI station. The displacement orbits on a horizontal plane obtained from

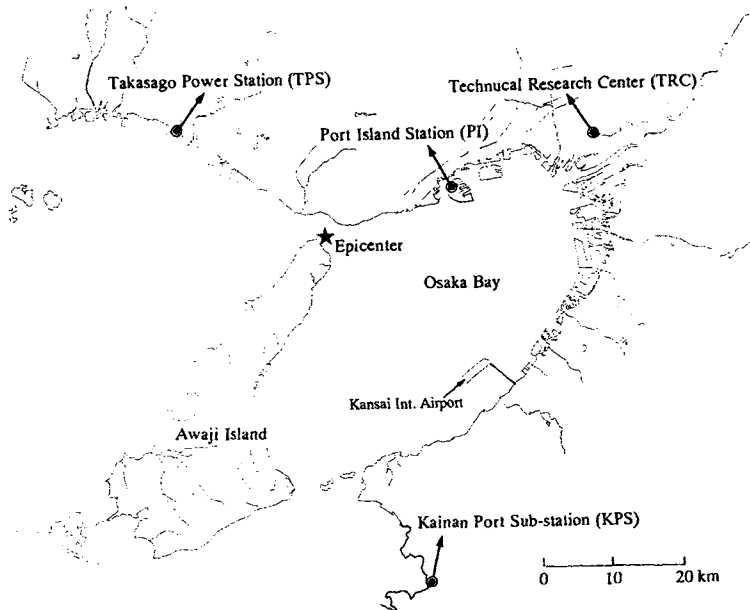


Fig. 5. Location of borehole array observation stations.

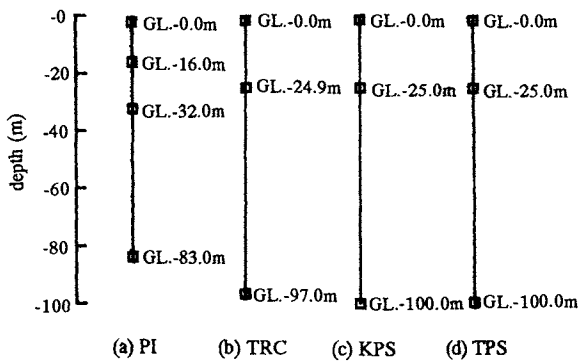


Fig. 6. Layout of borehole array observation stations.

the integration of the filtered accelerograms are used for the estimation of the orientation error (Sugito et al., 1995).

3.2. Correction of orientation error of borehole records and strong motion amplification characteristic

The orientation error of the buried seismometers have been frequently discussed (Yamazaki et al., 1989). It is an essential task for use of borehole array records to

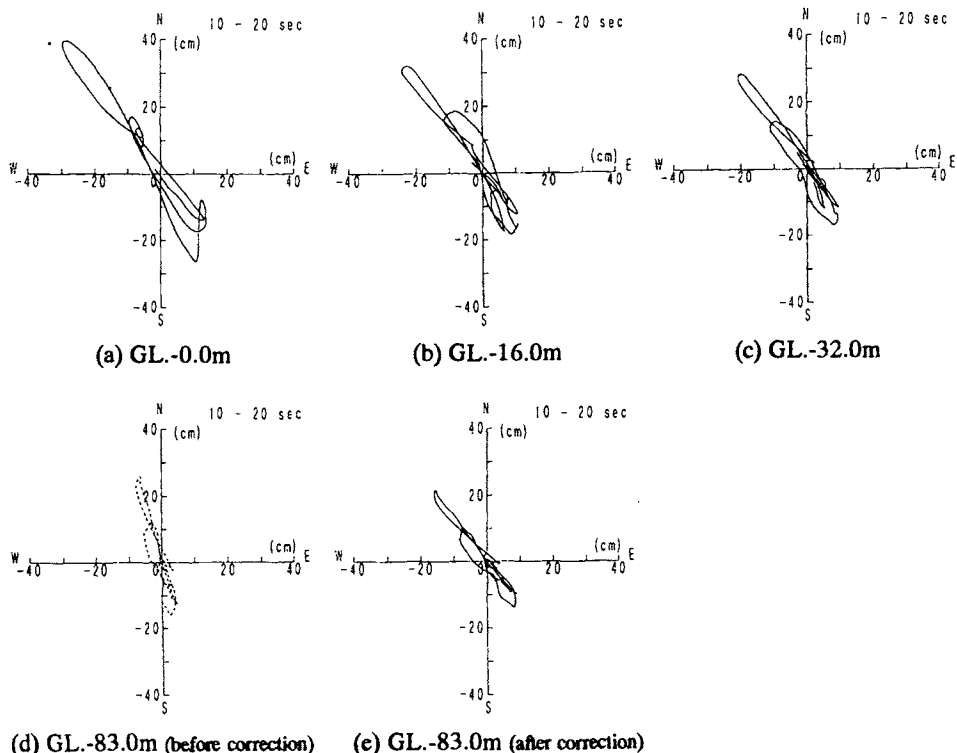


Fig. 7. Displacement orbits at various depths (Port Island, Kobe City, 10–20 s, 0.15–20.0 Hz).

examine the orientation error of seismometers. To examine the orientation error of the buried accelerographs, displacement orbits on the horizontal (NS-EW) plane at four depths during 10–20 s are prepared as shown in Fig. 7. The time histories of the displacements were calculated from the acceleration records using FFT and a trapezoidal digital filter with a flat frequency range of 0.15–20.0 Hz. From the comparisons of the four figures (Fig. 7a–d), it may be stated that the error of the buried direction of the accelerograph at GL – 83 m exists in the range between 15 and 25° counterclockwise. On the basis of the careful investigation by using the overlaid displacement orbits, it was concluded that the accelerograph at GL – 83 m was rotated about 22° from the proposed orientation. This assumption was also confirmed through the comparisons of the displacement orbits in other time ranges. Fig. 7e shows the displacement orbit based on the orientation-corrected time histories. Namely, the correction of the digital records can be performed by the rotation of the coordinates. To perform the operations mentioned in this paragraph efficiently, two sets of programs (Oishi and Sekiguchi, 1984; Kamata et al., 1987) were used.

The peak accelerations of the original time histories are $A_{\max} = -670.5 \text{ cm/s}^2$

(NS) and -304.6 cm/s^2 (EW), and those of the orientation-corrected time histories are $A_{\max} = -526.7$ (NS) and 486.2 (EW). Fig. 8 shows the acceleration time histories for each ground level including corrected time histories at GL -83 m. In Fig. 8 the drastic change in frequency content during the first S-wave phase, around 6 s on time axis, can be seen. It can be observed that the strong spikes are contained in the UD component at GL -16 m. Some electric noise occurring in the system could be one of the reasons for these strong spikes. Fig. 9 shows the amplification characteristic of peak acceleration, velocity, and displacement. It is observed that the horizontal peak accelerations at GL -0.0 m are drastically decreased because of soil liquefaction in the upper reclaimed sandy layers. These peak values are listed in Table 1 with those for the original time histories at GL -83.0 m.

The orientation errors of seismometers at the other three array stations have been

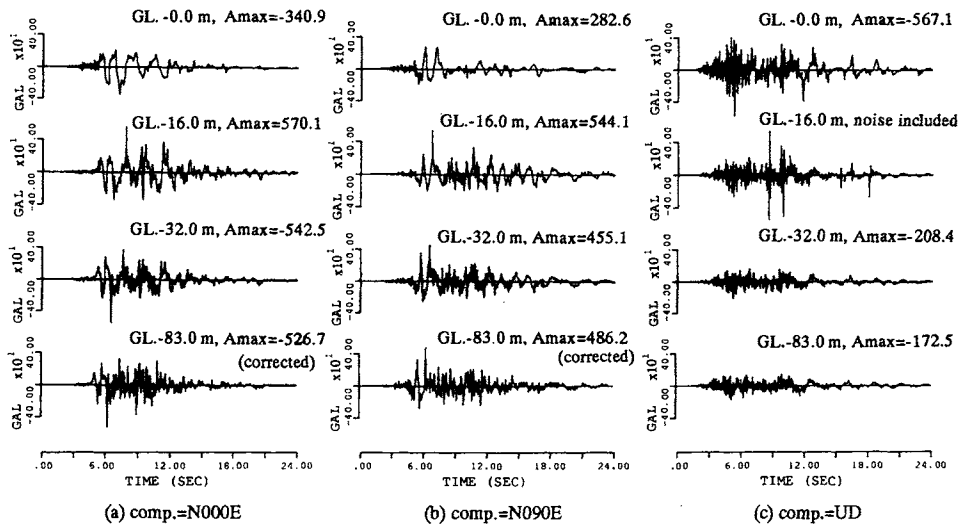


Fig. 8. Acceleration time histories (Port Island, Kobe City, 10–20 s, 0.15–20.0 Hz).

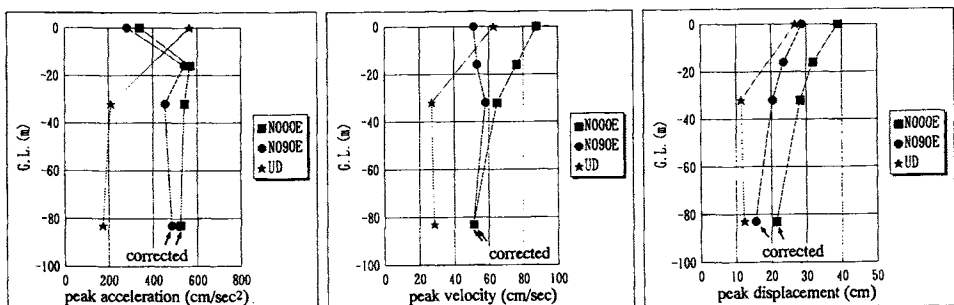


Fig. 9. Distribution of peak ground motions (Port Island, Kobe City, 10–20 s, 0.15–20.0 Hz).

TABLE I
Variation of peak ground motions at Port Island Borehole Array Station

Ground level (m)	Peak acceleration (cm/s ²)			Peak velocity (cm/s)			Peak displacement (cm)		
	NS	EW	UD	NS	EW	UD	NS	EW	UD
0.0	-340.9	282.6	-567.1	-88.8	-51.1	-62.8	39.7	-29.6	26.9
-16.0	470.1	544.1	547.5	-76.7	-53.3	-33.5	32.0	-24.1	-18.2
-32.0	-542.5	455.1	-208.4	-65.0	-58.2	-27.1	28.4	-20.8	11.5
-83.0	-670.5	-304.6	-172.5	66.2	-28.8	-28.4	25.9	12.0	12.2
	-526.7 ^a	486.2 ^a		50.7 ^a	-51.1 ^a		21.6 ^a	-16.0 ^a	

^aPeak value for orientation-corrected time histories.

also examined. Figs. 10–15 show the ground motion time histories and distribution of peak ground motions obtained from the orientation-corrected time histories. Table 2 gives a summary of the orientation errors of seismometers at these four array stations.

4. Application of response analysis to borehole array records

4.1. Frequency-dependent equi-linearized technique

The equi-linearized technique, in which nonlinear characteristics of shear modulus and damping of soils depending on its shear strain levels are modeled as an equivalent linear relation, has been applied frequently for earthquake response analysis of ground, especially in case of the practical fields. A strong point of the technique compared with the non-linear time domain analysis is that the algorithm

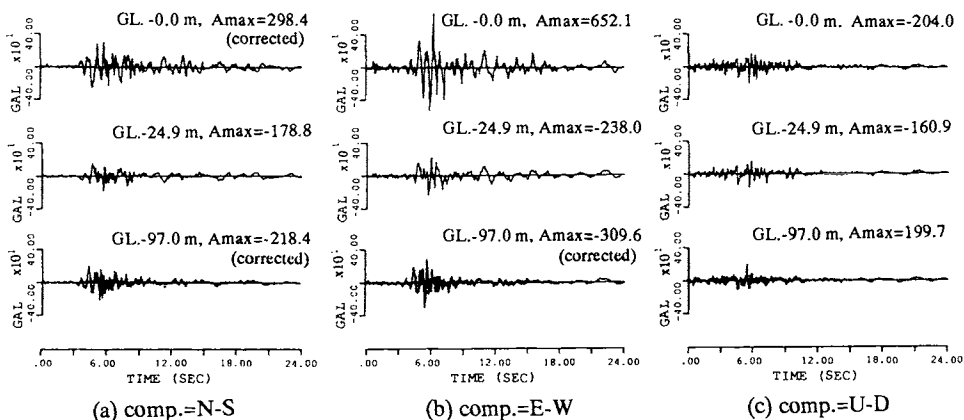


Fig. 10. Acceleration time histories (Technical Research Center, Kansai Electric Power Company).

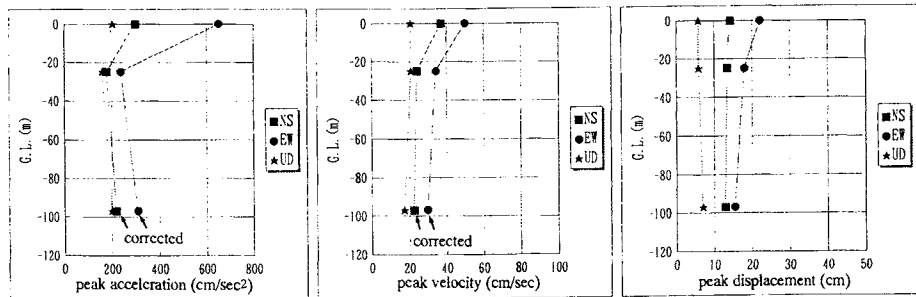


Fig. 11. Distribution of peak ground motions (Technical Research Center, Kansai Electric Power Company).

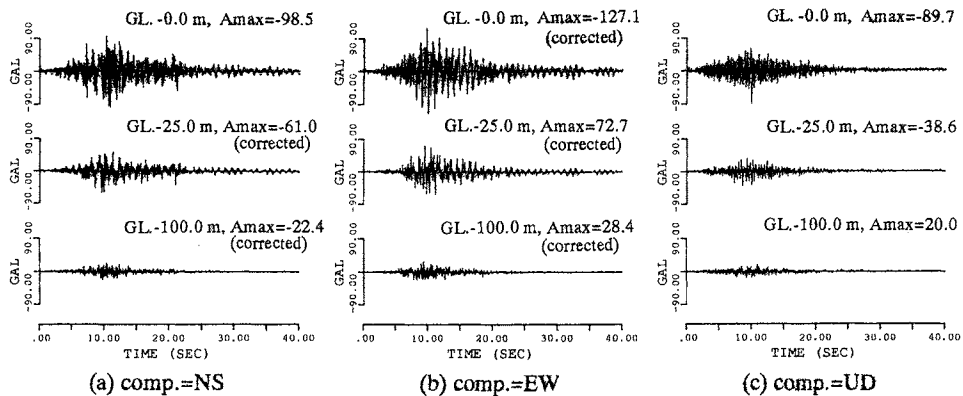


Fig. 12. Acceleration time histories (Kainan Port Sub-station, Kansai Electric Power Company).

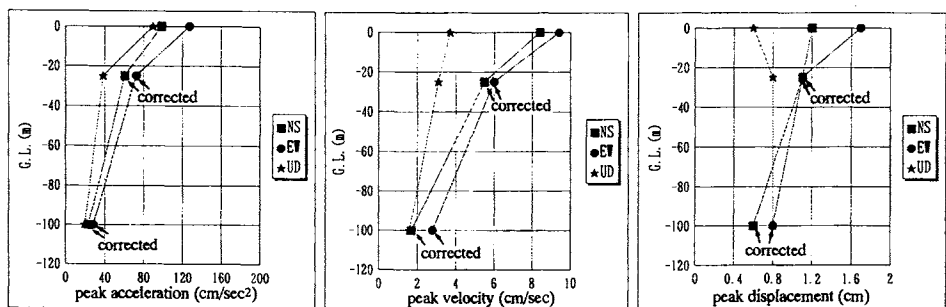


Fig. 13. Distribution of peak ground motions (Kainan Port Sub-station, Kansai Electric Power Company).

is quite simple and the inversion, such as the estimation of input bed rock motion from surface motion, is possible. The computer program, 'SHAKE' (Schnabel et al., 1972), is based on the equi-linearized technique and has contributed much in the

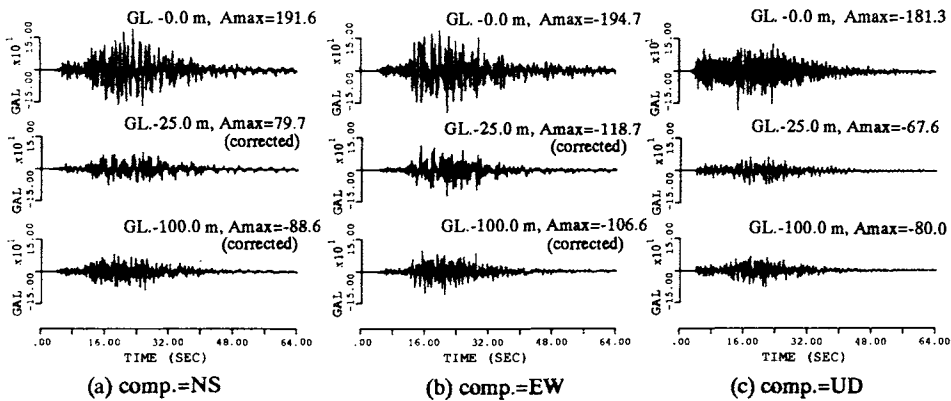


Fig. 14. Acceleration time histories (Takasago Power Station, Kansai Electric Power Company).

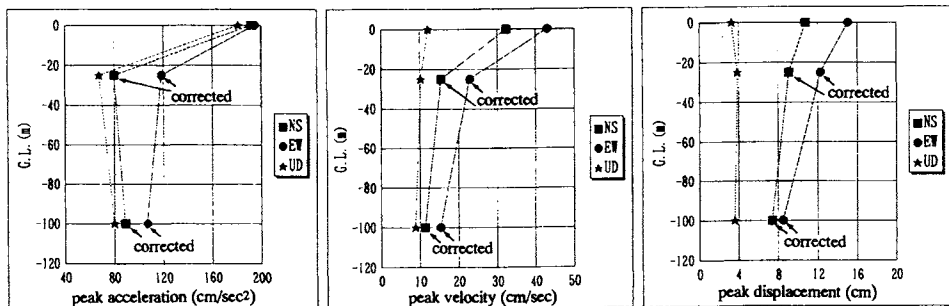


Fig. 15. Distribution of peak ground motions (Takasago Power Station, Kansai Electric Power Company).

TABLE II
Summary of orientation error of buried seismometers

Accelerograph ID	Depth (GL, m)	Error ^a (°)
PI1	-83	22
TRC3	-0	180 ^b
TRC1	-97	46
TPS2	-25	-20
TPS1	-100	16
KPS3	-0	180 ^c
KPS2	-25	67
KPS2	-25	67
KPS1	-100	46

PI, Port Island Borehole Array Station, Kobe City Development Bureau; TRC, Technical Research Center, Kansai Electric Power Company; TPS, Takasago Power Station, Kansai Electric Power Company; KPS, Kainan Port Sub-station, Kansai Electric Power Company.^aPositive number in counterclockwise direction.^bOrientation error in NS component only.^cOrientation error in EW component only.

field of earthquake engineering. However, it has been pointed out that the numerical results do not agree with the observed ground motion in case of very soft ground condition and strong ground motion levels.

To solve the problem of the conventional equi-linearized technique, the frequency-dependent equivalent strain was proposed for numerical calculation (Sugito, 1993; Sugito et al., 1994). The idea is described in the following.

Generally the ground motion includes some spectral characteristics, and the contribution of the frequency contents to strain time history strongly depends on the frequency characteristic. The typical example of the Fourier amplitude for shear strain time history is shown in Fig. 16. In Fig. 16 the Fourier amplitude of strain time history in the specific soft layer at Shin-Ohta Array Station located in Tokyo Bay is shown. The Fourier spectrum was smoothed by a triangle window with a band width of 1.0 Hz. The resonant frequency is at around 2 Hz, and the amplitude in a higher frequency range of 8–10 Hz, are much less than their maximum in order of magnitude. Since the strong spectral characteristics of shear strain amplitude are included in the earthquake ground response, it may be derived that appropriate shear modulus and damping depending on the frequency characteristic could be used for equi-linearized analysis. According to this assumption the frequency-dependent equivalent strain is proposed in the following form:

$$\gamma_f(\omega) = C \frac{F_y(\omega)}{F_{y_{\max}}} \quad (1)$$

where C =constant, γ_{\max} =maximum shear strain, $F_y(\omega)$ =Fourier spectrum of shear strain time history, and $F_{y_{\max}}$ represents the maximum of $F_y(\omega)$. The definition of $\gamma_f(\omega)$ in Eq. (1), described as the equivalent strain, which controls equivalent shear modulus and damping, is given in proportional to the spectral amplitude of

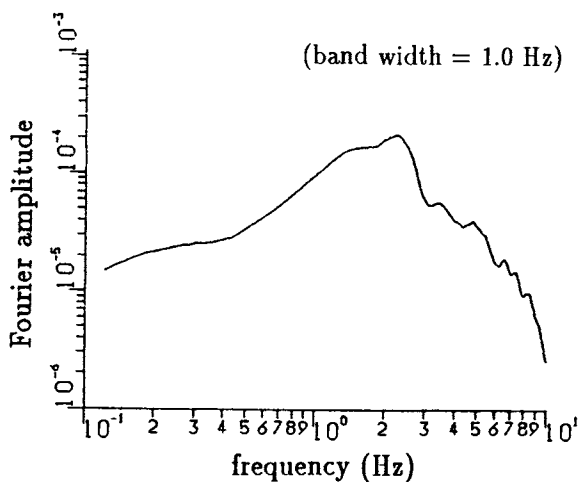


Fig. 16. Example of Fourier amplitude of strain time history.

strain time history. The constant C controls the level of equivalent strain uniformly along the frequency axis. The condition $F_\gamma(\omega)/\gamma_{\max} \equiv 1.0$ and $C = 0.65$ gives the same condition as the SHAKE program.

The constant C is supposed to be in the range between 0.65 and 1.0 corresponding to the SHAKE program. Generally the Fourier amplitude of strain time history is relatively small in the high frequency region, and fluctuates strongly along the frequency axis depending on its sampling time interval and number of sampling. It is important to incorporate the general trend of the Fourier amplitude of strain along the frequency axis into the frequency-dependent equivalent strain. Therefore, the smoothing of the Fourier amplitude by a triangle window with a band width of 1.0 Hz is performed for the evaluation of equivalent strain.

The technique is applied for borehole array observation stations. Table 3 gives the velocity structure models for these four stations. The base strong motion records, the peak acceleration of which is larger in two horizontal components, are used. Namely the base motion of NS component for PI station, and that of EW component for TRC, KPS, and TPS stations are used.

Figs. 17–20 show the result of numerical calculations; the peak acceleration, velocity, and displacement at the top of each layer are compared with the records. The amplification function between ground surface and basement both for recorded and calculated motion are given in each figure.

In Fig. 17a, the case for the PI station, the estimated peak acceleration in the depth between GL – 0.0 m and GL – 10.0 m is supposed to be much larger than that for the actual ground motion. This is certainly due to soil liquefaction phenomena. The peak velocity is also overestimated in the shallower ground level. It is very clear that the conventional equi-linearized technique cannot be applied to the soft sandy ground in the case that the soil liquefaction occurs. However, the technique used herein gives the reasonable estimation for deeper ground motion. The amplification function obtained by the recorded motion, shown in Fig. 17d, shows the large de-amplification characteristic in the frequency range of $f > 1.0$ Hz.

In Fig. 18, the case for the TRC station, the calculated peak ground motions agree with the records, except for the peak velocity at GL – 0.0 m. This array system has been installed at the alluvial site and no soil liquefaction was reported around the station. Because of the low shear velocity at the top layers, the peak ground motion is amplified in this region. In Fig. 18d the amplification function by numerical calculation agrees with the records.

In Fig. 19, the case for the KPS station, the estimated peak acceleration and velocity are smaller than those for records at GL – 0.0 m and GL – 25.0 m. This is the case that the input ground motion level is relatively low; the peak acceleration of input motion at GL – 100.0 m is 28.4 cm/s^2 . In Fig. 19d the second and the third modes for the amplification function obtained from the technique agree with those from the records, however, the predominant frequency of the first mode by numerical calculation is a little lower than that from the records.

Fig. 20 shows the results from the TPS station, which is located on the reclaimed

TABLE III

Velocity structure model for borehole array stations

Port Island (PI)				Technical Research Center (TRC)				Kainan Port Sub-station (KPS)				Takasago Power Station (TPS)			
Thickness (m)	Density (g/cm ³)	V _s (m/s)	Soil type ^a	Thickness (m)	Density (g/cm ³)	V _s (m/s)	Soil type ^a	Thickness (m)	Density (g/cm ³)	V _s (m/s)	Soil type ^a	Thickness (m)	Density (g/cm ³)	V _s (m/s)	Soil type ^a
2.0	1.9	170.0	3	2.0	1.4	98.0	1	1.8	1.6	238.0	3	3.40	1.7	140.0	4
3.0	1.9	170.0	3	1.0	1.4	117.0	2	2.0	1.6	100.0	2	3.75	1.7	130.0	2
7.5	1.9	210.0	3	3.0	1.7	117.0	4	13.2	1.7	179.0	3	6.25	1.6	200.0	1
6.5	1.9	210.0	3	1.0	1.7	149.0	3	6.5	1.6	220.0	2	5.6	1.9	310.0	4
8.0	1.6	180.0	2	3.0	1.6	149.0	2	1.9	1.7	270.0	3	6.00	1.9	400.0	4
6.0	1.9	245.0	3	6.0	2.0	342.0	4	4.6	1.7	188.0	3	5.05	1.8	330.0	4
17.0	1.9	305.0	3	1.0	2.0	222.0	1	7.1	1.6	216.0	1	2.95	1.7	230.0	1
11.0	1.9	350.0	3	2.0	2.0	154.0	3	2.6	1.7	206.0	3	4.00	1.7	320.0	1
18.0	1.6	303.0	2	10.0	2.0	400.0	1	7.2	1.7	315.0	3	6.70	1.9	560.0	4
4.0	1.9	320.0	3	3.0	2.0	375.0	4	6.5	1.6	263.0	2	4.80	1.8	250.0	3
	1.9	320.0	3	6.0	1.7	375.0	1	2.4	1.8	370.0	4	11.80	1.9	405.0	4
				3.0	1.7	231.0	1	5.2	1.7	274.0	2	13.20	1.9	650.0	3
				3.0	2.0	286.0	4	5.5	1.8	325.0	3	9.80	1.9	500.0	4
				7.0	2.0	255.0	3	7.4	1.8	700.0	4	16.70	1.8	460.0	1
				2.0	2.0	222.0	3	9.6	1.7	338.0	4		1.8	460.0	1
				4.0	2.0	177.0	1	16.5	2.7	1630.0	5				
				2.0	2.0	222.0	1		2.7	1630.0	5				
				7.0	2.0	389.0	1								
				7.0	2.0	333.0	1								
				20.0	2.0	303.0	1								
				3.0	2.0	455.0	1								
				0	2.0	455.0	1								

^aSoil type: 1, clay; 2, silt; 3, sand; 4, gravel; 5, rock.

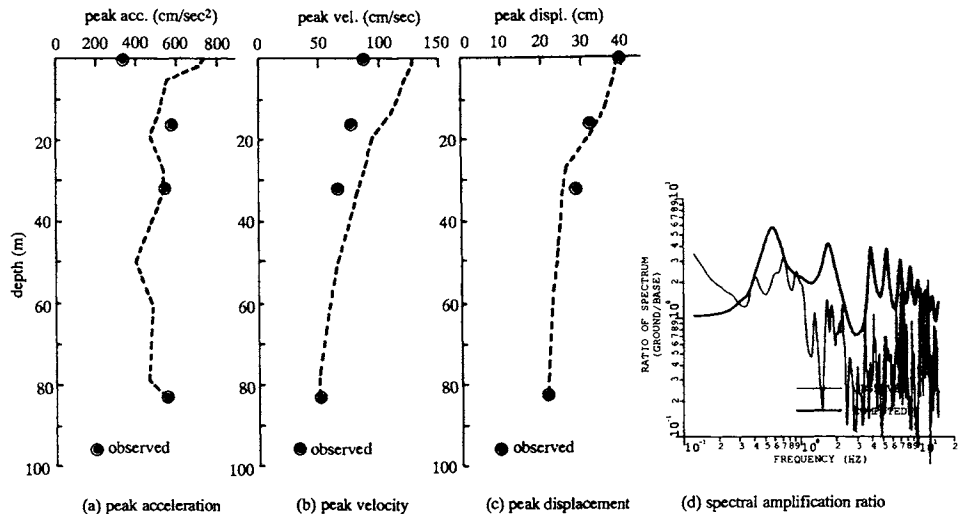


Fig. 17. Distribution of calculated peak ground motion and amplification function compared with records (PI Station).

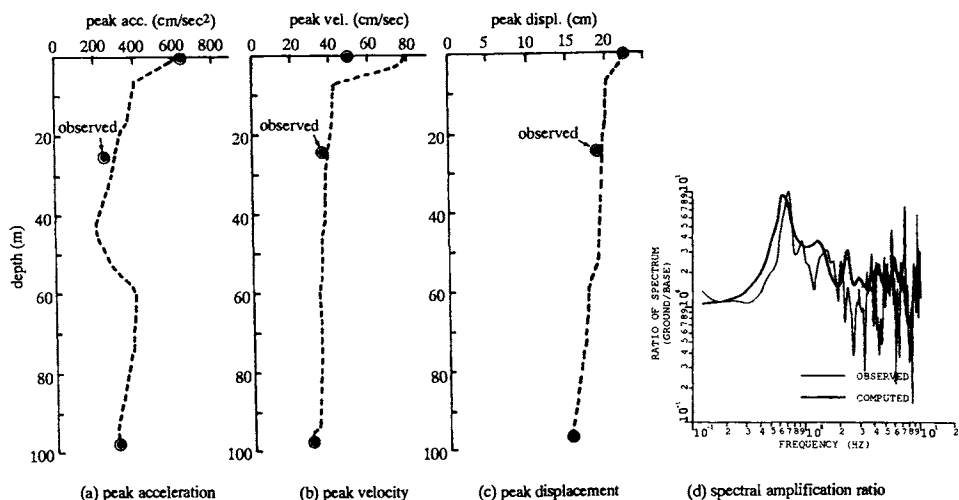


Fig. 18. Distribution of calculated peak ground motion and amplification function compared with records (TRS Station).

land. The calculated peak acceleration and velocity are relatively larger than those of the records. A lot of ground cracks were found in the area where the system was installed, and some soil liquefaction phenomena were found near this area. As shown in Fig. 20d, the severe de-amplification characteristics in the high frequency

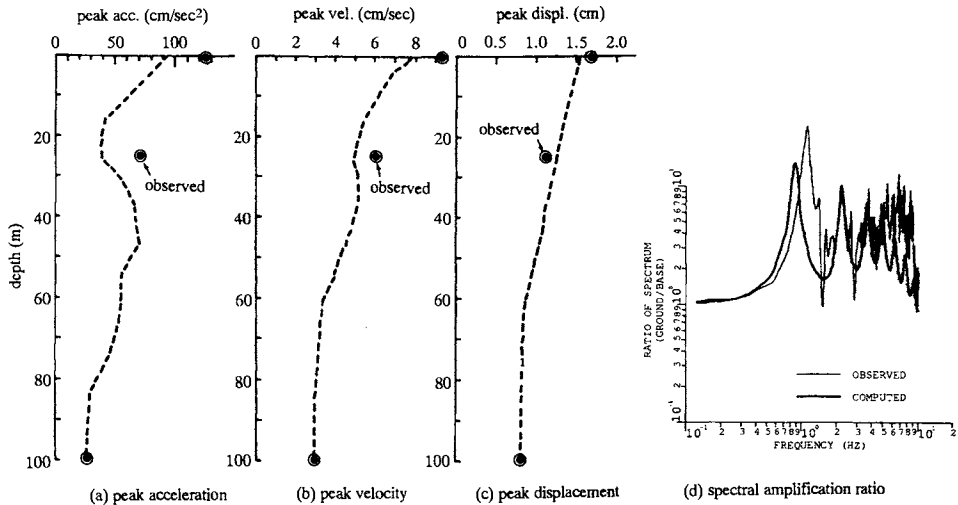


Fig. 19. Distribution of calculated peak ground motion and amplification function compared with records (KPS Station).

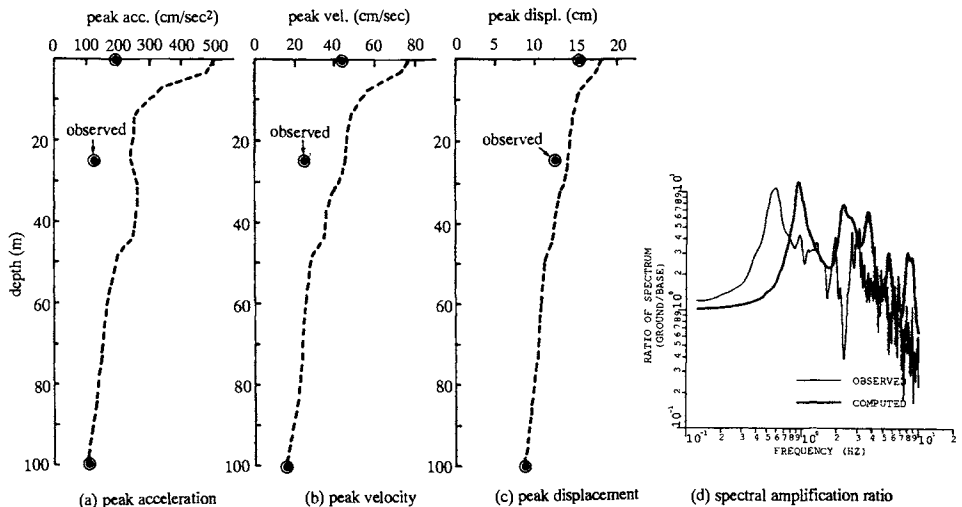


Fig. 20. Distribution of calculated peak ground motion and amplification function compared with records (TPS Station).

region are not found in the records. The predominant frequency of the first mode of calculated amplification function dose not coincide with that of the records. This might be derived from the error of the velocity structure model given in Table 3.

In conclusion, the technique used herein can generally estimate the ground motion

TABLE IV
Parameters for numerical analysis (Port Island Borehole Array Station)

Depth (GL, m)	Soil layer	Unit weight tf/m ₃ (N-value)	Void ratio, <i>e</i>	<i>V_s</i> (m/s)	Poisson's ratio, <i>v</i>	Coefficient of permeability (m/s)	Liquefaction strength	
							<i>N</i> =10	<i>N</i> =30
0.0	▲						—	—
-5.0	▽ Sandy gravel (reclaimed)	1.9 (5.2)	0.80	170	0.25	—	—	—
-12.6	Sandy gravel (reclaimed)	1.9 (6.5)	0.80	210	0.25	4.0×10^{-4}	0.16	0.13
-19.0	(-16 m) ▲ Sand with gravel (reclaimed)	1.9 (6.5)	0.80	210	0.25	4.0×10^{-4}	0.16	0.13
-27.0	Alluvial clay	1.6 (3.5)	1.20	180	0.30	1.0×10^{-8}	—	—
-33.0	(-32 m) Alluvial sand	1.9 (13.5)	0.75	245	0.25	1.0×10^{-4}	0.35	0.25
-50.0	▲ Diluvial sand with gravel	1.9 (36.5)	0.72	305	0.25	1.0×10^{-4}	0.40	0.30
-61.0	Diluvial sand	1.9 (61.9)	0.70	350	0.25	1.0×10^{-4}	—	—
-79.0	Diluvial clay	1.6 (11.7)	1.00	303	0.30	1.0×10^{-8}	—	—
-83.0	▲ (-83 m) dilu- vial sand with gravel	1.9 (61.9)	0.70	320	0.25	1.0×10^{-4}	—	—

▲, seismometer; $K_o = 0.5$.

except in the case of soil liquefaction. In the response analysis the shear stress is also given. Therefore the technique can be applied for the simple judgement of the occurrence possibility of soil liquefaction.

4.2. Effective stress-based liquefaction analysis method

Using the effective stress-based three-dimensional liquefaction analysis method, a simulation analysis of array record in Port Island is carried out to reproduce the liquefaction-induced damping of the horizontal ground motion and large amplification of the vertical ground motion in the reclaimed ground.

The constitutive model in the present study is based on the concept of non-linear kinematic hardening rule which had originally been used in the field of metal plasticity (Chaboche and Rousselier, 1983). Oka et al. (1992) derived a cyclic elasto-plastic constitutive model for sand through use of the concept of non-linear kinematic hardening. Tateishi et al. (1995) proposed a new stress dilatancy relationship and cumulative strain dependent characteristics of the shear modulus to modify the original model. Such a constitutive model is formulated under the three-dimensional stress conditions in the present study. The validity of the constitutive

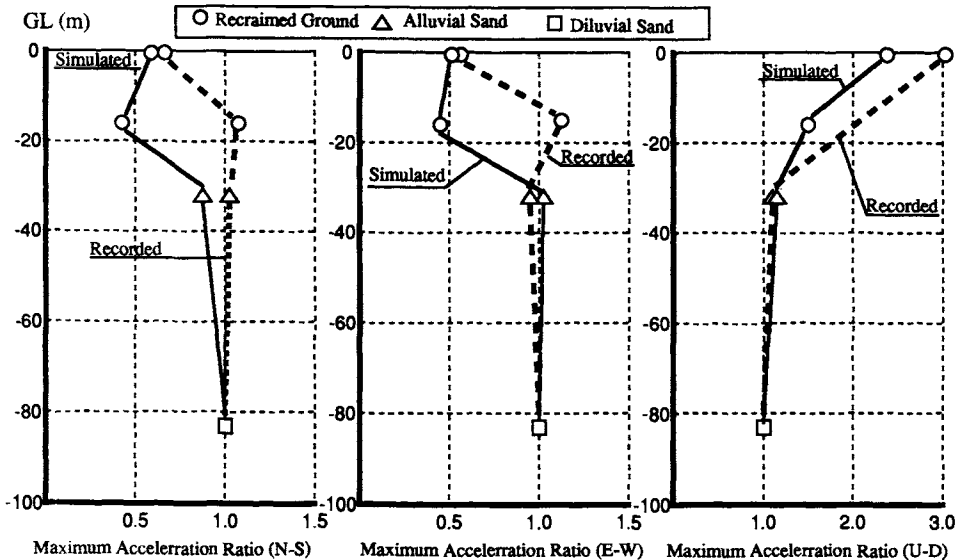


Fig. 21. Amplification properties of seismic motions at Port Island Array Observation Site (simulated and observed results).

model has been verified by the experimental evidence from the hollow cylindrical torsion tests under various stress conditions.

This constitutive model has been incorporated into a coupled finite element–finite difference (FEM–FDM) numerical method for the liquefaction analysis of a fluid-saturated ground. Using a u - p (displacement of the solid phase and pore water pressure of the liquid phase) formulation, the numerical method was developed (Shibata et al., 1991; Oka et al., 1994). The finite element method is used for the spatial discretization of the equilibrium equation, while the finite difference method is used for the spatial discretization of the continuity equation. Newmark's β -method is used for the time integration of both equations. The applicability of the proposed model for the actual ground (including model ground by centrifuge test) had been already verified by past studies (Taguchi et al., 1995a,b).

The single column ground model using the rectangular solid element mesh (39 elements and 160 nodes) is used for the analysis. Most numerical parameters for the analysis are determined based on the results of the past field investigations and laboratory tests. Some parameters which have not been given in such past studies are assumed. Basic numerical parameters are summarized in Table 4. Three components of acceleration records with correction of orientation error are applied at GL –83 m as the base input accelerations. One of the most important features of this analysis is the assumption of the unsaturation of the reclaimed layer below sea level. If the ground below sea level is assumed to be fully saturated, the P-wave velocity of that ground becomes very large. Under this circumstance, the response

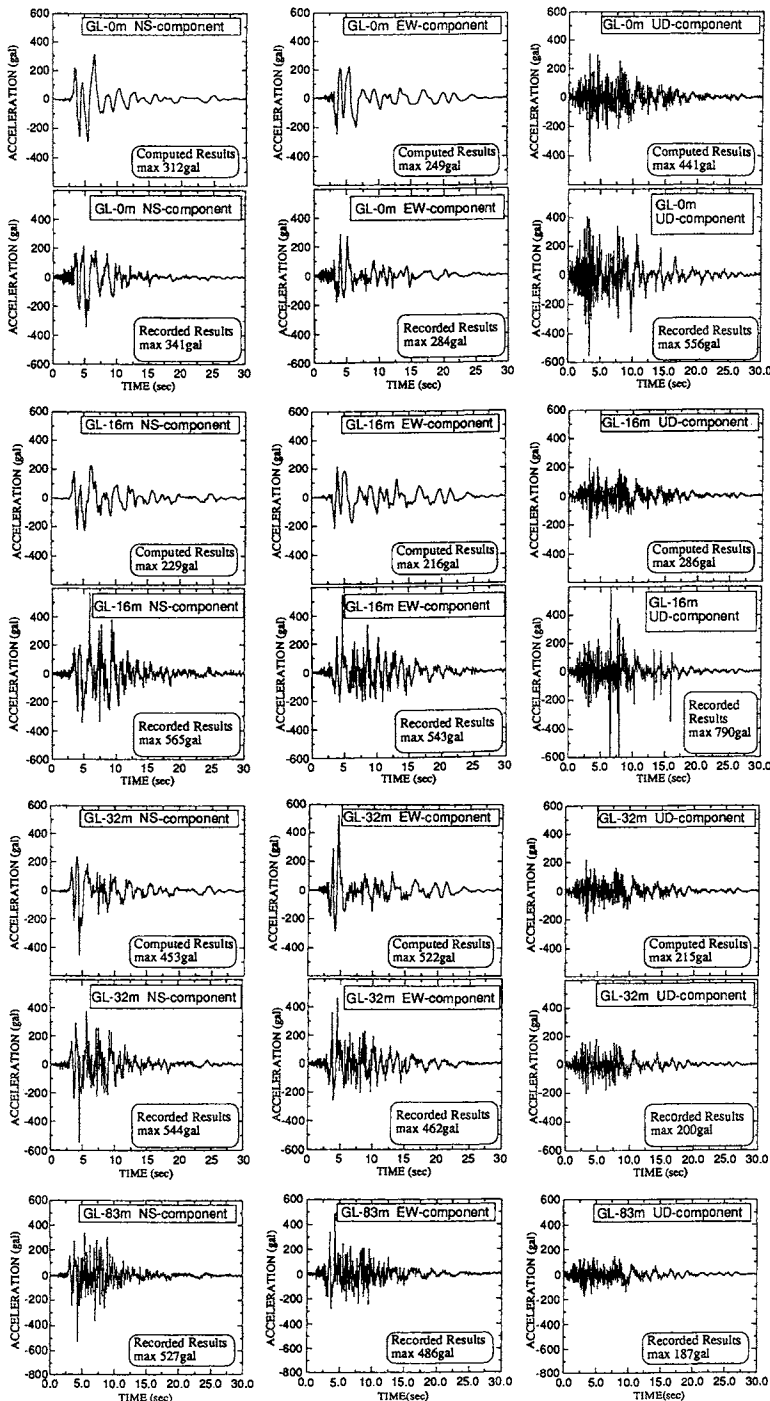


Fig. 22. Comparison of acceleration response (simulated and observed results).

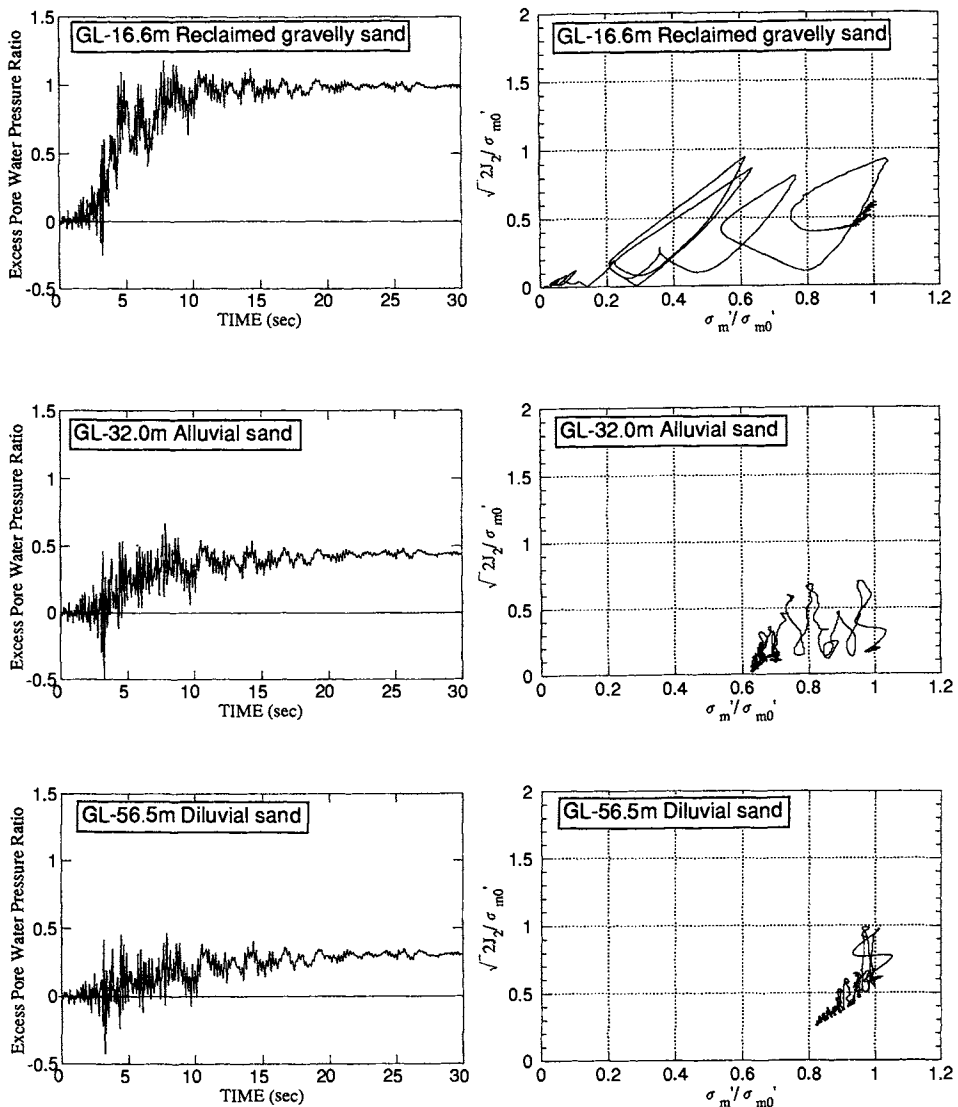


Fig. 23. Time histories of excess pore water pressure ratio and effective stress paths (simulated results).

of the ground due to P-wave almost coincides with that of the rigid body and little amplification of the vertical motion can be obtained. To get a finite value of the P-wave velocity in the reclaimed layer below sea level, the degree of saturation of 99.95% is introduced in this analysis which gives 2.1×10^6 kPa as the bulk modulus of the underground water.

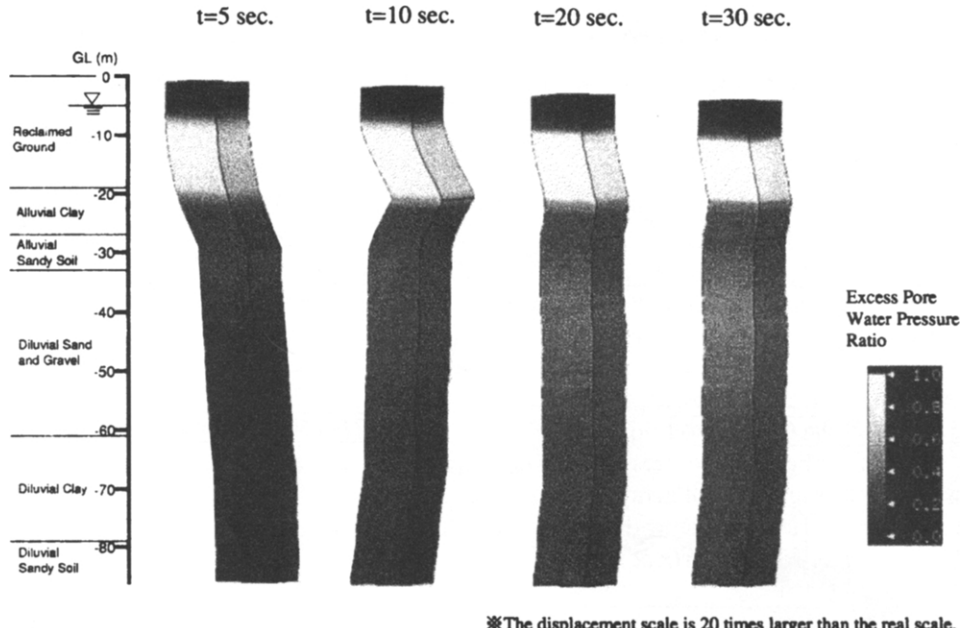


Fig. 24. Distributions of excess pore water pressure ratio along numerical columns.

The amplification properties of the seismic motions are summarized in Fig. 21. The simulated peak acceleration distributions of N–S, E–W and U–D components are plotted with the recorded ones. From this figure, it is shown that the numerical analysis can predict the liquefaction-induced damping of the horizontal accelerations in the reclaimed layer and large amplification of the vertical motion on the ground surface except at GL – 16 m. The measured record at GL – 16 m has little reliability as mentioned in Section 3.2. The time histories of the acceleration response in the simulation analysis are compared with those in the record in Fig. 22. The base (GL – 83 m) acceleration data shown in Fig. 8 are used in the simulation analysis. Fig. 23 shows the time histories of the excess pore water pressure ratios and the effective stress paths $\sqrt{2J_2}/\sigma'_{m0} \sim \sigma'_m/\sigma'_{m0}$ in the reclaimed ground (GL – 16 m), alluvial sandy soil layer (GL – 32 m) and diluvial sandy soil layer (GL – 57 m). Note that in the initial state, the excess pore water pressure ratio is zero. On the other hand, once the ground is liquefied, the excess pore water pressure ratio is 1.0. It can be readily seen that the reclaimed ground starts to liquefy at around 8 s on the time axis. On the other hand, the maximum values of the built up excess pore water pressure at deeper layers (GL – 32 and – 57 m), are found to be about 50–30% of the initial effective overburden pressures.

The distributions of the excess pore water pressure along the numerical column are plotted in Fig. 24. It is found from this figure that the whole reclaimed layer below sea level was liquefied by the strong motion during the event.

5. Conclusions

Major conclusions derived from this study may be summarized as follows.

(1) The strong motion records from the Southern Hyogo Earthquake of January 17, 1995, were overviewed. The two sets of strong motion records obtained in near field were introduced, and the horizontal displacement orbits for near field records were demonstrated with regard to the predominant direction of motions.

(2) The borehole array records at four stations were overviewed, and the corrections of the orientation errors of seismometers were discussed. The ground motion amplification characteristics at these stations were given.

(3) Seismic response analyses were performed for the four borehole stations. The frequency-dependent equi-linearized technique was applied and the results were compared with the records. The applicability of the technique was demonstrated, except for the case of soil liquefaction.

(4) Using the effective stress-based three-dimensional liquefaction analysis method, numerical simulations of array records in Port Island were carried out. The simulated result was found to reproduce the recorded time histories of accelerations in horizontal as well as vertical motions.

Acknowledgements

The authors would like to express their deep appreciation to Mr. Koichiro Yamada of Kobe City Development Bureau and Mr. Yoichi Kato of Kansai Electric Power Company for the strong motion array records used in this paper.

References

- Chaboche, J.L. and Rousselier, G., 1983. On the plastic and viscoplastic constitutive equations. Part I and Part II. *J. Pressure Vessel Technol.*, Trans. ASME, 105: 153–164.
- Committee of Earthquake Motion Observation and Research in Kansai Area, 1995. A Dataset of Strong Motion Records from the Hyogo, South Earthquake of 17 January 1995.
- Hanshin Public Expressway, 1995. A Dataset of Strong Motion Records from the Hyogo, South Earthquake of 17 January 1995.
- Japan Meteorological Agency, 1995. A Dataset of Strong Motion Records from the Hyogo, South Earthquake of 17 January 1995.
- Kamata, A., Oishi, H. and Sekiguchi, K., 1987. Three-dimensional earthquake observation of buried pipelines – Phase velocities of surface waves based on 3D-array observation records and evaluation of seismic vulnerability of Shitamachi Haisui-Kansen. *Suidou-Kyokai-Zasshi*, 56(5): 39–53 (in Japanese).
- Kameda, H., 1975. Evolutionary spectra of seismogram by multifilter. *J. Eng. Mech. Div. ASCE*, 101 (EM6): 787–80.
- Kashima, T. and Kitagawa, Y., 1995. The 1995 Hyogo-ken-nanbu Earthquake. Prompt Report on Strong Motion Records, Vol. 4, Building Research Institute, Ministry of Construction (in Japanese).
- Kobe City Development Bureau, 1995. A Dataset of Borehole Array Records at Port Island observed during the Hyogo, South Earthquake of 17 January 1995.

- Oka, F., Yashima, A., Kato, M. and Sekiguchi, K., 1992. A constitutive model for sand based on the non-linear kinematic hardening rule and its application. Proc. of 10th WCEE, 2529–2534.
- Oka, F., Yashima, A., Shibata, T., Kato, M. and Uzuoka, R., 1994. FEM-FDM coupled liquefaction analysis of a porous soil using an elasto-plastic model. Appl. Sci. Res., 52: 209–245.
- Oishi, H. and Sekiguchi, K., 1984. Earthquake observation of an underground pipeline and seismic response analysis. Proc. of 8th WCEE, 5: 295–302.
- Osaka Gas Company, 1995. A Dataset of Strong Motion Records from the Hyogo, South Earthquake of 17 January, 1995.
- Schnabel, P.B., Lysmer, L. and Seed, H.B., 1972. SHAKE a computer program for earthquake response analysis of horizontally layered sites. EERC, 72-12.
- Shibata, T., Satoh, T., Uzuoka, R., Oka, F., Yashima, A. and Kato, M., 1991. FEM-FDM coupled liquefaction analysis of a fluid saturated ground. Proc. of IACMG '91, pp. 869–874.
- Sugito, M., 1993. Frequency-dependent equivalent strain for earthquake response analysis of soft ground. Proc. of Third R.O.C. and Japan Joint Seminar on Natural Hazards Mitigation, Tainan, Taiwan, pp. 409–422.
- Sugito, M., Goda, H. and Masuda, T., 1994. Frequency dependent equi-linearized technique for seismic response analysis of multi-layered ground. J. Jpn. Soc. Civ. Eng., III-27: 493 (in Japanese).
- Sugito, M., Sekiguchi, K., Yashima, A., Oka, F., Taguchi, Y. and Kato, Y., 1995. Correction of orientation error of borehole strong motion array records obtained during the South Hyogo Earthquake of Jan. 17. J. Jpn. Soc. Civ. Eng., in press.
- Taguchi, Y., Tateishi, A., Higuchi, Y., Oka, F. and Yashima, A., 1995a. Cyclic constitutive model for sand using generalized flow rule and its verification with centrifuge tests. Proc. of 23rd JSCE Earthquake Engineering Symposium, pp. 329–332 (in Japanese).
- Taguchi, Y., Tateishi, A., Oka, F. and Yashima, A., 1995b. A cyclic elasto-plastic model for sand based on the generalized flow rule and its application. In: Pande and Pietruszack (Editors), 5th International Symposium on Numerical Models in Geomechanics. Balkema, Rotterdam, pp. 57–62.
- Tateishi, A., Taguchi, Y., Oka, F. and Yamashita, A., 1995. A cyclic elasto-plastic model for sand and its application under various stress conditions. In: K. Ishihara (Editor), 1st Int. Conf. on Earthquake Geotechnical Eng., IS-TOKYO '95. Balkema, Rotterdam, pp. 399–404.
- Technical Research Institute, Kansai Electric Power Company, 1995. A Dataset of Borehole Array Records at Osaka observed during the Hyogo, South Earthquake of 17 January 1995.
- The National Research Institute for Earth Science and Disaster Prevention, 1995. January 17, 1995 Southern Hyogo Prefecture (Prompt Report on Strong-Motion Accelerograms, No. 46) (in Japanese).
- Yamazaki, F., Lu, L. and Katayama, T., 1989. Orientation Error Estimation of Seismometers in Array Observation. Proc. JSCE, 432/I-16: 231–240 (in Japanese).

CHAPTER 3

Earthquake-related ground motion and groundwater pressure change at the Kamaishi Mine

ISAO SHIMIZU^{a,*}, HIDEAKI OSAWA^{a,1}, TOSHIHIRO SEO^b,
SHINJI YASUIKE^c and SYUNJI SASAKI^c

^aKamaishi Site Office, Power Reactor and Nuclear Fuel Development Corporation (PNC), Kamaishi, Iwate, Japan, ^bTono Geoscience Center, Power Reactor and Nuclear Fuel Development Corporation (PNC), Toki, Gifu, Japan and ^cAbiko Research Laboratory, Central Research Institute of Electric Power Industry, Abiko, Chiba, Japan

Abstract

The Power Reactor and Nuclear Fuel Development Corporation (PNC) has been conducting studies on earthquake effects at the Kamaishi Mine. The aims of the studies are to observe the attenuation characteristics of ground motion with depth, and to understand the influences of earthquakes on the deep groundwater. Seven seismographs have been installed at four different levels of the mine with depths varying from 0 to 600 m. According to the observations since January 1991, maximum acceleration recorded deeper than 150 m has a tendency to decrease to 1/4 to 1/2 of that at the ground surface. We also monitored water pressure in boreholes, inflow rate and electric conductivity of groundwater from drift wall, and the water chemistry before and after earthquakes. Twenty cases of earthquake-related changes in water pressure have been observed during the period from November 1991 to December 1994. The range of groundwater pressure changes are generally less than 0.1 kgf/cm² with a maximum of 0.35 kgf/cm². Almost all these changes tend to recover slowly to the original state within about one week. In these twenty cases the static crust strain calculated after Dobrovolsky et al. (1979) (*Estimation of the size of earthquake preparation zones. Pure Appl. Geophys.*, 117: 1025–1044) from the magnitudes and epicentral distances are larger than 10^{-8} . As interseismic variation, the annual groundwater pressure change is less than 1 kgf/cm², which corresponds well with the rainfall record.

1. Introduction

The PNC is conducting a comprehensive geoscientific research program to build a firm scientific basis for the safe disposal of high level radioactive waste in deep geological formations.

* Corresponding author.

¹Present address: Nuclear Materials Division, Nuclear Safety Bureau, Science and Technology Agency, Chiyoda, Tokyo, Japan.

Since 1988, in situ experiments in fractured rock have been performed at the Kamaishi Mine to try to understand the deep geological environment. Earthquake-related studies at the Kamaishi Mine have been carried out since 1990. The main objectives are to study model attenuation of ground motion due to earthquakes and to evaluate the influence of earthquakes on groundwater. In this paper we discuss some of the results concerning the attenuation of ground motions with depth and the groundwater pressure changes in boreholes in the Kamaishi Mine.

2. Geological setting

The Kamaishi Mine is located approximately 600 km north of Tokyo. The bedrock in the area consists mainly of Paleozoic to Mesozoic sedimentary formations, and early Cretaceous granitic rocks (Fig. 1).

The Ganidake igneous complex is mainly composed of granodiorite with minor amount of diorites and monzonites. The Kurihashi granodiorite is mainly composed of granodiorite and is distributed near the Ganidake igneous complexes. Skarns associated with the Ganidake granodiorite host the Fe–Cu ore bodies of the Kamaishi Mine along its contact with the sedimentary rocks.

The main experimental area is situated at the northern end of the EL. 550 m drift (550 m above sea level) located at a depth of about 300 m from ground surface, and the drift branches off to the northeast and northwest directions (NE and NW

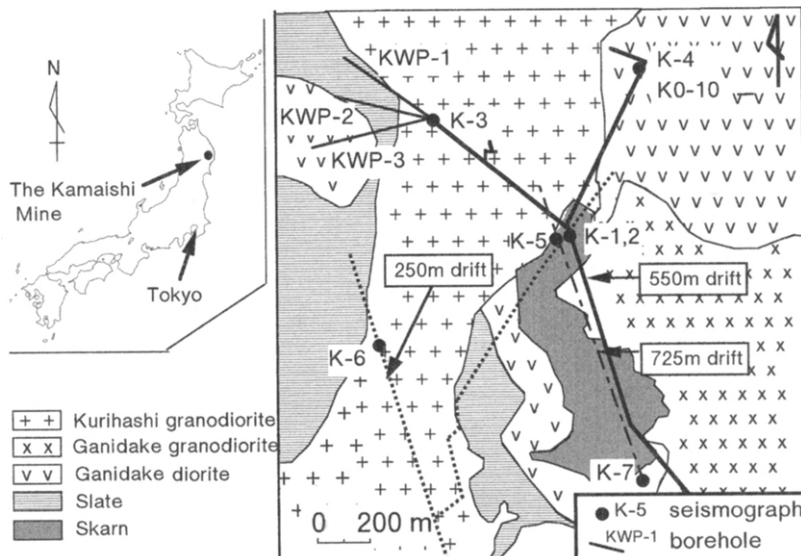


Fig. 1. Geological map of the area around the Kamaishi Mine. The map shows locations of seismographs and boreholes for monitoring of water pressure.

drifts). The NE drift runs mainly in diorite and the NW drift in granodiorite. Both areas have fractures developed mainly in the east–west direction. The KO-10 point of the NE drift is the main site for earthquake-related studies.

3. Observation methodology

3.1. Seismological observations

Seismological observations have been conducted since February 1990 to measure the attenuation characteristics of the ground motion at different levels in the Kamaishi Mine drifts (Fig. 2). Seismographs K-1, K-2, K-3 and K-4 were installed on February 1990, K-5 and K-6 were installed in January 1991. K-1, K-5, K-2 and K-6 seismographs are set on a vertical line. The K-6 seismograph is set at the deepest drift, approximately 650 m below the ground surface. The trigger level of seismographs K-1 to K-4 is 0.3 gal while that of K-5 to K-7 is 0.5 gal.

3.2. Monitoring of hydrology and chemistry of groundwater

The hydraulic and chemical characteristics of the groundwater have been observed at the locations indicated in Fig. 2. The monitored parameters are as listed in Table 1.

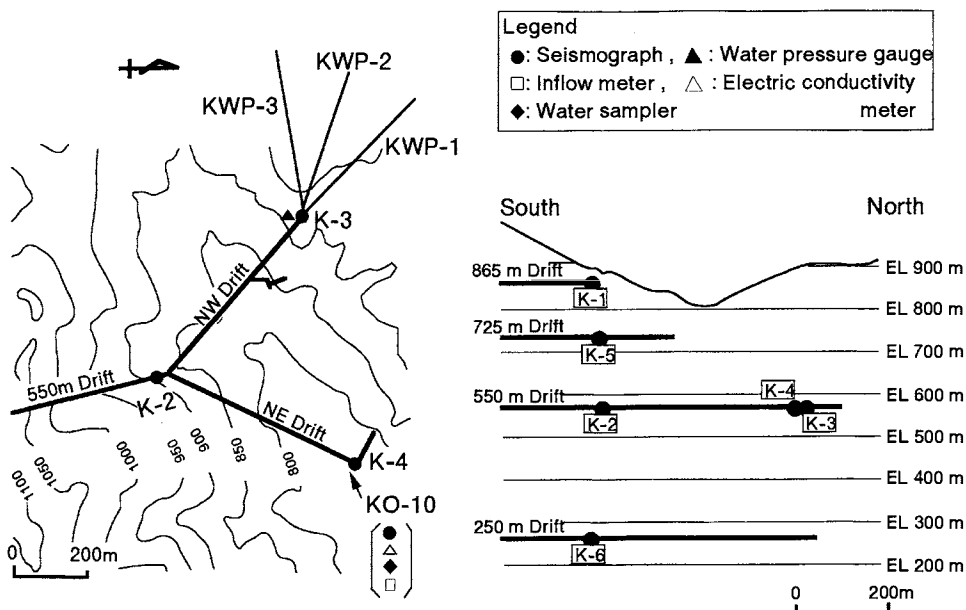


Fig. 2. Configuration of the instrumentation in the Kamaishi Mine

TABLE I
Monitored parameters

Items	Location	Rock type	Remarks
Water pressure	Borehole: drilled at end of 550 m drift KWP-1: length 458 m, horizontal KWP-2: length 393 m, -20 NW KWP-3: length 540 m, horizontal	Granodiorite/ sedimentary rock	Strain type, water pressure meters
Inflow rate	Drift wall: 550 m NE drift KO-10: fractures of E-W direction	Diorite	Weighing inflow by load cell
Electrical conductivity	Drift wall: 550 m NE drift KO-10: fractures of E-W direction	Diorite	Electrical conductivity (converted to 25°C)
Chemical components	Drift wall: 550 m NE drift KO-10: fractures of E-W direction	Diorite	Na, K, Ca, Mg, Cl, SO ₄ , HCO ₃ , SiO ₂

3.2.1. Monitoring of water pressure

Water pressure is monitored in three boreholes, which were drilled for mineral exploration during 1971 to 1973. These boreholes, located in the EL. 550 m drift approximately 300 m below ground surface, encounter sedimentary rocks at about 120 m from the drift wall. The monitoring was started in February 1990 by installing water pressure meters (resolution of approximating 0.001 kgf/cm²) of a strain guage type with measurement range of 0 to 50 kgf/cm². Measurement interval is set at 10 s.

3.2.2. Monitoring of inflow

The monitoring point of inflow is located at KO-10 in the EL. 550 m drift. The inflow from a drift ceiling dripped onto a vinyl sheet of about 2 m² size, and was introduced into a measuring tank (the size of the vinyl sheet was changed to about 1.5 m² from May 1993). The weight of the tank is measured by a load cell with a measurement range of 0–20 kg and a resolution of approximately 0.1 g. The tank is equipped with a siphon to drain excess water automatically. The measurement interval is set at 10 min.

3.2.3. Monitoring of electrical conductivity of groundwater

The monitoring point of electrical conductivity of groundwater is located at KO-10. The measurement error of the electrical conductivity is approximately 0.2 µS/cm. The data are converted automatically into those for water temperature of 25°C. The degree of electrical conductivity is highly dependent on water temperature, but the temperature of the inflow is stable at about 10°C. The measurement interval is set at 30 min.

3.2.4. Sampling and chemical analysis of groundwater

An automatic sampling system collects groundwater every 4 h. This system is equipped with 30 pairs of sampling containers (one pair consists of two 100 cc bottles), which rotate in a cycle of 120 h. An earthquake motion of over 4 gal is detected in the drift. The sampling system is set up to automatically stop after 96 h, thus we can get a rotation of the samples for the 24 h preceding the earthquake and the 96 h following the earthquake. The collected samples were analyzed in the laboratory for the chemical components listed in Table 1.

4. Results and discussion

4.1. Seismological observations

4.1.1. Seismic activity

Two hundred and eleven earthquakes with an acceleration of 0.5 gal and over were observed during the period from February 1990 to December 1994. The epicenters of these earthquakes, according to the Japan Meteorological Agency, were plotted on the Pacific Ocean side of Aomori to Fukushima prefectures, especially in the east off Iwate prefecture (epicentral distance of 20–120 km). The earthquakes were mostly of a magnitude smaller than 5. Maximum acceleration observed at the surface level of the Kamaishi Mine (K-1) were mostly below 4 gal. The distribution of epicenters for the 46 earthquakes over 0.5 gal which occurred between January and December 1994, is shown in Fig. 3. Table 2 shows major earthquakes observed at the Kamaishi Mine.

4.1.2. Comparison of acceleration observed at surface and underground levels

The ratios of maximum acceleration observed at seismographs K-1, K-5, K-2 and K-6 are shown in Fig. 4. Fig. 4 includes 41 ground motion data observed simultaneously by all four seismographs. The maximum accelerations at K-6 are about 1 to 1/2 times as large as those at K-2 and K-5, while accelerations at K-6 are only 1/2 to 1/4 times as large as those at K-1.

A numerical analysis was conducted using the superposed S-wave refraction theory (SHAKE code) to model the attenuation of earthquake motion. The “South off Kushiro” earthquake (Table 2) was quoted as the input seismic wave for SHAKE code. The results are given on the right-hand half of Fig. 5. The acceleration response obtained from the calculations corresponded closely with the data obtained from observations of both the east–west and the north–south components. It is thus possible to estimate the acceleration deep underground by using the “SHAKE” code.

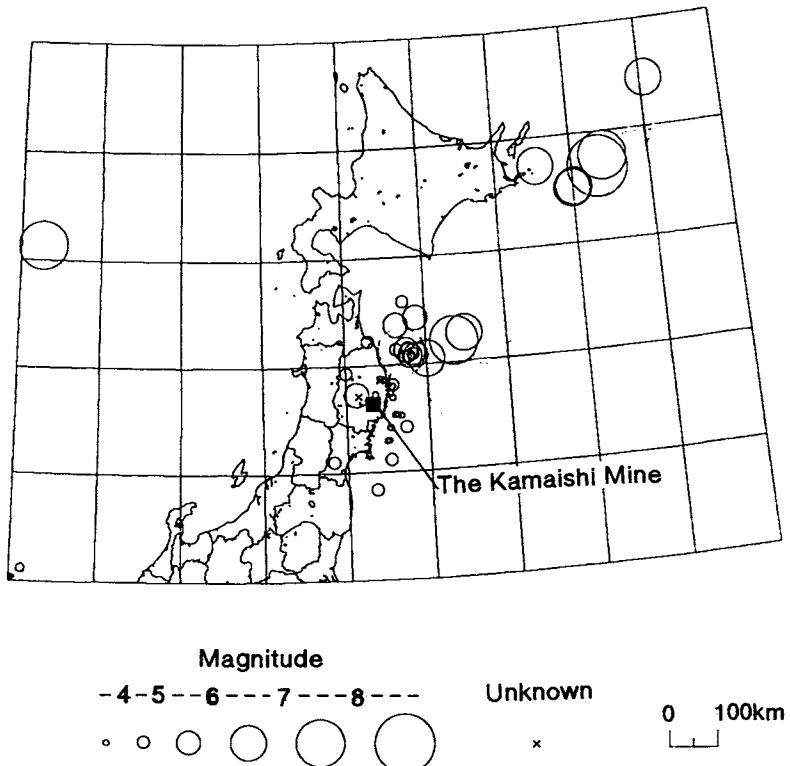


Fig. 3. Epicentral distribution of 46 earthquakes observed during the period from January 1994 to December 1994. The earthquakes larger than ~ 0.5 gal on the K-2 seismograph are plotted.

TABLE II
Major earthquakes observed at the Kamaishi Mine

Earthquake name and location	Data	Magnitude	Depth (km)	Epicentral distance (km)	Maximum acceleration (gal)
Major earthquakes by magnitude					
East off Hokkaido	10/4/94	8.1	30	675.1	36.9
South off Kushiro	1/15/93	7.8	107	455.7	24.5
Southeast off Hokkaido	7/12/93	7.8	34	438.9	1.4
Major earthquakes by acceleration					
North of Miyagi prefecture	11/27/93	5.9	112	84.5	53.0
East off Iwate prefecture	5/6/93	5.3	63	53.4	45.9
East off Hokkaido	10/4/94	8.1	30	675.1	36.9

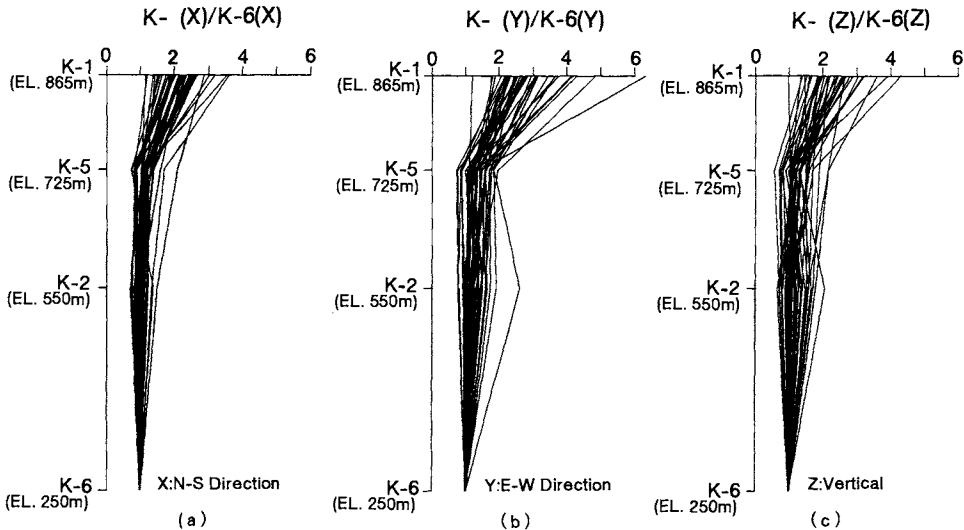


Fig. 4. Ratio of acceleration of earthquakes between the K-6 seismograph and another seismograph. (a) N-S direction, (b) E-W direction, (c) vertical direction. This figure includes 41 ground motions observed during the period from January 1991 to December 1994.

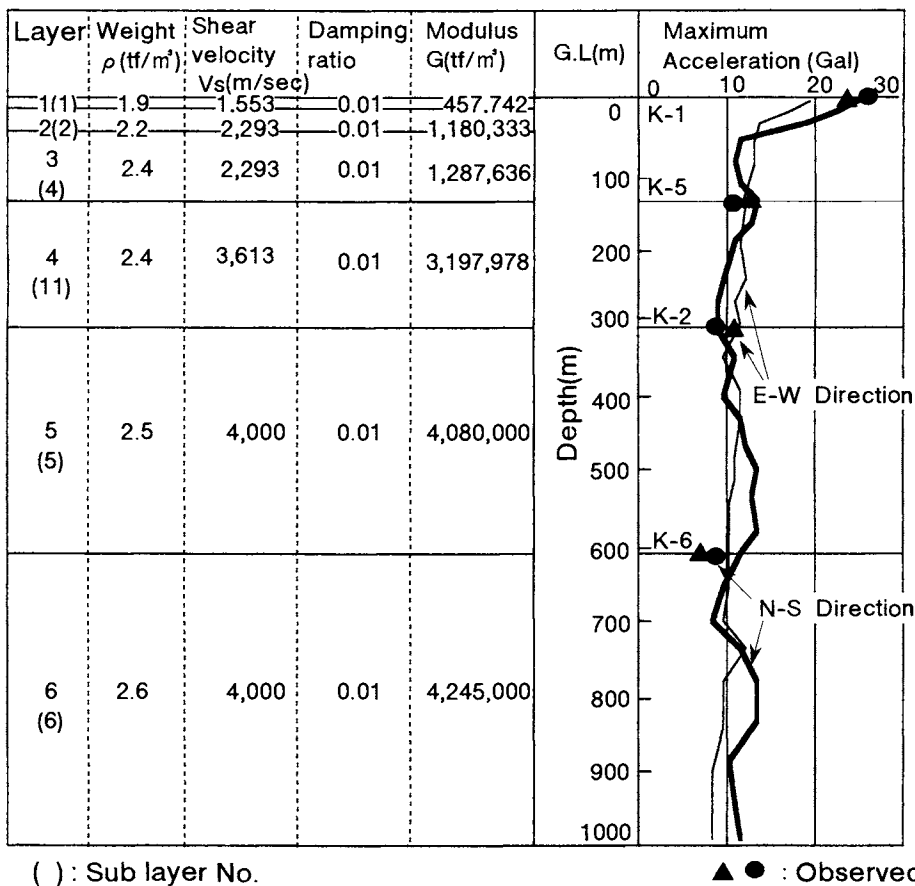
4.2. Monitoring of hydrology and chemistry of groundwater

4.2.1. Variation of water pressure

Fig. 6 shows an example of the long-term variation of water pressure for KWP-1 during November 1991 to December 1994. Data obtained were averaged for every 128 measurements (approximately every 21-min interval). The water pressure for KWP-1 is consistently low in winter (November to February) while it tends to rise rapidly in spring (April to May). Fig. 6 shows the monthly rainfall. Variations in the rainfall and water pressure for KWP-1 show a close correlation, and the annual range of water pressure variation is about 1 kgf/cm².

Fig. 7 shows the short-term periodic fluctuation of water pressure for KWP-1 which is considered to show an influence of the earth tide. In order to examine the relationship between the earth tides and water pressure fluctuation, the data for July 18–25, 1993, are shown in a greater detail. Tidal cycles shows a close correspondence to the water pressure fluctuation. The response of the water pressure spectrum to earth tides was examined using Fourier analysis. The results show that the amplitude of the water pressure fluctuation corresponding to the M2 earth tide is 6.2 cm for KWP-1, 3.5 cm for KWP-2, and 3.5 cm for KWP-3, as equivalent to water head value. According to Kawabe (1991), the calculated amplitude of water head corresponding to M2 earth tide using the equator conversion rate is 1–10 cm. The data for KWP-1 are also within this range. The boreholes for water pressure monitoring have been found to have a sensitive response to the earth tides.

As coseismic variation, Fig. 7 also shows the change in water pressure related to



() : Sub layer No.

▲ ● : Observed

Fig. 5. The result of SHAKE analysis. The data used for analysis is from the "South off Kushiro Earthquake" which occurred on January 15, 1993: the magnitude was 7.8, the epicentral distance is 455.7 km from the Kamaishi Mine.

an earthquake which occurred at 22:19, July 12, 1993. Immediately after the occurrence of the earthquake, the water head increased step-wise by approximately 20 cm and returned to the original trend in about a week. Such a change in water pressure was observed for 20 examples between January 1991 to December 1994. The ranges of the changes in water pressure observed at each borehole are shown in Fig. 8, and the location of epicenters for the earthquakes that triggered the changes in water pressure are shown in Fig. 9. As shown in Fig. 8, the maximum change in water pressure is the drop of 0.35 kgf/cm², while the others are within the range of approximately 0.1 kgf/cm². Almost all these changes recovered slowly to the original state within about one week.

Kawabe (1984, 1987, 1991), Igarashi and Wakita (1991) and Muir Wood (1994) have discussed the hydraulic and chemical phenomena related to earthquakes. In

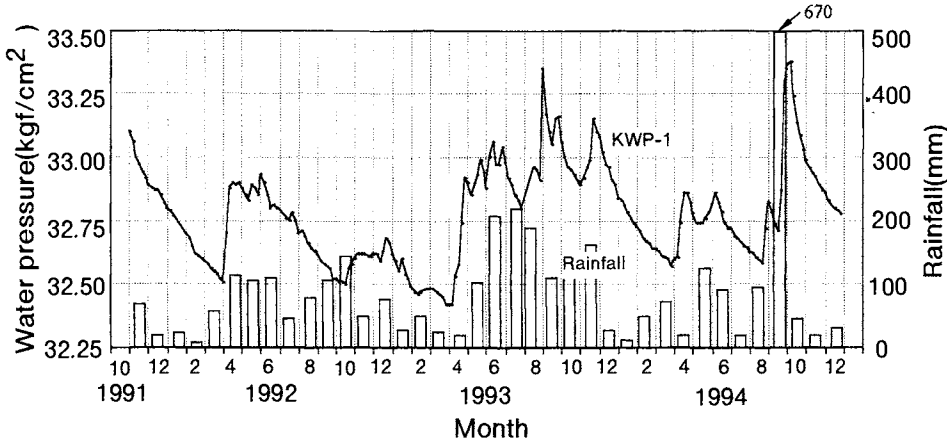


Fig. 6. Long-term variations of water pressure and rainfall during the period from November 1991 to December 1994. The water pressure was monitored for the KWP-1 borehole and the rainfall at Aonoki station which is located approximately 2 km north-east of the Kamaishi Mine.

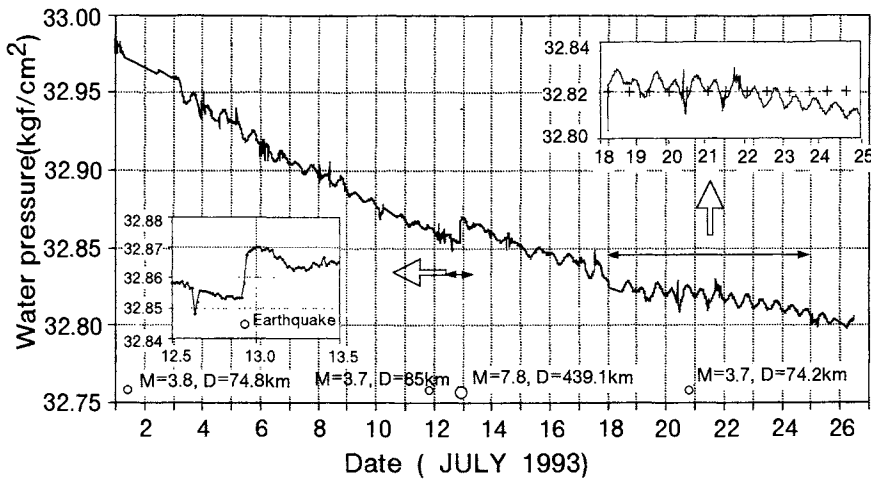


Fig. 7. Example of water pressure record for the KWP-1 borehole during the period from July 1 to July 26, 1993. Open circles indicate occurrence of earthquakes: M , magnitude; D , hypocentral distance. The + signs indicate the lunar half-day cycle (M2 principal lunar). The water pressure record shows periodic fluctuation and some step-changes when earthquakes occurred.

this paper, we discuss the water pressure changes from the viewpoints of maximum acceleration, magnitude and epicentral distance. The relationship between the maximum acceleration, observed by seismograph K-3 located in the vicinity of the water pressure monitoring boreholes, and the occurrence of changes in water pressure, is shown in Fig. 10. No water pressure change was observed for some earthquakes with accelerations as high as 18 gal, while water pressure changed in

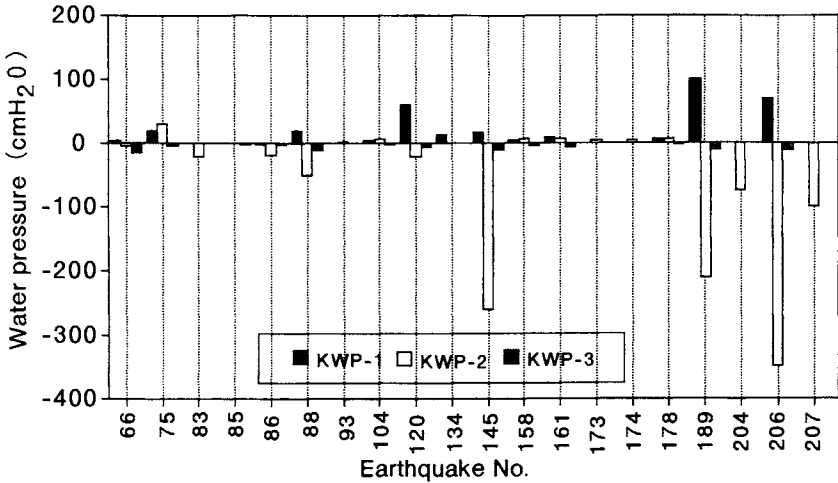


Fig. 8. Earthquake-related changes in water pressure during the period from January 1991 to December 1994. KWP-1 data show a tendency towards pressure rise, on the other hand KWP-2 data show a pressure drop.

response to the earthquakes with accelerations less than 2 gal. This implies that the maximum acceleration is not the critical factor in triggering a change in water pressure.

The comparison of magnitude and epicentral distance is shown in Fig. 11. The earthquakes, related to changes in water pressure, are plotted on an area of larger than 10^{-8} crustal strains, as calculated by using the soft inclusion model of Dobrovolsky et al. (1979). According to Shigetomi et al. (1992), the underground water pressure change induced by earthquakes reflects a static change in fault deformation rather than a dynamic vibration caused by earthquakes. In our observations, it appears that the changes in water pressure do not depend on principally maximum acceleration, but rather on theoretical crustal strain levels.

4.2.2. Variation of inflow

The long-term variation of inflow monitored at KO-10 is shown in Fig. 14. The inflow indicated no clear seasonal variation during the period from May 1993 to December 1994. The short-term variation is shown in Fig. 12. The flow is influenced by the earth tide. It is also closely related with atmospheric pressure. As the atmospheric pressure decreases, the total inflow increases. In Fig. 13, the influence of atmospheric pressure is eliminated from inflow data using the Simplex method to apply inverse Fourier analysis to the inflow. The results indicate that the range of inflow change caused by earth tide is 0.6 cc/min or 0.3% of the total inflow of 226 cc/min. So far, no clear change has been observed in the inflow with occurrence of earthquakes.

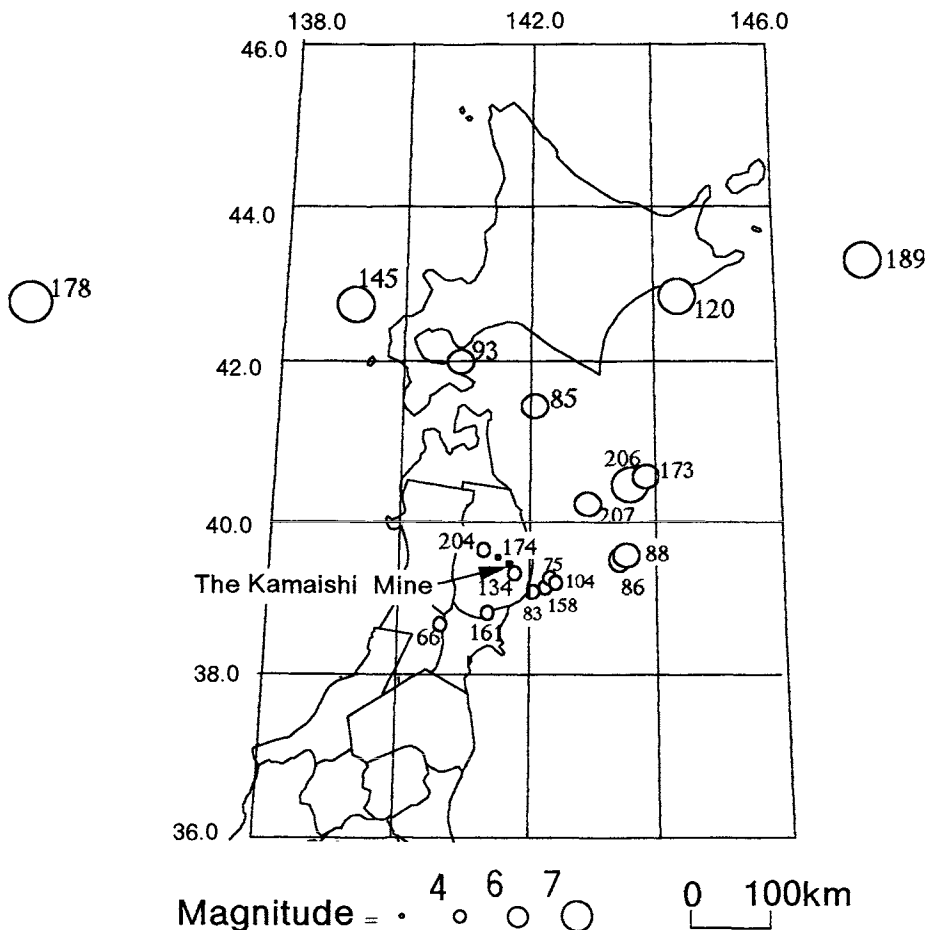


Fig. 9. Epicentral distribution of 20 earthquakes which induced changes in water pressure during the period from January 1991 to December 1994. The numbers in the figure indicate the earthquake number observed in the Kamaishi Mine.

4.2.3. Variation of electrical conductivity of groundwater

The long-term variation of electrical conductivity monitored at location KO-10 is shown in Fig. 14. A comparison between electrical conductivity and the water pressure for KWP-1 is also shown in Fig. 14. Electrical conductivity is low ($153 \mu\text{S}/\text{cm}$: the measurement error is $0.2 \mu\text{S}/\text{cm}$) during spring to summer when the KWP-1 water pressure is high. Likewise, electrical conductivity tends to become higher ($156 \mu\text{S}/\text{cm}$) during the winter season when KWP-1 water pressure is low. KWP-1 water pressure and electrical conductivity have a negative correlation. The value of seasonal variation of electrical conductivity is about 2%. So far, no clear change has been observed in the electrical conductivity due to occurrence of earthquakes.

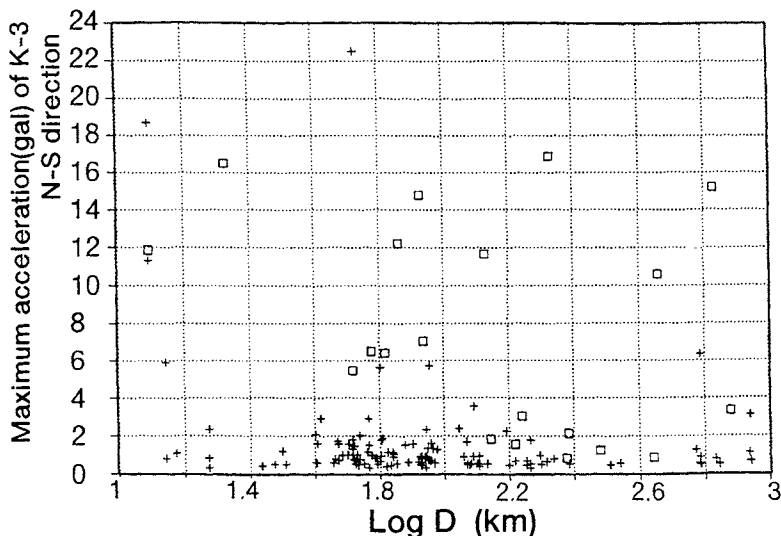


Fig. 10. Relationship between maximum acceleration and epicentral distance during the period from January 1991 to December 1994. \square , changes in water pressure observed; +, changes in water pressure are not observed.

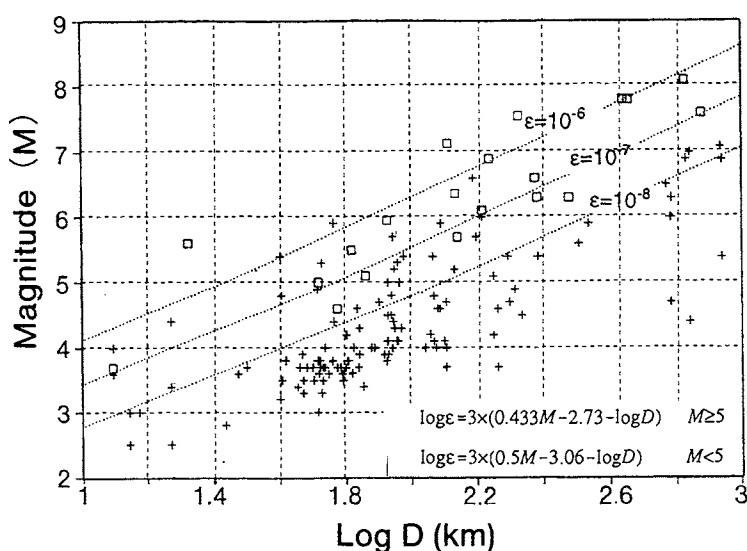


Fig. 11. Relationship between magnitude and epicentral distance (January 1991 to December 1994). D , epicentral distance from the mine., theoretical strain by Dobrovolsky et al. (1979). \square , changes in water pressure observed. +, no changes in water pressure observed. The formula by Dobrovolsky et al. (1979) is for the maximum deformation not the exact deformation in the mine.

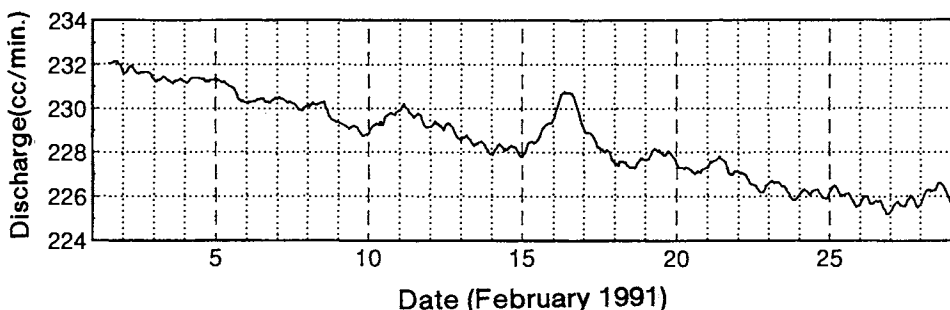


Fig. 12. An example of a groundwater inflow record from fractures at point KO-10. The record shows a periodic fluctuation of groundwater inflow. The inflow was gathered by using a 2-m² vinyl sheet.

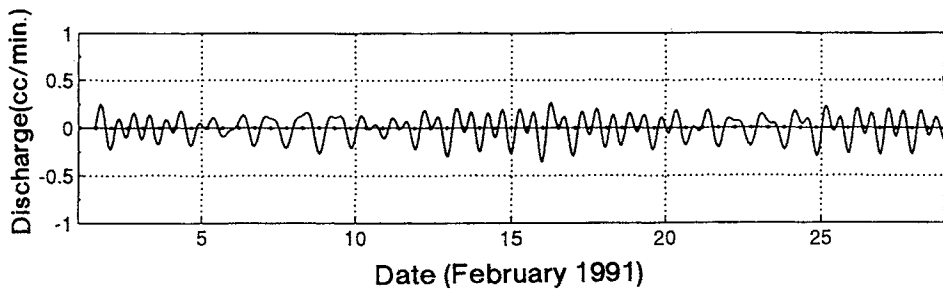


Fig. 13. Result of inverse Fourier transform of inflow data shown in Fig. 12.

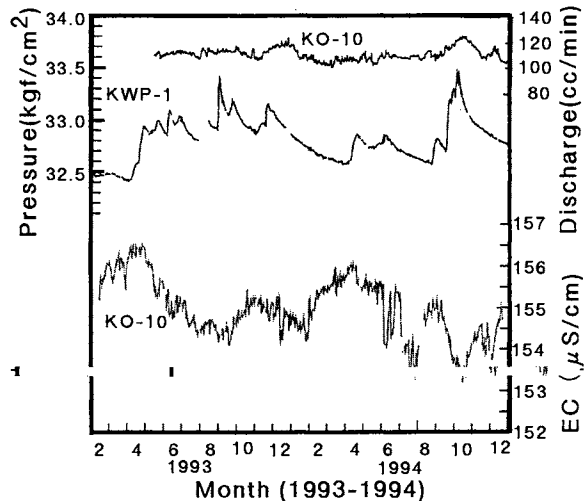


Fig. 14. Long-term variations of inflow and electrical conductivity in groundwater from fractures at point KO-10 and the water pressure at KWP-1. The inflow was gathered by using a 1.5-m² vinyl sheet.

4.2.4. Variation of water chemistry

With regard to seismogegeochemical studies before and after earthquakes, King et al. (1981) have reported on changes in ion concentrations of Na^+ and SO_4^{2-} in water taken from a well. In the Kamaishi Mine, the automatic water sampling system worked with 10 earthquakes as of December 1994. Of the 10 earthquakes, four have resulted in an apparent decrease in the ion concentration of SO_4^{2-} (maximum 4 mg/l) and an increasing trend for that of HCO_3^- , (Fig. 15). But it is not certain whether these change are related to the earthquake. It is necessary that further monitoring be continued.

5. Conclusions

From the earthquake observation and hydraulic studies conducted within the Kamaishi Mine, the following conclusions can be drawn. (1) Accelerations vary with depth, where accelerations at 650 and 150 m below ground surface are 1/2–1/4 times and 1–1/2 times, respectively, the surface values. (2) From the monitoring data of underground water pressure at depths below 300 m, water pressure changes

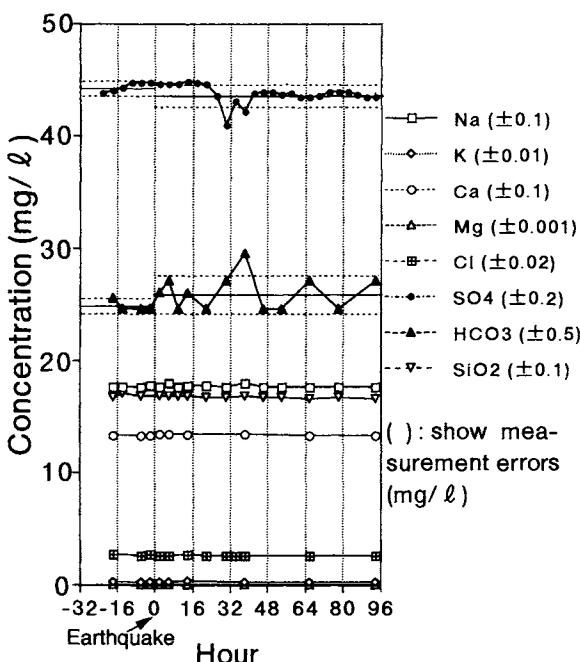


Fig. 15. Variations of ion concentrations of groundwater samples taken from fractures at point KO-10. Horizontal lines indicate average value, and horizontal dotted lines indicate one standard deviation. Hour "0" shows the exact time that the earthquake occurred (September 6, 1993, $M=4.0$, depth = 22 km, epicentral distance = 12.4 km).

about 1 kgf/cm² due to seasonal variation of rainfall and about 0.006 kgf/cm² due to the influence of earth tides. (3) The changes in water pressure related to earthquakes follow a step-wise change and these changes recover slowly to their original state: within about one week. These changes were mainly around 0.1 kgf/cm², with a maximum recording of 0.35 kgf/cm². (4) Earthquakes which cause changes in water pressure have theoretical earth crustal strain levels larger than 10⁻⁸. (5) With regard to inflow and electrical conductivity, no significant changes have been observed upon occurrences of earthquakes. (6) An apparent change in the chemistry of inflowing water occurred during earthquakes. However, further study is required to ascertain whether these changes are related to the earthquakes.

Acknowledgements

This study has been partially conducted under the guidance of an Advisory Committee of “The study on earthquakes in the in-situ experiments at the Kamaishi Mine”. We thank members of the Committee. The seismic information was kindly provided by the Japan Meteorological Agency.

References

- Dobrovolsky, I.P., Zubkov, S.I. and Miachin, V.I., 1979. Estimation of the size of earthquake preparation zones. *Pure Appl. Geophys.*, 117: 1025–1044.
- Igarashi, G. and Wakita, H., 1991. Tidal responses and earthquake-related changes in the water level of deep wells. *J. Geophys. Res.*, 96(B3): 4269–4278.
- Kawabe, I., 1984. Anomalous changes of CH₄/Ar ratio in subsurface gas bubbles as seismogegeochemical precursors at Matuyama Japan. *Pure Appl. Geophys.*, 122: 194–214.
- Kawabe, I., 1987. Identification of seismogegeochemical anomalies in subsurface gas CH₄/Ar ratio: Geochemical filtering of earthquakes. *Geochem. J.*, 21: 105–117.
- Kawabe, I., 1991. Hydro-geochemical anomalies associated with earthquakes. *Earthquakes*, 2(44): 341–364 (in Japanese with English abstract).
- King, C.Y., Evance, W.C., Presser, T. and Husk, R.H., 1981. Anomalous chemical changes in well waters and possible relation to earthquakes. *Geophys. Res. Lett.*, 8(5): 425–428.
- Muir Wood, R., 1994. Earthquakes, strain-cycling and the mobilization of fluids. In: *Geofluids: Origin, Migration and Evolution of Fluids in Sedimentary Basins*. *Geol. Soc. Spec. Publ.*, 78: 85–98.
- Shigetomi, K., Yamada, M. and Fujii, S., 1992. Coseismic changes in groundwater level at Osakayama. *Annu. Dis. Prev. Inst. Kyoto Univ.*, 35(B-1): 359–370 (in Japanese with English abstract).

CHAPTER 4

Fault movement and its impact on ground deformations and engineering structures

LUIS E. VALLEJO^{a,*} and MAHIRU SHETTIMA^b

^a*Department of Civil Engineering, 949 Benedum Hall, University of Pittsburgh, Pittsburgh, PA 15261, USA*
^b*J&L Environmental Management Corporation, Canonsburg, PA 15317, USA*

Abstract

In many regions around the world, engineering structures such as earth dams, buildings, pipelines, landfills, bridges, roads and railroads are often built in areas very close to strike-slip fault segments. For the safe design of these structures, earthquake and geotechnical engineers need a reliable estimate of the ground deformations that fault movements will induce at the sites of the proposed structures. The estimation of the vertical ground deformations associated with the movement of strike-slip fault segments is the focus of this proposed study. These vertical ground deformations are the result of stresses concentrated by the ends of active fault segments. In this study, the stresses and the resulting tri-dimensional vertical ground deformations that develop around moving fault segments were obtained using linear elastic fracture mechanics theory. The theoretical analysis was used to estimate the amount of vertical deformation experienced by the ground surrounding a strike-slip fault segment in China that mobilized during the 1970 Tonghai earthquake. The calculated vertical deformations and the ones measured in the field compared well.

1. Introduction

In many regions around the world, engineering structures such as embankment dams, tunnels, bridges, roads, railroads, commercial buildings, houses, water wells and sewer lines are often built in areas very close to strike-slip fault segments (Sherard et al., 1974; Seed et al., 1978; Seed, 1979; Billings, 1985; Bonilla, 1991). Many of these structures have been damaged as a result of fault movement. When a strike-slip fault segment moves, the ground surrounding the segment is subjected to two very different types of displacement. The first type of displacement is the one associated with the accumulated strain energy suddenly released by the rock during the slippage of the fault. The strain energy released causes the development of stress waves in the ground (ground shaking). The second type of ground displacement is the one associated with the fault end-induced stresses (Chinnery,

* Corresponding author. Tel.: 412 624 9884; Fax: 412 624 0135.

1961, 1963; Bilham and King, 1989). Chinnery (1961, 1963) used dislocation theory to calculate the deformations of the ground surrounding active strike-slip fault segments. Bilham and King (1989) used the boundary element method to calculate the deformations. Pollard and Segall (1987) developed the theoretical base to calculate the stresses and deformations around fault segments using fracture mechanics. However, in their analysis, the vertical ground deformations around active fault segments were not fully analyzed. In the present study, a tri-dimensional analysis of the vertical ground deformations associated with active strike-slip fault segments is obtained using the principles of linear elastic fracture mechanics theory.

2. Fault segmentation

Recent field investigations have demonstrated that faults are discontinuous geological features consisting of numerous discrete segments that have continuity, character, and orientation. Field research has also revealed that, during an earthquake, each segment forming part of a fault system mobilizes as a unit (i.e. the strike-slip fault segments forming part of the San Andreas fault system) (Chinnery, 1961; Segall and Pollard, 1980; Russ, 1982; Kasahara, 1985; Schwartz and Coppersmith, 1986). This discontinuous nature of faults allows them to be treated as large cracks in brittle materials. Thus, linear elastic fracture mechanics theory can be used to evaluate the stresses and the associated ground displacements resulting from fault movements (Shettima, 1990).

Examples of fault segmentation can be seen in Figs. 1–4. Fig. 1 shows three strike-slip fault segments in China (Zongjin et al., 1990). Fig. 1 also indicates the location of the vertical ground deformations that developed around the segments during earthquakes that took place between 1970 and 1976. Fig. 2 indicates the ground deformations associated with the Coyote Creek strike-slip fault system in California composed of two overlapping strike-slip faults (Segall and Pollard, 1980). Fig. 3 shows the strike-slip fault segments that form the Brawley and Imperial fault system at the Imperial Valley in southern California (Segall and Pollard, 1980). Fig. 4 shows the two strike slip fault segments in the area in New Madrid, Missouri (Russ, 1982).

3. Ground deformations around strike-slip faults

Fig. 1 and Table 1 show the location and amount of vertical deformation experienced by the strike-slip fault segments located in China. The ground deformations associated with the mobilization of the faults are concentrated at the tips of the segments. The vertical ground deformations take the form of subsidence and uplift zones. The subsidence and uplift zones are the result of stress concentrations developed at the ends of the segments. These stress concentrations are a function of the tectonic shear stresses that caused the mobilization of the fault segments (Vallejo, 1987; Vallejo and Liang, 1994).

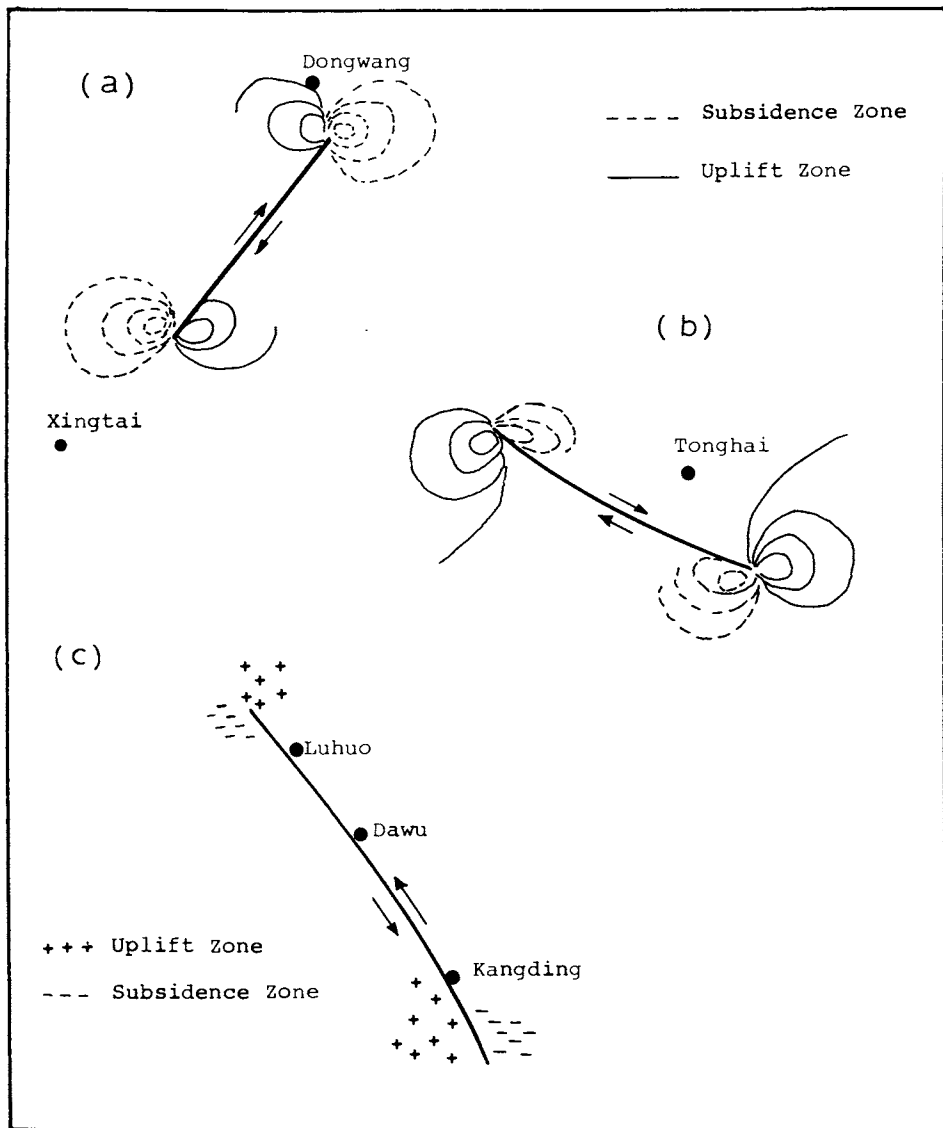


Fig. 1. Strike-slip fault segments in China with zones of subsidence and uplift (Zongjin et al., 1990).

Figs. 2–4 show the ground deformations associated with two overlapping strike-slip fault segments. The ground surface located between the two overlapping segments is subjected to the combined effect of the stress concentrations induced by the ends of the two segments. Fig. 2 shows two left-stepping strike-slip segments forming part of the Coyote Creek fault system in California. For a right lateral shear stress, the overlapping section between the fault segments warped into an

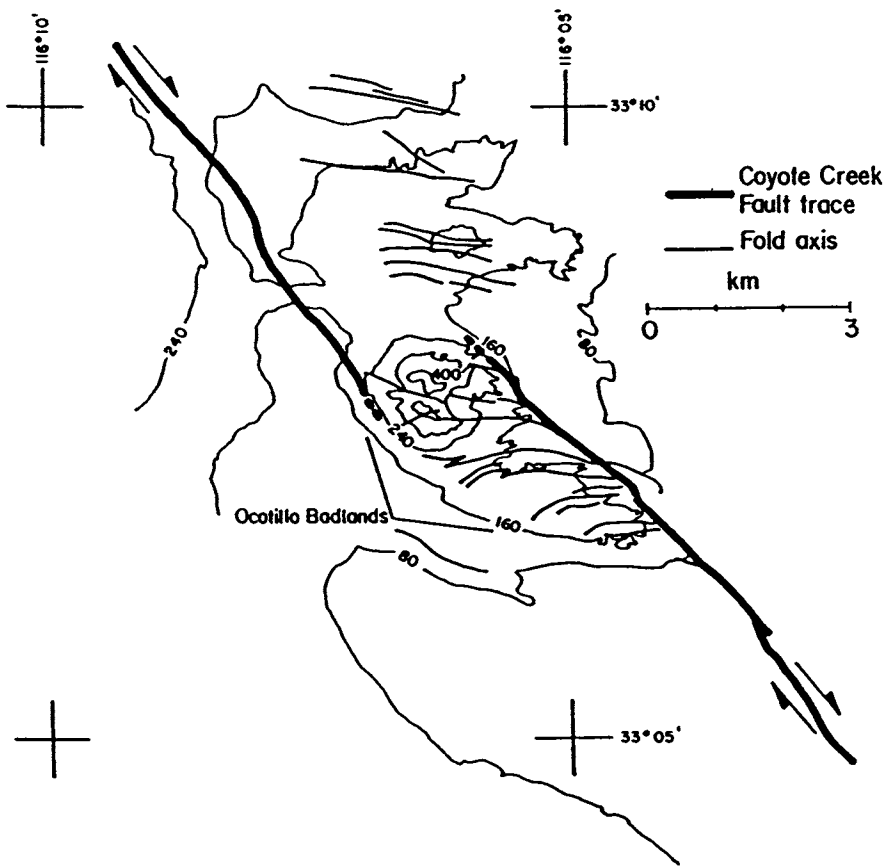


Fig. 2. Ground deformations around two left-stepping strike-slip fault segments forming the Coyote Creek fault system in California (Segall and Pollard, 1980).

anticlinal dome 200 m in height, known as the Ocotillo Badlands. The length of the dome is about 10 km. (Sharp and Clark, 1972). Fig. 3 shows two right-stepping strike-slip fault segments located near the town of Brawley, California. The two strike-slip fault segments developed in their overlapping section a 10-m deep topographic depression known as Mesquite Lake (Johnson and Hadley, 1976). The length of the depression zone is about 6 km. Fig. 4 shows the ground displacement induced when two left-stepping strike-slip fault segments interact and deform the ground between them. The two fault segments are located in the New Madrid area of Missouri (Russ, 1982). The region between the fault segments, called the Lake County uplift, was upwarped as much as 10 m above the general level of the Mississippi River Valley in parts of Tennessee, Missouri and Kentucky (Russ, 1982). The deformed area has a maximum length roughly north-south of about 50 km and a maximum width of about 23 km.

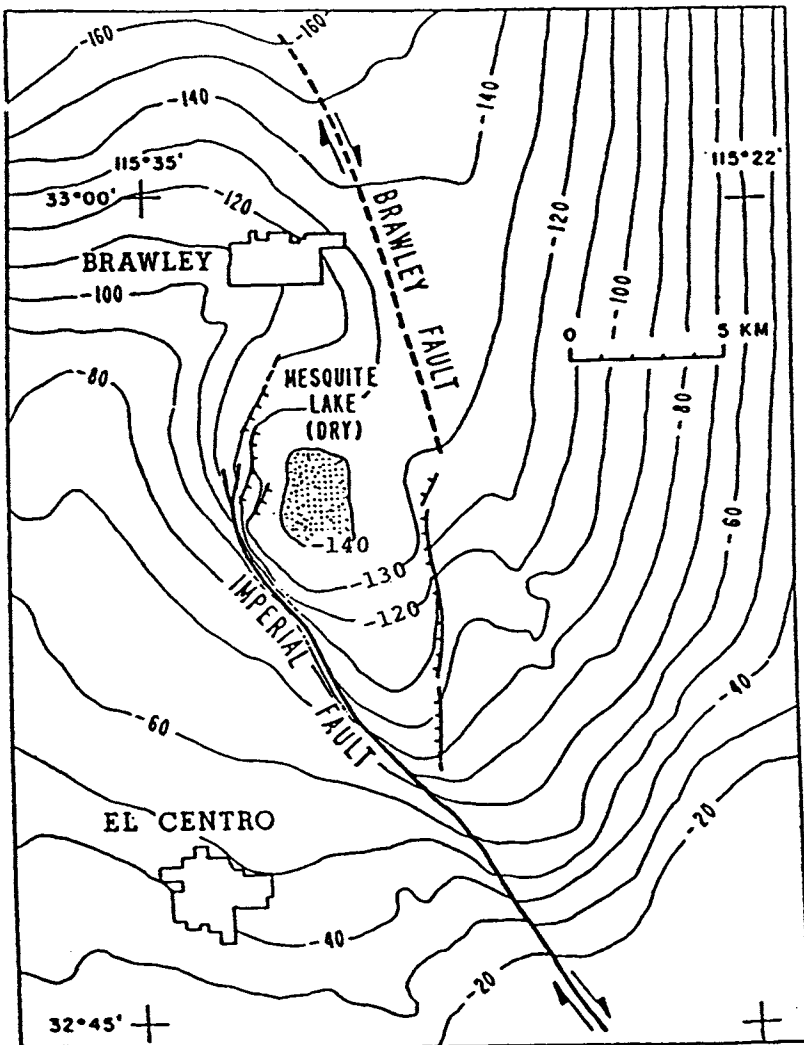


Fig. 3. Ground deformations around two right-stepping strike-slip fault segments at Imperial Valley, California (Segall and Pollard, 1980).

4. Impact of the ground deformations on engineering structures

As shown by Figs. 1–4, one of the effects of the mobilization of a strike-slip fault segment is to deform the ground that surrounds the tips of the segments. If a structure such as a building, earth dam, bridge, pipeline, etc., is located in the deformed zones, it could experience damage as a result of: (1) tensile and compressive

TABLE I

Subsidence and uplift at the tips of strike-slip fault segments shown in Fig. 1^a

Fault name	Length (km)	Maximum subsidence (cm)	Maximum uplift (cm)
Xingtai	90	-44	6
Tonghai	52	-23	6
Luhuo	110	-30	-

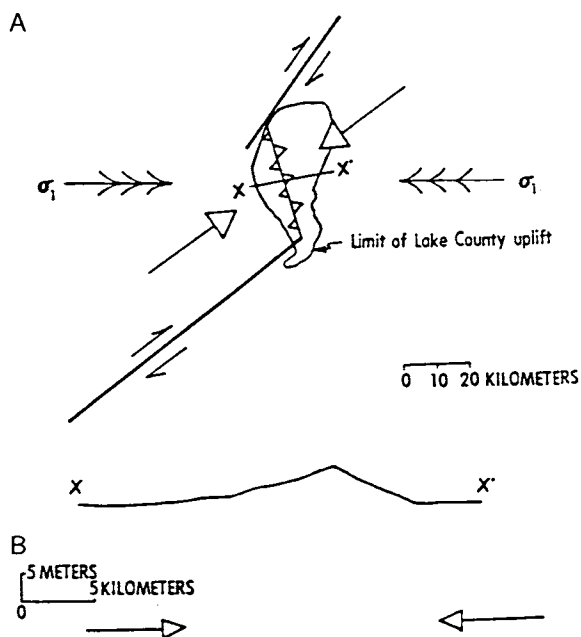
^aThe above data was obtained from Zongjin et al. (1990).

Fig. 4. Ground deformations around two left-stepping strike-slip fault segments near New Madrid, Missouri (zig-zag triangles indicate zone of compression; arrows represent direction of compressive stresses) (Russ, 1982).

strains that developed in the uplift and subsidence zones respectively, and (2) slope changes in the ground surface.

Slope changes in the ground surface, also referred to as differential settlements or tilt, could affect the gradient of roads, rail tracks, gas and water mains and the overall drainage pattern of the area surrounding strike-slip fault segments. Tilting can be detrimental to earth dams, buildings, machine and water tanks (Bjerrum, 1963; Wahls, 1981; Bonilla, 1991). In addition, an increase in the ground slope may increase the erosion potential of soils in agricultural areas. If structures located around strike-slip fault segments are going to be safe with respect to the strains and

slope changes induced in the ground by the fault end-induced stresses, a rational estimate of the ground displacements is of great importance for the safe design of the structures. Ground-structure interaction analysis requires a knowledge of the shape of the deformed ground surface in order to calculate the stresses and deformations induced in engineering structures when located on or near strike-slip fault segments.

The ground deformations around active strike-slip fault segments have been calculated by Chinnery (1961) using elastic dislocation theory. Bilham and King (1989) made use of the boundary element method to obtain the ground deformations. Pollard and Segall (1987) developed the theoretical base to calculate the stresses and deformations around fault segments using fracture mechanics. However, in their analysis, the vertical ground deformations around active fault segments were not fully analyzed. In the present study, a tri-dimensional analysis of the vertical ground deformations associated with active strike-slip fault segments is obtained using the principles of linear elastic fracture mechanics theory (Lawn and Wilshaw, 1975; Jayatilaka, 1979; Shettima, 1990; Vallejo and Liang, 1994).

5. Theoretical analysis

5.1. Stresses

In order to calculate the vertical ground deformations associated with the stresses induced by the ends (tips) of a strike-slip fault segment, the segment will be analyzed as a discrete planar crack of fixed depth, length, and orientation located in a homogeneous linear elastic layer of thickness, H , representing the depth of the earth's crust (Fig. 5). The crack is assumed to fully penetrate the crust, which is assumed to float on a fluid medium representing the earth's mantle. This crust-fluid medium approach has been found by Bilham and King (1989) to represent well the earth's upper crust for any theoretical analysis involving faults. The fault segment is assumed closed. Acting on the closed segment are: (a) a tectonic shear stress resulting from plate movement, σ_{tt} , and (b) a frictional shear stress, σ_{ff} , acting on the walls of the fault segment which is mobilized when the fault is activated. This frictional stress opposes the tectonic shear stress. During the mobilization of the fault segment, it will be subjected to a net far field shear stress, σ_{xy}^{∞} , that is equal to the tectonic shear stress, σ_{tt} , minus the frictional shear stress, σ_{ff} (Fig. 5).

According to Pollard and Segall (1987) and Shettima (1990), the system of stresses, σ_{xx} , σ_{yy} , and σ_{xy} , acting on an element in the elastic material surrounding the fault segment can be obtained from the following relationships (Fig. 5):

$$\sigma_{xx} = \frac{2\sigma_{xy}^{\infty}r}{\sqrt{r_1r_2}} \sin\left(\theta - \frac{\theta_1 + \theta_2}{2}\right) - \frac{\sigma_{xy}^{\infty}a^2r \sin\theta}{(r_1r_2)^{3/2}} \cos\left(3 \frac{\theta_1 + \theta_2}{2}\right) \quad (1)$$

$$\sigma_{yy} = \frac{\sigma_{xy}^{\infty}a^2r \sin\theta}{(r_1r_2)^{3/2}} \cos\left(3 \frac{\theta_1 + \theta_2}{2}\right) \quad (2)$$

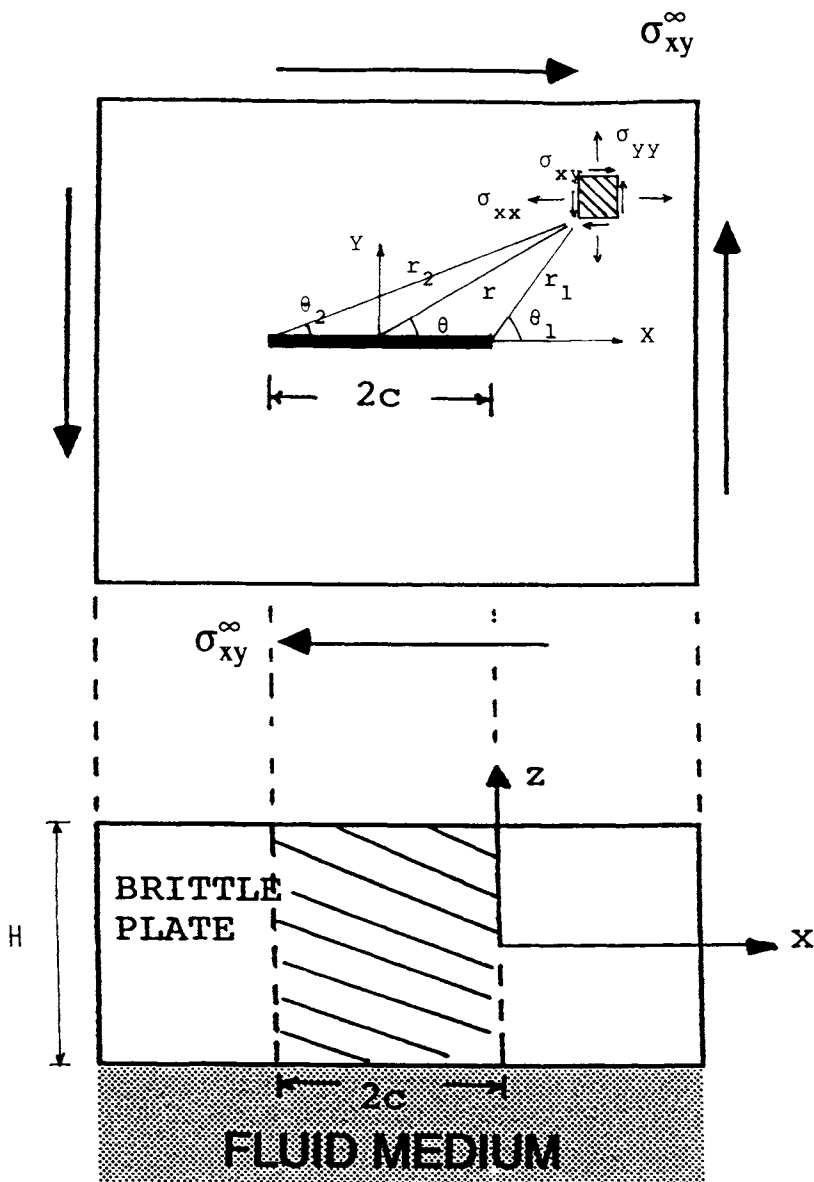


Fig. 5. System of stresses associated with a strike-slip fault segment idealized as a shear (Mode II) fault.

$$\sigma_{xy} = \frac{\sigma_{xy}^\infty r}{\sqrt{r_1 r_2}} \cos \left(\theta - \frac{\theta_1 + \theta_2}{2} \right) - \frac{\sigma_{xy}^\infty a^2 r \sin \theta}{(r_1 r_2)^{3/2}} \sin \left(3 \frac{\theta_1 + \theta_2}{2} \right) \quad (3)$$

where r_1 , r_2 and r are the radial distances from the tips and center of the segment

to the point around the fault segment where the stresses and deformations are required (Fig. 5). θ , θ_1 and θ_2 are the angles that r , r_1 , and r_2 make with the plane of the fault segment (Fig. 5). c is half the length of the fault segment.

For regions close to the tips of a fault segment ($r_1=0.01c$ in Fig. 5), the values of σ_{xx} , σ_{yy} and σ_{xy} from Eqs. (1)–(3) reduce to the following relationships (Jayatilaka, 1979):

$$\sigma_{xx} = -\frac{K_{II}}{\sqrt{2\pi r}} \sin\left(\frac{\theta}{2}\right) \left\{ 2 + \cos\left(\frac{\theta}{2}\right) \cos\left(\frac{3\theta}{2}\right) \right\} \quad (4)$$

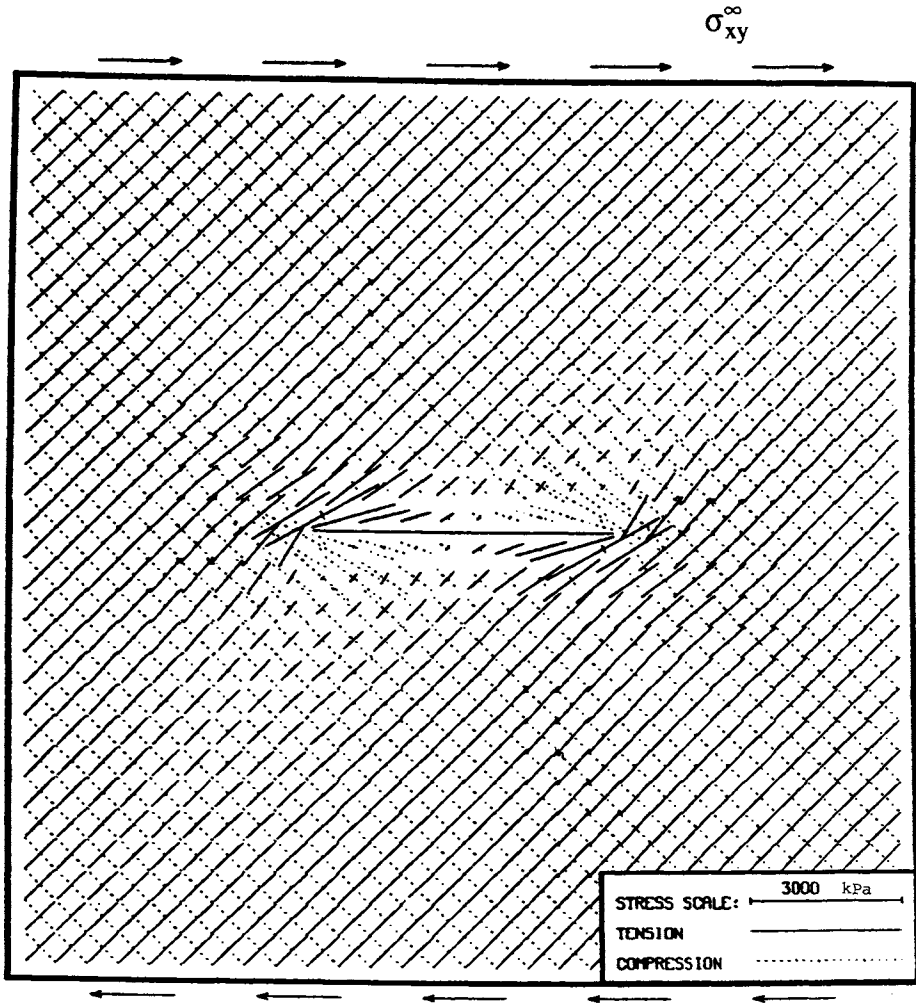


Fig. 6. Principal stresses around one strike-slip fault segment.

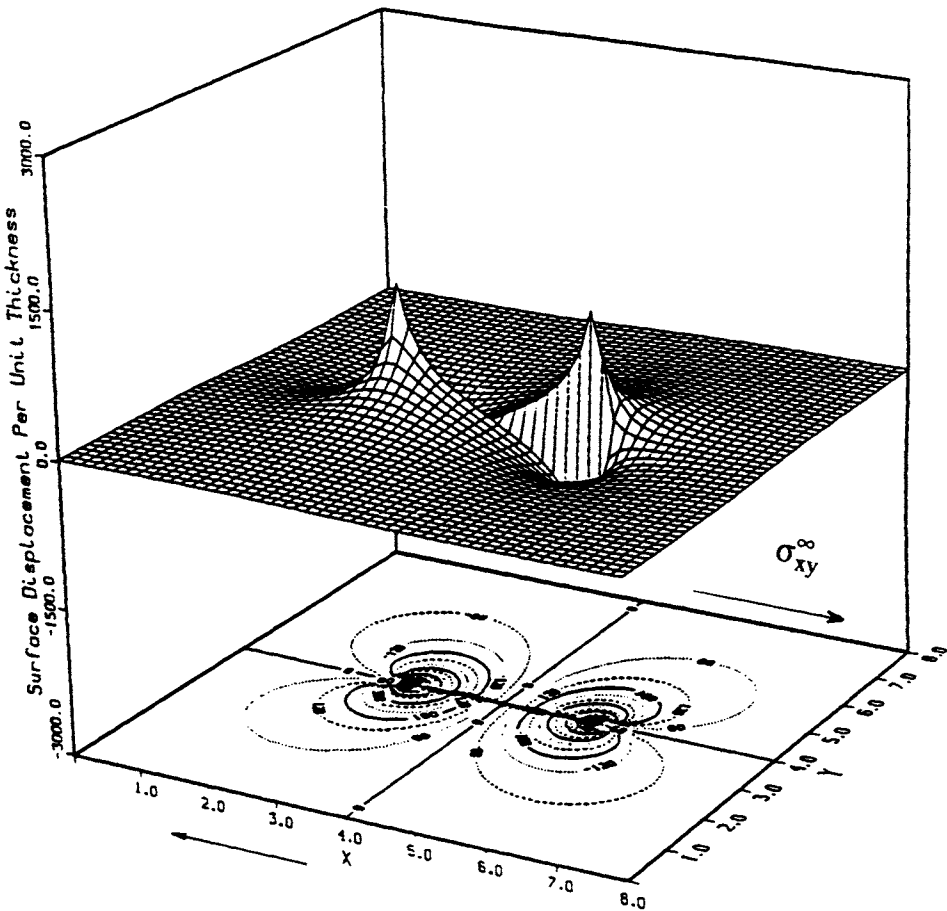


Fig. 7. Vertical ground deformations around one strike-slip fault segment.

$$\sigma_{xy} = \frac{K_{II}}{\sqrt{2\pi r}} \cos\left(\frac{\theta}{2}\right) \left\{ 1 - \sin\left(\frac{\theta}{2}\right) \sin\left(\frac{3\theta}{2}\right) \right\} \quad (5)$$

$$\sigma_{yy} = \frac{K_{II}}{\sqrt{2\pi r}} \sin\left(\frac{\theta}{2}\right) \cos\left(\frac{\theta}{2}\right) \cos\left(\frac{3\theta}{2}\right) \quad (6)$$

where r is the radial distance measured from the tip of the segment to the point where the stresses and deformations are required, θ is the angle that r makes with the X axis (Fig. 5), and K_{II} is the stress intensity factor that can be obtained from the following relationship:

$$K_{II} = \sigma_{xy}^{\infty} \sqrt{\pi c} \quad (7)$$

where c is half the length of the fault segment

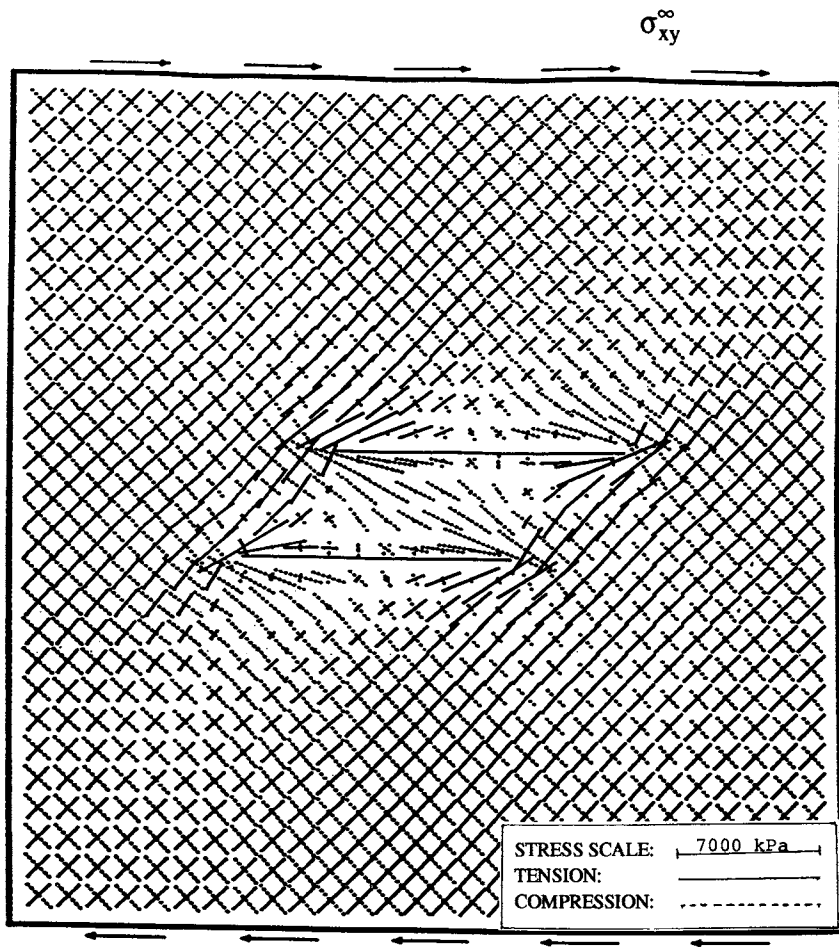


Fig. 8. Principal stresses around two left-stepping strike slip fault segment.

Using the value of the stresses given by Eqs. (1)–(3), or the values using Eqs. (4)–(7), the value of the principal stresses, σ_1 , and σ_3 , at locations around the fault segment or near the tips of the fault segment can be obtained using the following relationship:

$$\sigma_{1,3} = \frac{\sigma_{xx} + \sigma_{yy}}{2} \pm \left[\left(\frac{\sigma_{xx} - \sigma_{yy}}{2} \right) + (\sigma_{xy})^2 \right]^{1/2} \quad (8)$$

The direction of the principal stresses can be obtained from

$$\psi = \frac{1}{2} \tan^{-1} \left(\frac{2\sigma_{xy}}{\sigma_{xx} - \sigma_{yy}} \right) \quad (9)$$

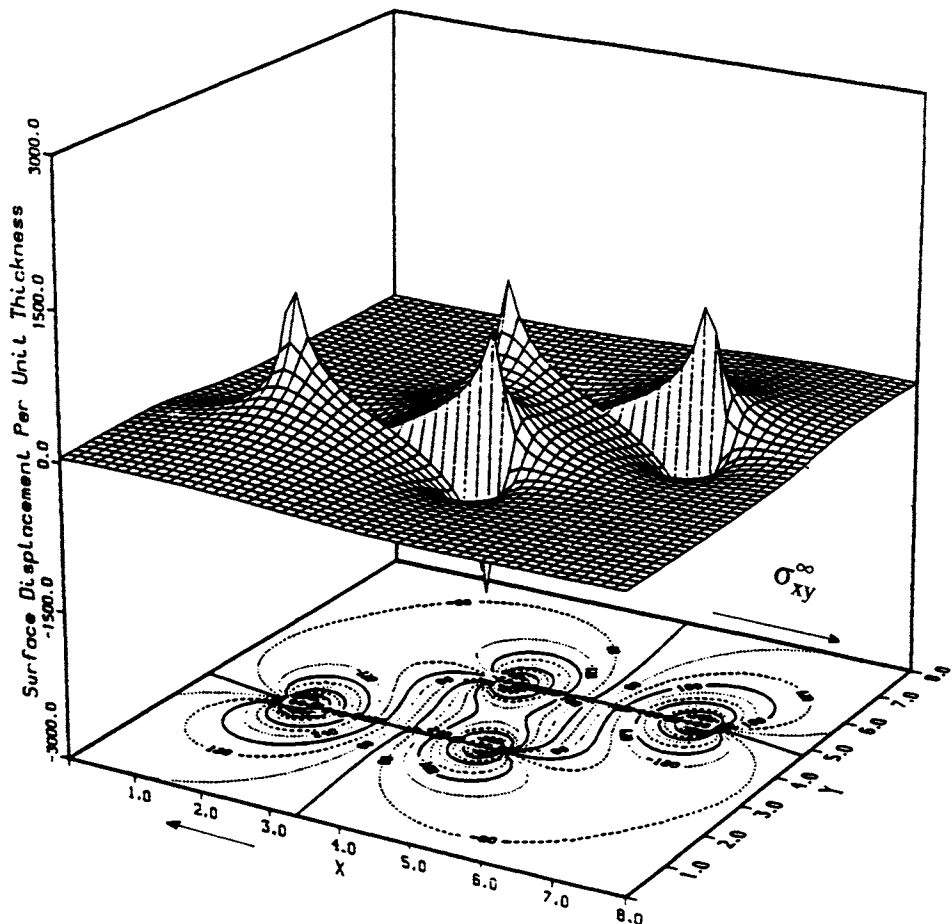


Fig. 9. Vertical ground deformations around two left-stepping strike slip fault segments.

$$\lambda = \psi + \frac{\pi}{2} \quad (10)$$

where ψ is the angle of inclination with respect to the X axis (Fig. 5) of the principal plane on which σ_1 acts. This plane has the same direction as the line of action of σ_3 . λ represents the inclination with the X axis of the principal plane on which σ_3 acts.

A computer program that uses Eqs. (1)–(9) was written to calculate and plot the magnitude and direction of the principal stresses in regions surrounding one or two fault segments. When more than one fault segment is considered in the analysis, the interaction between the segments was taken into account when calculating the principal stresses around the segments (Shettima, 1990).

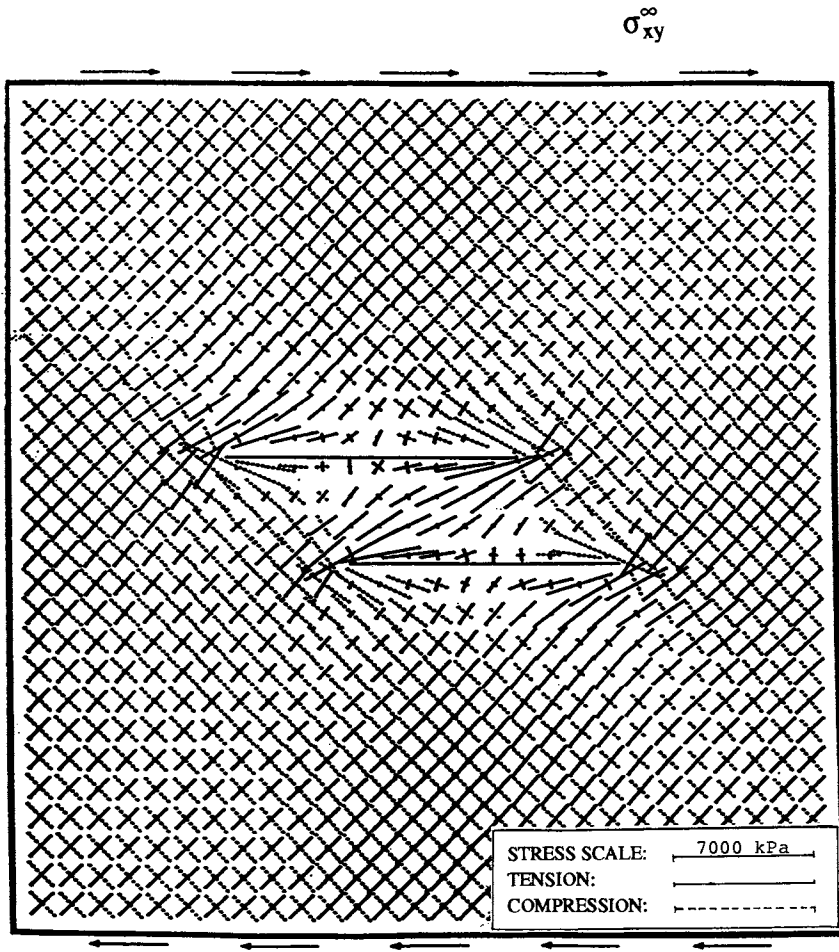


Fig. 10. Principal stresses around two right-stepping strike-slip fault segments.

5.2. Vertical ground displacements

The vertical ground displacements, u_z (normal to the ground surface, in the direction z in Fig. 5), of areas surrounding the strike-slip fault segment shown in Fig. 5 can be obtained from the following relationship (Lawn and Wilshaw, 1975):

$$u_z = \left[-\frac{\mu z}{E} \right] [\sigma_{xx} + \sigma_{yy}] \quad (11)$$

where μ and E are the Poisson's ratio and the Young's modulus of elasticity of

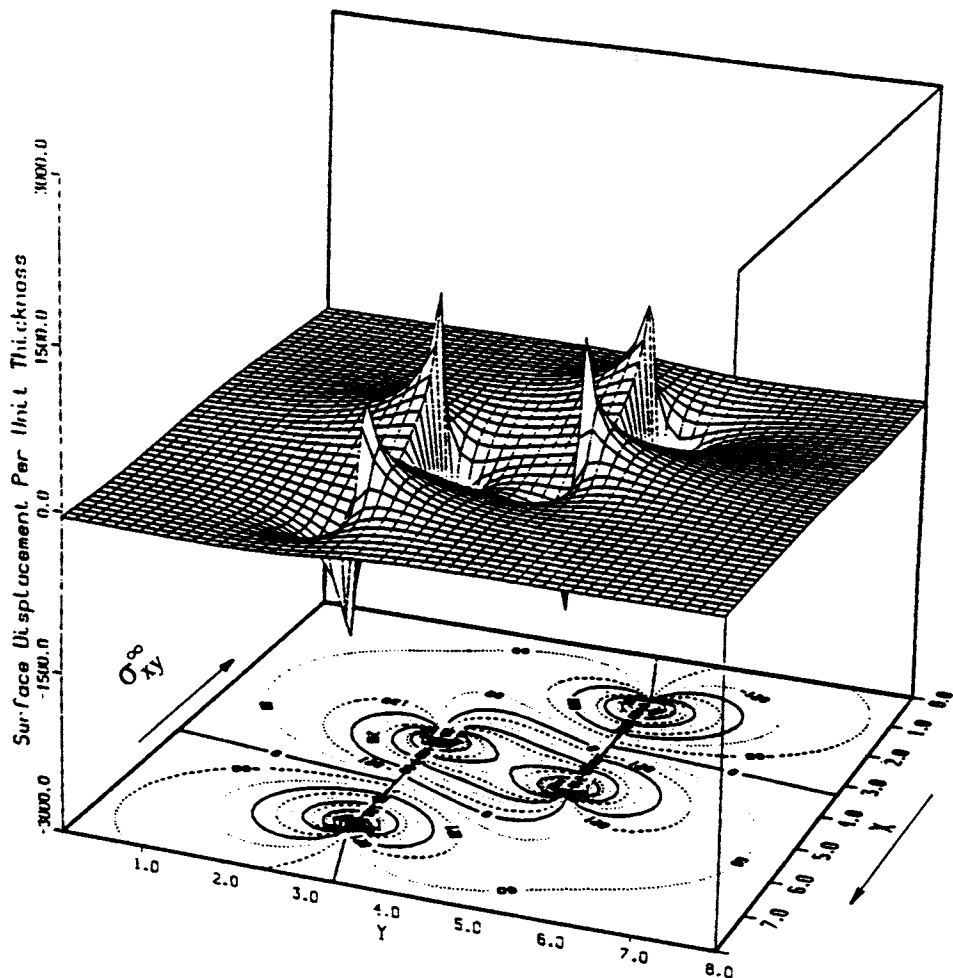


Fig. 11. Vertical ground deformations around two right-stepping strike-slip fault segments.

the material surrounding the fault segment, z is the vertical distance measured as shown in Fig. 5, and σ_{xx} and σ_{yy} are the stresses around the fault segment (Fig. 5). These stresses can be obtained from Eqs. (1) and (2) for regions around the fault segment, or from Eqs. (4) and (5) for regions close to the tips of the fault segment. Eq. (11) is for plane stress conditions with $\sigma_{zz} = \sigma_{xz} = \sigma_{yz} = 0$, and with deformations u_x and u_y being different than zero (Lawn and Wilshaw, 1975).

6. Substantiation of the theoretical method

6.1. Stresses and ground deformations around one- and two-fault segments

The stresses and vertical ground deformations that develop around one- and two-fault segments are plotted in Figs. 6–11. Figs. 6 and 7 represent the stresses and deformations that develop around one fault segment subjected to a right lateral shear stress, σ_{xy}^{∞} . Figs. 8 and 9 represent the stresses and deformations developed by two left-stepping fault segments subjected to a right lateral shear stress. Figs. 10 and 11 represent the stresses and deformations developed by two right-stepping fault segments also subjected to a right lateral shear stress. The stresses and deformations around the fault segments were obtained using Eqs. (1)–(3) and Eqs. (8)–(11).

The value of the shear stress, σ_{xy}^{∞} , used to obtain the plots was equal to 2000 kPa. The values of E and μ in Eq. (11) used to obtain the vertical ground displacement plots were equal to 6.9 kPa (1 psi) and 0.3, respectively. The value of z used in Eq. (11) was equal to 1 m.

Figs. 6–11 indicate that the strike-slip fault segments developed zones of subsidence and uplift around the tips of the segments or in the zones of overlapping.

The single strike-slip fault segment subjected to a net right lateral shear stress developed zones of uplift on the upper right and lower left sections of the segment. Zones of subsidence developed on the upper left and lower right portions of the segment. Similar zones of subsidence and uplift have been found to develop in strike-slip fault segments in China subjected to the same type of shear stresses (compare Figs. 1a and 1b with Figs. 6 and 7). The two left-stepping fault segments developed an uplift zone in the zone of overlap of the two segments (Figs. 8 and 9). This uplift zone is also present in the zone between the two strike fault segments that form the Coyote Creek fault system in California (Fig. 2) as well as the Lake County uplift zone that formed in the area of overlapping of the two strike-slip fault segments near New Madrid, Missouri (Fig. 4). The two right-stepping strike slip fault segments subjected to a right lateral shear stress developed a zone of subsidence in the zone of overlapping (Figs. 10 and 11). This zone of subsidence was observed in the field in the zone of overlapping of the Brawley and Imperial

TABLE II
Calculated and measured subsidence at point X in Fig. 12^a

r (km)	θ (°)	$2c$ (km)	z (km)	σ_{xy}^{∞} (kg/cm ²)	μ	E (kg/cm ²)	Subsidence (cm)	
							Calculated	Measured
5.7	–140	52	20	34.66	0.21	5.5×10^5	–19.5	–23

^aData for fault geometry and elastic properties were obtained from Zongjin et al. (1990). The calculated ground deformations were obtained using Eqs. (4), (5) and (11).

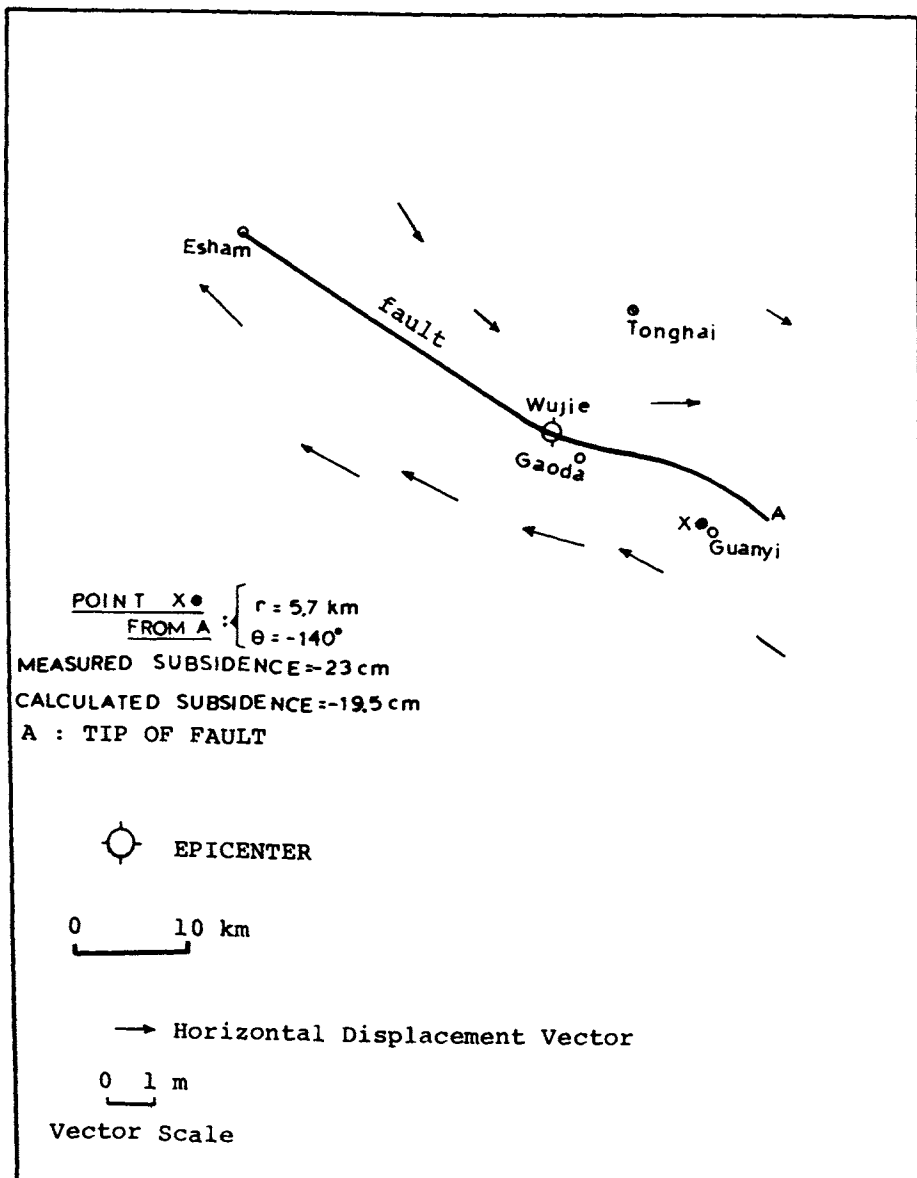


Fig. 12. Measured and calculated ground subsidence at point X located near the tip A of the Tonghai strike-slip fault segment in China.

strike slip fault segments in California (Fig. 3). Thus, the mode or pattern of vertical ground deformations induced by one or two strike-slip fault segments subjected in the field to a right lateral shear stress was predicted very well by linear elastic

fracture mechanics theory. Only the mode of ground deformations that the faults induced in the field was obtained using the theoretical analysis. The lack of information about the elastic properties for the rocks surrounding the faults in Fig. 1a and Figs. 2–4, and the depth H of the crust that contained the strike-slip fault segments at these sites prevented a more precise calculation of the ground deformations (Fig. 5).

6.2. Measured and predicted ground deformations near the Tonghai strike-slip fault segment

Zongjin et al. (1990) have compiled a complete set of information about fault length, elastic properties of the rock, shear stress causing fault movement, and ground deformation measurements for the case of the Tonghai strike-slip fault segment in China that mobilized in 1970 (Table 2). This data is used to check the reliability of the theoretical method presented in this study.

The theoretical vertical ground deformations were obtained using Eqs. (4), (5) and (11). The calculated and measured ground deformations for the case of the Tonghai fault segment are shown in Table 2 and Fig. 12. An examination of Table 2 and Fig. 12 indicates that the theoretical analysis that makes use of linear elastic fracture mechanics theory predicted well the vertical ground deformation measured at the right tip of the Tonghai strike-slip fault segment.

7. Conclusions

In the present study, a theoretical method based on linear elastic fracture mechanics theory has been presented to evaluate the stresses and vertical ground deformations around active strike-slip fault segments. The vertical ground deformations are the result of stresses concentrated by the ends of the fault segments. The pattern of ground deformations developed by the ground surrounding active strike-slip fault segments in China and the United States was predicted very well by the theoretical method. The vertical ground deformations measured near the tip of the Tonghai strike-slip fault segment in China compared well with the vertical ground deformation obtained using the theoretical analysis.

References

- Bilham, R. and King, G., 1989. The morphology of strike-slip faults: examples from the San Andreas Fault, California. *J. Geophys. Res.*, 94(B8): 10204–10216.
- Billings, H.J., 1985. Hydraulic fill dams made earthquake resistant. *Civ. Eng., Am. Soc. Civ. Eng.*, New York, June, pp. 55–59.
- Bjerrum, L., 1963. Allowable settlement of structures. *Proc. Eur. Conf. on Soil Mechanics and Found. Engineering*, Weisbaden, Germany, III: 135–137.
- Bonilla, M.G., 1991. Faulting and seismic activity. In: G.A. Kiersch (Editor), *The Heritage of Engineering*

- Geology; The First Hundred Years, Centennial Special Volume 3. Geol. Soc. Am., Boulder, CO, pp. 251–264.
- Chinnery, M.A., 1961. The deformation of the ground around surface faults. Bull. Seismol. Soc. Am., 51: 355–372.
- Chinnery, M.A., 1963. The stress changes that accompany strike-slip faulting. Bull. Seismol. Soc. Am., 53: 921–932.
- Jayatilaka, A.S., 1979. Fracture of Engineering Brittle Materials. Applied Science Publishers Ltd., London, England.
- Johnson, C.E. and Hadley, D.M., 1976. Tectonic implications of the Brawley earthquake swarm, Imperial Valley, California, January 1975. Bull. Seismol. Soc. Am., 66: 1132–1144.
- Kasahara, K., 1985. Earthquake Mechanics. Cambridge University Press, Cambridge, England.
- Lawn, B.R. and Wilshaw, T.R., 1975. Fracture of Brittle Solids. Cambridge University Press, Cambridge, England.
- Pollard, D.D. and Segall, P., 1987. Theoretical displacements and stresses near fractures in rock: with applications to faults, joints, veins, dikes, and solution surfaces. In: B.K. Atkinson (Editor), Fracture Mechanics of Rock. pp. 277–349.
- Russ, D.P., 1982. Style and significance of surface deformations in the vicinity of New Madrid, Missouri. U.S. Geol. Surv. Prof. Pap., 1236: 95–114.
- Schwartz, D.P. and Coppersmith, K.J., 1986. Seismic hazards: new trends in analysis using geological data. In: Active Tectonics. Studies in Geophysics, Natl. Res. Coun., Natl. Acad. Press, Washington, DC, pp. 215–230.
- Seed, H.B., 1979. Considerations in earthquake resistance design of earth and rock fill dams. Geotechnique, 29(3): 215–263.
- Seed, H.B., Makdisi, F.I. and DeAlba, P., 1978. Performance of earth dams during earthquakes. J. Geotech. Eng. Div., Am. Soc. Civ. Eng., 104(7): 967–994.
- Segall, P. and Pollard, D.D., 1980. Mechanics of discontinuous faults. J. Geophys. Res., 85(B8): 4337–4350.
- Sharp, R.V. and Clark, M.M., 1972. Geologic evidence of previous faulting near the 1968 rupture on the Coyote Creek Fault. U.S. Geol. Surv. Prof. Pap., 787: 131–140.
- Sherard, J.L., Cluff, L.S. and Allen, C.R., 1974. Potential active faults in dam foundations. Geotechnique, 24(3): 367–428.
- Shettima, M., 1990. Mechanics of Crack Propagation and Interaction in Stiff Clays. Ph.D. Thesis, Department of Civil and Environmental Engineering, University of Pittsburgh, Pittsburgh, PA.
- Vallejo, L.E., 1987. The influence of fissures in a stiff clay subjected to direct shear. Geotechnique, 37(1): 69–82.
- Vallejo, L.E. and Liang, R., 1994. Fracture Mechanics Applied to Geotechnical Engineering. Am. Soc. Civ. Eng., New York.
- Wahls, H.E., 1981. Tolerable settlement of buildings. J. Geotech. Eng. Div., Am. Soc. Civ. Eng., 107(11): 1489–1504.
- Zongjin, M., Zhengxiang, F., Yingzhen, Z., Chengmin, W., Guomin, Z. and Defu, L., 1990. Earthquake Prediction. Springer, New York.

CHAPTER 5

The 1995 7.2 magnitude Kobe earthquake and the Arima-Takatsuki tectonic line: implications of the seismic risk for central Japan

YUJI KANAORI^{a,*} and SHIN-ICHI KAWAKAMI^b

^aDepartment of Geological Sciences, Faculty of General Education, Gifu University, 1-1 Yanagido, Gifu City, 501-11, Japan and ^bDepartment of Earth and Planetary Sciences, Faculty of Education, Gifu University, 1-1 Yanagido, Gifu City, 501-11, Japan

Abstract

Along the Rokko Mountains and Awaji Island, NE-SW to ENE-WSW oriented active faults exist in an *en echelon* arrangement. They constitute a portion of the Arima-Takatsuki tectonic line (ATTL) which extends from Kyoto, through Awaji Island, to the Median Tectonic Line. The ATTL is also correlated to lineaments linking the saddles and steep slopes of gravity (Bouguer) anomalies. The main shock of the 1995 magnitude 7.2 (*M* 7.2) Kobe earthquake was located at the mid-point of the ATTL. The main shock also created a 9-km long rupture on the ground surface along the NE-SW Nojima fault line in the northern part of Awaji Island. The earthquake aftershocks were distributed over a 40-km long zone along the central segment of the line. Surface ruptures and cracks accompanying the Kobe earthquake were scattered along a 40-km segment centrally located on the ATTL. Spatial correlation of the surface ruptures and aftershock distribution on the ATTL suggests that the Kobe earthquake was the result of a 40-km long rupture of the central segment of the ATTL.

The average rate of seismic moment-release is an important parameter used in evaluating the seismic risk of a fault system. The moment-release rate averaged over the late Quaternary has been evaluated through the average slip rates and the dimensions of constituent faults. The average moment-release rate for the central portion of the ATTL has been estimated as $0.0017\text{--}0.0063 \times 10^{26}$ dyne cm year⁻¹. Evidence of liquefaction and flowage, probably associated with the 1596 *M* 7.5 Keicho-Fushimi earthquake, has been identified at several archaeological excavation sites along the ATTL. These observations suggest that the ATTL was also responsible for the Keicho-Fushimi earthquake which occurred about 400 years ago.

From the elapsed time since the Keicho-Fushimi earthquake and the average moment-release rate, the seismic moment accumulated during the interseismic period was calculated for the ATTL. The obtained value amounts to that of the seismic moment released by an earthquake having a magnitude ranging from 6.8 to 7.2, being comparable to that of the Kobe earthquake. The obtained result is consistent with the view that the Kobe earthquake was caused by a rupture of the ATTL which released almost all the moment accumulated since the previous event.

* Corresponding author.

1. Introduction

Earthquakes which have created serious disasters in the Japanese Islands can be classified into two types; the inter-plate earthquake which occurs along a trough or a trench, and the intra-plate earthquake which is generated inland (e.g., see Shimazaki, 1976). Since almost all inter-plate earthquakes are generated on the sea floor, they are accompanied by tsunamis. The occurrence of tsunamis has been frequently recorded in historical documents (Hatori, 1974). From historical records, inter-plate events are believed to repeat at an interval ranging from 100 to 150 years (Utsu, 1974; Ando, 1975).

On the other hand, intra-plate events have been widely accepted to result from movements of inland faults after the generation of the 1891 8.0 magnitude (M 8.0) Nobi earthquake (Koto, 1893). Following this event, three destructive earthquakes with magnitudes of around M 7 were sequentially generated in the western part of central Japan (Kanaori et al., 1994b). The sequence of events appeared to terminate in 1948 by the generation of the M 7.1 Fukui earthquake.

Following about 50 years of quiescence after the Fukui event, the M 7.2 Kobe earthquake occurred at 05:46 JST on January 17, 1995, covering the area from Hanshin to the northern part of Awaji Island in central Japan (Table 1). The Hanshin area consists of the coastal regions of the cities of Osaka and Kobe located along Osaka Bay. More than 5500 people were killed by the earthquake disaster, along with numerous buildings, houses, and railroad and highway bridges being destroyed or seriously damaged (Table 2). A 9-km long rupture appeared on the ground surface along the pre-existing Nojima fault in the northern part of Awaji Island immediately after the event. The earthquake has caused attention to be concentrated on active faults in and around the Japanese Islands.

In the Rokko Mountains, cracks showing displacements of less than a few tens of centimeters occurred on the ground surface along some of the active faults, while no cracks were detected along other active faults. The distribution of aftershocks was scattered over a zone, including the pre-existing active faults in the Rokko Mountains. In contrast, a belt in which the damaged structures were concentrated, was located along an alluvial fan and lowlands. The direction and location of the damaged belt significantly differ from those of pre-existing active faults and

TABLE I

Statistics of the Kobe earthquake (announced by the Japan Meteorological Agency)

Earthquake name	1995 Southern Hyogo earthquake
Date	05:46 JST on 17 January, 1995
Epicenter	Akashi strait
Location	latitude 34.61°N longitude 135.04°E depth 14.3 km
Magnitude	7.2

TABLE II

Damage induced by the Kobe earthquake (based on data compiled by the Fire Defence Agency on 14 April, 1995)

Casualties	
Killed	5 501
Missing	2
Injured	41 501
Damage	
Housing	
complete	100 823
half	90 104
Buildings	3 669
Roads	9 403
Fire	293

aftershock distribution. Shimamoto (1995) assumed a blind fault existed below the damaged belt and claimed that the blind fault moved to create such damages. To date, however, no evidence for the existence of a blind fault has been found. Hashimoto et al. (1995), based on a numerical analysis of geodetic data which were obtained from the global positioning system (GPS) and levelling, rejected the blind fault assumption. Presently, a casual fault which created the Kobe earthquake and the activity of pre-existing active faults are still under investigation. It is of great significance to reveal the existence of the casual fault in order to lessen the disastrous effects of inland earthquakes, and for the design of structures located in regions close to the active faults.

Major fault systems in central Japan, including the Kinki and Chubu district, can be recognized as lines linking large-scale active faults (Kanaori et al., 1992a). Many of the epicenters of historical earthquakes which have damaged central Japan are located along these fault systems. From the spatial association between the epicenters and the fault systems, Kanaori et al. (1991, 1992b, d) claimed that destructive inland earthquakes are generated by the movement of fault systems and that active faults are only the surface manifestation which appear on the ground surface to be due to the faulting. Based on a series of studies, Kanaori et al. (1993a) proposed a model in which central Japan was separated into several microplates by the major fault systems. An attempt was then made to explain the sequential occurrence of destructive inland and great offshore earthquakes by the relative motion of the microplates.

In the present paper, descriptions are given of the tectonic setting of the ATTL, the statistics of the disaster, and ruptures accompanying the Kobe earthquake. An estimate of the seismic moment-release rate is then calculated from the slip rate of the active faults constituting the ATTL. The occurrence of destructive earthquakes is interpreted in the context of the tectonics of central Japan. Finally, the possible earthquakes which may inflict damage in central Japan in the near future are discussed.

2. Block structure and the Arima-Takatsuki tectonic line (ATTL)

Central Japan, which is situated at the inflection point of the Japanese Islands, occupies the eastern margin of the Eurasia plate. It makes contact with the North America plate to the east and the Philippine Sea plate to the southeast. Due to this tectonic setting, a number of active faults exist in central Japan, which has been seriously damaged by great offshore and inland earthquakes (Usami, 1987). As shown in Fig. 1, central Japan is separated into several blocks by fault systems which consist of large-scale active faults.

Fig. 2 is a Landsat image which includes the area studied. In this image, geomorphological lineaments can be easily seen between mountainous areas and alluvial plains or basins. When compared to the distribution of active faults as shown in Fig. 1, these lineaments can be correlated to the major fault systems consisting of large-scale active faults. It can be seen that the mountains around the Osaka plain are bounded by three fault systems: the Hanaore-Kongo fault line (HKFL), the Arima-Takatsuki tectonic line (ATTL) and the Median Tectonic Line (MTL).

The eastern 20-km long segment of the ATTL has been previously defined as the geological boundary between Mesozoic granitic basements and Neogene or younger sedimentary cover (Huzita and Okuda, 1973). In the Rokko Mountains to the west-southwest, NE-SW to ENE-WSW oriented active faults having a right-lateral slip sense are developed in an *en echelon* arrangement (Research Group for Active Faults in Japan, 1991). Further southwest, right-lateral active faults, such as the Nojima fault, exist in the northern part of Awaji Island. From the existence of active faults, Kanaori et al. (1992a) redefined the ATTL as the fault system which continues from the previous definition of the ATTL through Awaji Island to the MTL. The length of the redefined ATTL reaches 100 km.

The HKFL is defined as the fault system which links the NNE-SSW oriented Hanaore fault and the N-S oriented Ikoma and Kongo faults (Kanaori et al., 1992c). The ATTL separates from the HKFL in the area around the Kyoto basin. Along the MTL, E-W oriented active faults having right-lateral slips are arranged *en echelon* (Okada and Sangawa, 1978).

Fig. 3 shows a contour map of gravity (Bouguer) anomalies. Fault systems can be recognized as lineaments linking saddles and steep slopes of gravity anomalies. In particular, the ATTL is easily identified as a zone of steep slope from Kyoto through the northern margin of the Osaka plain to the southern part of Awaji Island. This indicates that the structure of the Earth's crust is separated by fault systems.

3. The 1995 Kobe earthquake

3.1. Outlines of seismicity and damages

The main shock of the M 7.2 Kobe earthquake was located at a depth of approximately 15 km under the Akashi strait, between the Hanshin area and Awaji

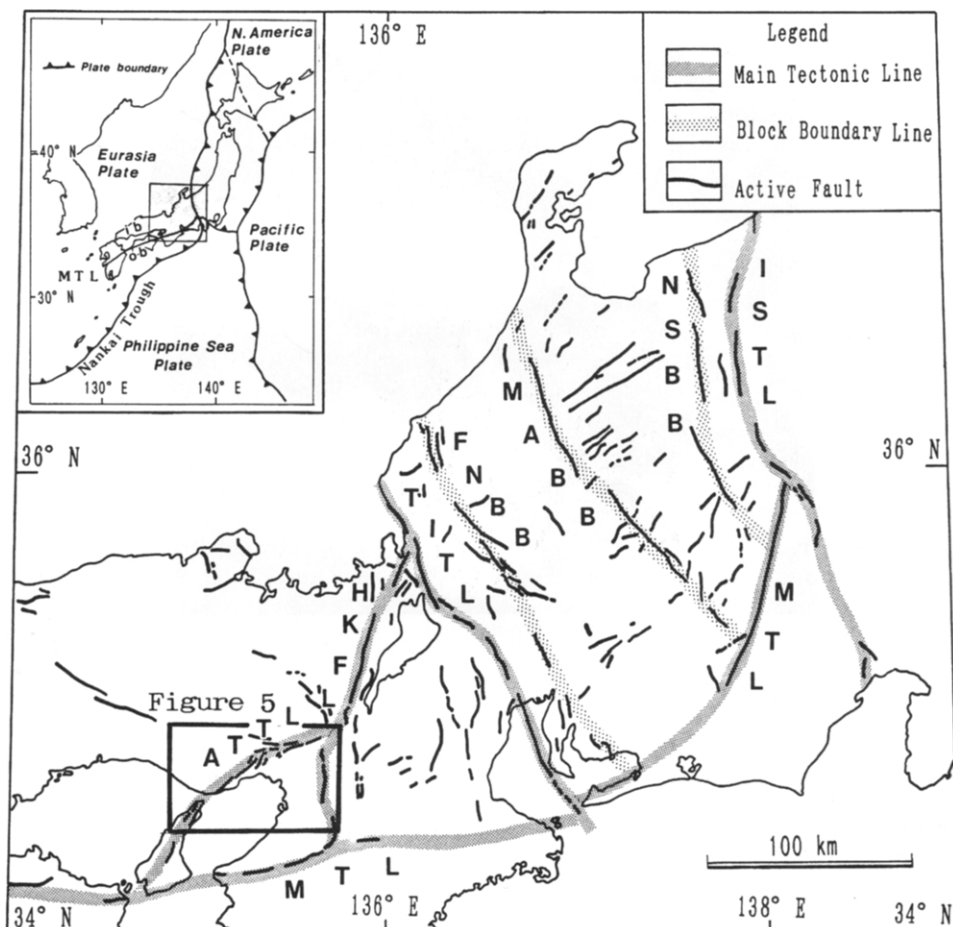


Fig. 1. Map showing major the fault systems in central Japan (based on Kanaori et al., 1992a, 1993a). The fault systems are defined as lines linking large-scale active faults. The inset shows the plate boundaries in and around the Japanese Islands and the location of central Japan. The fault systems are: ATTL, the Arima-Takatsuki tectonic line; HKFL, the Hanaore-Kongo fault line; ISTL, the Itoigawa-Shizuoka tectonic line; MTL, the Median Tectonic Line; and TITL, the Tsurugawan-Isewan tectonic line. The block boundary line is: FNBB, the Fukui-Neodani block boundary; MABB, the Miboro-Atera block boundary; NSBB, the Nekomata-Sakaitoge block boundary. The zones are: ib, the inner belt; and ob, the outer belt.

Island (see Table 1). It has been reported that the acceleration of ground motions caused by this earthquake reached a maximum value of 833 gal (cm/s^2). Fig. 4 shows distributions of aftershocks of the Kobe earthquake: the horizontal distribution in the upper panel and the vertical to depths of 30 km in the lower panel. Most aftershocks were distributed along a NE–SW oriented zone and occurred at depths of less than 20 km.

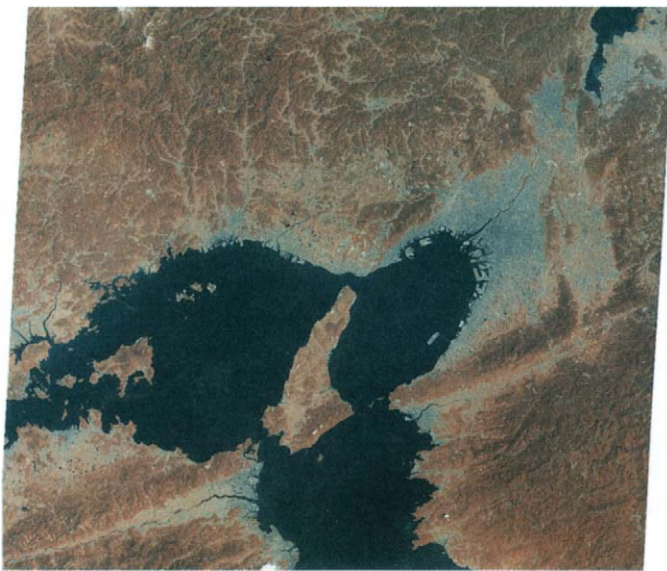


Fig. 2. Landsat image including the Hanshin area and Awaji Island (taken on 19 May, 1992; reproduced with the permission of the Research Center for Remote Sensing). Fault systems are displayed as lineaments which separate mountainous areas from alluvial plains or basins. The shaded rectangle in the inset map shows the area covered by the Landsat image. The Hanshin area is considered as the coastal regions of Osaka and Kobe along Osaka Bay.

Numerous houses, buildings, and roads were destroyed, with fires occurring at 293 locations (Table 2). Liquefaction and flowage was extensively induced in reclamation soils in the coastal region and in filled soils in housing development areas. More than 5500 people were killed by this seismic disaster. This was the most destructive inland earthquake to have occurred during the past half-century in Japan.

3.2. Surface ruptures

Fig. 5 shows a belt in which more than 30% of the houses were completely destroyed (this corresponds to seismic intensity 7 on the Japan Meteorological Agency scale). Also shown are the localities or zones of surface ruptures in a map of pre-existing active faults. A distinct rupture plane appears on the ground surface along the Nojima fault in the northern part of Awaji Island. This can be traced for approximately 9 km, oriented in a NE-SW trend. The maximum displacement of the surface rupture is 1.7 m of right-lateral slip and 1.3 m of southwestern dip slip

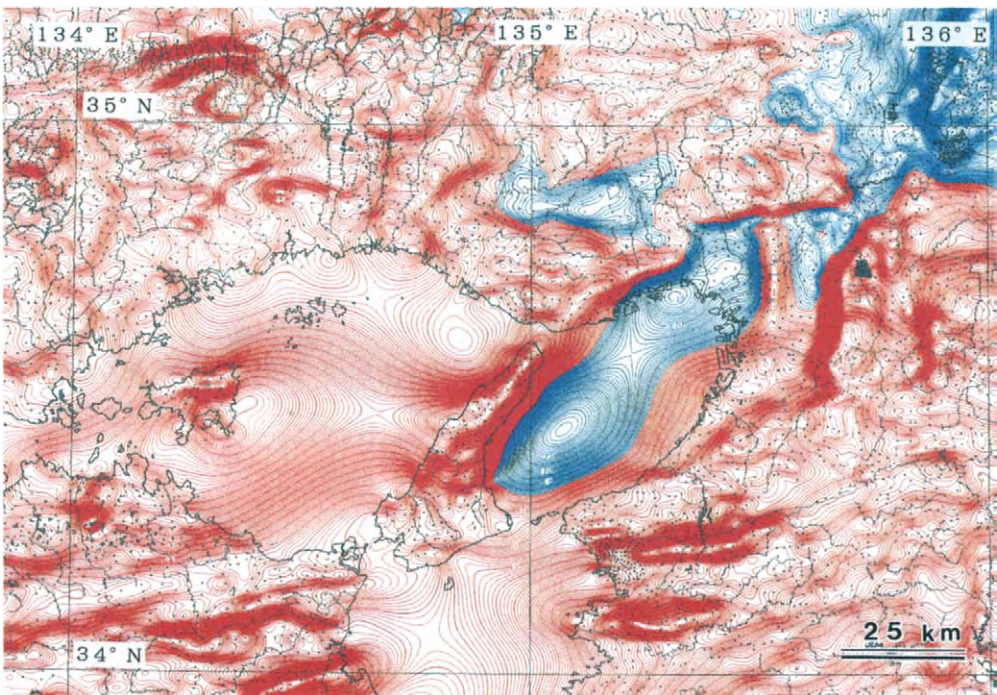


Fig. 3. Contour map of gravity (Bouguer) anomalies (after Gravity Research Group in Southwest Japan, 1994). The contour interval is 0.1 mGal.

(Awata et al., 1995). Fig. 6 is an aerial photograph of *en echelon* surface cracks in rice fields along the Nojima fault. Four months after the Kobe earthquake, a 1.5-km long surface rupture, parallel to and 5 km east of the Nojima fault, was discovered. This rupture had right-lateral slip of several tens of centimeters.

In the Rokko Mountains, several-meter long surface cracks were sporadically found along pre-existing active faults. These cracks had a right-lateral slip of no more than 10 cm (e.g., see Fig. 7). The damaged belt of seismic intensity 7 in the Hanshin area is oriented parallel to the coast line. The damaged belt does not match the active fault zone and zones of the seismic ruptures and cracks.

The main shock of the Kobe earthquake occurred at the mid-point of the Arima-Takatsuki tectonic line (see Fig. 8). The aftershock and surface rupture distributions confirm that the Kobe earthquake was generated due to a rupture of the 40-km long and 20-km wide plane located in the middle segment of the ATTL.

4. The 1596 Keicho-Fushimi earthquake

Epicenters of inland earthquakes ($M \geq 6.4$) which have caused damage in the Kinki district are shown in Fig. 8. The locations of most epicenters can be found plotted

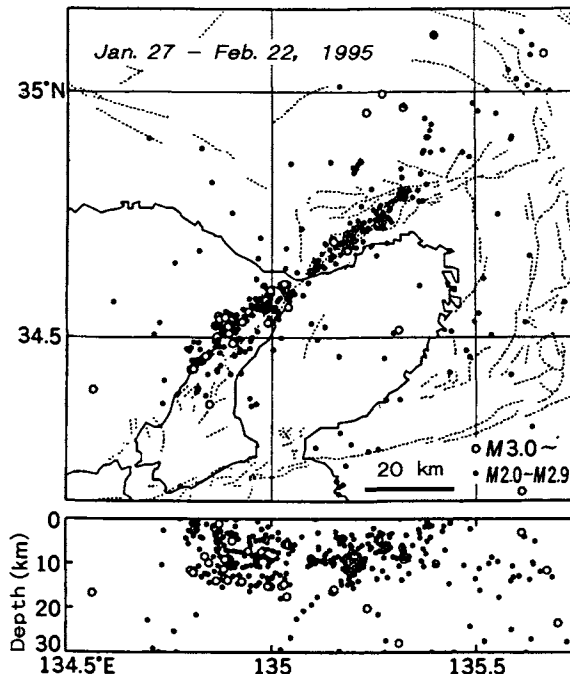


Fig. 4. Aftershock distributions of the Kobe earthquake observed by the network of the Urgent Research Group for Crustal Activity (after Hirata, 1995). The upper panel displays the horizontal distribution, the lower panel the vertical cross-section to depths of 30 km.

along major fault systems and tectonic lines which consist of large-scale active faults. From this spatial relationship, Kanaori et al. (1991) claimed that destructive inland earthquakes were caused by the movement of fault systems.

The 1596 Keicho-Fushimi earthquake was one of the great historical earthquakes to have occurred in the Kinki district (shown as ke in Fig. 8). Based on descriptions recorded in historical documents, Usami (1987) estimated the area which experienced a seismic intensity of 6 or greater, and determined from the extent of this area that the magnitude of the event was around M 7.5. The area of seismic intensity 6 fits the region that is surrounded by the three fault systems: the ATTL, the HKFL and the MTL.

Recently, more than ten thousand archaeological sites have been excavated. Evidence of liquefaction and flowage has been identified at a number of the excavated sites (Sangawa, 1989a, 1992). The liquefaction and flowage must have been induced by seismic ground motions of seismic intensity 6 or greater. Using the available data of archaeological excavations, locations of the excavated sites revealing evidence of paleoliquefaction and flowage are plotted in Fig. 9. It should be noted here that several sites exhibiting such evidence are aligned along the ATTL.

The ages of the paleoliquefaction and flowage can be constrained to given time

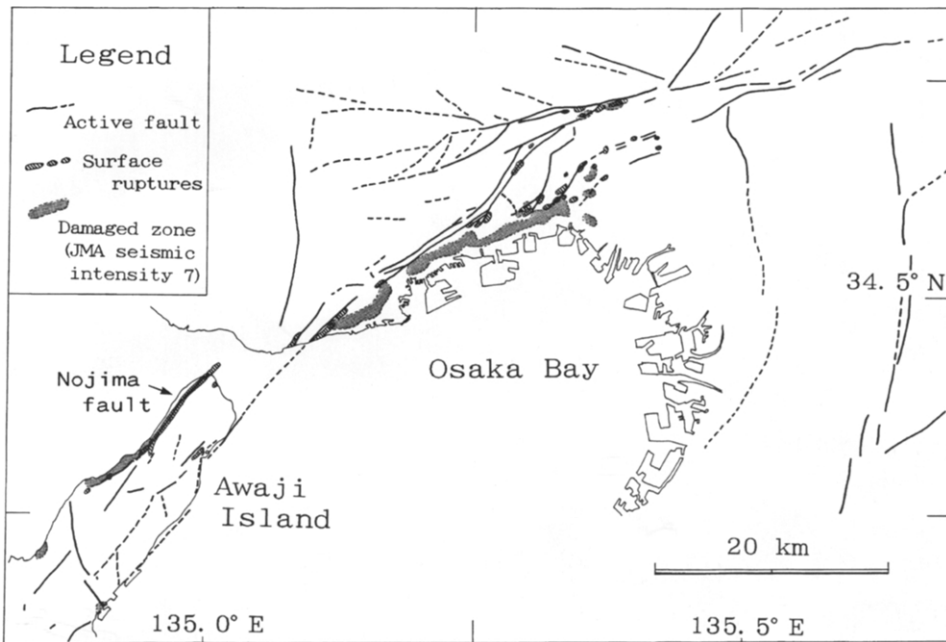


Fig. 5. Damaged and ruptured zones induced by the Kobe earthquake, and the distribution of active faults previously detected by Research Group for Active Faults in Japan (1991). The distributions of the damaged and ruptured zones were compiled from the field work of the authors, together with data from Nagoya Road Engineers Co. Ltd (1995), Earthquake Damage Investigation Group of Central Research Institute of Electric Power Industry (1995), Japanese Union of Geological Survey Companies (1995), Chuo-Kaihatsu Co. Ltd (1995), Toyo Geological Survey Co. Ltd (1995) and Sakurai (1995).

periods by archaeological estimation (e.g., Sangawa, 1990b; Kanaori et al., 1993b). Fig. 10 shows the time range of paleoliquefaction and flowage events which were constrained by archaeological estimation. This figure indicates that the paleoliquefaction and flowage occurred mainly during three periods: ca. 500 B.C., ca. 500 A.D., and ca. 1500 A.D. The latest paleoliquefaction and flowage events, which have been identified at seven excavation sites over the ATTL, occurred during the ca. 1500 A.D. period. These events can be correlated to the 1596 Keicho-Fushimi earthquake.

In summary, the ATTL, the movement of which probably caused the Kobe earthquake, might also have moved at the time of Keicho-Fushimi earthquake 400 years ago.

5. Seismic risk assessment and the Kobe earthquake

5.1. Average rate of seismic moment-release

The method for calculating the average rate of seismic moment-release was described in Kanaori et al. (1992c, d) and is briefly explained in the following.



Fig. 6. Aerial photograph of *en echelon* ruptures appearing on the ground surface in the northern part of Awaji Island due to the Kobe earthquake (photographed by Naka-Nippon Air Co. Ltd.). The surface ruptures are traced along the Nojima fault which had been geomorphologically discovered prior to the earthquake.



Fig. 7. Photograph of a crack cutting through a concrete wall. This crack has right-lateral slip sense. The scale (white bar) is approximately 10 cm long.

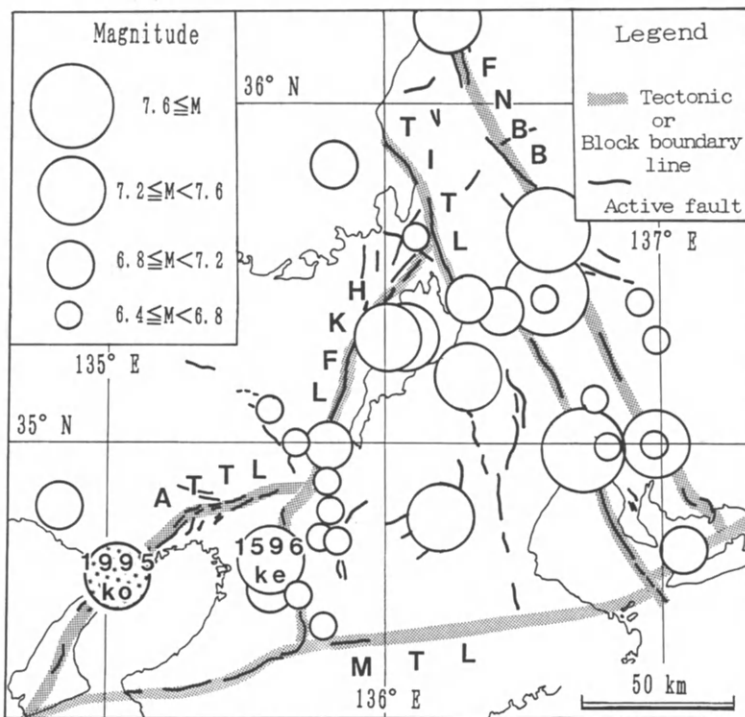


Fig. 8. Epicenters of destructive inland earthquakes in the Kinki district that have occurred since 599 A.D. Magnitudes are represented by the circle size according to the legend. Earthquake data are based on Usami (1987). The abbreviations are; ke = the Keicho-Fushimi earthquake; and ko = the Kobe earthquake.

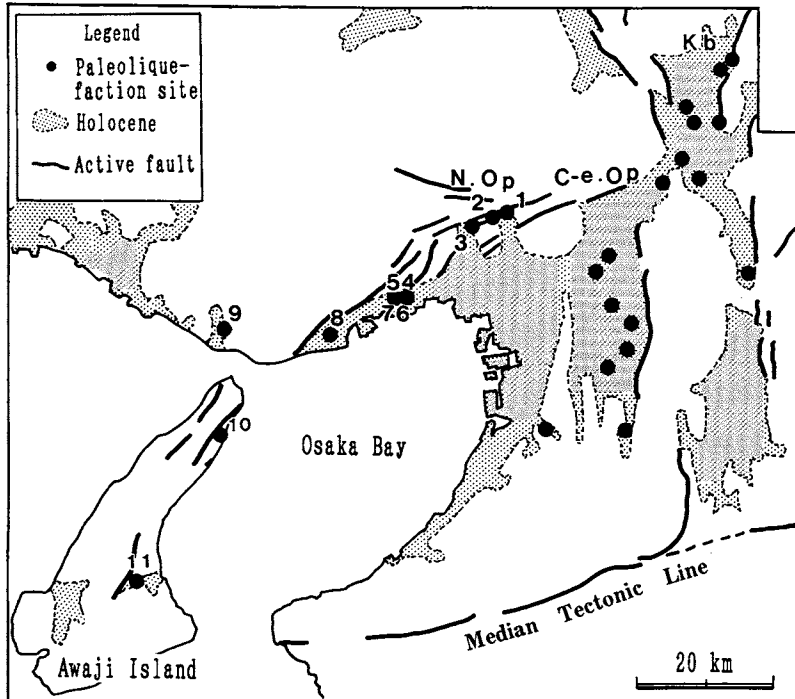


Fig. 9. Distribution of Holocene deposits and excavated sites (solid circles) exhibiting evidence of liquefaction and flowage in the Hanshin area and Awaji Island (based on Kanaori et al., 1993b). The numbers accompanying the solid circles are those used in Fig. 10.

When a fault of length L slips by an amount d , the seismically released moment m_o is given by $\mu W L d$. Here, μ is the rigidity and W the width of the fault. The total amount of the moments released along the fault or fault system during an arbitrary time period t is given as $\mu L W \Sigma d$. Here, Σd equals the cumulative slip amount D . The average rate r of the seismic moment-release m_o obtained by dividing the total amount of seismic moment by an arbitrary time period τ as

$$r = \mu W L D / \tau \quad (1)$$

Here, D/τ is the average slip rate of the fault during the Quaternary. The average slip rate can be estimated by morphological methods as the amount averaged over a time period ranging from several tens of thousands to a million years.

On the other hand, the relationship between the magnitude M and moment m_o released by earthquakes generated in and around the Japanese Islands has been empirically estimated (Wesnousky et al., 1982) as

$$\log m_o = 17.0 + 1.3M \quad (2)$$

With use of Eq. (2), the seismically-released moment m_o can be calculated for

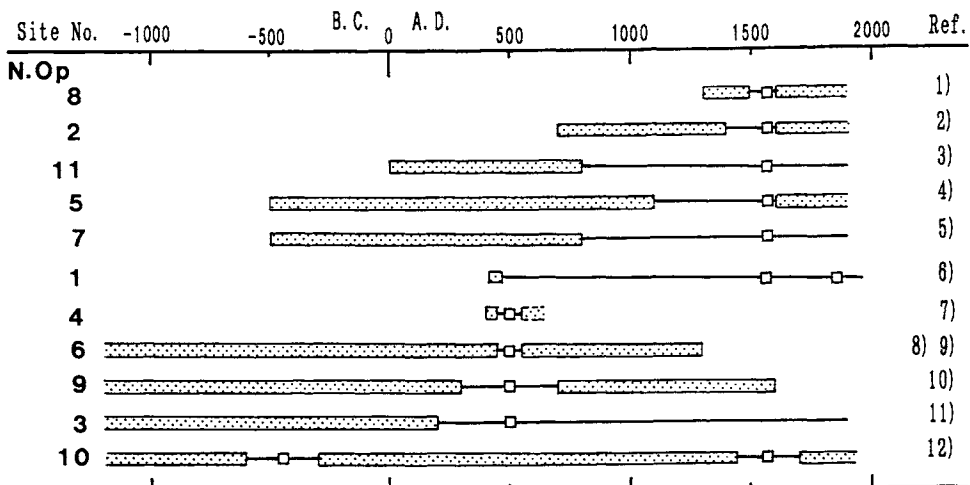


Fig. 10. Archaeological determination of the probable time periods exhibiting no evidence of liquefaction and flowage, and earthquake induced liquefaction and flowage at each archaeological site excavated. One or two earthquakes are estimated to have occurred within the latter period. Each time range associated with a symbol includes an error ranging from several tens to a hundred years, due to the uncertainty in archaeological age determination of the ancient life surfaces. The shaded bars show the length of time that each archaeological site recorded no liquefaction and/or flowage events. References listed on the right-hand side are (1) Sangawa (1990a), (2) Site Research Committee of Kawanishi City (1989), (3) Education Board of Hyogo Prefecture (1992a), (4) Takahashi (1990), (5) Sangawa (1989b), (6) Education Board of Ikeda City (1989), (7) Education Board of Kobe City (unpublished), (8) Association of Tan-Shin Cultural Properties (unpublished), (9) Otemae Women's University (unpublished), Umeda et al. (1984), and Education Board of Hyogo Prefecture (1992b).

each historical earthquake from the magnitude M , which in turn can be estimated from the records of historical documents. The average moment-release rate r is obtained by first summing all of the moments released by the historical earthquakes along the given fault system. This sum is divided by the elapsed time from the date of the oldest historical event to the present. The average rate r presently calculated is the amount averaged over about 1000 years.

The average moment-release rate r calculated from the slip rates averaged over the Quaternary period on each fault system in central Japan nearly equals that determined from the magnitude of the historical earthquakes (Kanaori et al., 1992b, d). This near equality supports the concept that the generation of destructive earthquakes results from the slip of fault systems. Accordingly, the average moment-release rate is an important parameter in evaluating the seismic risk of a fault system.

From the aftershock and rupture distributions of the Kobe earthquake, the length L and width W of the casual fault are estimated as 40 and 20 km, respectively. The average slip rate of the ATTL has been geomorphologically estimated from the displacements of dated terraces (Sangawa, 1978). Making use of Eq. (2), the average

moment-release rate r of the central segment responsible for the Kobe earthquake, is calculated to be in the range from 0.0017 to 0.0063×10^{26} dyne cm year $^{-1}$ (Table 3).

The total length of the ATTL is 100 km. Assuming that the moment-release rate for the eastern and western segments is the same as that of the central segment, the average moment-release rate of the entire length of the ATTL will be 2.5 times that of the 40-km segment. The average moment-release rate for the entire ATTL therefore ranges from 0.0043 to 0.0157×10^{26} dyne cm year $^{-1}$. This average rate is equivalent to that of the Tsurugawan-Isewan tectonic line or the Fukui-Neodani block boundary. This indicates that the ATTL is one of the fault systems categorized by the highest rank A of the seismic risk categories (Kanaori et al., 1992d). It is important to ascertain whether or not the moment-release rate for the eastern and western segments are as high as that of the central segment.

5.2. Elapsed time until the next earthquake and its magnitude

When the average moment-release rate r and the possible moment that will be released by the next earthquake to occur along the fault system are given, the elapsed time until the occurrence of the next earthquake t should equal m_o/r (Kanaori et al., 1992d). From the elapsed time and use of Eq. (2), the next relationship can be expressed as

$$\log t = 1.3M + 17.0 - \log r \quad (3)$$

Fig. 11 shows the relationship between the elapsed time t and the magnitude M of the next earthquake for seven different average moment-release rates r . Using this figure, the probable magnitude M of the next earthquake or the elapsed time t until the next event can be estimated from the average moment-release rate for each fault system. This figure can be used to evaluate the seismic risk of a given fault system.

As mentioned above, it was concluded that movement of the ATTL was also responsible for the Keicho-Fushimi earthquake which occurred about 400 years ago. From the elapsed time since that earthquake and the average moment-release rate of the ATTL central segment, the magnitude of an event is estimated to range

TABLE III

The average slip rate of the constituent faults and the average moment-release rate of the central 40-km segment of the ATTL

Slip sense	Average slip rate, D/τ (mm year $^{-1}$) ^a	Average moment-release rate, $r \times 10^{26}$ dyne cm year $^{-1}$
Right-lateral	0.5–1.5	0.0014–0.0041
Dip-slip	0.1–0.8	0.0003–0.0022
Total		0.0017–0.0063

$L = 40$ km, $W = 20$ km and $\mu = 3.4 \times 10^{11}$ dyne cm $^{-2}$.

^aBased on Sangawa (1978).

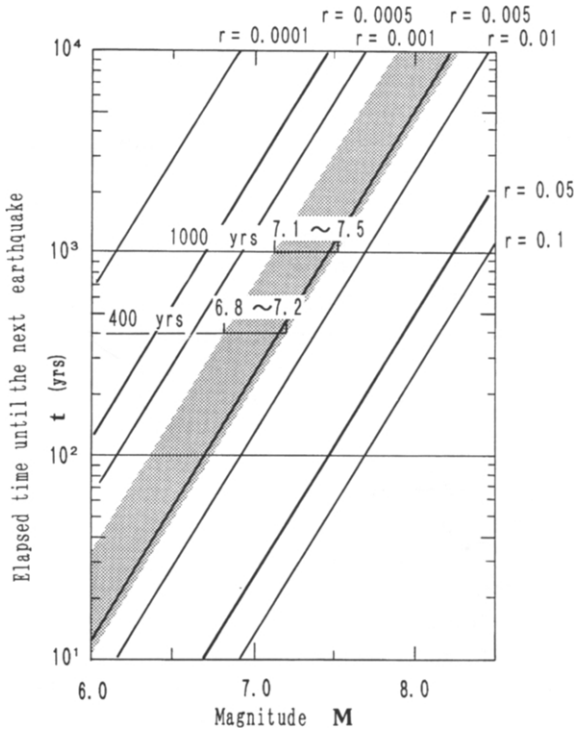


Fig. 11. Relationship between the magnitude M of a possible earthquake and the elapsed time t until the next earthquake. Shown are seven lines for different average rates r ($\times 10^{26}$ dyne cm year $^{-1}$). The shaded zone is the range of the average moment-release rate of the ATTL, estimated from the average slip rates of the constituent faults.

from M 6.8 to M 7.2 by use of either Fig. 10 or Eq. (3). The determined maximum value of the magnitude equals that of the Kobe earthquake, suggesting that the moments accumulated along the 40-km central segment since the former event were completely released by the Kobe event.

Archaeological excavations have produced evidence that movement of the ATTL resulted in another event around 500 A.D., prior to the Keicho-Fushimi earthquake (see Fig. 9). The interseismic period between the two earthquakes was approximately 1000 years. In the same manner as mentioned above, this interseismic period and the average moment-release rate of the ATTL central segment yield a magnitude M ranging from 7.1 to 7.5, as shown in Fig. 10. It is concluded that the maximum value of the magnitude equals that of the Keicho-Fushimi earthquake.

The above argument confirms the suggestion that both the Kobe and Keicho-Fushimi earthquakes were created by the movement of a segment of the ATTL. This is also consistent with the interpretation that the average moment-release rate of a fault system can be an important indicator used in evaluating the seismic risk of a fault system (Kanaori et al., 1992d).

6. Discussion

6.1. Sequential occurrence of inland earthquakes

Kanaori et al. (1991) examined the spatial and temporal relationship between historical inland earthquakes which damaged central Japan and the movements of fault systems. From this relationship, a seismic cycle was identified, consisting of active and quiet periods along a fault system. When an active period is initiated, a portion of the fault system begins to rupture, creating earthquakes. The active period is terminated when the entire length of the fault system is covered by seismic ruptures with no overlapping. The quiet period of the fault system is then established, lasting until the next active period.

For example, the 1891 M 8.0 Nobi earthquake, generated along a centrally located 80-km long segment of the Fukui-Neodani block boundary, was followed by the occurrence of the 1945 M 6.8 Mikawa and the 1948 M 7.1 Fukui earthquakes along the respective southern and northern segments. Eventually, the Fukui-Neodani block boundary was probably completely covered by the ruptures of these three destructive earthquakes (Kanaori et al., 1994b).

The rupture of the central 40-km segment of the ATTL appears to have produced the Kobe earthquake, as was pointed out above. Since the total length of the ATTL is 100 km, both the eastern and western 30-km segments remain unruptured during the present time period. Along the Fukui-Neodani block boundary, both the southern and northern segments ruptured approximately 50 years after the rupture of the central segment (Kanaori et al., 1994b). If the seismicity of the ATTL is similar to that of the Fukui-Neodani block boundary, the unruptured eastern and western segments of the ATTL represent dangerous areas which could produce destructive earthquakes within the next several tens of years.

It is predicted from the average moment-release rate that an unruptured 30-km long segment has the potential of creating an earthquake having a magnitude of M 6.7 to M 7.1.

6.2. Seismic sequences and the next possible earthquake

Fig. 12 shows sequences of inland earthquakes along the fault systems in central Japan and the great offshore earthquakes along the Nankai trough (NT) which have occurred since 1500 A.D. The HKFL and the ATTL separate at the Kyoto basin and join the MTL to the south. Here, the ATTL events can be regarded as the HKFL events when sequential earthquake occurrence is studied as shown in Fig. 12.

As pointed out by Kanaori et al. (1993b, 1994a), five seismic sequences in which earthquake occurrence migrated from east to west, have been identified among fault systems west of the Tsurugawan-Isewan tectonic line (TITL). Each sequence was terminated by the occurrence of a Nankai trough event. An HKFL or ATTL event occurred within the 30 years following an event on the TITL. A great offshore

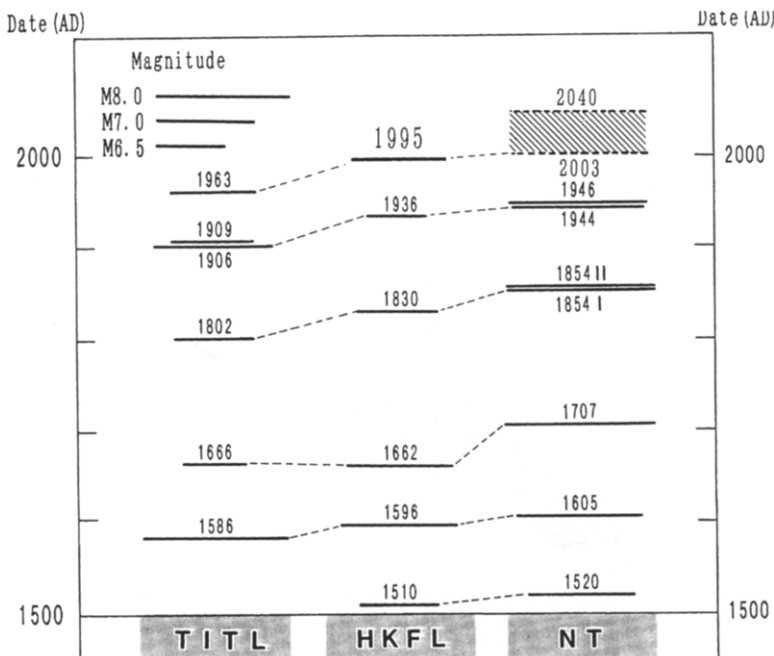


Fig. 12. Earthquake sequences along the Tsurugawan-Isewan tectonic line (TITL), the Hanaore-Kongo fault line (HKFL) or the Arima-Takatsuki tectonic line (ATTL), and the Nankai trough (NT). Earthquake occurrence tends to migrate from east to west. A single sequence appears to be terminated by an event on the Nankai trough.

earthquake along the Nankai trough was then generated during the period ranging from 8 to 45 years after the HKFL or ATTL event. The latest sequence, including the 1995 Kobe earthquake, is following the regularity of the previous sequences.

If this seismic sequence continues in the future, the 1995 Kobe earthquake should be followed by a Nankai trough event, which is hereby predicted to occur during a year between 2005 and 2040 A.D. Proceeding or following the Nankai trough event, movement of the MTL may also create a destructive earthquake (Kanaori et al., 1994a).

6.3. Microplate model

Inland earthquakes which have damaged central Japan west of the Itoigawa-Shizukaga tectonic line were generated along major fault systems. Since these fault systems entirely cut through the brittle crust of the earth (Kanaori et al., 1991), they are regarded as boundaries of microplates. As shown in Fig. 13, central Japan can be separated into several microplates by the fault systems. Lower depth limits of the microseismicity in central Japan (Mikumo et al., 1988) and aftershocks

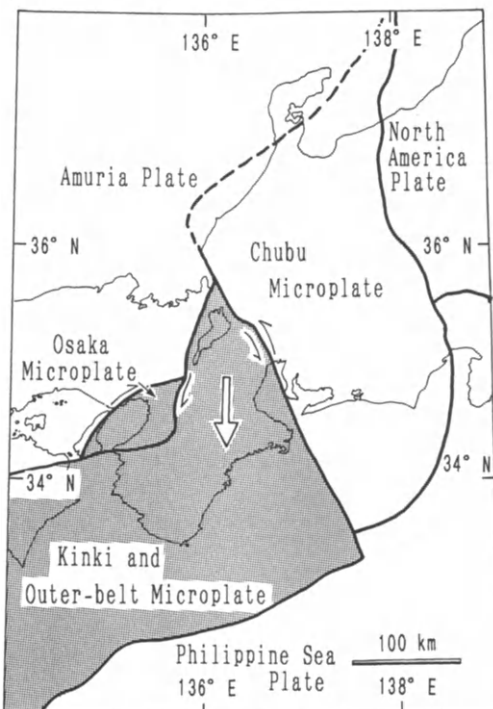


Fig. 13. Interpretation of sequential occurrence of destructive earthquakes by the microplate model of central Japan as described in Kanaori et al. (1993b, 1994a).

of the Kobe earthquake occurred at depths of less than 20 km. This gives the thickness of the microplates which behave in a brittle fashion.

Based on a microplate model, Kanaori et al. (1993a) gave an explanation of the sequential occurrence of destructive inland earthquakes along the fault systems and the great offshore earthquakes along the Nankai trough. According to their model, the coupling of the left-lateral slip on the TITL and the right-lateral slip on the HKFL or ATTL forces the Kinki-Outer microplate southward. Since this forcing reduces the normal stresses acting on the MTL, it becomes relatively easy for the MTL to slip. Simultaneously, the stress concentrations are accelerated along the Nankai trough which constitutes the south-southeast boundary of the Kinki-Outer microplate. The normal stress reduction and stress concentration will induce inland earthquakes along the MTL and offshore earthquake along the Nankai trough, respectively. This suggests that plate subduction along the Nankai trough is not generally responsible for inland earthquakes.

On the other hand, in the context of plate tectonics, the generation of the Kobe earthquake was the result of either: (1) east-west compression by the Pacific plate (Huzita, 1980), (2) subduction of the Philippine Sea plate from the southeast (Seno, 1977), or (3) the eastward migration of the Amuria plate occupying the eastern

part of the Eurasia plate (Tamaki and Honza, 1985). It is difficult from these plate kinematics, however, to understand the generation of inland earthquakes, including the Kobe earthquake, and to predict the locations of such earthquakes. According to the present microplate model, it can be pointed out that a counterclockwise rotation of the Osaka microplate was induced by the generation of the Kobe earthquake, since the ATT that constituted the northwestern boundary of the microplate slipped in a right-lateral sense.

Whereas a number of active faults are distributed in the epicentral region of the Kobe earthquake, no historical earthquakes have been recorded in the area. From this inconsistency, Matsuda (1981) pointed out that the epicentral region was one of several dangerous areas suffering destructive inland earthquakes in the Japanese Islands. It was concluded from this indication that the Kobe earthquake was predicted to occur. This is a misunderstanding, however, since the suggestion can neither explain why the earthquake hit the Kobe area nor why it was currently generated. Furthermore, such regions are sporadically located over the Japanese Islands, particularly in central Japan.

The characteristic earthquake model, in which an active fault moves independently to generate a constant magnitude earthquake (Schwartz and Coppersmith, 1984), has long been accepted by Japanese active fault researchers. In the model, specific characteristics of each active fault have been overestimated and the active interval of the fault has been subjectively regarded as approximately 1000 years (e.g., Matsuda, 1975). In contrast, the Kobe earthquake could have been produced by the movement of a fault system consisting of multiple active faults, and the interseismic elapsed time of approximately 400 years between the Kobe and Keicho-Fushimi earthquakes is shorter than that accepted by the characteristic model. This implies that the characteristic earthquake model is too simple to explain the sequential occurrence of large earthquakes along the fault systems. Also, it must be considered that an inland earthquake is created by the movement of a fault system. Since inland earthquakes naturally occur by reflecting the tectonic setting of the Japanese Islands, the existence of a fault system should be precisely evaluated in the framework of the microplate model.

7. Conclusions

The Kobe earthquake which suddenly hit the Hanshin area and Awaji Island, resulting in serious damage and a large loss of life, came as great shock to a number of researchers and engineers. One reason was that the damage was so serious that it was beyond that expected by anyone. The other was that the ground motions generated by the event were far greater than the proposed seismic standard for earthquake-proof designs in Japan. It can be stated that most academic progress in the fields of geology and geophysics is not sufficiently transferred to the earthquake-proof designs which would help in the mitigation of seismic disasters. This situation must be corrected by emphasizing an interdisciplinary study to link the geological

aspects of active faults and seismological aspects of inland earthquakes, and to then transfer new knowledge to the earthquake-proof designs of large structures. Only then will the impact of seismic disasters become less severe for the regional society.

In the present paper, based on the study of distributions of aftershocks and surface ruptures, and calculations of seismic moments released along the ATTL, it was concluded that the Kobe earthquake was probably caused by movement of the ATTL. Since the ATTL can be regarded as constituting the northern boundary of the Osaka microplate, the Kobe earthquake appears to have been generated by reflecting the motion of the microplate. Accordingly, it becomes increasingly important to evaluate the activity of fault systems in the tectonic setting of the Japanese Islands in order to learn of the occurrence of inland earthquakes and to mitigate natural disasters caused by seismic ground motions.

Acknowledgements

The authors wish to thank Prof. K. Yairi of Gifu University for useful discussions. They also express appreciation to Prof. T. Yanagidani of Nihon University, Mr. M. Seno of the Kokusai Kogyo Co. Ltd, Mr. S. Kushida of Nagoya Road Engineers Co. Ltd, and T. Nakai of Toyo Geological Survey Co. Ltd for assistance in field work in the damaged region of the Kobe earthquake. Their appreciation is also extended to Profs. F. Oka, M. Sugito, and A. Yashima of Gifu University for field work in the Nojima fault which appeared on the ground surface as a result of the Kobe earthquake.

References

- Ando, M., 1975. Source mechanisms and tectonic significance of historical earthquakes along the Nankai trough, Japan. *Tectonophysics*, 27: 119–140.
- Awata, Y., Mizuno, K., Sugiyama, Y., Shimokawa, K., Imura, R. and Kimura, K., 1995. Surface faults associated with the Hyogo-nanbu earthquake of 1995. *Chishitsu News*, 486: 6–11 (in Japanese).
- Chuo-Kaihatsu Co. Ltd, 1995. Research report of the Great Hanshi earthquake disasters. Chuo-Kaihatsu Co. Ltd, Tokyo, 51 pp. (in Japanese).
- Earthquake Damage Investigation Group of Central Research Institute of Electric Power Industry, 1995. Preliminary report on characteristics and damages investigation of the 1995 Hyougoken-nanbu earthquake. Research Report of Central Research Institute of Electric Power Industry, U94042, 133 pp. (in Japanese with English Abstr.).
- Education Board of Hyogo Prefecture, 1992a. A field guide to the Hake excavation site. 43 pp. (in Japanese).
- Education Board of Hyogo Prefecture, 1992b. A field guide to the Tsukuda archaeological site. 8 pp. (in Japanese).
- Education Board of Ikeda City, 1989. Gosando Tumulus, Ikeda City, Osaka Pref., 35 pp. (in Japanese).
- Gravity Research Group in Southwest Japan, 1994. A Bouguer gravity anomaly map in central Japan. Appended Map of Rept. Geol. Surv. Japan, 280: 29–36.
- Hashimoto, M., Sagiya, T., Tsuji, H., Hatanaka, Y. and Tada, T., 1995. Coseismic displacement of the 1995 Kobe earthquake. *J. Phys. Earth*, in press.

- Hatori, T., 1974. Sources of large tsunamis in southwest Japan. *Zishin* 2 (J. Seismol. Soc. Japan), 27: 10–24 (in Japanese with English Abstr.).
- Hirata, S., 1995. Aftershock activity accompanying the 1995 Kobe earthquake. Kagaku, Iwanami Publishing Co., Tokyo, 65: 199 (in Japanese).
- Huzita, K., 1980. Role of the Median Tectonic Line in the Quaternary tectonics of the Japanese islands. *Geol. Soc. Mem.*, 18: 187–210.
- Huzita, K. and Okuda, S., 1973. Neotectonics of Median Tectonic Line in Kinki and Shikoku, Southwest Japan. In: R. Sugiyama (Editors), *Median Tectonic Line*, Tokai Univ. Press, Tokyo, 97–109 (in Japanese with English Abstr.).
- Japanese Union of Geological Survey Companies, 1995. Record of Urgent Research meeting on “the Great Hanshin earthquake” from the view points of structural basements, Tokyo, 113 pp. (in Japanese).
- Kanaori, Y., Kawakami, S. and Yairi, K., 1991. Space-time distribution patterns of destructive earthquakes in the inner belt of central Japan: activity intervals and locations of earthquakes. *Eng. Geol.*, 31: 209–230.
- Kanaori, Y., Kawakami, S. and Yairi, K., 1992a. The block structure and Quaternary strike-slip block rotation of central Japan. *Tectonics*, 11: 47–56.
- Kanaori, Y., Kawakami, S. and Yairi, K., 1992b. Space-time distribution patterns of destructive earthquakes in the inner belt of central Japan (part 2): moment-release rates and earthquake prediction. *Eng. Geol.*, 32: 113–122.
- Kanaori, Y., Kawakami, S. and Yairi, K., 1992c. Space-time distribution patterns of destructive earthquakes in the Kinki district, central Japan: implications of the Hanaore-Kongo fault and Tsurugawani-Isewan tectonic lines. *J. Jpn Soc. Eng. Geol.*, 33: 187–201. (in Japanese with English Abstr.).
- Kanaori, Y., Kawakami, S. and Yairi, K., 1992d. Space-time distribution patterns of destructive earthquakes in the inner belt of central Japan (part 3): seismic hazard assessment. *Eng. Geol.*, 33: 99–110.
- Kanaori, Y., Kawakami, S. and Yairi, K., 1993a. Space-time correlations between inland earthquakes in central Japan and great offshore earthquakes along the Nankai trough. *Eng. Geol.*, 33: 289–303.
- Kanaori, Y., Kawakami, S., Yairi, K. and Hattori, T., 1993b. Liquefaction and flowage at archaeological sites in the inner belt of central Japan: tectonic and hazard implications. *Eng. Geol.*, 35: 65–80.
- Kanaori, Y., Kawakami, S. and Yairi, K., 1994a. Seismotectonics of the Median Tectonic Line in southwest Japan: implications for coupling among major fault system. *Pure Appl. Geophys.*, 142: 589–607.
- Kanaori, Y., Kawakami, S., Yairi, K. and Niwa, S. 1994b. A sequence of destructive earthquakes and the coupling of fault systems in central Japan. *Eng. Geol.*, 37: 167–180.
- Koto, B., 1893. On the cause of the great earthquake in Central Japan, 1891. *J. Coll. Sci. Imp. Univ. Japan*, 5: 196–353.
- Matsuda, T., 1975. Magnitude and recurrence interval of earthquakes from a fault. *Zishin* 2, 28, 169–283 (in Japanese with English Abstr.).
- Matsuda, T., 1981. Active faults and damaging earthquakes in Japan – macroscopic zoning and precaution fault zones. In: D.W. Simpson and P.G. Richard (Editors), *Prediction; an International review*, Am. Geophys. Union, 279–289.
- Mikumo, T., Wada, H. and Koizumi, M., 1988. Seismotectonics of the Hida region. *Tectonophysics*, 14: 95–119.
- Nagoya Road Engineers Co. Ltd, 1995. Damages of the Chugoku highway induced by the 1995 Southern Hyogo earthquake. Department of Disaster Prevention, Nagoya Road Engineers Co. Ltd, Nagoya, 15 pp. (in Japanese).
- Okada, A. and Sangawa, A., 1978. Fault morphology and Quaternary faulting along the Median Tectonic Line in the southern parts of the Izumi Range. *Geogr. Rev. Japan*, 51: 385–405 (in Japanese with English Abstr.).
- Research Group for Active Faults in Japan, 1991. Active faults in Japan, sheet maps and inventories, revised edition. University of Tokyo Press, Tokyo, 437 pp. (in Japanese with English Abstr.).
- Sakurai, T., 1995. Ground surface disturbance near Yokohsan fault produced by seismic movement of the Southern Hyogoken earthquake 1995. *J. Japan Soc. Eng. Geol.*, 36: 63–68 (in Japanese).

- Sangawa, A., 1978. Fault topography and Quaternary faulting along the middle and eastern parts of the Arima-Takatsuki tectonic line, Kinki district, central Japan. *Geogr. Rev. Japan*, 51: 760–775 (in Japanese with English Abstr.).
- Sangawa, A., 1989a. Point of contact between archaeology and paleo-earthquake research. *Quaternary Res.*, 27: 241–252 (in Japanese with English Abstr.).
- Sangawa, A., 1989b. Earthquake traces. In: *Kosaka site (part 8)*, edited by Archaeol. Res. Centr., Osaka Pref., 24–27 (in Japanese).
- Sangawa, A., 1990a. Evidences of paleoearthquakes found out in some archaeological sites. *J. Geogr.*, 99: 471–482 (in Japanese with English Abstr.).
- Sangawa, A., 1990b. Paleoearthquake evidence. Report of Gunge Site 1990 by Education Board of Kobe City, 85–88.
- Sangawa, A., 1992. Traces of paleoearthquakes observed in many archaeological sites. *Jpn Soc. Soil Mech. Fundam. Eng.*, 40: 13–18 (in Japanese).
- Schwartz, D.P. and Coppersmith, K.J., 1984. Fault behavior and characteristic earthquakes: examples from the Wasatch and San Andreas faults. *J. Geophys. Res.*, 89: 5681–5698.
- Seno, T., 1977. The instantaneous rotation vectors of the Philippine Sea plate relative to the Eurasian plate. *Tectonophysics*, 42: 209–226.
- Shimamoto, T., 1995. Mystery of “belt of seismic disasters”. *Kagaku*, Iwanami Publishing Co., Tokyo, 65: 195–198 (in Japanese).
- Shimazaki, K., 1976. Intra-plate seismicity and inter-palte earthquakes: historical activity in southwest Japan. *Tectonophysics*, 33: 33–42.
- Site Research Committee of Kawanishi City, 1989. Sakane site – research report by the 19th excavation study. Kawanishi City, Osaka Pref., 160 p. (in Japanese).
- Takahashi, M., 1990. Geomorphological and environmental analysis of Bogatsuwa site. Education Board of Kobe City, 121–133 (in Japanese).
- Tamaki, K. and Honza, E., 1985. Incipient subduction and obduction along the eastern margin of the Japan Sea. In: N.L. Carter and S. Uyeda (Editors), *Deformation of Continental Lithosphere*, Tectonophysics, 119: 381–406.
- Toyo Geological Survey Co. Ltd, 1995. Research news on damages by the Southern Hyogo earthquake (Great Hanshin Disaster). Toyo Geol. Surv. Co. Ltd, Kyoto, 122 pp. (in Japanese).
- Umeda, Y., Murakami, H., Io, Y., Cho, A., Ando, M. and Daicho, A., 1984. Earthquake traces impressed on the Yayoi-age dwelling site. *Zishin* 2, 37, 465–473 (in Japanese with English Abstr.).
- Usami, T., 1987. Descriptive catalogue of disastrous earthquakes in Japan, new edition. University of Tokyo Press, Tokyo, 434 pp. (in Japanese).
- Utsu, T., 1974. Space-time pattern of large earthquakes occurring off the Pacific coast of the Japanese islands. *J. Phys. Earth*, 22: 325–342.
- Wesnousky, S.G., Scholz, C.H. and Shimazaki, K., 1982. Deformation of an island arc: rates of moment release and crustal shortening in intraplate Japan determined from seismicity and Quaternary fault data. *J. Geophys. Res.*, 87: 6829–6852.

CHAPTER 6

The 1995 Kobe earthquake and problems of evaluation of active faults in Japan

SHINJI TODA *, RYUTA HATAYA, SHINTARO ABE and
KATSUYOSHI MIYAKOSHI

*Department of Geology and Geotechnology, Central Research Institute of Electric Power Industry, 1646
Abiko, Abiko City, Chiba Prefecture 270-11, Japan*

Abstract

The Kobe earthquake (M 7.2) of January 17, 1995, which was the most damaging earthquake in recent Japanese history, made manifest the need for reconsidering the method of evaluating active faults. An earthquake of this magnitude at this time was unexpected according to conventional evaluation, in which the potential magnitude of earthquakes at a certain site is estimated by considering the greatest earthquake in the past 400 years and the length of the active fault. The following characteristics of this earthquake made it appear unlikely by conventional understanding: (1) the Kobe earthquake involved several neighboring faults, which had been previously been identified as separate fault systems; (2) the surface rupture of about 10 km length was much shorter than the 50 km seismic faulting; (3) the interval of 400 years between the Kobe and penultimate Keicho earthquake of 1596 AD (M 7.5), which has been revealed by historical documents and some excavations, is much shorter than the 2000 years estimated by calculating the average slip rate of displaced landforms. These shortcomings imply that active fault evaluation with the traditional characteristic earthquake model which deals with each fault separately, is not adequate for an area like Japan where active faults swarm. New concepts such as the block rotation model (Kanaori, 1990; Late Mesozoic-Cenozoic strike-slip and block rotation in the inner belt of Southwest Japan. Tectonophysics, 177: 381–399) considering the macroscopic tectonic framework for fault interactions are needed. Furthermore, fault dynamics cannot be ignored; physical and temporal parameters associated with faulting, such as moment release rate, must be considered for realistic and precise evaluation.

1. Introduction

On January 17 at 5:46 a.m. the most damaging inland earthquake in southwest Japan since the 1948 Fukui earthquake M 7.1 (M , Japan Meteorological Agency Magnitude) occurred around Kobe City and northern Awaji Island (Figs. 1 and 2).

* Corresponding author. Tel.: 81471 82 1181; fax: 81471 83 3182; e-mail: toda@criepi.denken.or.jp.

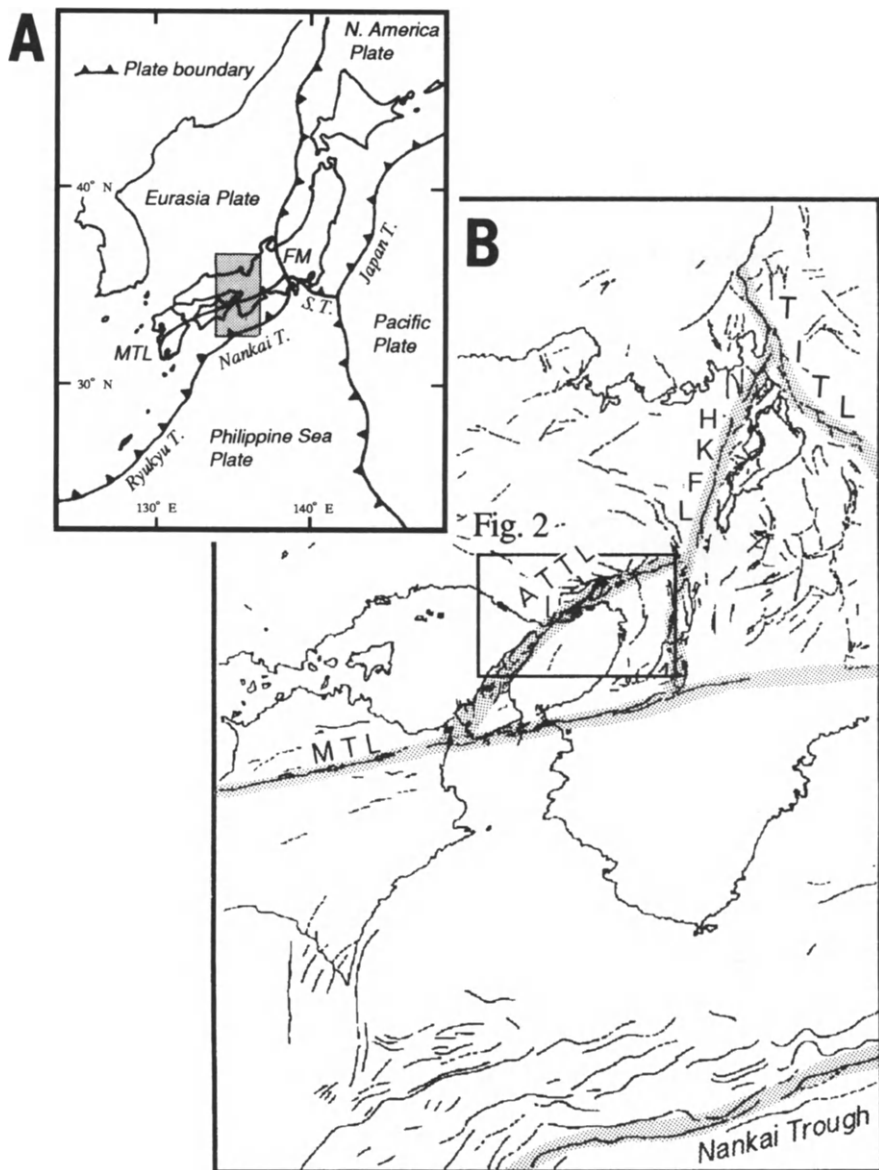


Fig. 1. (A) The distribution of major plate boundaries in and around the Japanese Islands. (B) The distribution of active faults around the Kobe area. This is a magnified view of the shaded box in (A). Abbreviations of the tectonic lines are: FM, fossa magna; MTL, median tectonic line; TITL, Tsurugawan-Isewan tectonic line; HKFL, Hanaore-Kongo fault line; and ATTL, the Arima-Takatsuki tectonic line (Kanaori et al., 1993). S.T., Sagami trough. The Kinki triangle active fault zone (Huzita, 1962, 1980) is the area surrounded by the MTL, TITL, HKFL and ATTL. Active faults are based on the Research Group for Active Faults in Japan (1991).

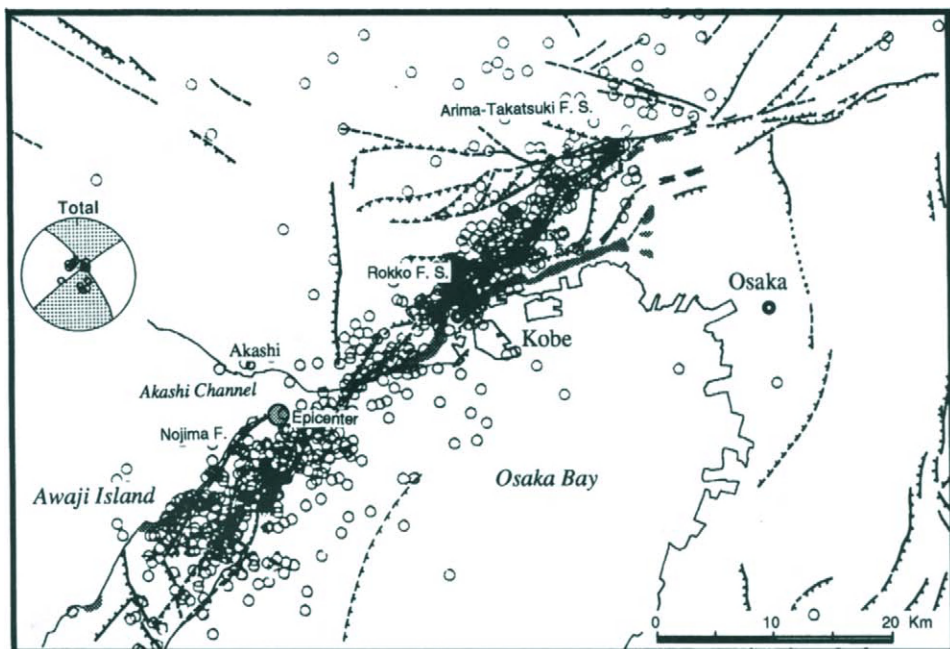


Fig. 2. Map of seismological features and previously mapped active faults in the area of the Kobe earthquake. Shading indicates the area of ground-motion of a severe shock of JMS (Japan Meteorological Agency intensity scale) VII. Small open circles indicate aftershock epicenters from January 17, 10:03 to January 20, 04:59 (data from Disaster Prevention Research Institute, Kyoto University). The focal mechanism of mainshock (Kikuchi, 1995a) indicates almost purely lateral faulting. Active faults are based on the Research Group for Active Faults in Japan (1991).

The earthquake resulted in at least 5500 deaths, 35 000 injuries and as many as 100 000 collapsed houses. The Meteorological Agency stated that it had a magnitude of M 7.2. According to the US Geological Survey, the quake registered a moment magnitude reading of 6.8. Studies of aftershocks and permanent ground deformation have provided a clear image of the earthquake mechanism and related geological phenomena. The earthquake had a focal depth of 14.3 km and right-lateral mechanism. The epicenter was approximately 20 km southwest of Kobe City center. Ground motion records from several sources have been compiled by Koketsu (1995). The duration of strong shaking (peak accelerations exceeding 0.5 and up to 0.8 g) was about 15 s in many locations.

This devastating earthquake was caused by the movement of several active faults in southwest Japan, where no destructive earthquakes have occurred since the 1946 Nankai earthquake, M 8.0. A historical record of major earthquakes affecting Japan has been maintained since 416 AD (e.g., Usami 1987). Destructive earthquakes have been well recorded for the past 400 years and instrumental devices have been used since the 1891 Nobi earthquake (M 8.0). The mechanics of earthquakes and

faulting have been also discussed since the Nobi earthquake which involved 80 km of surface faulting (Koto, 1893). On the basis of the experience and recognition of shallow destructive earthquakes with surface faults, geological and geomorphological studies for active faults have been performed for the purpose of revealing their presence and measuring activity such as slip rate (e.g., Sugimura and Matsuda, 1965). As the result of many surveys, the dense distribution of active faults was recognized and summarized in a series of active fault maps of Japan (Research Group for Active Faults in Japan, 1991). Based on the active fault maps, historical earthquakes, and geological structure, some seismotectonic zonation maps (e.g., Omote et al., 1980; Matsuda, 1981; Kinugasa, 1990; Kakimi et al., 1994) and seismic hazard risk maps (e.g., Kanaori et al., 1992c) have been proposed. The seismic zoning maps, which indicate maximum potential magnitude in a given district, are used as a basic data set in the design of large earthquake-resistant construction projects and to estimate the regional earthquake risk. However, as compared with the conditional probability of rupture of the San Andreas fault in California (Working Group on California Earthquake Probability, 1988), temporal factors such as recurrence interval and regional patterns of earthquake generation have not been sufficiently investigated.

To try to detect the temporal factors, trench excavation surveys have been performed on several active faults in Japan (e.g., Tsukuda and Yamazaki, 1984; Tsutsumi et al., 1991). However, the results of them could not be helped but evaluating based on the characteristic earthquake model (Wallace, 1970; Matsuda, 1975; Schwartz and Coppersmith, 1984) because of insufficient information of paleo-events. Paradoxically, the characteristic earthquake model has been believed and applied by many researchers. For practical examples, "precaution faults," which are those particularly expected to generate future destructive earthquakes, have been extracted from among the many major active faults in Japan (e.g., Matsuda, 1977).

On the other hand, it has recently been suggested that quasi-periodicity or temporal clustered behavior concerning fault interaction is much more realistic than the characteristic earthquake model in intraplate Japan (e.g., Kanaori et al., 1991; Toda et al., 1994) and in certain regions of California (e.g., Sieh et al., 1989; Grant and Sieh, 1994). The rupture area is also thought to vary from cycle to cycle depending upon fault interaction.

Ironically, the Kobe earthquake dramatically illustrated the problem of evaluating active faults with respect to the seismic hazard assessment and long-term earthquake prediction. In this paper, we summarize the Kobe earthquake, particularly from the viewpoint of faulting process. Understanding of the faulting process in intraplate Japan indicates that destructive earthquakes such as the one in Kobe are caused by multiple events associated with several adjacent faults. Secondly, on the basis of this recognition and recent studies, some problems of evaluating active faults and long-term earthquake prediction are presented. Finally, we argue that new concepts concerning fault interaction and dynamics promise more realistic evaluation than the conventional method.

2. Geological and tectonic background

The Japanese island arc is located at the eastern border of the Eurasian plate and the North America plate, and is bounded to the east and south by the Pacific and Philippine Sea plates, respectively (Fig. 1). The majority of earthquakes in Japan, including the largest, occur along the Japan trench and the Sagami and Nankai troughs (e.g., Usami, 1987). Focal mechanisms of large earthquakes along these features are usually of the low-angle thrust type and interpreted to indicate that the Pacific and Philippine Sea plates are being subducted beneath northeastern and southwestern Japan, respectively (Fitch and Scholz, 1971; Kanamori, 1972; Ando, 1974, 1975; Scholz and Kato, 1978).

On the other hand, a number of active faults have developed inland in Japan (Research Group for Active Faults in Japan, 1991). These fault systems accommodate part of the relative plate motions as a deformation zone (Wesnousky et al., 1982; Kanaori et al., 1992a; Thatcher, 1995). Fault mechanisms of inland (intraplate) earthquakes are usually strike slip or reverse, and the distribution of P axes reveals that the largest island Honshu is, in general, subject to a regional maximum compressive stress that trends easterly. Normal faulting is found in south island Kyusyu, adjacent to the junction of the Nankai Trough and Ryukyu Trench. Horizontal compressive tectonic stresses due to the subduction of the Pacific plate are transferred through the comparatively rigid crust block of the eastern half of northeast Japan to the folded zone of the Japan Sea side, and the tectonic forces are transmitted further to the inner zone of southwest Japan through the northern Fossa Magna region (Huzita, 1980; Huzita and Oike, 1981). Although faults are distributed densely and without obvious order in the inner belt of central to southwest Japan, systematic fault groups make tectonic lines that divide the region into several blocks (Huzita, 1962, 1980; Kanaori, 1990; Kanaori et al., 1993) (Fig. 1). Areas of destruction due to historical earthquakes, and liquefaction and flowage events due to prehistoric earthquakes, have occurred along these lines (Kanaori et al., 1991, 1993).

The area of damaged due to the Kobe earthquake corresponds to the western edge of the Kinki triangle active fault zone (Huzita, 1962, 1980), or the southwest part of the Arima-Takatsuki tectonic line (ATTL) as a block boundary (Kanaori et al., 1992a) (Fig. 1), which consists of many NE–SW striking right-lateral slip faults (Rokko fault system) with northwest-up vertical components. Activity on these faults divides the landform between the Rokko Mountain area and the Kobe lowlands. Thus, the Rokko Mountain area, where the granite blocks are elevated more than 900 m, are considered to be swollen fault blocks due to tectonic compression in the E–W direction (Huzita et al., 1973). The average slip rate of each fault is 0.1–0.9 mm/year right-laterally and vertically. However, the total slip rate summing up parallel running faults is over 1 mm/year in the late Quaternary (Huzita and Kasama, 1982; Research Group for Active Faults in Japan, 1991). On the other hand, in the northern Awaji Island, the granite block sandwiched by two faults along the northwest and southeast coasts has been raised. These faults consists

of many NE-SW striking right-lateral slip faults like those of the Rokko fault system at Kobe, but the vertical component is different.

In spite of the significant fault landforms around Kobe and Awaji Island and many documents of the historical earthquakes in southwest Japan, no big earthquakes around Kobe had been documented since 1500 AD. Regional microseismicity had also been low.

3. The 1995 Kobe earthquake

The rupture that caused the January 17, 1995, Kobe earthquake was initiated in northernmost Awaji Island, at a depth of 14.3 km (the Meteorological Agency, 1995) (Fig. 2), and propagated bilaterally. Swarms of aftershock epicenters after a few days imply NE-SW striking seismic faults with a total length of 50 km. A series of several separate severely damaged areas corresponding to JMS (Japan Meteorological Agency intensity scale) VII (MMS XI-XII) is distributed from the northwest coast of Awaji Island to Nishinomiya and Itami City, extending about 70 km in length.

Surface rupture associated with this earthquake occurred along 9 km northernmost Awaji Island (Fig. 3). It was the most remarkable fault-rupture event in Japan since the 1945 Mikawa earthquake on the Fukui-Neodani block boundary (Kanaori, 1990). Rupture during the Kobe event was on the Nojima fault which had been previously mapped as an active one (Research Group for Active Faults in Japan, 1991: fig. 2). However, no surface ruptures appeared in the Kobe area, in spite of the more devastating damage than on Awaji Island.

3.1. Surface ruptures in northern Awaji Island

Most of the rupture on the Nojima fault was right-lateral strike-slip with down-to-the-northwest vertical component, generally striking N40°E. The trace of the surface rupture was quite simple on the map scale. The fault plane, which was exposed by faulting on the ground surface, dips southeast at 60–80°. Slip distribution is characterized as nonuniform (Fig. 3). Maximum net slip was 2.3 m (right-lateral, 2.0 m; vertical, 1.2 m) at Nojima-Hirabayashi (Fig. 4), which is located in the central part of the Nojima fault. Most of the northeast part of the surface rupture displayed more than 1 m of slip. Displacement along the southwest part of the surface rupture is much less than along the northeast, except around Ogura. At the southern end of the Nojima fault, the surface rupture died out at the Mizukoshi flexure.

Although surface rupture corresponds to the previous mapped Nojima fault, the clusters of aftershock epicenters do not (Fig. 2). The subsurface fault plane inferred from surface rupture also seems to be dipping to the southeast. Therefore, the position of the Nojima fault in seismogenic depth probably shifts to the southeast, where the aftershock epicenters swarm.

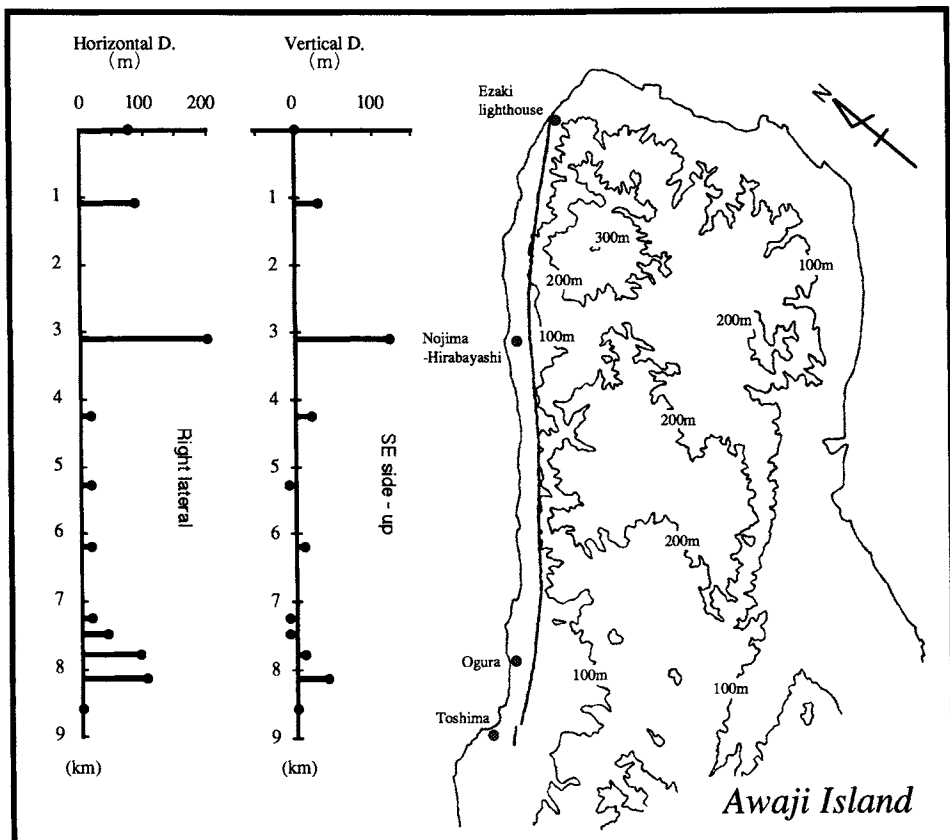


Fig. 3. Displacement along the surface rupture of the Nojima fault in Awaji Island.

In northernmost Awaji Island, despite the surface appearance of the earthquake fault, there were fewer collapsed houses than in Kobe and in the rest of northern Awaji Island (see Fig. 5). In Awaji Island, areas of a severe shock of JMS VII (MMS XI–XII) were restricted to a region southeast of the Nojima fault (Fig. 2). They are generally located not on strongly-built granite but on soft alluvium.

3.2. The disaster belt in the Kobe area and estimated faulting

In the Kobe area, devastating damage of JMS VII (MMS XI–XII) scale occurred in a northeast–southwest belt, about 50 km long and less than 2 km wide (Figs. 2 and 6). Although the areas hardest hit by the tremor (attaining 818 gal in maximum acceleration) were narrow, urban and residential areas unfortunately overlapped them. In these areas, a number of buildings and highways were collapsed by strong ground motion (Fig. 7). Liquefaction and flowage were induced around Kobe Port

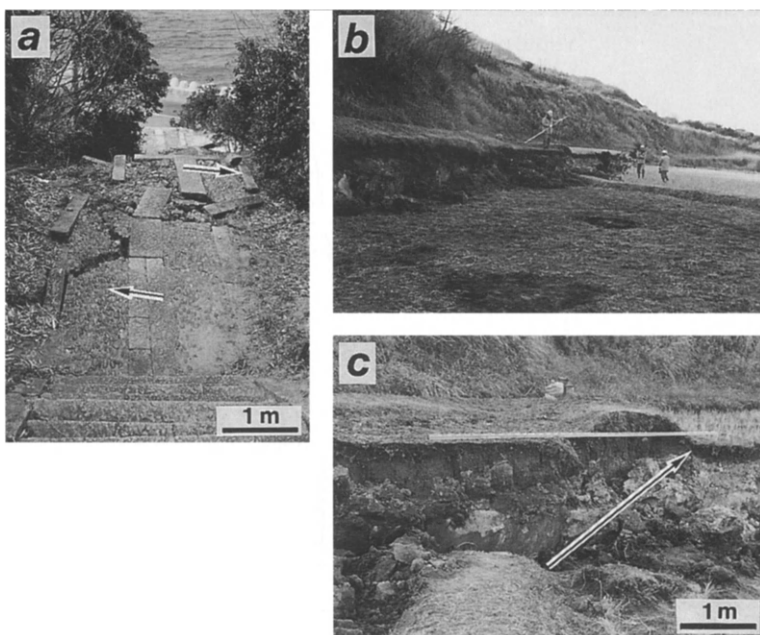


Fig. 4. Photographs of surface rupture along the Nojima fault in Awaji Island. (a) Stone steps destroyed with 70 cm of right-lateral offset at Ezaki lighthouse. Vertical displacement was scarcely recognized. (b) Fault scarp at Nojima-Hirabayashi. (c) Magnified view of (b). Surface rupture along the Nojima fault offsets a footpath in the rice fields 2 m right-laterally and 1.2 m vertically, which is nearly maximum fault displacement measured for the Kobe earthquake.

and included two artificial islands (Fig. 8). More than 100 000 houses collapsed entirely and burned (Fig. 8). Reinforced concrete buildings also suffered most or partial collapse (Fig. 7). The damage conditions were significantly different inside and outside the disaster belt.

Cracks and swells on the ground caused by strong ground motion were noted at many places. Many ruptures and displacements accompanied by landslide, liquefaction and flowage, which some researchers initially mistook as tectonic, also appeared. Nevertheless, no evidence for tectonic surface faulting along previously known active faults appeared around the severely damaged Kobe area. Some reports described earthquake faults with insignificant displacement, such as several centimeters, but they were probably very local phenomena and discontinuous. Definitely, their distribution is quite different from the aftershock zone which probably implies seismic faulting (Fig. 2). Kikuchi (1995b) investigated the precise position of the seismic fault to utilize the closed-circuit video cameras at many convenience stores. By considering the idealized ground motion associated with right-lateral fault propagation, he concluded that the fault trace runs between the heavily damaged zone and the aftershock zone.

The discrepancy between the position of the seismic fault and the disaster belt in

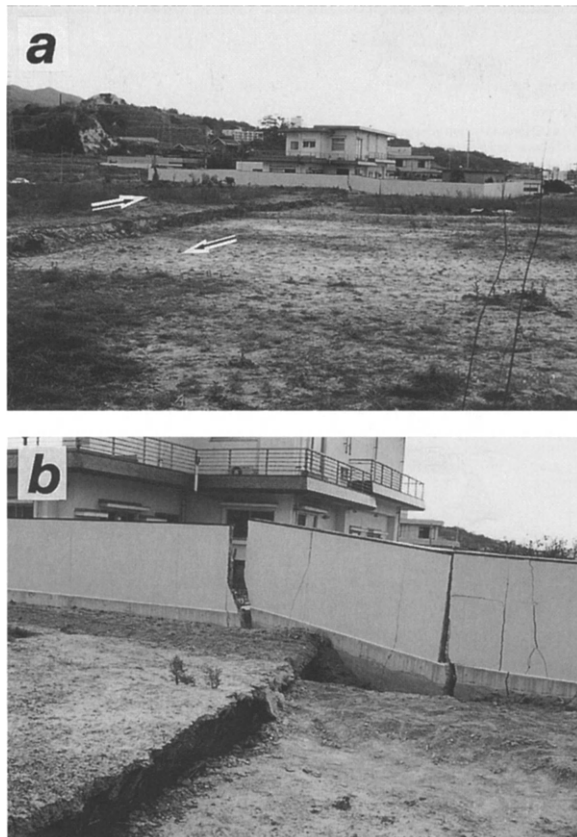


Fig. 5. Photographs of surface rupture along the Nojima fault in Awaji Island. (a) A disturbed house near the surface rupture at Ogura. The surface fault passes through the garden and offsets walls 1 m right-laterally with 40 cm southeast side uplift. Despite its extreme proximity to the Nojima fault, the house was not destroyed. (b) Magnified view of (a).

the Kobe area indicates that the fault position does not necessarily coincide with the region of severe ground-motion (Figs. 2 and 6). In Awaji Island, the most severely damaged area was also concentrated several kilometers southwest of the Nojima fault in contrast to undisturbed houses near the fault (Fig. 5). In both areas, the distribution of disaster belts is probably affected by surface geology, i.e., whether the region consists of soft alluvium or hard bedrock. In fact, the northern boundaries of the disaster belt in the Kobe area are nearly aligned with geological boundaries between the Plio-Pleistocene Osaka Group or terrace and alluvium. Waveforms might be amplified in the disaster belt which is composed of loose sediments.

However, the question of why severe damage is distributed in narrow bands is not a simple one. Koketsu (1995) compiled maximum accelerations and velocities

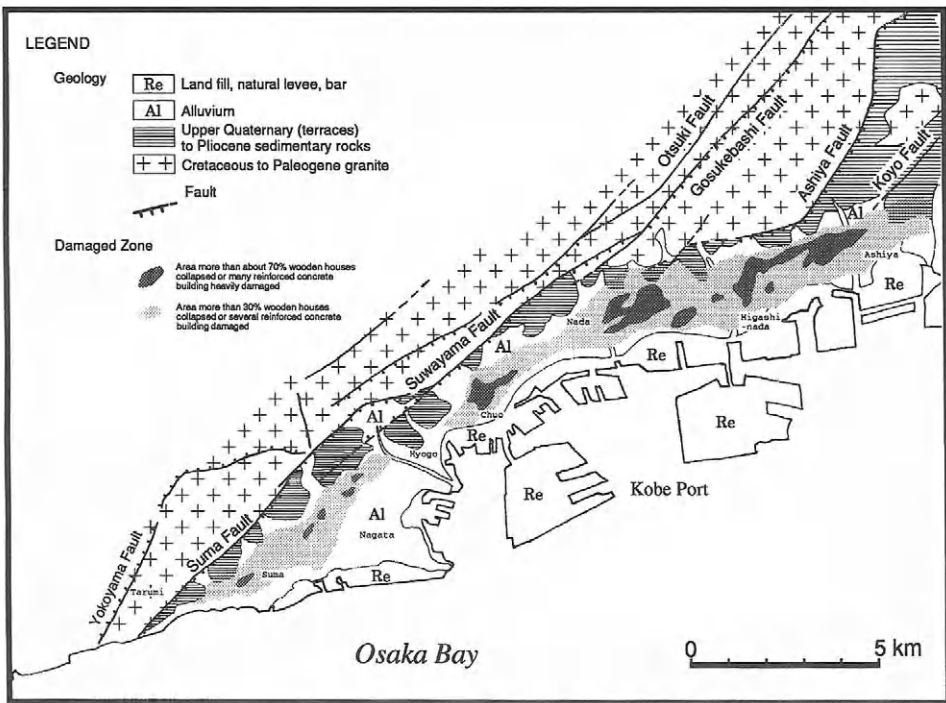


Fig. 6. Relationship between surface geology and damaged zones. Note that the disaster belt corresponds not to the pre-known faults but to the alluvium. Active faults are based on the Research Group for Active Faults in Japan (1991) and Huzita and Kasama (1982).

around the Kansai district during this earthquake, and concluded that degree of damage depends not on maximum acceleration but on the response frequency spectrum. In addition, the nonlinear behavior of ground-motion makes it difficult to evaluate (Irikura, 1995). In other words, thicker soft sediment does not necessarily amplify waveforms. For example, in two artificial islands and fills around Kobe Port, where thicker sediments and fills attain several tens of meters, damage by strong ground acceleration is much less than in the disaster belt. Many engineering researchers have been trying to solve the relationship between damaged areas and ground-motion, from the viewpoint of not only ground accelerations but also of response frequency spectra. In making detailed seismic risk maps (e.g., Ziony et al., 1985) for each Japanese region, we should emphasize that foundation geology is important as well as accurate evaluation of fault activities.

4. Destructive earthquakes with regard to multiple shock

According to the inversion analysis by Kikuchi (1995a), the focal mechanism of the mainshock was divided into three sub-events. The initial event, which had larger

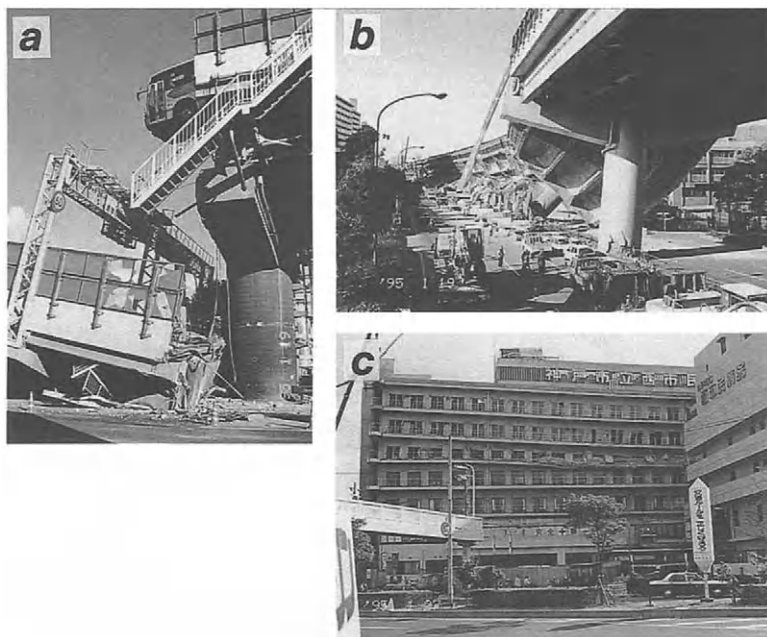


Fig. 7. Photographs showing devastation in the disaster belt in the Kobe area. (a) Collapsed road bridge on the Osaka-Kobe Highway. (b) The Osaka-Kobe Highway fell sideways due to the failure of columns. (c) The fifth floor only of a seven-story hospital collapsed. Collapse of buildings in this earthquake is characterized by the failure of a middle floor or the first floor.

magnitude ($M_w=6.8$) than the others ($M_w=6.3, 6.4$), corresponds to the movement of the Nojima fault. The other two sub-events seem to have occurred in the Kobe area. As no surface faults appeared in the Kobe area, rupture under the Kobe area is restricted to the lower part of the upper crust and has a displacement of less than 1 m (Fig. 9; Ide et al., 1995). According to the detailed inversion analysis of Ide et al. (1995), a northeast position near the epicenter acted as a barrier and delayed rupture propagation. In contrast to this, the Nojima fault had much larger displacement. One surprising character of the displacement of the Nojima fault is that much more slippage occurred near the ground surface than in the lower part of the upper crust. Previous studies of slip distributions along fault planes have indicated that maximum displacement nearly always occurs in the middle to bottom of the upper crust (e.g., Archuleta, 1984; Bakun et al., 1986; Wald and Heaton, 1994). In the coupling model of elastic upper crust and viscoelastic lower crust (Lyzenga et al., 1991), uniform driving stress through the crust causes maximum displacement near the ground surface, whereas stress concentrated at the base of upper crust causes uniform displacement through the upper crust. Therefore, the loading stress prior to rupture on the Nojima fault might have been uniformly distributed. Faults under the Kobe area may have been triggered by only the lowest

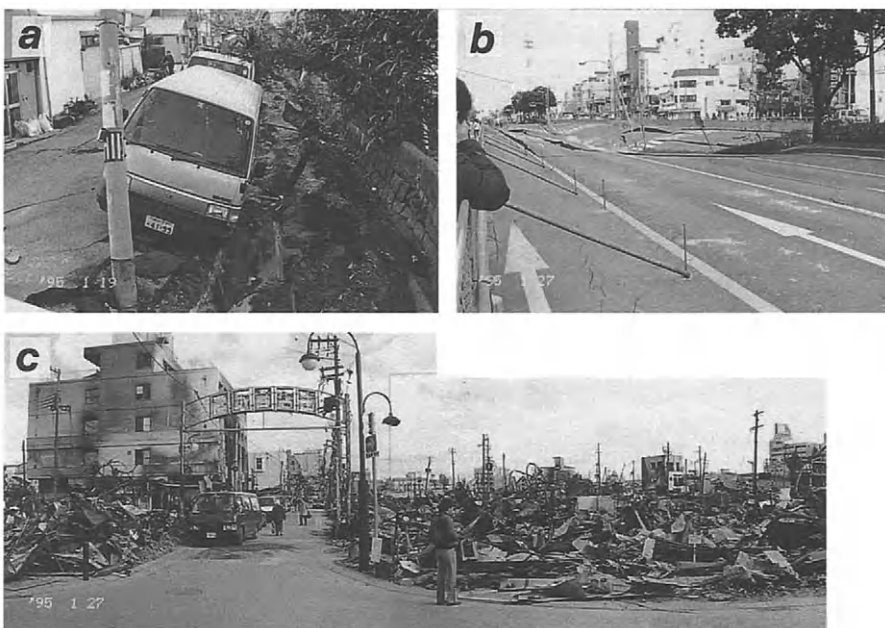


Fig. 8. Photographs showing devastation in the disaster belt of the Kobe area. (a) Liquefaction and flowage at an artificial fill. (b) Road depression caused by the collapse of Taikai subway station in Hyogo-ku. (c) The burned and ravaged district at Nagata-ku. This damaged district was located at the center of the disaster belt and many fires occurred around here.

elastic upper crust by slippage of the viscoelastic lower crust effected by the Nojima fault.

Many destructive inland earthquakes in Japan, besides the Kobe one, have indicated that a single fault does not move independently but that a set of faults moves simultaneously to produce a larger earthquake. For example, the 1891 Nobi earthquake ($M 8.0$) involved seven surface faults such as the Neodani and Nukumi faults, totally 80 km length (Matsuda, 1974). The 1896 Rikuu earthquake and the 1927 Tango earthquake also produced five and two surface continuous ruptures, respectively. These facts suggest that the interlocking of faults holds the key to the solution of the evaluation of active faults.

5. Discussion

5.1. Expected magnitude and fault interaction

The long-term prediction of earthquakes or seismic hazard assessment, based on the evaluation of active faults, must lead to the expected magnitude, place and time. If these elements can be perfectly estimated, it enables major engineering works to

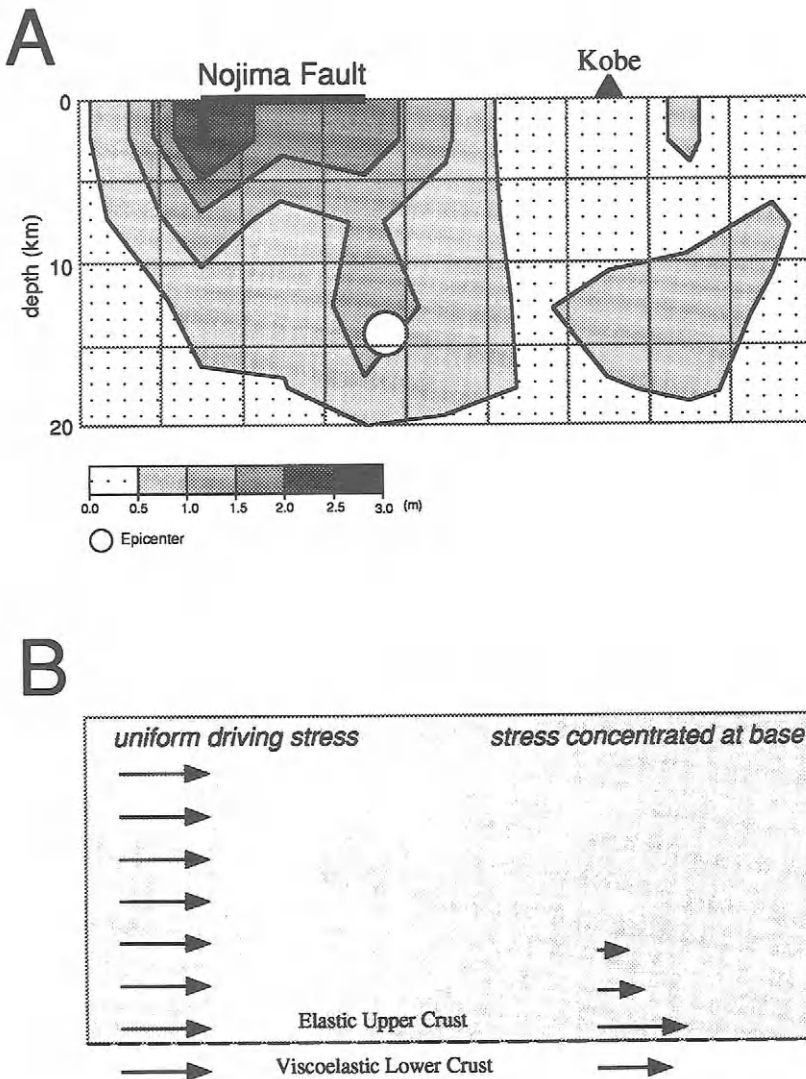


Fig. 9. (A) Cross-section of the strike-slip distribution determined from inversion analysis by Ide et al. (1995). (B) Inferred state of crustal stress just before the earthquake.

be undertaken to reduce damage and loss of life. Particularly, for designing large earthquake-resistant construction projects, the expected magnitude during the anticipated lifetime of the building at a certain site must be evaluated accurately.

The conventional way of estimating the magnitude of earthquakes at a certain site is to consider the maximum historical earthquake during the past 400 years and the length of the active fault. Practically, evaluation by the empirical relationship

between magnitude M and fault length L ($\log L$ (km) = $0.6M - 2.9$; Matsuda, 1975; Fig. 10) has been applied rather than the maximum historical earthquake, because the period documenting historical earthquakes is much shorter than the general recurrence interval of active faults. This relationship was derived from the relationship between the magnitude M of an earthquake and the ruptured length of the fault L which appeared on the ground surface at the time of the earthquake from 1891 to 1970. While useful and convenient for estimation of an approximate value, this relationship has the following problems. (1) Scattering of source data is so large that misestimation of one magnitude over and under is possible. (2) Data are confused by values of surface faulting and values obtained from seismological or geodetic data. Recently, Wells and Coppersmith (1994) have noted that the length of rupture at the surface is equal to 75% of the subsurface rupture length and that the ratio of surface rupture length to subsurface rupture length increases with magnitude. In this connection, the appearance rate of surface faults inland of Japan over $M=6.4$ is actually about 25% since the 1891 Nobi earthquake. (3) Definition or evaluation of fault length which is likely to rupture simultaneously, is difficult. Matsuda (1990) grouped all the active faults in Japan into "seismogenic fault groups", based on having steps narrower than 5 km, which repeatedly produce independent large earthquakes. The "5 km step" criterion seems to be derived from the frequency distribution of widths of the main fault zone appearing in historical earthquakes (Bonilla, 1970; Wesnousky, 1988). However, ambiguous factors (fault bends and sense) and seismotectonic consideration may have been ignored. Furthermore, if this definition is carried out automatically in Japan, an unrealistic

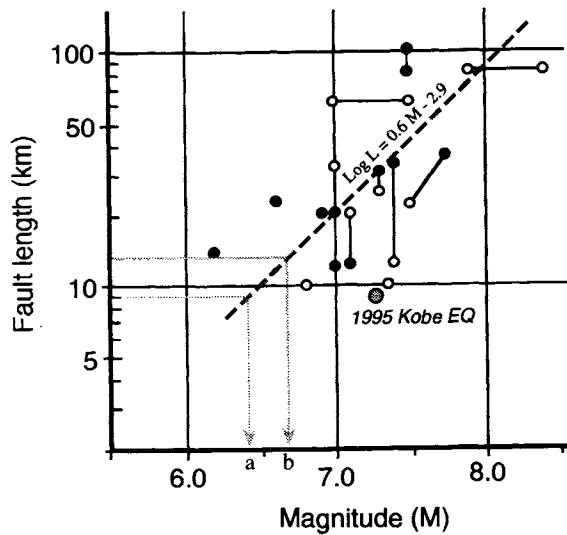


Fig. 10. The relationship between magnitude M and fault length L (Matsuda, 1975), and the position of the Kobe earthquake. Note the extreme difference between estimation by length of the surface rupture of this earthquake (a) or of the pre-known Nojima fault (b) and actual magnitude.

overestimate would be calculated for swarms of active faults. Plausible segmentation for long-term earthquake hazard evaluation should be revealed by high resolution paleoseismic study (e.g., Grant and Sieh, 1994; Toda et al., 1994).

In the case of Kobe, we are wondering whether an earthquake of this magnitude would have been predicted or not. In fact, Matsuda (1990) expected an earthquake on the Nojima fault to be M 6.7 (Fig. 10), which was an underestimation due to separation of the Nojima fault from the Rokko fault system. For evaluation from the paleoseismic point of view, we should recognize, as mentioned above, that the fault does not necessarily appear at the surface. Although the seismic fault extended over 50 km, the surface fault was only 9 km long: less than 20%. Therefore, future researchers would underestimate this earthquake magnitude from the geological aspect and overestimate the recurrence interval from the lack of surface evidence. Furthermore, if the 9 km length of the Nojima fault should be evaluated, the expected magnitude M would be only 6.4 (Fig. 10), whereas a value of M 7.2 would appear to need to be from a fault 26 km in length. Meanwhile, the empirical relationship between the magnitude M of an earthquake and the displacement of the fault D , which appeared on the ground surface at the time of the earthquake from 1891 to 1970, is also shown ($\log D = 0.6M - 4.0$; Matsuda, 1975). Kakimi (1995) found that maximum displacement D_{\max} , rather than surface rupture length L , corresponds to the estimation by empirical relationship of the Kobe earthquake. Although he implies that evaluation by displacement offers a better estimation than by fault length, it is difficult in practice to detect the paleo-displacement from trench logs or displaced landforms in Japan.

Considering the earthquake caused by the faulting, the evaluation should be performed using physical quantities, such as stress drop or seismic moment. Wesnousky et al. (1982, 1983, 1984) proposed an evaluation method using the moment release rate which is calculated from the 400-year historical record of seismicity and geologically determined slip rates of Quaternary faults. The moment release rate involves physical factors associated with faulting and temporal factors, which are not contained in the above-mentioned empirical relationship between the magnitude of an earthquake and its fault length. In addition, they derived a systematic relation between seismic moment M_o and rupture length L ($\log M_o = 23.5 + 1.94 \cdot \log L$) in Japan and displayed maps of instantaneous seismic hazard based on moment release rate. Such evaluation was thought to be epoch-making, although the maps were not concerned with the character of fault systems or the most recent rupture.

From the viewpoint of earthquake stress drop, Kanamori and Allen (1986) show that a shorter fault length for a given magnitude indicates a larger average stress drop which reflects the average strength of the fault zone. They also considered stress accumulation, and suggested that faults with longer recurrence intervals are stronger than those with shorter recurrence intervals. Their conclusion not only explains the significant scattering of the data relating fault length and magnitude but also implies that imprudent magnitude estimation should not be made based on a given fault length or seismic gap.

Recently, Kanaori et al. (1992b) proposed a new method for evaluation, which enables prediction of possible magnitude in the region of a seismic gap using the seismic moments release rates through the block boundaries or tectonic lines. It basically resembles the concept of Wesnousky et al. (1982, 1983, 1984) and Kanamori and Allen (1986) in involving the stress accumulation theory. It seems better than the evaluation from the empirical formula using the surface faults. Assuming a specific time for next earthquake, the expected magnitude can be calculated by the average seismic moment release rate and the elapse time from the most recent earthquake through the block boundaries or tectonic lines. This is regarded as an “earthquake moment predictable model” in contrast to the slip predictable model proposed by Shimazaki and Nakata (1980). Although the time cannot be predicted by this method, selecting short periods such as the desired lifetime of a new building allows us to predict relatively precise magnitude through the block boundaries or tectonic line. The remaining problem we have to resolve is whether the seismic gap can be grasped or not. In this connection, Kanaori and Kawakami (1995) suggested that the expected magnitude through the Arima-Takatsuki tectonic line including the Kobe area would have been M 6.9–7.2 if the estimation had been based on the moment release rate and the most recent 1596 Keicho earthquake (Fig. 11).

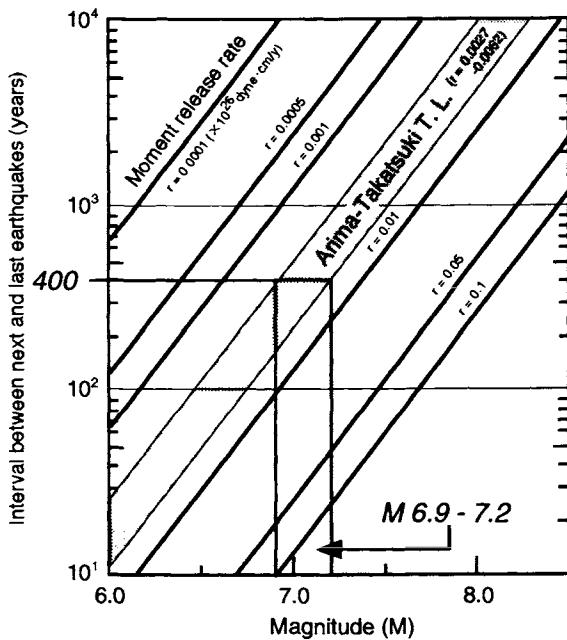


Fig. 11. Magnitude of the Kobe earthquake estimated by the moment release rate and the most recent faulting through the Arima-Takatsuki tectonic line (Kanaori and Kawakami, 1995). The moment release rate of 0.0027–0.0062 ($\times 10^{26}$ dyne/cm) and the 400-year interval between 1995 AD and the penultimate 1569 Keicho earthquake provide an expected Kobe earthquake magnitude of M 6.9–7.2.

5.2. Seismic cycle and fault interaction

The average probability of shaking for some arbitrary time interval based on the desired lifetime of a building is given by the average recurrence interval of some active faults. An active fault has been generally believed to move with a characteristic (recurrence) interval to produce earthquakes periodically (e.g., Wallace, 1970; Matsuda, 1975; Schwartz and Coppersmith, 1984). Indeed, Nishenko and Buland (1987) have collected data from a number of plate boundaries and showed that these data are well described with a log normal distribution. However, recent more precise paleoseismic data (e.g., Sieh et al., 1989; Grant and Sieh, 1994), seismic cycles of subduction zones (e.g., Thatcher, 1989, 1990), and theoretical models (Scholz, 1988, 1989; Huang and Turcotte, 1990; Brown et al., 1991) indicate quasi-periodic or temporal cluster behavior of earthquakes or faulting events. Their seismic cycles embrace wide fluctuations. Especially, the longer the suggested average recurrence interval, the more indefinite elements are increased. Meanwhile, from the fault interaction point of view, Huang and Turcotte (1990) proposed that a single fault does not move independently to produce a larger earthquake. They also raised a significant question about the widely accepted concept that a fault periodically generates earthquakes at a characteristic interval. The clustering or fluctuation of earthquakes may plausibly be attributed to fault interactions.

We speculate below on the Kobe earthquake from the viewpoint of paleoseismicity. With respect to the seismic cycle, evidence of paleoseismic events of the Nojima fault has been revealed by trench excavations after the earthquake (Suzuki, 1995; Suzuki et al., 1995). The date of the penultimate earthquake has been approximately restricted to post-1200 AD. According to historical earthquake records in Japan (e.g., Usami, 1987), the penultimate movement of the Nojima fault might have been during the faulting of the 1596 Keicho earthquake ($M 7.5$). This suggests that the interval between the last two events is about 400 years, which is much shorter than recurrence intervals of other intraplate faults in Japan (e.g., Okada and Ikeda, 1991). Offset of the terrace edge at Nojima-Hirabayashi has provided a slip rate of 1 mm/year (Mizuno et al., 1990), which means a 2000-year interval for this earthquake type. In comparing this with the interval from the paleoseismic evidence and estimation by average slip rate from landforms, we must consider aperiodic or quasi-periodic behavior of the earthquake. On the other hand, in the Kobe area, although landforms formed by lateral offset and scarps have indicated a slip rate faster than 1 mm/year by summing up parallel running faults of 0.1–1 mm/year slip rate, no evidence of paleoseismic faulting events has been revealed along the Rokko and Arima-Takatsuki fault system constituting the ATTL (Figs. 1, 2). However, there are not only a number of historical records of earthquakes (e.g., Usami, 1987) but also evidence of paleoliquefaction and flowage along the Arima-Takatsuki Tectonic Line around the Kobe area (Kanaori et al., 1993). This paleoliquefactional evidence at archaeological sites shows that the Rokko fault system moved in the 1596 Keicho earthquake as described above. Surprisingly, the Keicho earthquake involved some liquefaction on the Kyoto plain, while no liquefaction was reported

during the Kobe earthquake. This fact suggests that longer seismic faulting than that of 1995, involving the Nojima, Rokko and Arima-Takatsuki fault system (constituting the central to eastern ATTL), took place in 1596 and there was a huge amount of energy released in the Kobe area.

If the speculation above is correct, then the rupture length or area on each cycle varies and aperiodicity or temporal clustering occurs on a fault segment. Heaton (1990) and Grant and Sieh (1994) proposed that incomplete strain release during large earthquakes may allow temporal clustering. Incomplete strain release after motion on intraplate faults is plausible, in contrast to interplate underthrustings repeating about every 100 years. Therefore, static stress and strain changes around adjacent faults by an earthquake might hasten or delay the next earthquake (King et al., 1994; Harris et al., 1995). Fault interaction such as multiple shock or delayed multiple shock (Das and Scholz, 1981) is also affected by the difference of stress condition per seismic cycle. Furthermore, considering the concept of self-organized criticality (Bak et al., 1988; Carlson and Langer, 1989; Ito and Matsuzaki, 1990), stress and strain condition for the next large earthquake is formed not only by cyclic loading process and the effects of adjacent large earthquakes but also the occurrence of numerous small earthquakes. Hereafter, we must ascertain not only the safety factor considering fluctuation from average recurrence interval, but also the patterns of spatial and temporal interlocking on the fault systems or tectonic lines.

6. Conclusion

On January 17, 1995, a major inland earthquake occurred around the Kobe area in southwest Japan. Unprecedented damage, distributed in a narrow belt, was caused by multiple faulting as well as the surface geology conditions for ground motion. This earthquake provides evidence that the conventional method of fault assessment, based on the characteristic earthquake model without considering fault interaction, is unrealistic, because there are numerous active faults in intraplate Japan. New approaches such as the block rotation model (Kanaori, 1990), considering the macroscopic tectonic framework for fault interactions and analyzing the dynamics associated with faulting, will enable more accurate evaluation than the conventional method.

Acknowledgements

The authors wish to express their sincere appreciation to Prof. Y. Kanaori of Gifu University for the opportunity to contribute this paper, and to Dr. D. Inoue and Dr. Y. Sawada of Central Research Institute of Electric Power Industry for providing research funds and encouragement.

References

- Ando, M., 1974. Seismotectonics of the 1923 Kanto earthquake. *J. Phys. Earth*, 22: 263–277.
- Ando, M., 1975. Source mechanisms and tectonic significance of historical earthquakes along the Nankai trough, Japan. *Tectonophysics*, 27: 119–140.
- Archuleta, R., 1984. A faulting model for the 1979 Imperial Valley earthquake. *J. Geophys. Res.*, 89: 4559–4585.
- Bak, P., Tang, C. and Wiesenfeld, K., 1988. Self-organized criticality. *Phys. Rev. A*, 38: 364–374.
- Bakun, W., King, G.C.P. and Cockerham, R.S., 1986. Seismic slip, aseismic slip, and the mechanics of repeating earthquakes on the Calaveras fault, California. In: S. Das, C. Scholz and J. Boatwright (Editors), *Earthquake Source Mechanics*. AGU Geophys. Mono. 37, Washington, DC, American Geophysical Union, 195–207.
- Bonilla, M.G., 1970. Surface faulting and related effects. In: R.L. Wiegel (Editor), *Earthquake Engineering*. Prentice-Hall, NJ, pp. 47–74.
- Brown, S.R., Scholz, C.H. and Rundle, J.B., 1991. A simplified spring-block model of earthquakes. *Geophys. Res. Lett.*, 18: 215–218.
- Carlson, J.M. and Langer, J.S., 1989. Mechanical model of an earthquake fault. *Phys. Rev. A*, 40: 6470–6484.
- Das, S. and Scholz, C.H., 1981. Theory of time-dependent rupture in the earth. *J. Geophys. Res.*, 86: 6039–6051.
- Fitch, T.J. and Scholz, C.H., 1971. Mechanisms of underthrusting in southwest Japan: a model of convergent plate interactions. *J. Geophys. Res.*, 76: 7260–7292.
- Grant, L.B. and Sieh, K., 1994. Paleoseismic evidence of clustered earthquakes on the San Andreas fault in the Carrizo Plain, California. *J. Geophys. Res.*, 99: 6819–6841.
- Harris, R.A., Simpson, R.W. and Reasenberg, P.A., 1995. Influence of static stress changes on earthquake locations in southern California. *Nature*, 375: 221–224.
- Heaton, T.H., 1990. Evidence for and implications of self-healing pulses of slip in earthquake rupture. *Phys. Earth Planet. Interact.*, 64: 1–20.
- Huang, J. and Turcotte, D.L., 1990. Evidence for chaotic fault interactions in the seismicity of the San Andreas fault and Nankai trough. *Nature*, 248: 234–236.
- Huzita, K., 1962. Tectonic development of the median zone (Setouti) of Southwest Japan, since Miocene. *J. Geosci. Osaka City Univ.*, 6: 103–144 (in Japanese with English abstract).
- Huzita, K., 1980. Role of the median tectonic line in the Quaternary tectonics of the Japanese Islands. *Memoirs Geol. Soc.*, 18: 129–153.
- Huzita, K. and Oike, K., 1981. Active tectonic structure and seismic activity in the Honshu arc. *Kagaku*, 51: 704–711 (in Japanese).
- Huzita, K. and Kasama, T., 1982. Geology of the Osaka-Seihokubu district: with geological sheet map at 1:50,000. *Geol. Surv. Japan*, 112 pp. (in Japanese with English abstract).
- Huzita, K., Kishimoto, Y. and Shiono, K., 1973. Neotectonics and seismic activity in the Kinki area, southwest Japan. *J. Geosci. Osaka City Univ.*, 16: 93–124.
- Ide, S., Takeo, M. and Yoshida, Y., 1995. Source process of the 1995 Hyogo-ken Nanbu earthquake: determination of spatio-temporal slip distribution by Bayesian modeling. *Abstr. Seism. Soc. Jpn.* 1995, A77 (in Japanese).
- Irikura, K., 1995. The ground motion amplified in the disaster belt and declined in Port Island (Article). *Kagaku-Asahi*, July 1995: 116–117 (in Japanese).
- Ito, K. and Matsuzaki, M., 1990. Earthquakes as self-organized critical phenomena. *J. Geophys. Res.*, 95: 6853–6860.
- Kakimi, T., 1995. Problems for assessing future earthquakes based on active faults, with special regard to the 1995 Hyogoken-Nanbu Earthquake. *1995 Japan Society of Engineering Geology Meeting Abstr.*, 5–12 (in Japanese).
- Kakimi, T., Okada, A., Kinugasa, Y., Matsuda, T. and Yonekura N., 1994. Seismotectonic province map

- of Japanese island, with the upperbound earthquake magnitudes. 1994 Japan Earth and Planetary Science Joint Meeting Abstr., 302 (in Japanese).
- Kanamori, H., 1972. Tectonic implications of the 1944 Tonankai and the 1946 Nankaido earthquakes. *Phys. Earth Planet. Interact.*, 5: 129–139.
- Kanamori, H. and Allen, C.R., 1986. Earthquake repeat time and average stress drop. *A.G.U. Geophys. Monogr.*, 37: 227–236.
- Kanaori, Y., 1990. Late Mesozoic-Cenozoic strike-slip and block rotation in the inner belt of Southwest Japan. *Tectonophysics*, 177: 381–399.
- Kanaori, Y. and Kawakami, S., 1995. Casual fault creating the 1995 Southern Hyogo earthquake (M7.2): Did the Arima-Takatsuki fault system move? *Bull. Fac. Gen. Edu., Gifu. Univ.*, 32: 183–202 (in Japanese with English Abstr.).
- Kanaori, Y., Kawakami, S. and Yairi, K., 1991. Space-time distribution patterns of destructive earthquakes in the inner belt of central Japan: activity intervals and locations of earthquakes. *Eng. Geol.*, 31: 209–230.
- Kanaori, Y., Kawakami, S. and Yairi, K., 1992a. Space-time distribution patterns of destructive earthquakes in the Kinki district, central Japan: implications of the Hanaore-Kongo fault and Tsurugawan-Isewan tectonic lines. *J. Jpn. Soc. Eng. Geol.*, 33: 187–201 (in Japanese with English Abstr.).
- Kanaori, Y., Kawakami, S. and Yairi, K., 1992b. Space-time distribution patterns of destructive earthquakes in the inner belt of central Japan (part 2): moment-release rates and earthquake prediction. *Eng. Geol.*, 32: 113–122.
- Kanaori, Y., Kawakami, S. and Yairi, K., 1992c. Space-time distribution patterns of destructive earthquakes in the inner belt of central Japan (part 3): seismic risk assessment. *Eng. Geol.*, 33: 99–110.
- Kanaori, Y., Kawakami, S., Yairi, K. and Hattori, T., 1993. Liquefaction and flowage at archaeological sites in the inner belt of central Japan: Tectonic and hazard implications. *Eng. Geol.*, 35: 65–80.
- Kikuchi, M., 1995a Focal mechanism of the 1995 Kobe earthquake. Abstract of the Great Hanshin Earthquake Disaster quick report, 117–120 (in Japanese).
- Kikuchi, M., 1995b. A shopping trolley seismograph. *Nature*, 377: 19.
- King, G.C., Stein, R.S. and Lin, J., 1994. Static stress changes and the triggering of earthquakes. *Bull. Seism. Soc. Am.*, 84: 935–953.
- Kinugasa, Y., 1990. Seismotectonic zonation based on the characteristics of active faults in Japan. USGS Open-File Rept., 90-98: 15–17.
- Koketsu, K., 1995. Frequency of ground motion as the cause of devastated damage (Article). *Kagaku-Asahi* (special issue), 11–14 (in Japanese).
- Koto, B., 1893. On the cause of the great earthquake in Central Japan, 1891. *J. Coll. Sci. Imp. Univ. Jpn.*, 5: 196–353.
- Lyzenga, G.A., Raefsky, A. and Mulligan, S.G., 1991. Models of recurrent strike-slip earthquake cycles and the state of crustal stress. *J. Geophys. Res.*, 96: 21623–21640.
- Matsuda, T., 1974. Surface faults associated with Nobi (Mino-Owari) earthquake of 1891. *Jpn. Bull. Earthquake Res. Inst.*, 13: 85–126 (in Japanese with English abstract).
- Matsuda, T., 1975. Magnitude and recurrence interval of earthquakes from a fault. *Zisin* 2, 28: 269–283 (in Japanese with English abstract).
- Matsuda, T., 1977. Estimation of future destructive earthquakes from active faults on land in Japan. *J. Phys. Earth*, 25 (Suppl.): s251–s260.
- Matsuda, T., 1981. Active faults and damaging earthquakes in Japan – macroseismic zoning and precaution fault zones. In: *Earthquake Prediction – An International Review*. Ewing Ser., Am. Geophys. Union, Washington, DC, 4: 279–289.
- Matsuda, T., 1990. Seismic zoning map of Japanese Islands, with maximum magnitudes derived from active fault data. *Bull. Earthquake Res. Inst.*, 65: 289–319 (in Japanese with English abstract).
- Meteorological Agency, 1995.
- Mizuno, K., Hattori, H., Sangawa, A. and Takahashi, H., 1990. Geology of the Akashi district with geological sheet map at 1:50,000. *Geol. Surv. Japan*, 90 pp. (in Japanese with English abstract).

- Nishenko, S.P. and Buland, R., 1987. A generic recurrence interval distribution for earthquake forecasting. *Bull. Seism. Soc. Am.*, 77: 1382–1399.
- Okada, A. and Ikeda, Y., 1991. Active faults and neotectonics in Japan. *Quaternary Res.*, 30: 161–174.
- Omote, S., Ohsaki, Y., Kakimi, T. and Matsuda, T., 1980. Japanese practice for estimating the expected maximum earthquake force at a nuclear power plant site. *Bull. NZ Natl. Soc. Earthquake Eng.*, 13: 37–48.
- Research Group for Active Faults in Japan, 1991. Active faults in Japan, sheet maps and inventories, revised edition. Univ. Tokyo Press, Tokyo, 437 pp. (in Japanese with English abstract).
- Scholz, C.H., 1988. Comments on models of earthquake recurrence. In: *Fault segmentation and controls of rupture initiation and termination*. USGS. Open-File Rep., 350–360.
- Scholz, C.H., 1989. Global perspectives of chaos. *Nature*, 355: 71–73.
- Scholz, C.H. and Kato, T., 1978. The behavior of a convergent plate boundary: crustal deformation in the South Kanto District, Japan. *J. Geophys. Res.*, 83: 783–797.
- Schwartz, D.P. and Coppersmith, K.J., 1984. Fault behavior and characteristic earthquakes: examples from the Wasatch and San Andreas fault zones. *J. Geophys. Res.*, 89: 5681–5698.
- Shimazaki, K. and Nakata, T., 1980. Time-predictable recurrence model for large earthquakes. *Geophys. Res. Lett.*, 7: 279–282.
- Sieh, K.E., Stuiver, M. and Brillinger, D., 1989. A more precise chronology of earthquakes produced by the San Andreas fault in Southern California. *J. Geophys. Res.*, 94: 603–623.
- Sugimura, A. and Matsuda, T., 1965. Atera fault and its displacement vector. *Geol. Soc. Am. Bull.*, 76: 509–522.
- Suzuki, Y., 1995. Trench survey across the Nojima fault. *Kagaku-Asahi*, June 1995: 96–99 (in Japanese).
- Suzuki, Y., Watanabe, M., Nakata, T., Okada, A., Sawa, H., Imaizumi, T., Hirano, S. and Maemoku, H., 1995. Excavation study of the Nojima fault. *Abstr. Seism. Soc. Jpn.* 1995, A70 (in Japanese).
- Thatcher, W., 1989. Earthquake recurrence and risk assessment in circum-Pacific seismic gaps. *Nature*, 341: 432–434.
- Thatcher, W., 1990. Order and diversity in the modes of circum-Pacific earthquake recurrence. *J. Geophys. Res.*, 95: 2609–2623.
- Thatcher, W., 1995. Microplate versus continuum descriptions of active tectonic deformation. *J. Geophys. Res.*, 100: 3885–3894.
- Toda, S., Inoue, D., Takase, N. and Kubouchi, A., 1994. Paleoseismicity and modified uniform slip model of the Atera fault system in central Japan during the Holocene. *EOS Trans. AGU*, 74 (44; Fall Meeting Suppl.): 451.
- Tsukuda, E. and Yamazaki, H., 1984. Excavation survey of active faults for earthquake prediction in Japan with spacial reference to the Ukihashi-central fault and the Atera fault. *Geol. Surv. Jpn. Rep.*, 263: 349–361.
- Tsutsumi, H., Okada, A., Nakata, T., Ando, M. and Tsukuda, T., 1991. Timing and displacement of Holocene faulting on the Median Tectonic Line in central Shikoku, southwest Japan. *J. Struct. Geol.*, 13: 227–233.
- Usami, T., 1987. Descriptive Catalogue of Disastrous Earthquakes in Japan, new edition. Univ. Tokyo Press, Tokyo, 434 pp. (in Japanese).
- Wald, D.J. and Heaton, T.H., 1994. Spatial and temporal distribution of slip for the 1992 Landers, California, earthquake. *Bull. Seism. Soc. Am.*, 84: 668–691.
- Wallace, R.E., 1970. Profiles and ages of young fault scarps, north-central Nevada. *Geol. Soc. Am. Bull.*, 88: 1276–1281.
- Wells, D.L. and Coppersmith, K.J., 1994. New empirical relationships among magnitude, rupture length, rupture width, rupture area, and surface displacement. *Bull. Seism. Soc. Am.*, 84: 974–1002.
- Wesnousky, G.S., Scholz, C.H. and Shimazaki, K., 1982. Deformation of an island arc: rates of moment release and crustal shortening in intraplate Japan determined from seismicity and Quaternary fault data. *J. Geophys. Res.*, 87, 6829–6852.
- Wesnousky, G.S., Scholz, C.H., Shimazaki, K. and Matsuda, T., 1983. Earthquake frequency distribution and the mechanics of faulting. *J. Geophys. Res.*, 88: 9331–9341.

- Wesnousky, G.S., Scholz, C.H., Shimazaki, K. and Matsuda, T., 1984. Integration of geological and seismological data for the analysis of seismic hazard: a case study of Japan. Bull. Seism. Soc. Am., 74: 687–708.
- Wesnousky, G.S., 1988. Seismological and structural evolution of strike-slip faults. Nature, 335: 340–343.
- Working Group on California Earthquake Probability, 1988. Probabilities of large earthquake occurring in California on the San Andreas fault. USGS Open-File Rept., 88-398, 61 pp.
- Ziony, J.I., Evernden, J.F., Fumal, T.E., Harp, E.L., Hartzell, S.H., Joyner, W.B., Keefer, D.K., Spudich, P.A., Tinsley, J.C., Yerkes, R.F. and Youd, T.L., 1985. Predicted geologic and seismologic effects of a postulated magnitude 6.5 earthquake along the northern part of the Newport-Inglewood zone. USGS Professional Rept., 136: 415–442.

CHAPTER 7

Modeling of the interaction between destructive inland earthquakes and large off coast earthquakes in central and south-west Japan

MITSUHIRO MATSUZAKI^{a,*}, SHIN-ICHI KAWAKAMI^b, YUJI KANAORI^c and KENJI YAIRI^c

^a*Osaka College, Hirao, Mihara, Minamikawachi, Osaka, 587, Japan*, ^b*Faculty of Education, Gifu University, Gifu, 501-11, Japan* and ^c*Faculty of General Education, Gifu University, Gifu, 501-11, Japan*

Abstract

A one-dimensional Stick-slip model, which is introduced to explain the fractal features of earthquake phenomena is applied to describe the destructive earthquake occurrences in central and south-west Japan. Space time patterns of events are simulated and the predictability is discussed. On the basis of the "Block-rotation model", epicenters of historical destructive earthquakes with magnitude 6.4 or greater are relocated to the tectonic or block boundary lines. This model has revealed that these events show a periodicity of about 1000 years of active and quiet alternative intervals. In each active period, individual block boundary lines generate several large earthquakes without overlapping rupture areas. The space-time pattern and moment release rate for the Hanaore-Kongo Fault Line (HKFL) can be represented well with the one-dimensional stick-slip model. The seismic coupling of large offshore earthquakes along the Nankai trough is also found to be well modeled by this model. This model may be useful for estimation of seismic risk in this region. Further, this model can be applied to see the situation of the M7.2 Kobe earthquake and interpret this earthquake to be the event that comes from the block structure in later section.

1. Introduction

Now long-term earthquake prediction and earthquake-proof designs for large structures are one of the most important problems in countries located on plate margins with high seismic activity. The characteristic earthquake model, proposed by Schwartz and Coppersmith (1984), postulates that each active fault or fault segment ruptures periodically to generate earthquakes with similar magnitude. The model has been regarded as a useful guide for long-term earthquake prediction in central Japan. Many excavation studies of active faults have been performed to

* Corresponding author.

obtain the recurrence intervals and the dates of the latest events (e.g. Tsukuda and Yamazaki, 1984).

In conventional seismology, fractal properties have been ascribed to the complex configurations of fault segments in the regions where major plates contact with each other (e.g. Kagan, 1981). Why are such fractal patterns observed, and why do many earthquakes of other fault segments occur within a very short time, especially under one hundred years? The reason may be, for example, that each segment of fault undergoes its own characteristic cycle of earthquakes with only relatively weak coupling to its neighboring segments. If so, then the statistical distribution of earthquake magnitudes will be determined primarily by the statistics of fault segments and the most important concepts in theoretical seismology will be geometric in nature. However, re-analysis of the characteristic earthquake model has shown that the model is far too simple, not only because the postulated recurrence intervals show a larger variation than those previously estimated (e.g. Thatcher, 1990). In addition, two or more adjacent segments rupture simultaneously to generate a larger event (Huang and Turcotte, 1990).

Kanaori et al. (1991a, b, 1992, 1993) investigated space-time patterns of destructive earthquake occurrences in central Japan and proposed a new idea of seismic cycles. In this model, block boundaries or tectonic lines are defined as linking major active faults distributed in the study area as shown in Fig. 1. The space-time patterns of destructive earthquakes with magnitude 6.4 or greater have been analyzed by relocating the previously postulated epicenters to the corresponding block boundaries or tectonic lines. The time sequence of destructive earthquakes shows clear periodicities of active and quiet periods of about 1000 years. Durations of active periods are several hundreds of years in which each block boundary or tectonic line generates several destructive earthquakes with rupture zones without overlapping. Further spatial patterns of destructive events have revealed seismic coupling between block boundary lines. A peculiar feature of spatial patterns is that inland earthquakes at the Hanaore-Kongo Fault Line (HKFL) appear to predate the great off-coast earthquakes along the Nankai Trough (Kanaori et al., 1993). Recently, a great destructive earthquake occurred along the Arima-Takatsuki Tectonic Line (ATTL) neighboring the HKFL. In this study, we will discuss the interaction between this earthquake (M7.2 Kobe Earthquake) and the postulated large off-coast earthquake along the West-Nankai Trough.

Carlson (1991) have used a one-dimensional stick-slip model to study the nature of the characteristic earthquake model. Shaw et al. (1992) used the same model to predict occurrences of large events from those of small events. Brown et al. (1991), on the other hand, have studied a two-dimensional stick-slip model and discussed the property of the characteristic earthquake model. We think it is important to apply these simple models to describe sequential occurrences of large earthquakes in an area consisting of several crustal blocks and to use the results for seismic hazard assessment or earthquake prediction.

In this study, we show two different types of numerical simulations of destructive earthquakes. First, the one-dimensional stick-slip model developed by Matsuzaki and Takayasu (1991) is used to simulate the space-time correlations of events. This

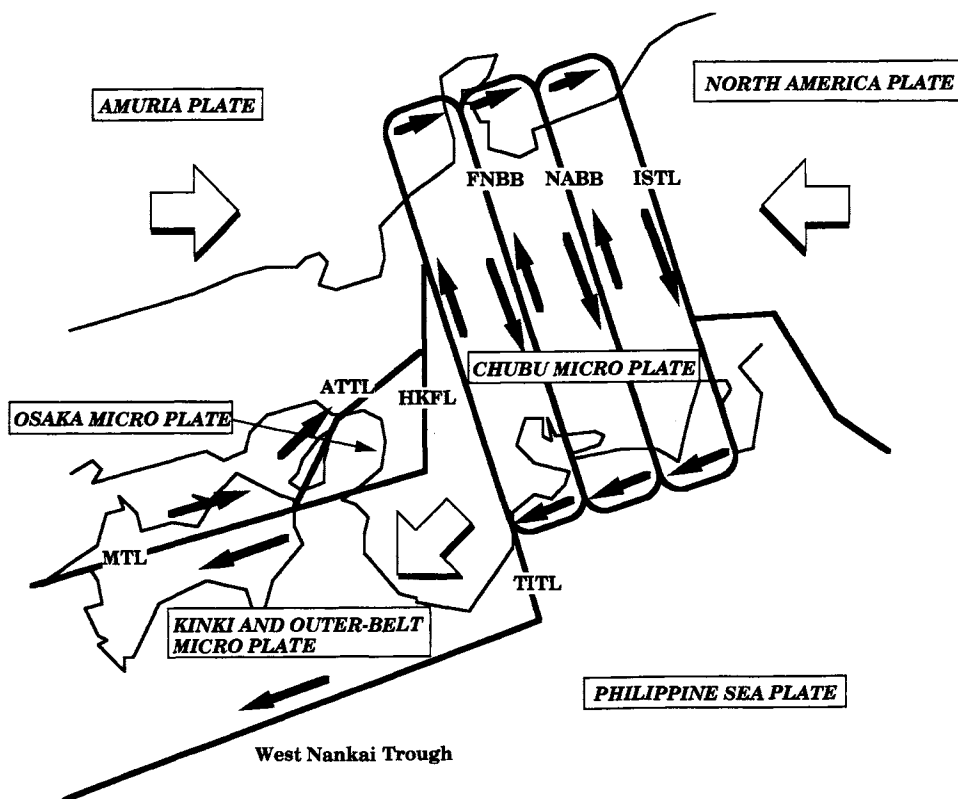


Fig. 1. The block rotation model of south-west Japan (Kanaori et al., 1993). This area is under pressure due to the plate motion, and the rotation of the three or four blocks makes the coupling of the earthquake phenomena. ISTL, Itoigawa-Shizuoka Tectonic Line; MABB, Miboro-Atera Block Boundary; FNBB, Fukui-Neodani Block Boundary; HKFL, Hanaore-Kongo Fault Line; ATT, Arima-Takatsuki Tectonic Line; MTL, Median Tectonic Line.

model is applied to the HKFL and shows the characteristic earthquake occurrence during a short period: within thousands of years. Second, we arranged the advanced version of the one-dimensional stick-slip model (Caterpillar Model) to the Block rotation model of south-west Japan. The Caterpillar Model enables us to show the dynamics of several faults, which have strong interactions, for a long period: over 100 000 years. These numerical simulations should provide useful knowledges on the nature of complete seismic cycles and its secular variation since the recurrence intervals of the active periods in central Japan is of the order of 1000 years.

2. One-dimensional stick-slip model

The one-dimensional version of the stick-slip model described in the paper by Matsuzaki and Takayasu (1991) is applied for active fault planes facing two crustal

blocks. Frictional boxes on a constantly moving crustal block are connected to the adjacent crustal block by a leaf spring, g , and also connected to the two nearest neighbor boxes by coil springs, k (Fig. 2). While the sum of the forces from the coil springs and leaf spring, f , at every site is smaller than the frictional force f_c , the oscillators move with a constant velocity V and their spring forces increase by $V \cdot g$. When the sum of the spring forces $f(i)$ at the i -th site exceeds the threshold frictional force $f_c(i)$, the oscillator slips back to the position at which the total spring force is equal to 0, and the forces that were acting on it are distributed to the neighboring oscillators except the ones that have already slipped at the same time step.

The evolution rule of this system normalized by the thresholds is described as follows

$$dF(i)/dt = v(i)$$

If $F(i) > 1.0$, then

$$F(i) = 0,$$

$$F(i+1) = F(i+1) + d \text{ and}$$

$$F(i-1) = F(i-1) + d$$

where

$$F(i) = f(i)/f_c(i),$$

$$v(i) = V \cdot g/f_c(i) \text{ and } d = k/(g + 2k).$$

When we assume that the system is homogeneous, the temporal behavior of this system is determined by a single parameter d . Because the thresholds are randomly distributed, the normalized time derivatives of forces, $v(i)$, distribute randomly. A

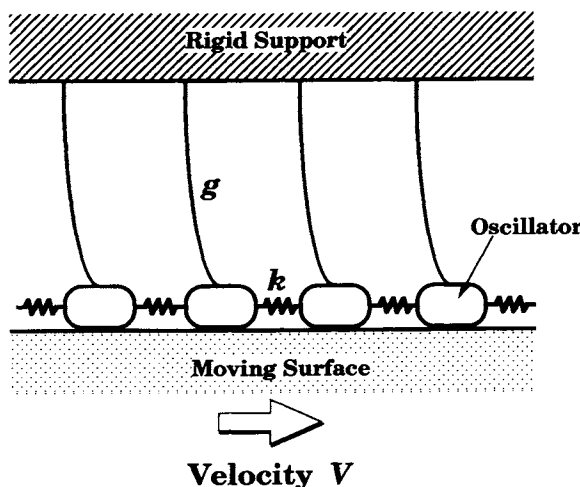


Fig. 2. The schematic representation of the one-dimensional stick-slip model.

slip of the oscillator at the i -th site creates an increase of the force on the neighboring oscillators by d . If $F(i+1)$ or $F(i-1)$ becomes larger than 1.0 by this effect, the slip extends to the neighboring oscillators except the ones which have already slipped. When entire force values become less than 1.0, the slip propagation stops. A cluster is defined as a group of oscillators which slipped, at one time step, through this process. The parameter d which represents the stiffness of this system is very important. In the case of the one-dimensional model, this parameter is expressed as $d=k/(g+2k)$. When d is small, the force drop by slipping oscillators would not spread and the event tends to be localized. This feature corresponds to the creeping of the fault. On the contrary, when d is large, the force drop would spread over the connected oscillators and the event tends to propagate over a large region. In this model, the number of slipped oscillators gives a quantity proportional to the size of the fracture zone and the sum of the force drop is proportional to the moment of an earthquake.

If we change the value of the model parameter d in the range from 0.2 to 0.3, we can get the following result. A model with smaller d values (for example $d=0.2$) generates a number of small events, while the model with larger d values (for example $d=0.3$) generates only one great event, comparable to the system size, as mentioned above. For $d=0.23$, the results exhibit a few large events similar to patterns obtained by the historical earthquake analysis. It is very interesting to note that the two-dimensional stick-slip model with the value of $d=0.23$ generates a number of events whose size distribution obeys the Gutenberg-Richter's law (Matsuzaki and Takayasu, 1991). Although the basic type of the one-dimensional stick-slip model studied here couldn't exhibit fractal features of the earthquake phenomena, it will provide us with a lot of knowledge on seismic couplings between adjacent fault segments (Huang and Turcotte, 1990).

Fig. 3a–c shows the space–time patterns of simulated earthquakes (Fig. 3a,b) along a model fault and HKFL (Fig. 3c). It should be noted that the spatial patterns of rupture zones of large events are stable for a short period: within thousands of years (Fig. 3a). This suggests that the fault segments generate earthquakes with similar size and recurrence time intervals at almost the same locations. This result is consistent with the characteristic earthquake model proposal by Kanaori et al. (1991b). However, the result for much longer time periods (over 10 000 years) shows a very different pattern. Segmentation in the later stage of the model has evolved quite different from the earlier stage (Fig. 3b). This suggests that the present segmentation of the fault system is not stable for a period longer than 10 000 years. The total output of this simulation is rather consistent with the study of Huang and Turcotte (1990).

3. The caterpillar model

Kanaori et al. (1991a, b, 1992, 1993) investigated space time patterns of destructive earthquake occurrences in central Japan and proposed a new model of seismic

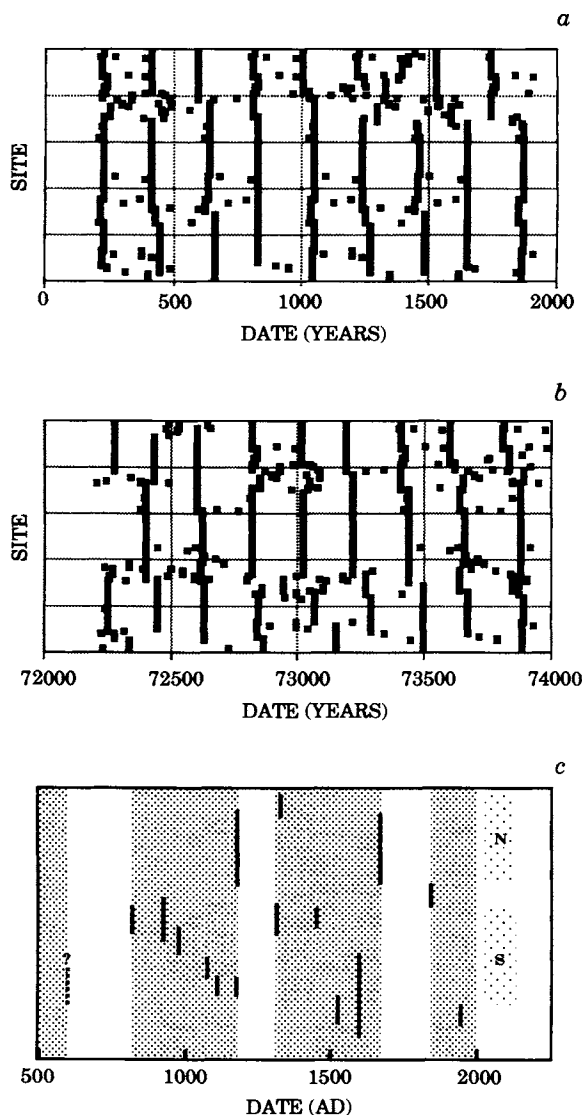


Fig. 3. A space-time pattern of earthquakes along the simulated fault (a,b) and the HKFL (c). We can see the regular space-time pattern for a short period within thousands of years (a) just like the real space-time pattern along the HKFL (c). However, we can also see a different pattern in later stages (b).

cycles. In this model, block boundaries or tectonic lines are defined as linking major active faults distributed in this area (Fig. 1). In this region, we can see a sliding block and four rotating block systems. Thus if we assume such a block rotation model, we can see the seismic coupling between these block boundaries.

The space-time patterns of destructive earthquakes with magnitude 6.4 or greater

are investigated by relocating the postulated epicenters to the corresponding block boundaries or tectonic lines. This study revealed that the destructive earthquakes in this area have clear periodicities of active and quiet intervals with recurrence times of about 1000 years. The durations of active periods are several hundreds of years. We can also see the seismic coupling between the West Nankai Trough and other block boundaries. This is the empirical feature of the seismicity along the West Nankai Trough in the 30 years since the earthquake of the HKFL (Hanaore-Kongo Fault Line) and in the order of 100 years after the events along the eastern block boundaries.

We modified the one-dimensional stick-slip model to describe the Block rotation model of south-west Japan which was studied by Kanaori et al. (1991a, b, 1992, 1993). We assume four circles of stick-slip chains and a pair of straight stick-slip chains to explain the seismic coupling in this area (Fig. 4).

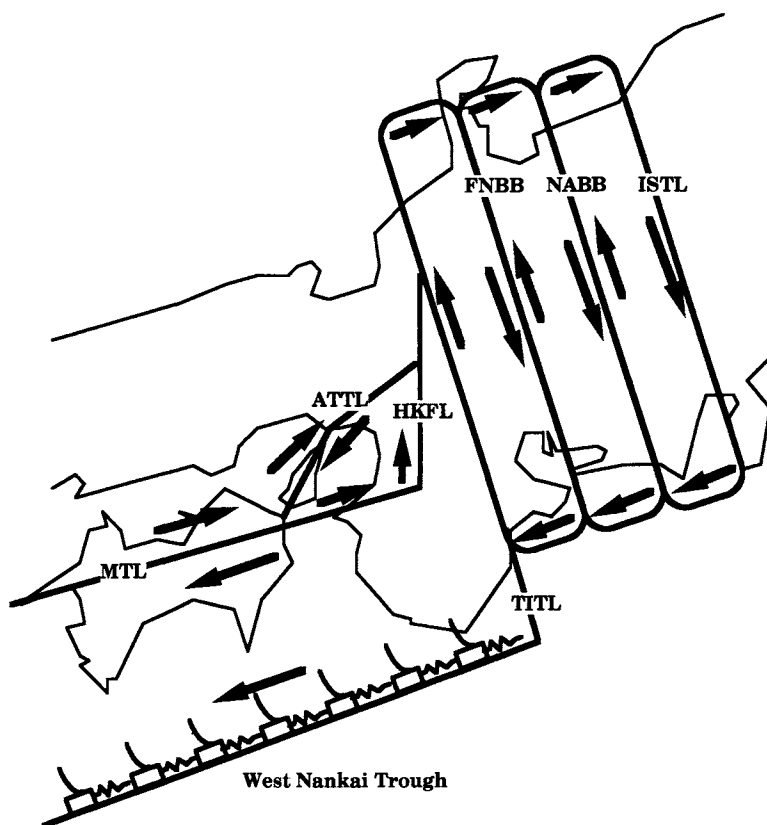


Fig. 4. The schematic representation of the caterpillar model. In this model, we assume four rotating stick-slip chains which correspond to the block rotations in the Chubu and the Osaka micro plates. We also assume one sliding block system due to the plate motion which corresponds to the sliding Kinki and Outer-belt micro plates. Each block is considered to be rigid, like the rigid support in Fig. 2.

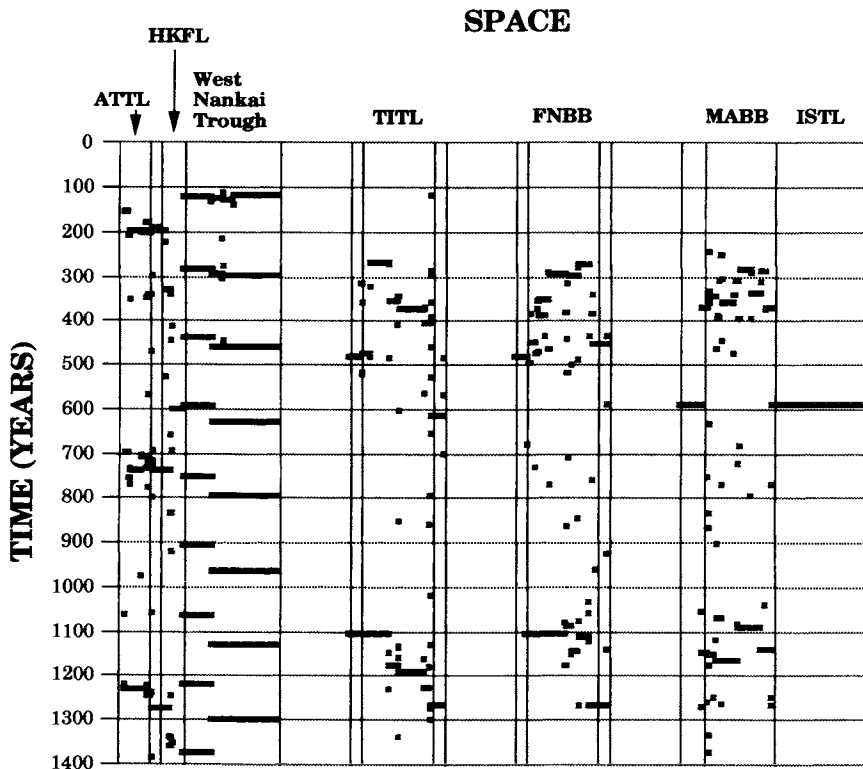


Fig. 5. The simulated space–time patterns of the caterpillar model. The length of each line corresponds to the magnitude of each event. In this model, a destructive event is assumed along the Arima-Takatsuki Tectonic Line at time = 0. We can see the strong interaction between inland earthquakes along the tectonic lines or block boundaries and big off-coast earthquakes.

The simulated earthquake activity is shown in Fig. 5 which agrees well with the space–time pattern of real historical destructive earthquakes in this area. It should be noted that the spatial patterns of rupture zones of large events are stable for a long period. This indicates that the block boundary lines can be classified into several segments which generate earthquakes of quite similar sizes in each active period. This result is consistent with the characteristic earthquake model.

4. Implications for the M7.2 Kobe earthquake

We can also see the seismic coupling between the block boundaries. Especially, when we assume a large earthquake along the Arima-Takatsuki Tectonic Line (ATTL) in the numerical simulation, the Hanaore-Kongo Fault Line (HKFL) and the east end of the Median Tectonic Line (MTL) would move after 10–30 years,

and then a large off-coast earthquake may occur along the West Nankai trough after the event along the ATTL.

The M7.2 Kobe earthquake was the largest disaster during the past 50 years in the Japan islands. Historically a large-off coast earthquake occurred along the West-Nankai Trough in 1605 (Keicho-tsunami) 9 years after the Keicho-Fushimi earthquake (1596), and an inland earthquake occurred at the west end of the MTL just after the Keicho-Fushimi earthquake. Hence, we should regard the events along the HKFL and the ATTL as precursors for the large off-coast earthquakes along the West Nankai Trough.

Recurrence times of large events of this model at the West Nankai Trough are about 150 or 180 years and consistent with the actual observations. However, a large inland event along a tectonic line in this numerical simulation induces some other events along the other tectonic lines and complicates the recurrence time of the off-coast earthquake (Fig. 5). According to this caterpillar model, the couplings between these block boundaries are tight and stable for a long time. This result shows us the feasibility of destructive earthquake prediction in this region.

SPACE

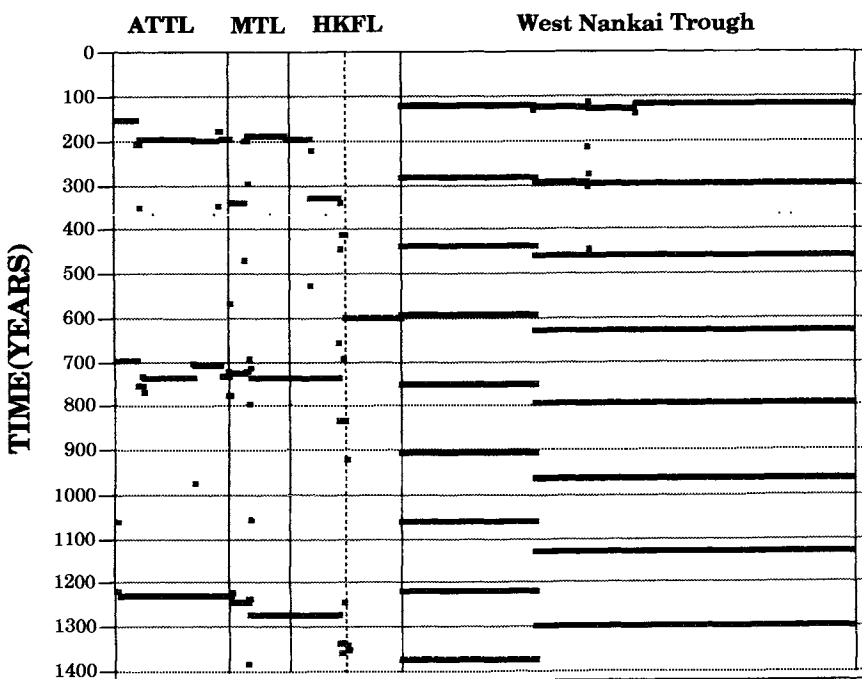


Fig. 6. The detail of the simulated space-time patterns along ATTL, HKFL, MTL and West Nankai Trough. We can see the strong interaction between inland earthquakes along ATTL, HKFL, MTL and large off-coast earthquakes along West Nankai Trough.

The situation of historical earthquake occurrences is quite consistent with the present simulation (Fig. 6). Also, the model study suggests that the MTL and the West Nankai trough have high potentials of generating large earthquakes among many active faults in south-west Japan. It is recommended that local or regional governments should pay more attention to disasters associated with large earthquakes along these active lines.

5. Conclusions

The conclusion of this simulation is that the seismic coupling of large events can be represented by this caterpillar model. The recurrence time of active periods is fairly regular. However, spatial patterns of seismic events along the block boundaries are regular for short time scales but become irregular for long time scales. Thus, the analysis of historical earthquakes in this study area, as well as the present model simulation, will provide a valuable insight for future earthquake occurrences. In other words, the caterpillar model studied here will provide a physical basis for the empirical approaches to destructive earthquake prediction.

References

- Brown, S.R., Scholz, C.H. and Rundle, J.B., 1991. A simplified spring-block model of earthquakes. *Geophys. Res. Lett.*, 18: 215–218.
- Carlson, J.M., 1991. Time intervals between characteristic earthquakes and correlations with smaller events: an analysis based on a mechanical model of a fault. *J. Geophys. Res.*, 96: 4255–4267.
- Huang, J. and Turcotte, D.L., 1990. Evidence for chaotic fault interactions in the seismicity of the San Andreas fault and Nankai trough. *Nature*, 348: 234–236.
- Kagan, Y.Y., 1981. Spatial distribution of earthquakes: The three point moment function. *Geophys. J. R. Astron. Soc.*, 67: 697–717.
- Kanaori, Y., Kawakami, S. and Yairi, K., 1991a. The block structure and Quaternary strike-slip block rotation of central Japan. *Tectonics*, 11: 47–56.
- Kanaori, Y., Kawakami, S. and Yairi, K., 1991b. Space-time distribution patterns of destructive earthquakes in central Japan: activity intervals and locations of earthquakes. *Eng. Geol.*, 31: 209–230.
- Kanaori Y., Kawakami, S. and Yairi, K., 1992. The block structure and quaternary strike-slip block rotation. *Tectonics*, 11: 47–56.
- Kanaori, Y., Kawakami, S. and Yairi, K., 1993. Space-time correlations between inland earthquakes in central Japan and great off coast earthquakes along the Nankai trough: implications for destructive earthquake prediction. *Eng. Geol.*, 33: 289–303.
- Matsuzaki, M. and Takayasu, H., 1991. Fractal features of the earthquake phenomenon and a simple mechanical model. *J. Geophys. Res.*, 96: 19925–19931.
- Schwartz, D.P. and Coppersmith, K.J., 1984. Fault behavior and characteristic earthquakes: examples from the Wasatch and San Andreas fault zones. *J. Geophys. Res.*, 89: 5681–5698.
- Shaw, B.E., Carlson, J.M. and Langer, J.S., 1992. Patterns of seismic activity preceding large earthquakes. *J. Geophys. Res.*, 97: 479–488.

- Thatcher, W., 1990. Order and diversity in the models of circum-Pacific earthquake recurrence. *J. Geophys. Res.*, 95: 2609–2633.
- Tsukuda, T. and Yamazaki, H., 1984. Excavation survey of active faults for earthquake prediction in Japan with special reference to the Ukihashi-central fault and the Atera fault. *Geol. Surv., Jpn. Rep.*, 263: 349–361.

A new opportunity to detect paleo-earthquake events dating back to the past 10 millennia: a record from lacustrine sediment

SHIN-ICHI KAWAKAMI^{a,*}, HITOSHI FUKUSAWA^b
and YUJI KANAORI^c

^a*Faculty of Education, Gifu University, Gifu, 501-11, Japan*, ^b*Department of Geography, Tokyo Metropolitan University, Hachioji, 192-03, Japan* and ^c*Faculty of General Education, Gifu University, Gifu, 501-11, Japan*

Abstract

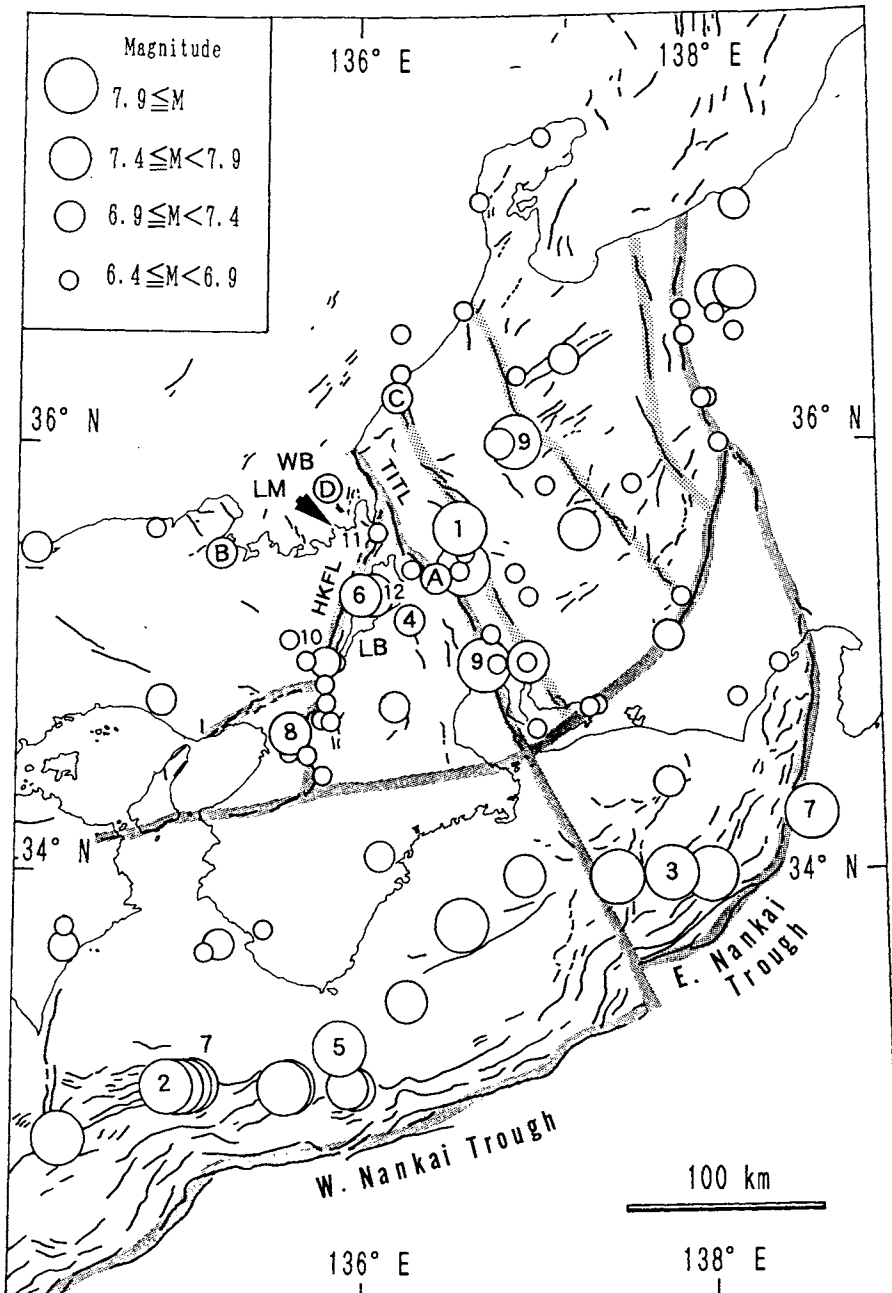
Bulk density and grain density profiles of the uppermost 90 cm portion of lacustrine sediment from Lake Suigetsu, one of the five major lakes of Lake Mikatagoko, located in central Japan, indicate the occurrence of at least 10 depositional events characterized by anomalously high density spikes. Two events are accompanied by turbidites. The dates of the sedimentary events estimated here are correlated with the occurrence of destructive earthquakes since 1100 A.D. Close examination of the sedimentological signatures recorded in the lake sediment and historical literature describing destructive earthquake phenomena provides a new opportunity to detect paleo-earthquake events in a high seismic area having a long history.

1. Introduction

Long-term earthquake prediction is currently one of the most important problems facing a country situated on a plate margin with high seismic activity. Although a wide variety of data have been accumulated concerning paleo-earthquake phenomena, including historical documents (Usami, 1987), trench excavation of active faults (Sieh, 1978, 1984), tree-ring signatures (Page, 1970; Sheppard and Jacoby, 1989; Jacoby et al., 1992), geological archives such as liquefaction features (Obermeier et al., 1991; Kanaori et al., 1993a), turbidites (Sims, 1975; Doig, 1990), or debris flow deposits (Kawakami et al., 1991), it remains a difficult problem to precisely predict the recurrence of destructive earthquakes and to assess seismic risks.

A large number of historical documents have revealed that the central part of the Japanese Islands has been strongly shaken by large inland earthquakes as well as great offshore earthquakes along the Nankai trough, dating back to 599 A.D.

* Corresponding author. Tel.: +81 58 2932262; fax: +81 58 2932207.



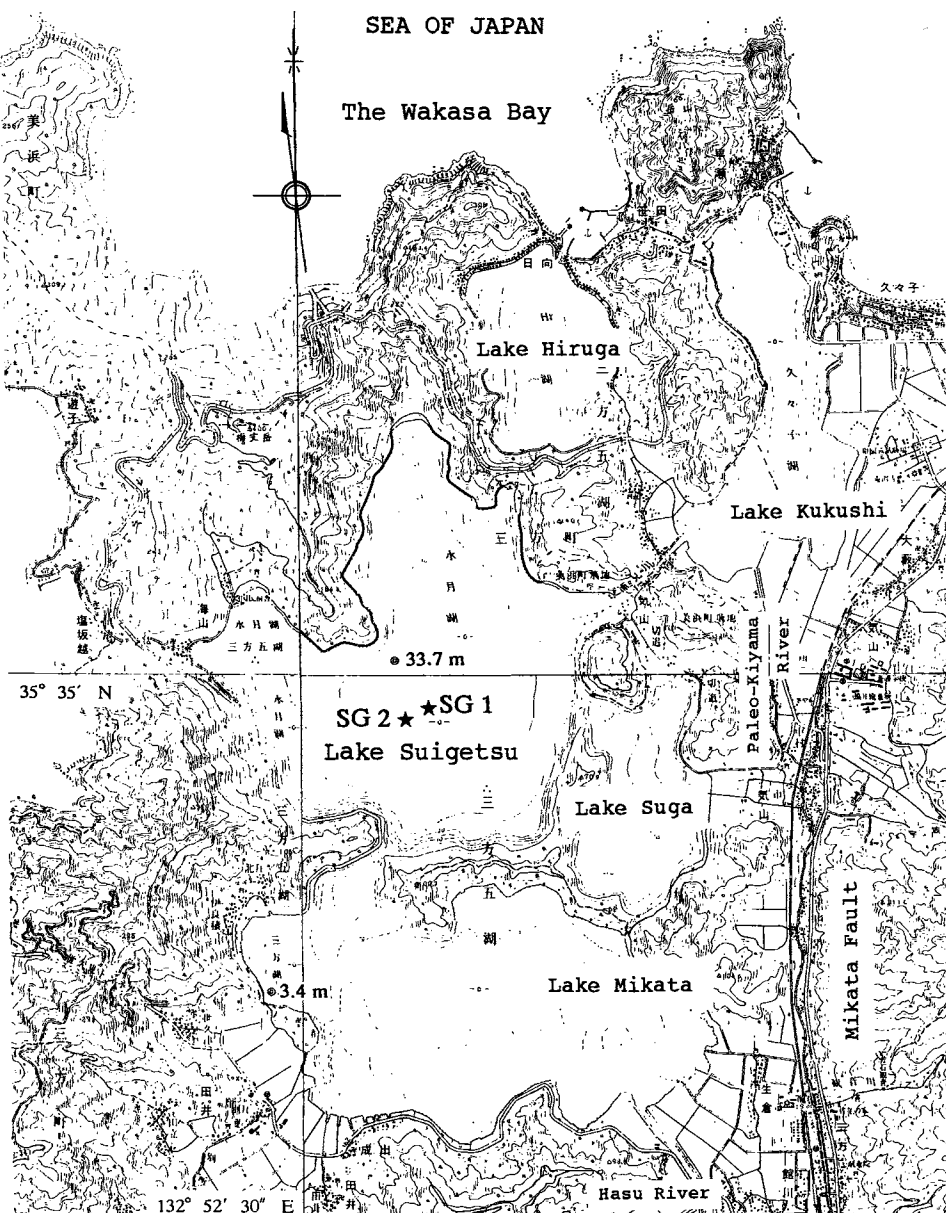


Fig. 1. (a) Location of Lake Mikatagoko (LM, indicated by the arrow) and the epicenters of historical earthquakes in central Japan. Historical events correlated with the depositional events are shown in Table 1. LB: Lake Biwa, WB: Wakasa Bay. (b) Geographic distribution of Lake Mikatagoko. Double circles: position of maximum water depth. Positions of coring sites were quoted from Fukusawa (1995); original base maps were modified from 1:25 000 maps by the Geographical Survey Institute of Japan.

(Usami, 1987; Kanaori et al., 1991, 1992, 1993b). Since historical documents before 1000 A.D. are rather fragmentary, a number of events have not been identified. Trench excavation studies of the active faults distributed in central Japan, which have been regarded as a valuable data base (Tsukuda and Yamazaki, 1984), have shown that the identification of events and their ages are frequently hampered owing to the low temporal and/or spatial resolution. Here it will be shown that the lacustrine sediment from Lake Mikatagoko provides invaluable information on past destructive earthquakes by correlating the sedimentary events with destructive earthquakes recorded in historical documents.

2. Tectonic and hydrological setting

Lake Mikatagoko is located in the northern apex of the Kinki triangle where the Isewan-Tsurugawa Tectonic Line (ISTL) and the Hanaore-Kongo Fault Line (HKFL) converge (Kanaori et al., 1993a) as shown in Fig. 1. Lakes Kugushi and Hiruga are connected to Wakasa Bay through small channels. The region is characterized by a ria coast where tectonic subsidence of crustal blocks has occurred through the late Pleistocene by fault displacements along many active faults composing the TITL and the HKFL. The latest example is the uplift of the eastern hill along the Mikata fault by the 1662 A.D. Kanbun earthquake ($M=7.5$) (Hagiwara, 1982). This earthquake caused uplift of the floor of the Kiyama River, the major drainage channel connecting Lake Mikatagoko to the Sea of Japan, and resulted in the submergence of rice fields and villages facing the lakes. Geomorphological characteristics and the latest example of crustal movement suggest that many large earthquakes have occurred around the area. One of the motivations of this study came from the expectation that environmental changes caused by past large earthquakes might have been recorded in sediments deposited beneath the lakes.

It is important to point out the unique hydrological setting of Lake Suigetsu where we sampled the core. A large fraction of water coming into the lakes is supplied from only one small river (the Hasu River), which enters Lake Mikata having a maximum depth of only 2 m. Since Lake Suigetsu is connected to Lake Mikata by a narrow natural waterway, a large fraction of sediments supplied from the Hasu River is expected to be deposited in Lake Mikata. The slow sedimentation rate and the homogeneous composition of the core described below meet our expectation.

3. The SG-2 core

A continuous core (SG-2) measuring 11 m in length was recovered by hydraulic piston coring during 1991 at the center of Lake Suigetsu, one of the five major lakes of Lake Mikatagoko (Figs. 1, 2). A sedimentological description of the

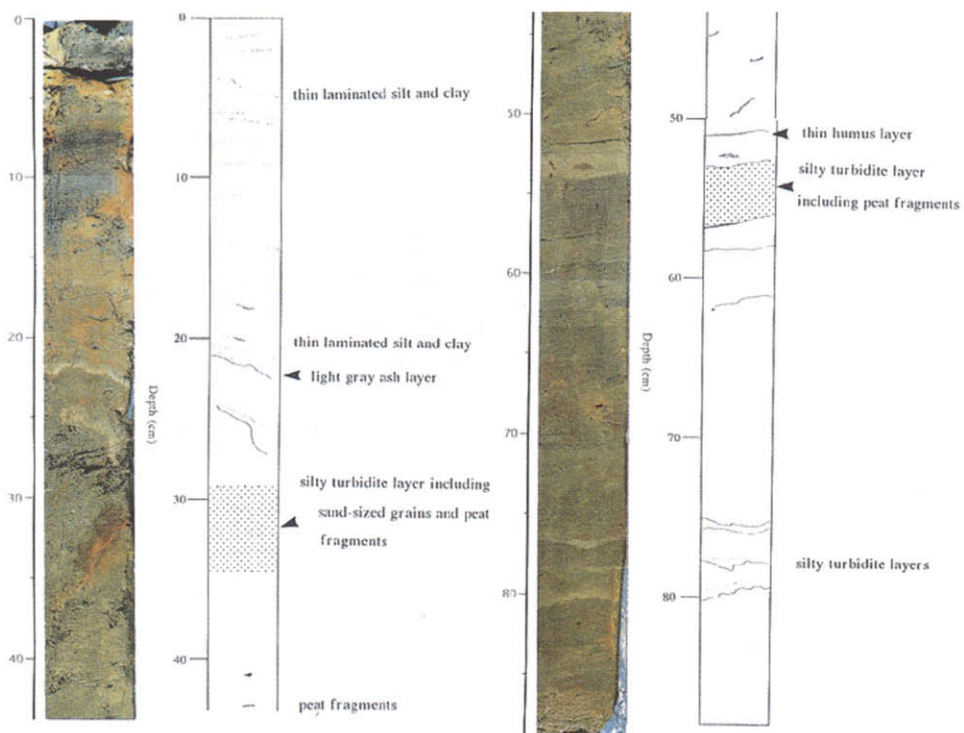


Fig. 2. Photograph of uppermost 90 cm of the core SG-2. Two turbidite layers and a volcanic ash layer were indicated. Environmental condition of lake water changed from fresh to brackish after the deposition of upper turbidite layer.

uppermost 88.5 cm portion of the core revealed two turbidite layers at depths of 29.5–34.0 and 51.5–55.5 cm, sandwiched between diatom-rich clay sediment layers (Fukusawa et al., 1994). Turbidites found in the SG-2 core are characterized by upward-fining graded bedding with sharp apparent discontinuities at the lower boundaries. Several additional thin silt/tuff layers were also observed. A detailed analysis of the sediment core was performed to obtain the bulk density and grain density profiles. The bulk density was measured by a Hg pycnometer after the drying of the sediment. Porosities were measured by a method that uses the adsorption of carbon tetrachloride. The grain density was calculated from the bulk density and porosity data. Figure 3 shows the derived bulk density (solid circles) and grain density (open circles) profiles. Generally, the densities of the diatom-rich clay sediment are in the range from 1.6 to 2.0 g/cm³. The high grain densities found in Fig. 3 reflect a high concentration of iron sulfides (pyrites, marcasites) or iron carbonates (siderites). These iron minerals were formed in high-porosity layers by the secondary precipitation processes. Large porosities corresponding to the turbidite

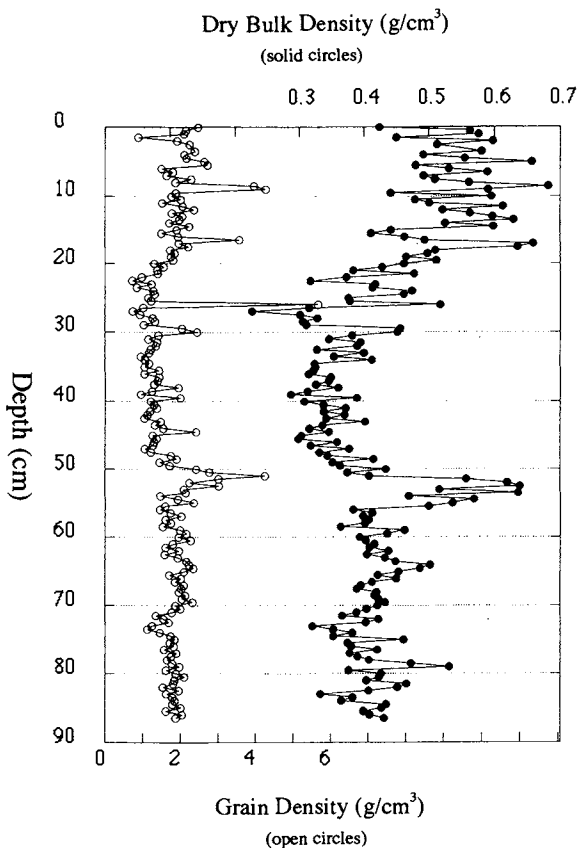
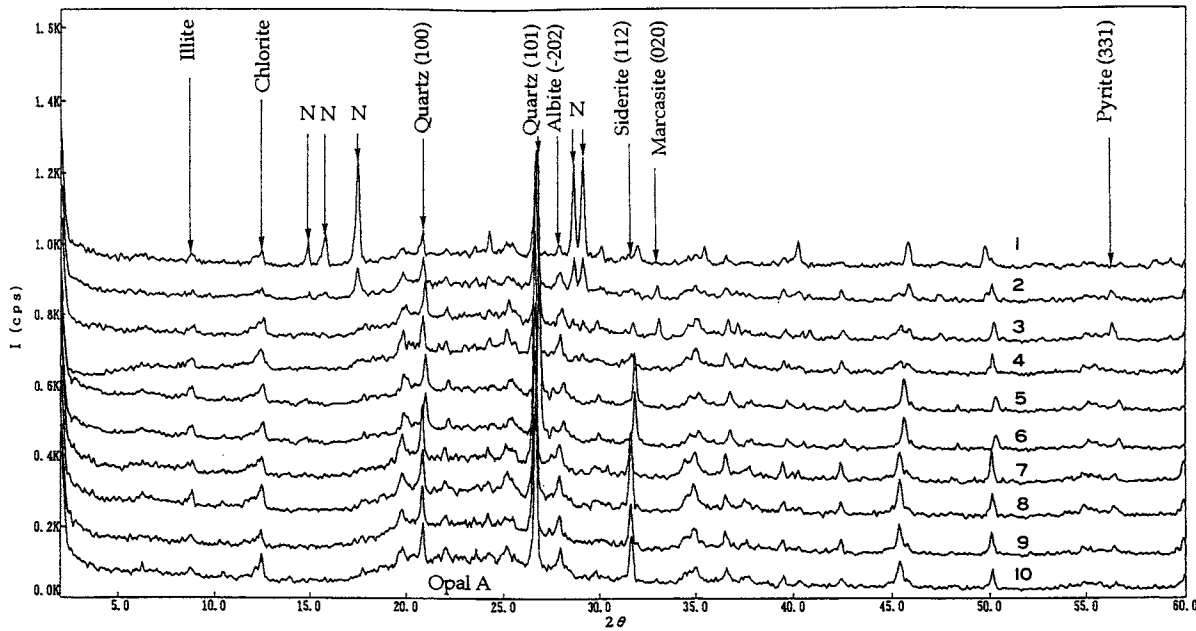


Fig. 3. Bulk density and grain density profiles of the core SG-2. The depths at 29.5–34.0 and 51.5–55.5 cm correspond to turbidite layers. The 1662 turbidite event and the drastic transition from fresh to brackish water at 1664 yields a sedimentation rate of 0.9 mm/year.

layers enabled an efficient groundwater circulation which provided a suitable environment for iron mineral precipitation.

Abundance profiles of siderite and pyrites were obtained through an X-ray analysis (Fig. 4). The results indicate that siderites are the predominant iron mineral below the upper turbidite layer and that pyrites and marcasites increased after turbidite deposition. This means that the environmental conditions of the lake water were drastically changed from fresh to brackish at the time corresponding to a core depth of 34.0 cm.

Historical documents and geomorphic examinations (Usami, 1987; Hagiwara, 1982) have revealed that the 1662 Kanbun earthquake was accompanied by a ground uplift which crossed the Kiyama River, resulting in a flood disaster in the area around the lake. A new discharge channel excavated in 1664 enabled sea water to enter the lake, resulting in the brackish water environment. This indicates that



sample 1 - 4 : brackish water conditions

N : Natrojarosite, $\text{NaFe}(\text{SO}_4)_2(\text{OH})_6$

sample 5-10 : fresh water conditions

Fig. 4. X-ray diffraction patterns of authigenic and detrital minerals in several varved sediments recovered from the SG-2 core.

TABLE I

The dates of depositional events and corresponding historical earthquakes in central Japan

Dates (A.D.)	Historical large earthquake name or location	Dates (A.D.)	Magnitude	Remarks
<i>Event I</i>				
ca. 1891	Nobi (1)	Oct. 28, 1891	8.0	The largest earthquake since 1880. Seismic intensity attained the JMA intensity scale of V or VI around the lake.
	Ansei-Nankai (2)	Dec. 24, 1854	8.4	Large offshore earthquake with tsunami disaster in southwest Japan. Seismic intensity was weaker than the previous day (see below).
	Ansei-Tokai (3)	Dec. 23, 1854	8.4	Large offshore earthquake with tsunami disaster in the Tokai area facing the Pacific ocean. Seismic intensity was degree V. No conspicuous depositional event in the core.
<i>Event II</i>				
ca. 1810	Ohmi (4)	June 12, 1819	7.5	Damage around the Lake Biwa. Seismic intensity attained degree V in the Wakasa area.
<i>Event III</i>				
ca. 1700	Hoei (5)	Oct. 28, 1707	8.4	The largest offshore earthquake in southwest Japan. Seismic intensity was V or VI around the lake.
<i>Event IV</i>				
1662	Ohmi/Wakasa (6)	June 16, 1662	7.4	Great damage around Lake Biwa and Lake Mikatagoko. See text.
<i>Event V</i>				
ca. 1610	not named	Nov. 26, 1614	?	Enigmatic. Few records.
	Goki-Shichido (7)	Feb. 3, 1605	7.9	Large offshore earthquake with tsunami disaster in southwest Japan. Seismic intensity no greater than degree V.
	Fushimi (8)	Sept. 5, 1596	7.5	Strong damage in Kyoto and the south. Seismic intensity no greater than V.
<i>Event VI</i>				
ca. 1590	Tensho (9)	Jan. 18, 1586	8.1	Great inland earthquake in central Japan. Seismic intensity V or greater around the lake.
<i>Event VII</i>				
ca. 1530	Kyoto/Ohmi	July 12, 1532	?	Enigmatic.
<i>Event VIII</i>				
ca. 1450	Kyoto/Nara (10)	May 13, 1449	6.4	A landslide occurred somewhere along the ancient road connecting Kyoto and Wakasa area.
<i>Event IX</i>				
ca. 1340	Ohmi/Wakasa (11)	July 5, 1325	6.5	Damage north of Lake Biwa and also in the Wakasa area.
<i>Event X</i>				
ca. 1170	Ohmi/Kyoto (12)	Aug. 13, 1185	7.4	Damage in Kyoto, Nara, and around Lake Biwa.

Epicenters of the historical earthquakes listed are shown in Fig. 1 as numbered circles.

the existence of the turbidite layer with a steep transition of the lake water environment from fresh to brackish was caused by this sequence of events, providing a well-dated time marker.

The date of the lower turbidite event at a depth of 51.5–55.5 cm was inferred from extrapolating the depth-age relationship of the core, assuming a constant accumulation rate, except for the two turbidite layers. The estimated date of the layer is ca. 1450. Historical documents (Usami, 1987) have also recorded a destructive earthquake in 1449, which caused serious disasters in the areas around Kyoto and Nara, the former capital cities of Japan. The earthquake also induced a land slide somewhere along the ancient road connecting the Kyoto and Wakasa areas (the area which includes the lake), claiming many human and animal lives. On the basis of this literature information (Usami, 1987), it was interpreted that the lower turbidite layer was the result of the 1449 seismic event.

Figure 5 shows the profiles of core density variations as a function of the estimated age. It is noted that many spike-like anomalies occur in both density profiles at the same time. The depositional events identified as turbidite layers are accompanied by anomalies in both the bulk density and grain density profiles. However, the bulk density after 1700 exhibits larger values and erratic fluctuations. These signatures were probably caused by the volume contraction of the sediment during desiccation.

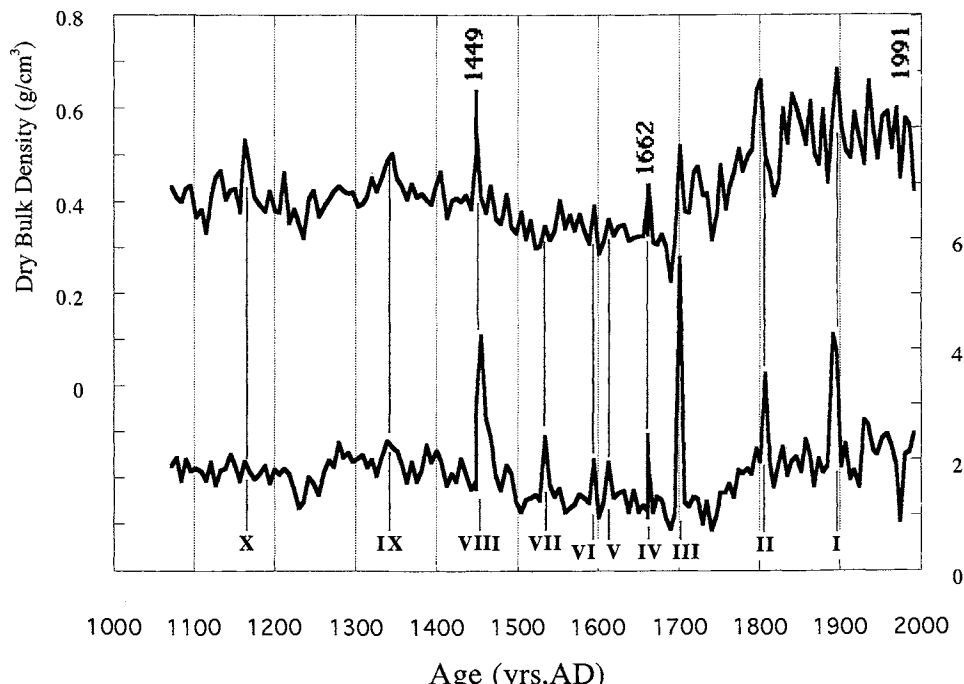


Fig. 5. Core density variations as a function of time. Conspicuous density anomalies are regarded as depositional events and indicated by Roman numerals I–X.

Therefore, the grain density peaks were used to identify depositional events after 1700.

Recently, it was found that clear laminations composed of diatom-rich layers interbedded with clay-rich layers or siderite-rich layers were caused by annual environmental changes of the lake (Fig. 6). The diatom-rich layers were accumulated during the spring and autumn seasons when vertical circulation of the lake water became strong enough to cause the blooming of diatoms, while siderite-rich layers

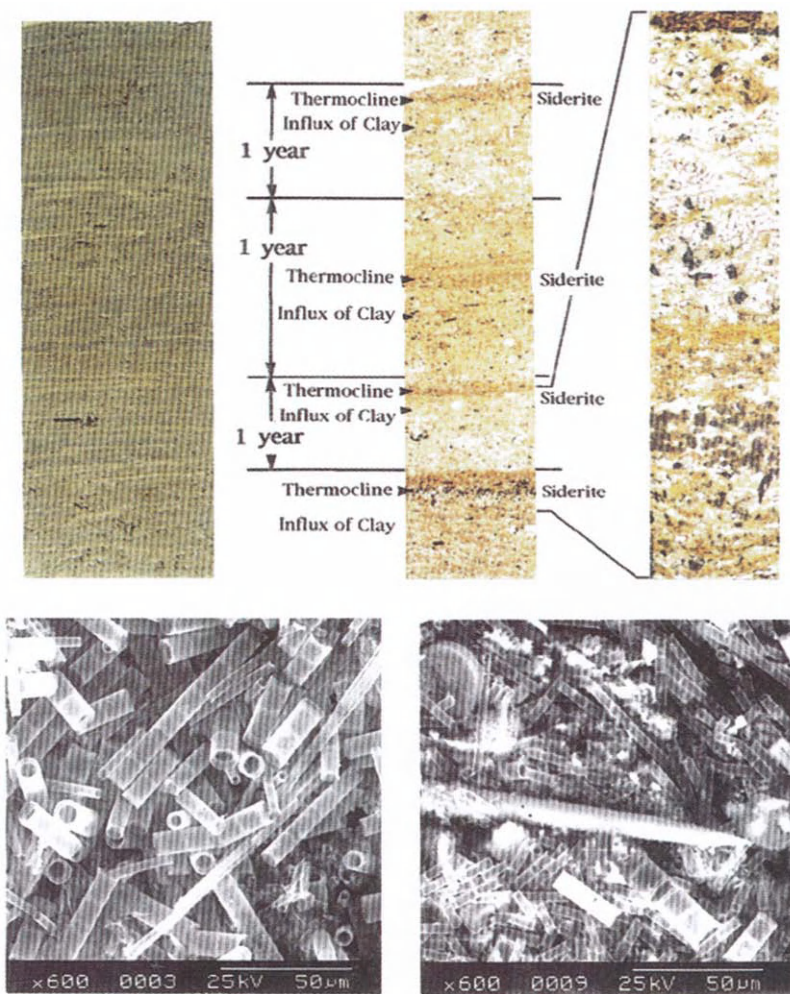


Fig. 6. Photographs of laminations found in the SG-2 core. Left-hand side is a visual image of the varves. Central parts are optical microscopic features. Light and dark gray laminae are composed of diatom-rich and clay- or siderite-rich sediments, respectively. The left-hand side is a comparison of SEM images of diatom-rich sediments deposited during spring and autumn.

were accumulated during the summer season when formation of warm surface water resulted in a stably stratified condition with anoxic deep waters (Fukusawa, 1995). Preliminary analysis of varve chronological dating shows remarkably consistent results with those obtained by the present method assuming the constant sedimentation rate.

A thin volcanic ash layer identified at about 22 cm depth is estimated to have been deposited at about 1780. Many historical documents and geological studies of Mt. Sakurajima revealed that large explosive eruptions occurred in 1449, 1779 and 1914 (National Astronomical Observatory, 1994; Kobayashi, 1982). Trace amount of volcanic ash was recognized for the 1914 explosion in the Wakasa area (Omori, 1914). However, there is no documents concerning whether volcanic ash ejected by the 1779 An-ei eruption reached the study area. The secular compositional variation of pyroclastic materials of Sakurajima Volcano during the historical era revealed by Aramaki and Kobayashi (1996) was used for an examination, which resulted in a consistent result. Since no other large volcanic eruption was identified in and around the Japanese Islands at about 1780, the ash layer was interpreted to have originated from the 1779 Sakurajima explosion. The identification of the ash layer may further strengthen the reliability of our chronological results.

A visual inspection of the lower portion of the core has revealed at least 46 turbidite layers (Fig. 7). Some of the events with inferred ages between ca. 750 and 100 A.D. may be correlated with the liquefaction events found in the archaeological sites (Kanaori et al., 1993b). Recently, Fukusawa (1995) suggested that varve chronological dates of the Akahoya volcanic ash layer found in the SG-2 core are consistent with the tephrochronological database in Japan (Machida and Arai, 1992), and that dates of the onset and end of a cold period characterized with low sedimentation rates are comparable to those for the Yanger Drias period (e.g., Johnsen et al., 1992). These results suggest that the SG-2 core can be regarded as standard data for correlating the environmental history dating back through the past 10 millennia.

4. Discussion

Numbers are assigned to the depositional events before 1900, as shown in Fig. 5 and Table 1. Four large earthquakes have occurred around the Wakasa area during the instrumental era (Usami, 1987): the 1909 Anegawa earthquake ($M=6.8$), the 1927 Kitatango earthquake ($M=7.3$), the 1948 Fukui earthquake ($M=7.1$), and the 1963 Off-Echizenmisaki earthquake ($M=6.8$). The epicenters of these events are shown in Fig. 1 as A, B, C, and D, respectively. It is not certain if some of the peaks in the grain density profile can be correlated with these events.

It is noted in Table 1 that all the events recorded in the lake sediment between 1100 and 1900 (indicated by the Roman numerals in Fig. 4) can be correlated with historically documented earthquake damage. The ages of the events are estimated assuming a constant sedimentation rate of 0.9 mm/year. The degree of fluctuation in the sediment accumulation rate is presently not clear. However, the good

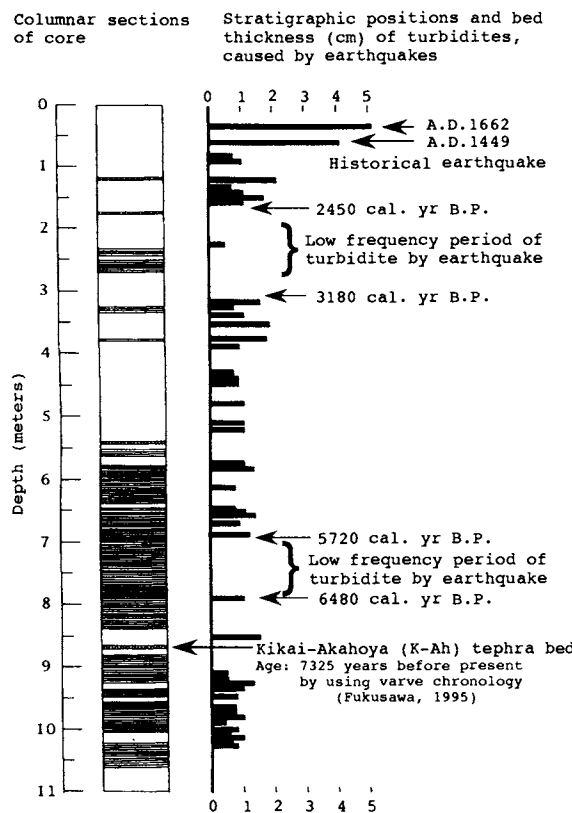


Fig. 7. Stratigraphic position of the 46 turbidite events with their thickness represented by the length of solid lines.

correlation of depositional events with known historical earthquakes as well as crosscheck by varve chronology suggests that uncertainties in the estimated ages should be within 10–15 years.

Event I is correlated with the 1891 Nobi earthquake ($M=8.0$, number 1 in Table 1 and Fig. 1), the largest inland earthquake to occur during the instrumental era. This event was associated with the movement of the Neodani fault (Richter, 1958). The ground motion around the lake generated by this event has been estimated to exceed the JMA intensity scales of V or VI (Muramatsu, 1976).

Event III is correlated with the 1707 Hoei earthquake ($M=8.4$, number 5 in Table 1 and Fig. 1), the largest offshore earthquake to severely devastate southwest Japan (Usami, 1987). The ground motion around the lake induced by this event exceeded intensity V or VI.

Event VI is correlated with the 1586 Tensho earthquake ($M=8.0$, number 9 in Table 1 and Fig. 1) (Usami, 1987). It has been suggested (Iida, 1987; Sugiyama et al., 1991; Kanaori et al., 1993c) that this earthquake was accompanied by the

movements of the Miboro, Atera, and Isewan faults, and is presently regarded as one of the largest inland earthquakes to ever occur in Japan. The ground motion around the lake resulting from this event may have reached intensity V or greater.

It is important to note that all the earthquakes that caused possible damage to the area around the lake have been recorded as density anomalies in the lake sediment and/or turbidites. Further, no clear depositional events were recorded at times when no earthquake damage was identified in previous studies. This means that the lake sediment beneath Lake Suigetsu acted as a good natural seismometer to record seismic ground motion exceeding intensity V. The implication of Event III is quite significant because it suggests that if the ground motion resulting from offshore earthquakes along the Nankai trough is sufficiently strong, this motion should be recorded in the lacustrine sediment as a density anomaly.

One important problem to be answered here is to evaluate any possibility of a heavy rainfall or floods as a cause of the high-density anomalies. Fortunately, many historical flood events in the study area were recorded in many historical documents. Fukusawa et al. (1994) obtained the profile of X-ray intensity ratios between chlorite and illite and found that high chlorite/illite ratios are correlated with the occurrence of historical floods. Since the high density events and high chlorite/illite events were temporarily discriminated in the present analysis, one could safely conclude that the high density events discussed above were caused by ground shaking induced by historical earthquakes.

In order to justify further the result obtained from the SG-2 core, one must confirm whether the same events are recorded in cores recovered from the other sites of the same lake or nearby lakes. Inouchi et al. (1993) described several core samples from Lake Biwa, located about 30 km to the south of the present study area, and found many density anomalies. They interpreted that many of the high density events corresponded to turbidites which were induced by earthquake ground shaking with intensities exceeding the JMA intensity scale of IV at the sampling sites. The fact that many of the historical earthquake events they detected are correlated with those detected in this analysis led to a research program of systematic sampling and analysis of lacustrine sediments.

Several cores from Lake Mikatagoko were recently sampled by the authors. The SG-1 core obtained at the nearby site was used for paleomagnetic and rock magnetic measurements, providing a sedimentation rate of 0.94 mm/year (Itota et al., 1993). The estimated value is consistent with the present study. Detailed description of depositional events recorded in the other cores and their mutual correlations will be given in the near future in order to clarify whether lacustrine sediments are useful archives for paleo-environmental studies.

5. Conclusion

The near perfect correlation between the high density events found in the uppermost 90 cm portion of the core SG-2 and historical earthquakes suggests that the 11 m sedimentary core currently under analysis will provide a record of strong ground

motions induced by large earthquakes dating back through the past 10 millennia, even when no historical literature exists. Since the core is characterized by non-glacial varves produced by annual environmental change (Fukusawa, 1995), more accurate dating of the events will be made through the varve chronological approach. In the near future, the utility of lacustrine sediments in paleoseismological studies in Japan will be examined extensively through systematic sampling and analysis.

Acknowledgements

The authors thank Dr. Y. Yasuda, International Japan Culture Research Center and Dr. M. Okamura, Kochi University for providing the sample. A part of this study was supported by the Decoding Earth Evolution Program (DEEP), a Grant-in-Aid for Scientific Research on Priority Areas from the Ministry of Education, Science, and Culture of Japan (No. 07238104) and by the Earthquake Research Institute cooperative research program (1995-B0-02). The authors also thank Drs. M. Torii and H. Sakai for valuable comments on the manuscript.

References

- Aramaki, S. and Kobayashi, T., 1996. Whole rock composition of the ejected materials from Aira Caldera and Sakurajima Volcano and the An-ei eruption, Report of 5th Cooperative Observations of Sakurajima Volcano, pp. 115–129, Disaster Prevention Res. Inst., Kyoto Univ. (in Japanese).
- Doig, R., 1990. 2300 yr history of seismicity from silting events in Lake Tadoussac, Charlevoix, Quebec. *Geology*, 18: 820–823.
- Fukusawa, H., 1995. Non-glacial varved lake sediment as a natural timekeeper and detector on environmental changes. *Quaternary Res.*, 34: 135–149 (in Japanese with English abstract).
- Fukusawa, H., Koizumi, I., Okamura, M. and Yasuda, Y., 1994. Historical earthquake, flood and Human activity events recorded in the Holocene sediments of Lake Suigetsu, Fukui Prefecture, central Japan. *J. Geography*, 103: 127–139 (in Japanese with English abstract).
- Hagiwara, T., (Editor) 1982. *Paleoearthquakes* (in Japanese). Univ. Tokyo Press, Tokyo, 312 pp.
- Iida, K., 1987. The record of the Great Tensho earthquake (in Japanese). Nagoya Univ. Press, Nagoya, 552 pp.
- Inouchi, Y., Kinugasa, Y., Kumon, F., Yasumatsu, S., Nakano, S. and Shiki, T., 1993. Turbidites in Lake Biwa as indicators of intensity of paleoearthquakes. *Mem. Geol. Soc. Japan*, 39: 61–71 (in Japanese with English abstract).
- Itota, C., Hyodo, M., Hayashida, A., Kitagawa, H. and Yasuda, Y., 1993. Paleoenvironmental study of sediments from Lake Suigetsu by rock magnetic and paleomagnetic analyses. *Proc. Inst. Natural Sci., Nihon Univ.*, 28: 55–60 (in Japanese with English abstract).
- Jacoby, G.C., Williams, P.L. and Buckley, B.M., 1992. Tree ring correlation between prehistoric landslides and abrupt tectonic events in Seattle, Washington. *Science*, 258: 1621–1623.
- Johnsen, S.G., Clausen, H.B., Dansgaard, K., Fuhrer, W., Gundestrup, N., Hammer, G.U., Iversen, P., Jouzel, J., Stauffer, B. and Steffensen, J.P., 1992. Irregular glacial interstadials recorded in a new Greenland ice core. *Nature*, 359: 311–313.
- Kanaori, Y., Kawakami, S. and Yairi, K., 1991. Space-time distribution patterns of destructive earthquakes in the inner belt of Central Japan: activity intervals and locations of earthquakes. *Eng. Geol.*, 31: 209–230.

- Kanaori, Y., Kawakami, S. and Yairi, K., 1992. Space-time distribution patterns of destructive earthquakes in the inner belt of Central Japan (Part 3): Seismic hazard assessment. *Eng. Geol.*, 33: 99–110.
- Kanaori, Y., Kawakami, S. and Yairi, K., 1993a. Space-time correlations between inland earthquakes in central Japan and great offshore earthquakes along the Nankai trough. *Eng. Geol.*, 33: 289–303.
- Kanaori, Y., Kawakami, S., Yairi, K. and Hattori, T., 1993b. Liquefaction and flowage at archaeological sites in the inner belt of central Japan: Tectonic and hazard implications. *Eng. Geol.*, 35: 65–80.
- Kanaori, Y., Kawakami, S., Yairi, K. and Hattori, T., 1993c. Comment on the epicenter of the 1586 Tensho earthquake: Liquefaction found at archaeological sites in the Nobi Plain, Central Japan. *Zishin*, II, 46: 143–147 (in Japanese).
- Kawakami, S., Kanaori, Y., Arakawa, S., Nagaya, K. and Hasegawa, Y., 1991. Debris flow deposits and minor folds in rhythmical lacustrine sediments – implications for cyclic debris flows and inland earthquakes. *Jpn. J. Eng. Geol.*, 32: 9–18 (in Japanese with English abstract).
- Kobayashi, T., 1982. Geology of Sakurajima Volcano: a review. *Bull. Volcan. Soc. Japan*, 22: 277–292 (in Japanese with English abstract).
- Machida, H. and Arai, F., 1992. Atlas of Tephra in and around Japan. Univ. Tokyo Press, Tokyo, 276 pp.
- Muramatsu, I., 1976. Neodani fault and Nobi earthquake. In: K. Fujita, A. Sugimura, T. Kakimi and T. Matsuda (Editors), *Fault and Earthquake*. Mem. Geol. Soc. Jpn., 12: 117–127 (in Japanese with English abstract).
- National Astronomical Observatory, 1994. *Chronological Scientific Tables*, Maruzen, Tokyo, 1037 pp.
- Obermeier, S.F., Bleuer, N.R., Munson, C.A., Martin, W.S., McWilliams, K.M., Tabaczynski, D.A., Odum, J.K., Rubin, M. and Eggert, D.L., 1991. Evidence of strong earthquake shaking in the lower Wabash Valley from prehistorical liquefaction features. *Science*, 252: 1061–1063.
- Omori, H., 1914. The Sakura-jima eruptions and earthquakes, I–III, *Bull. Imp. Earthq. Invest. Commit.*, 8: 1–321.
- Page, R., 1970. Dating episodes of faulting from tree rings: effects of the 1958 rupture of the Fairweather Fault on tree growth. *Geol. Soc. Am. Bull.*, 81: 3085–3094.
- Richter, C.F., 1958. *Elementary Seismology*. W.H. Freeman and Co., New York, 768 pp.
- Sheppard, P.R. and Jacoby, G.C., 1989. Application of tree-ring analysis to paleoseismology: Two case studies. *Geology*, 17: 226–229.
- Sieh, K., 1978. Slip along the San Andreas Fault associated with the Great 1857 earthquake. *Bull. Seis. Soc. Am.*, 68: 1421–1448.
- Sieh, K., 1984. Lateral offsets and revised dates of large prehistoric earthquakes at Pallet Creek, southern California. *J. Geophys. Res.*, 89: 7641–7670.
- Sims, J.D., 1975. Determining earthquake recurrence intervals from deformational structures in young lacustrine sediments. *Tectonophysics*, 29: 141–152.
- Sugiyama, Y., Awata, Y. and Tsukuda, E., 1991. Holocene activity of the Miboro fault system, central Japan and its implication for the Tensho earthquake of 1586 – verification by excavation survey. *Zishin* II, 44: 283–295 (in Japanese with English abstract).
- Tsukuda, E. and Yamazaki, H., 1984. Excavation survey of active faults for earthquake prediction in Japan with special reference to the Ukihashi-central fault and the Atera fault. *Geol. Surv. Jpn Rep.*, No. 263: 349–361 (in Japanese with English abstract).
- Usami, T., 1987. Descriptive catalog of disastrous earthquakes in Japan (in Japanese). Univ. Tokyo Press, Tokyo, 434 pp.

Seismotectonic environment and design basis earthquake for the Darlington nuclear power station

C.F. LEE¹

Department of Civil and Structural Engineering, The University of Hong Kong, Hong Kong

Abstract

This paper presents the case history of a 4×950 MW nuclear power station located in the intraplate seismic environment of Eastern Canada. The pertinent seismotectonic features of such an environment are described, including the prevalence of a state of high horizontal compressive stress, and the absence of surface rupturing during most intraplate seismic events. The design earthquakes for the various potential source zones are determined, including the Western Quebec Zone, the Niagara Region and the Clarendon-Linden Fault System in western New York State. The design basis seismic ground motion parameters are then deduced for the Darlington site, along with the ground response spectra. Differences between the intraplate and plate-boundary seismic environments are discussed.

1. Introduction

In the seismic design of nuclear power plants, each seismogenic fault within the area of interest constitutes a potential source zone. A design earthquake (DE) is deduced for each source zone based on historical seismicity and/or evidence of neotectonic movement. The design basis earthquake (DBE) is then taken as the most severe of all DEs from the various possible source zones, incorporating an appropriate safety margin. A seismogenic fault normally manifests itself by co-locating with a significant number of epicentres, or by showing signs of neotectonic movement. In many cases, particularly at the boundaries of tectonic plates, the identification of seismogenic faults based on their surface expressions is a viable task, given due diligence in geological investigation and a good knowledge of regional seismicity. This may or may not be the case, however, in the intraplate environment where the seismogenic faults are located at great depth, without surface expressions or evidence of surface rupturing due to seismic events. This renders the determination of the design basis seismic ground motion (DBSGM) parameters a

¹Formerly, Manager of Civil Engineering Department and Manager of Geotechnical Engineering Department, Ontario Hydro, Toronto, Canada.

rather challenging task. The present paper provides such an example of earthquake-resistant design in the intraplate environment. Specifically, the case history of the 4 × 950 MW Darlington Nuclear Power Station design will be used to illustrate the challenges encountered and the methodologies adopted under such circumstances.

2. The intraplate seismic environment

In tectonic terms, Eastern Canada is located in the interior of the North American Plate, remote from the plate boundaries on the Pacific Coast and at the Mid-Atlantic Ridge. Seismicity in Eastern Canada is, to a large extent, related to its glacial history. It has been postulated to be the result of rejuvenation of fault activities under the condition of glacio-isostatic uplift (Sanford et al., 1984). At the peak of the Wisconsinian Glaciation, the land subsided by as much as several hundred metres, depending on the specific locale under consideration (Paterson, 1972; Cathles, 1975). Upon deglaciation, some 13 000 years B.P., the land rebounded. While the bulk of the glacio-isostatic uplift has since occurred, much of Eastern Canada is still rebounding today at the rate of a few millimetres per year. Crustal deformation during glaciation and deglaciation resulted in significant changes to the state of stress and strain in the rock mass at depth, leading to the rejuvenation of ancient fault systems and hence seismicity in the region (Lee, 1978). Such a mode of seismic occurrence has also been observed in other glaciated regions such as Scandinavia (e.g. Mörner, 1985; Mörner et al., 1989).

Intraplate seismicity in Eastern Canada differs from plate-margin seismicity (or interplate seismicity) in two fundamental aspects. Firstly, deformation at plate margins often resulted in a highly fractured or disintegrated rock mass around the seismogenic fault (e.g. the San Andreas Fault System in California). This led to a larger damping effect for the seismic motions generated by fault rupture. In contrast, the rock mass conditions in much of Eastern Canada tend to be generally more massive and more competent. This means that the rock formations in Eastern Canada have a better ability to transmit seismic waves and a smaller damping effect for seismic motions. Thus, seismic motions would be attenuated more rapidly at plate margins than in the intraplate environment. Fig. 1 illustrates such a comparison in terms of Modified Mercalli intensity, starting with same maximum intensity near the source. This difference also explains why intraplate earthquakes are felt over relatively large areas, e.g. the Cornwall-Massena earthquake of September 5, 1944 (Berkey, 1945). Comparing a plate-margin earthquake to an intraplate earthquake of the same magnitude, one may notice that the former is often characterized by greater damage near the seismogenic fault zone, particularly at the apex of a rupturing fault. For an intraplate earthquake of the same magnitude, the felt area will normally be larger while the damage will generally be less substantial, reflecting the dissipation of seismic energy over a wider area (Lee, 1978). This comparison, of course, refers to intraplate and plate-margin earthquakes of the same magnitude.

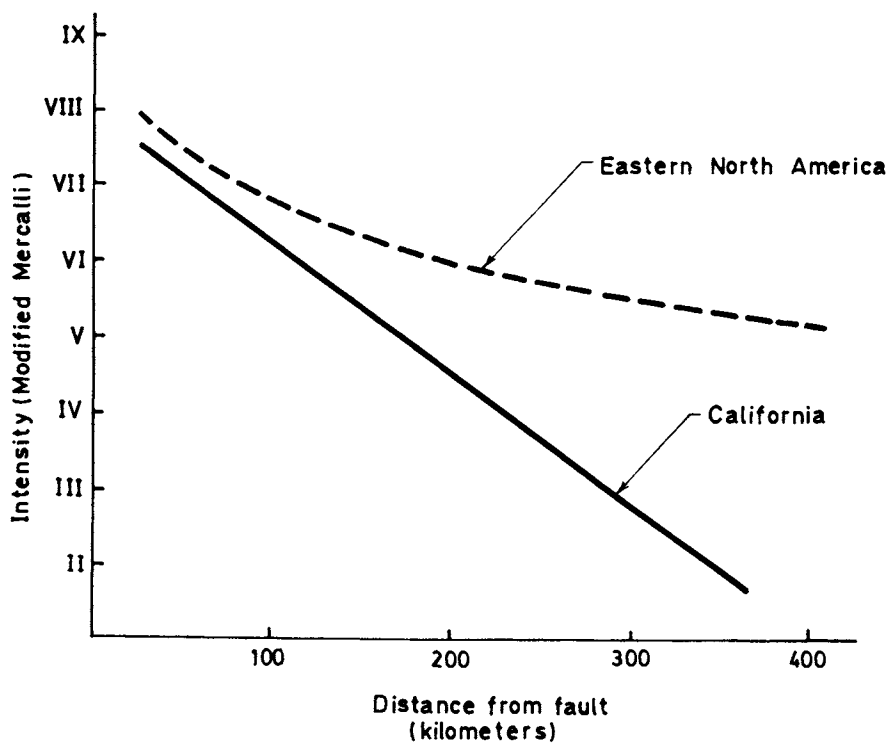


Fig. 1. Attenuation of intensity for California (plate boundary environment) and Eastern North America (intraplate environment), after Evernden et al. (1981).

Fig. 1, on the other hand, refers to intensity attenuation, starting with the same maximum intensity near the source.

The second major difference between plate-margin and intraplate earthquakes lies in the stress field around the seismogenic fault. Field measurements indicate that the magnitude of the normal compressive stress tends to decrease towards a plate boundary fault, such as the San Andreas Fault (Tullis, 1977; Engelder et al., 1978). In other words, the fault plane itself is not subject to a state of high lateral compression. This makes it easier for the fault to slip under shear loading. In contrast, much of Eastern Canada is subject to a state of high horizontal compression. The value of horizontal compressive stress measured generally ranges from 5 to 10 MPa near the bedrock surface, tending also to increase with depth (Herget, 1974, 1980; Lee, 1978, 1981; Haimson and Lee, 1980; Lee and White, 1994). This state of compressive stress often led to the occurrence of "pop-ups" in the bedrock surface, which are folds or buckles in the bedrock surface due to horizontal compression (White et al., 1973; Franklin and Hungr, 1976; Lee and White, 1994). This state of horizontal compression also results in a high degree of tightness in the rock mass. Thus there are numerous tunnels which were associated with little or no

seepage during excavation, despite being located under large bodies of surface water and having relatively thin rock covers (Lee et al., 1988; Lee and White, 1994). In fracture mechanics, the predominant direction of fracture propagation is parallel to the direction of the major principal stress (Fairhurst and Cook, 1966). This means that the seismogenic fault may well propagate in a predominantly horizontal direction at a considerable depth in the crust. Thus intraplate seismicity may or may not be associated with surface rupturing or a surface expression of the seismogenic fault. This is in direct contrast to the case of plate-margin earthquake, where surface rupturing is routinely observed, with most of the damage occurring at the apex of a rupturing fault. It also explains why intraplate earthquakes generally have greater focal depths than plate-margin earthquakes. While the focal depths of intraplate earthquakes vary considerably, the Geological Survey of Canada has traditionally assumed mid-crustal depth as a reference depth in the determination of epicentral locations of Eastern Canadian earthquakes.

The state of high horizontal compressive stress generally observed in Eastern Canada is believed to be also related to the glacial history of the region. At the peak of the Wisconsinian Glaciation, the maximum thickness of the Laurentide ice sheet reached 3000–3750 m (Paterson, 1972; Cathles, 1975). This sustained heavy glacial load resulted in the viscoelastic deformation of crustal rocks in much of Eastern Canada. It has been demonstrated that, under the condition of lateral confinement, a significant amount of horizontal residual stress could be inherited by the rock mass upon deglaciation (Lee, 1978; Lee and Asmis, 1979). Another possible major contributing factor is plate tectonics. The spreading of the seafloor at the Mid-Atlantic Ridge produces a compression effect on the North American Plate, predominantly in a westerly direction. This is generally consistent with the predominant direction of the major principal stress observed in much of Eastern North America (Sbar and Sykes, 1973; Sykes, 1978).

3. Site and regional geology

The site of the Darlington Nuclear Generating Station is located on the north shore of Lake Ontario, approximately 65 km to the east of the City of Toronto (Fig. 2). The station features four 950 MW nuclear power reactors of the CANDU type, which is a Canadian design that uses natural uranium as fuel and heavy water as moderator. Construction on the site began in 1978 and the four reactor units were commissioned respectively between 1990 and 1993. The overall project cost was in the order of US\$10 B, including interest during construction. The station was designed, constructed and operated by Ontario Hydro, a provincial electrical utility that supplies electricity to the Province of Ontario, Canada. Ontario Hydro currently has an installed generating capacity of approximately 32 000 MW, including nuclear, coal-fired and hydroelectric power stations.

The Darlington site is underlain by approximately 20 m of Quaternary glacial deposits of till and granular materials. Beneath the Quaternary deposits are

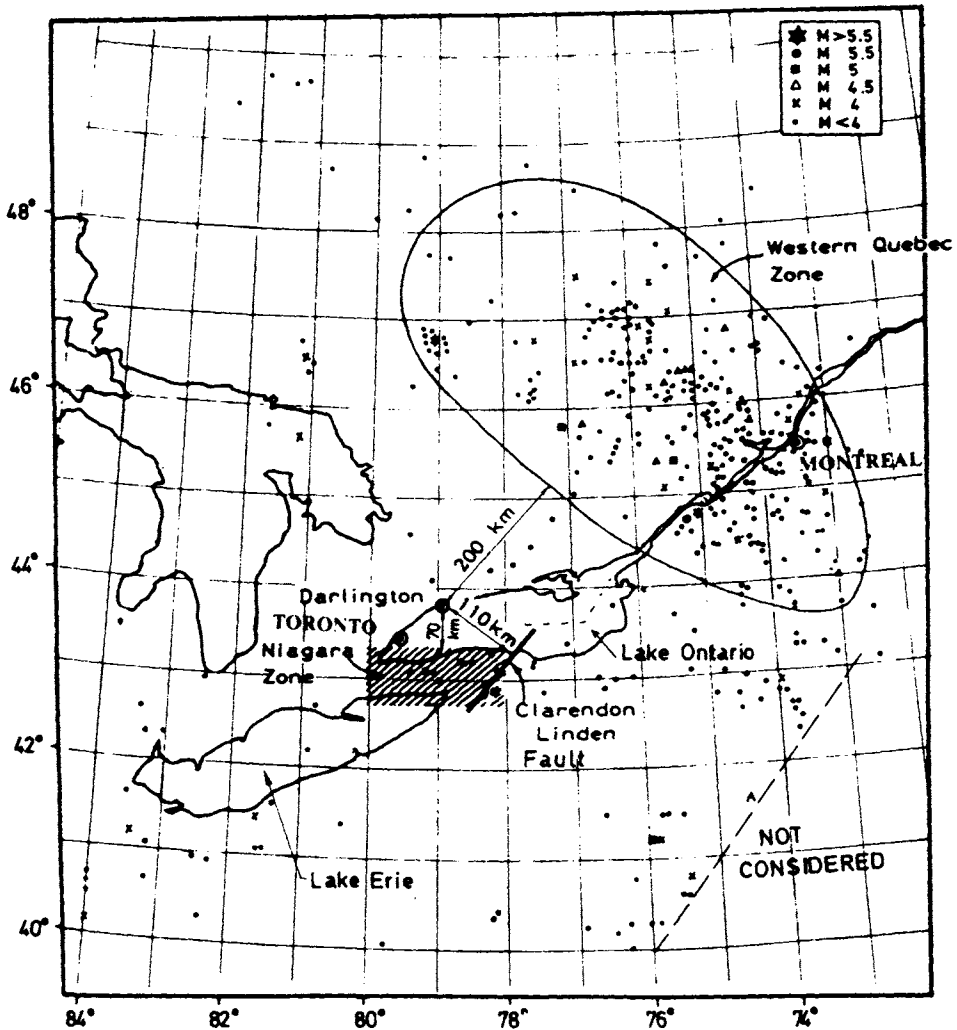


Fig. 2. Darlington site location, regional seismicity and design earthquakes (after Basham, 1975).

approximately 200 m of flat-lying (or very gently dipping) Ordovician limestones, shaly limestones, shales, siltstones/sandstones, which are in turn underlain by Precambrian basement rocks of massive, migmatitic gneisses. The Paleozoic sediments dip very gently to the south, at an angle of about half a degree, thickening considerably at the Niagara Escarpment to the west of Toronto, where Silurian (and further west, Devonian) sediments overlie those of Ordovician age (Fig. 3).

The Darlington site was selected in the early 1970s, largely due to its proximity to the major load centres (i.e. Toronto and Southern Ontario). Other pertinent factors such as proximity to a large body of cooling water (i.e. Lake Ontario),

geological and seismotectonic conditions, and environmental and socioeconomical impacts were also carefully considered in the site selection process.

A comprehensive program of state-of-the-art geophysical, geological, seismological and geotechnical investigations was carried out for the Darlington project, beginning in the mid-1970s. This included regional airborne and surface geophysical surveys, extensive drilling, in-situ stress measurement by overcoring and hydrofracturing, high-precision packer testing for hydraulic conductivity, and a variety of specialized geomechanical testing (Rutledge, 1983; Lee, 1984; Tang and Lee, 1993). The geophysical work focused on regional faulting and lineament tracing, including aeromagnetic gradiometer survey, maxi-probe electrical resistivity survey, mini-sosie seismic reflection survey, ground radar survey, etc. The results of geophysical surveys were cross-checked prior to confirmation drilling. There were incidences when innovative geophysical techniques of a research nature hinted at the possibility of faulting in river beds or along creeks and streams that drain into Lake Ontario. Such a possibility, however, was not substantiated by systematic drilling carried out subsequently to validate the results of geophysical surveys. There are, of course, faults in the sedimentary sequence as well as in the Precambrian basement rocks in the vicinity of the site and the general region of interest. With the exception of the Clarendon-Linden Fault System in western New York State (Fig. 2), however, there

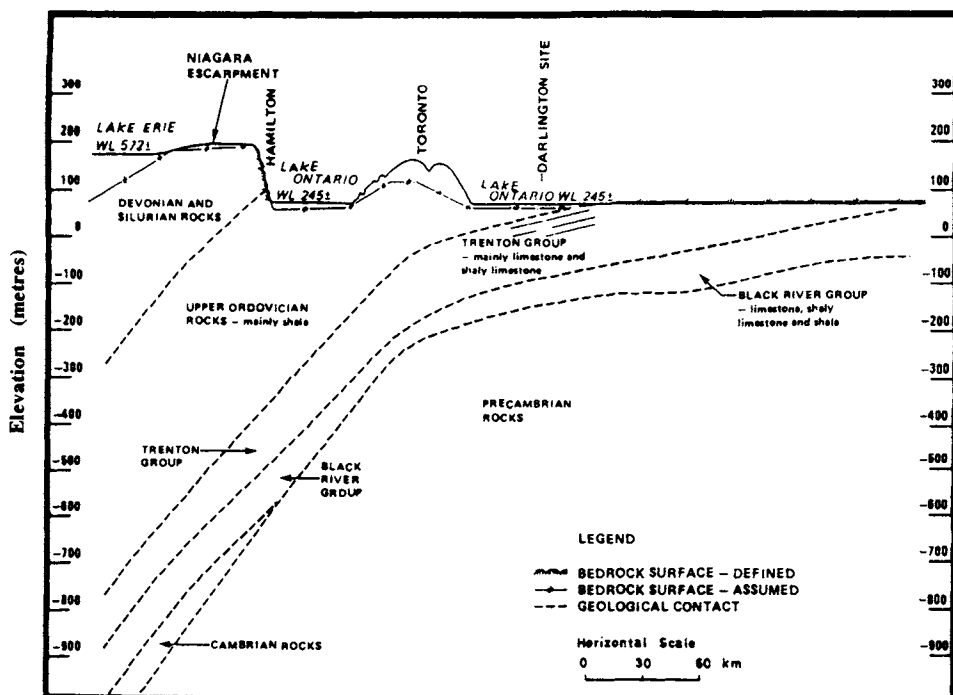


Fig. 3. Geological section along north shore of Lake Ontario.

appears to be no spatial correlation between such faults and the epicentres of historical and contemporary seismic events recorded in the region. The faults in the Precambrian basement show no signs of penetrating the overlying sedimentary sequence. This applies also to the Central Metasedimentary Belt Boundary Zone (CMBBZ) of the Grenville basement rocks, which manifests itself as a major shear zone with a width of several kilometres in outcrops at approximately 100 km north of the Lake Ontario shoreline (Easton and Carter, 1991; Easton, 1992; Lee and White, 1994).

The Clarendon-Linden Fault System is a north-northeasterly trending, high-angle reverse fault system in Ordovician sediments in western New York State. Since the late 1920s, a number of seismic events have been recorded and attributed to fluid injection and solution mining activities in the vicinity of the fault system (Van Tyne, 1975; Fletcher and Sykes, 1977). The largest event, which occurred in 1929, has been given a Richter magnitude rating of M5.8. This fault system has been postulated to extent northeasterly into Lake Ontario, possibly also into Prince Edward County on the north shore of Lake Ontario. While the fault system has been associated with induced seismicity due to fluid injection, it was nonetheless taken as an active fault and a source zone for the seismic design of the Darlington Nuclear Generating Station.

Otherwise, there is no conclusive evidence to date of any major, deep-seated neotectonic movement along any of the reported faults in the sedimentary sequence of southern Ontario. A number of minor faults were reported by White et al. (1973) in the sedimentary bedrocks of the region. They are not considered to be deep-seated and are believed to be related to the occurrence of high horizontal stresses in the southern Ontario region (Lee and White, 1994), similar to other near-surface, high-angle reverse faults observed by Oliver et al. (1970) in New York State and in the Province of Quebec, Canada.

In engineering geology terms, both the Ordovician sediments and the Precambrian basement rocks are generally massive and competent rocks. The Ordovician sediments exhibit well-defined, virtually horizontal bedding planes. The regional strike is approximately east-west, while the dip is to the south. The thickness of the beds vary from 2.5 to 75 cm. There are two dominant joint sets with orientations of N70–90°E and N45°W–N40°E, respectively. Joint spacing is close at the bedrock surface (0.1–0.3 m, approximately) and much more widely spaced at depth. In the cooling water intake and discharge tunnels, constructed at the Darlington site at a depth of some 35 m below the Lake Ontario bottom (bedrock) surface, the east-west joints were mapped at a spacing of 40 m apart. The tunnel excavations were found to be “bone dry”, requiring water to be brought down from the surface for dust control (Lee and White, 1993, 1994). The Ordovician sediments as exposed in the walls of the tunnel excavations were obviously very tight and massive, with no signs of faulting or shear zones. The uniaxial compressive strength of the sediments is typically in the range of 50–100 MPa. All nuclear structures for the Darlington project are founded on competent limestone bedrock of the Ordovician age.

As noted earlier, the Precambrian basement rocks at the Darlington site consist

of massive and migmatitic/granitic gneisses of the Grenville Province. While foliation shear and minor alteration along fractures are not uncommon, the basement rocks are generally tight and massive, with a uniaxial compressive strength which is typically twice of that of the Ordovician limestones. Fig. 4 illustrates the in situ horizontal stresses measured at a 300 m deep test hole drilled at the Darlington site. The solid symbols refer to results obtained at shallow depths using the stress-relief, overcoring technique and the United States Bureau of Mines borehole deformation gauge. The open symbols represent data from hydrofracturing tests carried at greater depths in the same test hole. It is clear from Fig. 4 that a state of high horizontal compressive stress prevails at the Darlington site, similar to many other parts of Eastern North America. The horizontal stresses measured also show a trend to increase with depth. For comparison purposes, the pressure due to the weight of the overlying rock is plotted in Fig. 4. Also presented in this figure are the values of hydraulic conductivity measured using a high-precision double packer system. The measured values typically range from 10^{-13} to 10^{-12} m/s, with higher values locally in fracture zones. Both the in situ stresses and the hydraulic conductivity values measured reflect a high degree of compression and watertightness in the rock mass at the Darlington site (Haimson and Lee, 1980; Lee, 1981; Lee and White, 1993, 1994).

4. Design basis earthquake

To determine the Design Basis Earthquake (DBE) for the Darlington Nuclear Power Station, all potential source zones were first identified and evaluated, including seismological zones and known active fault zones (Basham, 1975). For each potential source zone, a design earthquake (DE) was then established based either on a predetermined recurrence rate or the maximum recorded earthquake along with an appropriate safety margin. The peak ground motion parameters for each of these DEs were then determined based on a pertinent set of attenuation equations. The maximum values of the peak ground motion parameters were then used to define the DBE.

Fig. 2 illustrates the distribution of epicentres of historical earthquakes in the region of interest to Darlington seismic design (Basham, 1975). The highest density of seismic events is found in the Western Quebec Zone (WQZ), located northwest of the site (Fig. 2). This seismological zone includes much of the Ottawa-St. Lawrence Valleys. Fault rejuvenation has been postulated to be the main cause of seismicity within this zone (Sanford et al., 1984). For the seismic design of the Darlington station, the WQZ was taken as a major far-field source zone of a seismological nature. Fig. 5 shows the magnitude recurrence relation for the WQZ. A recurrence rate of 1 in 1000 years was adopted for the seismic design of the Darlington station (Basham, 1975), reflecting the state-of-the-art of the mid-1970s. The corresponding Richter magnitude of Design Earthquake #1 (DE 1), due to

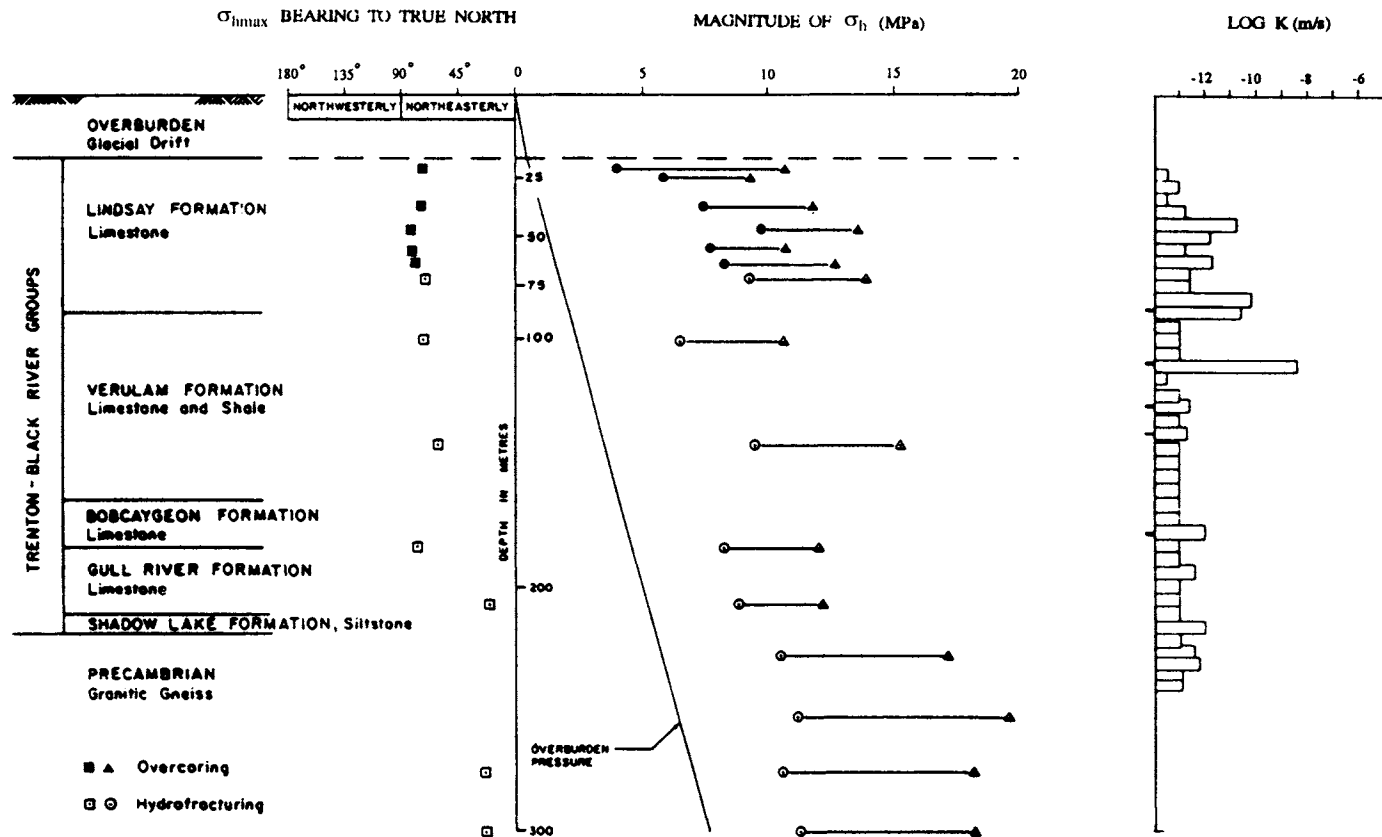


Fig. 4. In situ horizontal stresses and hydraulic conductivity measured at Darlington site.

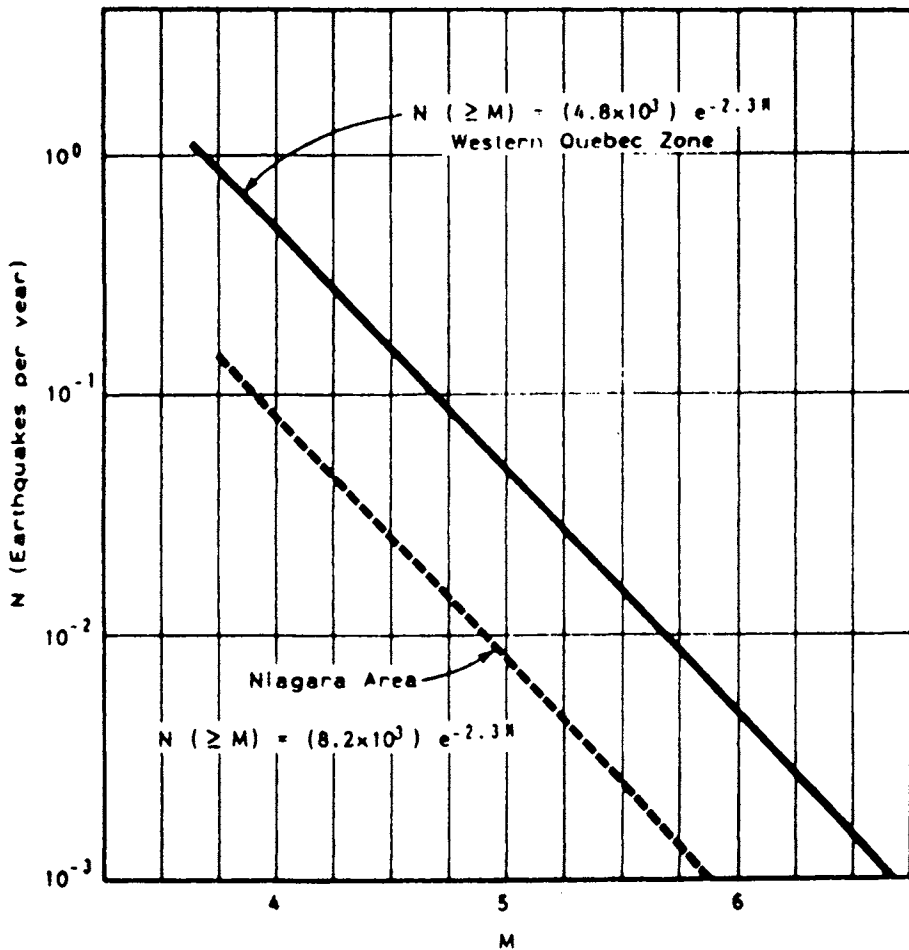


Fig. 5. Magnitude recurrence relations for Western Quebec Zone and Niagara Region (after Basham, 1975).

WQZ, was hence determined as M6.7. The shortest possible distance from the boundary of WQZ to the Darlington site is 200 km.

The second major source zone for the Darlington site is the Clarendon-Linden Fault System in western New York State. As noted earlier, fluid injection and solution mining led to induced seismicity around this fault system since the 1920s, with a maximum event of M5.8 which occurred in 1929. For the Darlington project, Design Earthquake #2 (DE 2) was taken as an M6.5 event, occurring on the fault system and its postulated projection into Lake Ontario, at a point which is closest to the Darlington site. The shortest possible distance to the site is approximately 110 km (Fig. 2).

Design Earthquake #3 (DE 3) is based on the Niagara Region seismological zone, to the south of the site (Fig. 3). The region includes the Clarendon-Linden Fault System as well as the Niagara Peninsula. The magnitude recurrence relation for this region is given in Fig. 5. For a recurrence rate of 1 in 1000 years, a Richter magnitude M6 event was determined for DE 3, at a shortest possible distance of 70 km from the site (Fig. 2).

With the three design earthquakes thus determined, the peak ground motion parameters for the Darlington site could be deduced using an appropriate set of attenuation equations based on strong ground motion statistics. For the Darlington project, the attenuation equations developed by Milne and Davenport (1969) specifically for Eastern Canada were used:

$$a = 0.06 e^{0.92M} R^{-1.38}$$

$$v = 0.43 e^{1.31M} R^{-1.36}$$

$$d = 0.18 e^{1.11M} R^{-1.0}$$

where a =peak acceleration in %g; v =velocity in cm/s; d =displacement in cm; M =Richter magnitude (of design earthquake in this case); $R = \sqrt{\Delta^2 + h^2}$; Δ =epicentral distance in km (i.e. shortest distance to site in this case); h =focal depth in km.

Given the relatively deep-seated nature of intraplate earthquakes in Eastern Canada, a focal depth equivalent to mid-crustal depth was commonly assumed in seismicity studies for Eastern Canada. This assumption was also adopted in the Darlington study.

Table 1 shows the peak ground motion parameters thus calculated for the Darlington site, based on the three DEs and attenuation equations aforementioned. Accordingly, the design basis seismic ground motion (DBSGM) parameters for the Darlington project were determined to be: $a = 0.08$ g; $v = 90$ mm/s; $d = 60$ mm.

The corresponding design base response spectrum, at 5% damping, is illustrated in Fig. 6. These design parameters were used in the seismic qualification of the Darlington nuclear structures and equipment (Tang and Lee, 1993).

The above case study illustrates the methodology used in the mid-1970s for

TABLE I
Design earthquakes and peak ground motion parameters

Design earthquake	Richter magnitude	Epicentral distance (km)	Peak ground motion parameters		
			a (%g)	v (mm/s)	d (mm)
DE 1	6.7	200	0.06	42	30
DE 2	6.5	110	0.07	70	44
DE 3	6	70	0.08	66	40

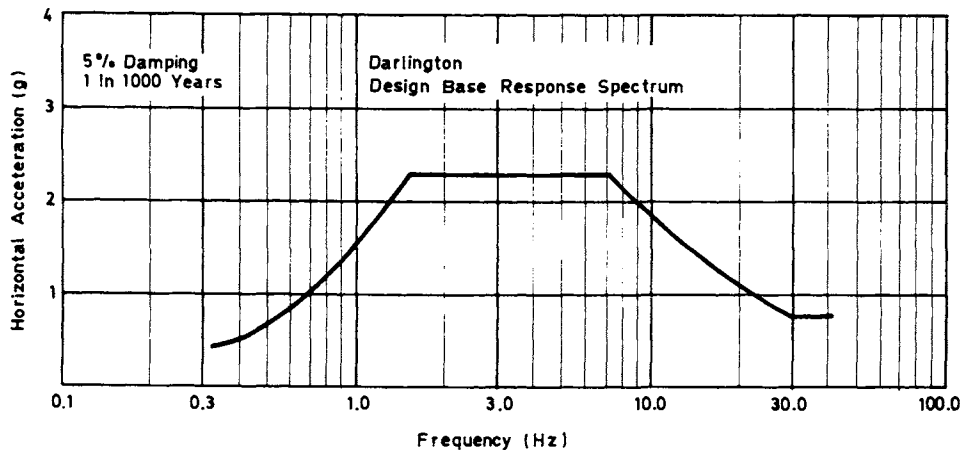


Fig. 6. Design base response spectrum for Darlington Nuclear Generating Station.

establishing the seismic design criteria of a nuclear power station in Eastern Canada. Due considerations were given to the intraplate seismotectonic environment of the region. Unlike the plate-margin situation, there is an absence of major active faults with clearly discernible surface expressions. The design process tends to be influenced more by seismological source zones than by well-defined major active faults. The DBE and design basis seismic ground motion parameters thus selected for the Darlington station are dominated by the relatively near-field Niagara seismological zone, represented by design earthquake DE2. It should be noted that the effect of the Clarendon-Linden Fault System in western New York State, along with its record of induced seismicity, is also reflected in DE2.

The fact that earthquakes occur in Eastern Canada reflects that there are faulting activities occurring at depth in that part of the Earth's crust and mantle. However, because of the prevalence of high horizontal compression, fault propagation may occur in a predominantly horizontal or sub-horizontal direction. This means that the seismogenic faults may or may not have surface expressions. An appreciation of such an intraplate seismotectonic environment is hence required. Otherwise, a large amount of resources could be consumed in fruitless attempts to tract down non-existing surface expressions of seismogenic faults, leading to unnecessary confusion. The state of high horizontal compression does have surface expressions in the form of bedrock surface buckles and pop-ups. However, there is no geomechanical relation between such surficial features and the seismogenic faults at depth (Lee and White, 1994).

5. Concluding remarks

Seismic design of the Darlington Station as outlined in this paper reflects the seismotectonic framework of Eastern Canada, with particular reference to the

intraplate seismotectonic features of the general region. Such features include the prevalence of a state of high horizontal compressive stress in bedrock, largely due to viscoelastic deformation during glaciation. This state of stress facilitates fault propagation in a horizontal rather than vertical direction. Seismicity in Eastern Canada is postulated to be caused mainly by the rejuvenation of faults at depth in response to glacio-isostatic uplift. The prevalent state of stress thus implies that intraplate seismicity may not necessarily be associated with surface rupturing of the seismogenic faults. In other words, the seismotectonic investigation programs should not focus just on the surface expressions of the faults. Without a proper understanding of the intraplate seismic environment, one might risk misinterpreting surficial stress-relief features (such as pop-ups, bedding planes slips and offset boreholes) as neotectonic deformation of seismological significance. These features are simply the surface manifestation of the state of stress in the bedrock, being consistent with its mechanical behaviour and the mechanics of surficial unloading. It follows that for the earthquake-resistant design of nuclear power stations and other critical facilities in Eastern Canada, a proper understanding of the intraplate seismotectonic environment is required.

Acknowledgements

The author is indebted to his many colleagues for their collaboration on seismotectonic studies over a period of almost two decades. He is particularly grateful to Harold Asmis of Ontario Hydro; Peter Basham, John Adams, Ann Stevens and David Forsyth of the Geological Survey of Canada; Gail Atkinson of Carleton University; and Owen White of the Ontario Geological Survey, for sharing their expertise and insights throughout this long (and sometimes challenging) period.

References

- Basham, P.W., 1975. Design basis seismic ground motion for Darlington Nuclear Generating Station A. Seismological Service of Canada, Report 75-16, Earth Physics Branch, Department of Energy, Mines and Resources, Canada, December 1995.
- Berkey, C.P., 1945. A geological study of the Massena-Cornwall earthquake of September 5, 1944 and its bearing on the proposed St. Lawrence River project. United States Engineer Office, New York District.
- Cathles, L.M., 1975. The viscosity of the Earth's mantle. Princeton University Press, 386 pp.
- Easton, R.M., 1992. The Grenville Province and the Proterozoic history of central and southern Ontario. In: Geology of Ontario. Ontario Geol. Surv., Spec. Vol., 4(2): 715-904.
- Easton, R.M. and Carter, T.R., 1991. Extension of Grenville basement beneath southwestern Ontario. Ontario Geol. Surv., Open File Map, 162.
- Engelder, T., Sbar, M.L., Marshak, S. and Plumb, R., 1978. Near surface in situ stress pattern adjacent to the San Andreas Fault, Palmdale, California. Proc. 19th US Rock Mechanics Symposium, pp. 95-101.

- Evernden, J.F., Kohler, W.M. and Clow, G.D., 1981. Seismic intensities of earthquakes of conterminous United States – their prediction and interpretation. U.S. Geol. Surv. Prof. Pap., 1223.
- Fairhurst, C. and Cook, N.G.W., 1966. The phenomenon of rock splitting parallel to the direction of maximum compression in the neighbourhood of a surface. Proc. 1st International Congress on Rock Mechanics, Lisbon, Vol. 1. pp. 687–692.
- Fletcher, J.B. and Sykes, L.R., 1977. Earthquakes related to hydraulic mining and natural seismic activity in Western New York State. *J. Geophys. Res.*, 32(26): 3767–3780.
- Franklin, J.A. and Hungr, O., 1976. Rock stresses in Canada. Proc. 25th Geomechanical Coll., Salzburg, Austria.
- Haimson, B.C. and Lee, C.F., 1980. Hydrofracturing stress determinations at Darlington, Ontario. Proc. 13th Canadian Rock Mechanics Symposium, Toronto, Canada, pp. 42–50.
- Herget, G., 1974. Ground stress determinations in Canada. *Rock Mechanics*, 6: 53–64.
- Herget, G., 1980. Regional stresses in the Canadian Shield. Proc. 13th Canadian Rock Mechanics Symposium, Toronto, Canada, pp. 9–16.
- Lee, C.F., 1978. A rock mechanics approach to seismic risk evaluation. Proc. 19th US Rock Mechanics Symposium, Reno, Nevada, pp. 77–88.
- Lee, C.F., 1981. In-situ stress measurements in southern Ontario. Proc. 22nd US Rock Mechanics Symposium, Cambridge, Massachusetts, pp. 435–442.
- Lee, C.F., 1984. Geotechnical investigations and evaluation of the Darlington site. Ontario Hydro Rep., 1984. (Unpubl.)
- Lee, C.F. and Asmis, H.W., 1979. An interpretation of the crustal stress field in northeast North America. Proc. 20th US Rock Mechanics Symposium, Austin, Texas, Vol. 1. pp. 655–662.
- Lee, C.F. and White, O.L., 1993. Engineering geology in underground aggregate mining and space utilization. *Eng. Geol.*, 35: 247–257.
- Lee, C.F. and White, O.L., 1994. One some goemechanical aspects of high horizontal stress. Proc. 7th IAEG International Congress, Lisbon, 1: 295–302.
- Milne, W.G. and Davenport, A.G., 1969. Distribution of earthquake risk in Canada. *Bull. Seismol. Soc. Am.*, 59: 729–754.
- Mörner, N.A., 1985. Paleoseismicity and geodynamics in Sweden. *Tectonophysics*, 117: 139–153.
- Mörner, N.A., Somi, E. and Zuchiewicz, W., 1989. Neotectonics and paleoseismicity within the Stockholm intracratonal region in Sweden. *Tectonophysics*, 163: 289–303.
- Oliver, J., Johnson, T. and Dorman, J., 1970. Postglacial faulting and seismicity in New York and Quebec. *Can. J. Earth Sci.*, 7: 579–590.
- Paterson, W.S.B., 1972. Laurentide ice sheets: estimated volumes during Late Wisconsin. *Rev. Geophys.*, 10: 885–917.
- Rutledge, F., 1983. Darlington Generating Station-Regional Structural Geology Study. Ontario Hydro Rep., 1983. (Unpubl.)
- Sanford, B.V., Thompson, F. and McFall, G., 1984. Phanerozoic and recent tectonic movements in the Canadian Shield and their significance to the Nuclear Fuel Waste Management Program. Proceedings, Workshop on Transitional Processes. Atomic Energy of Canada Limited Rep., 7822, pp. 73–96.
- Sbar, M.L. and Sykes, L.R., 1973. Contemporary compressive stress and seismicity in Eastern North America: an example of intraplate tectonics. *Bull. Geol. Soc. Am.*, 84: 1861–1882.
- Sykes, L.N., 1978. Earthquakes and recent tectonics of Eastern North America: Reactivation of old zones of weakness. Symposium on Intraplate Seismicity and Tectonics in Eastern North America, Toronto, 1978.
- Tang, J.H.K. and Lee, C.F., 1993. Seismic design of Ontario Hydro nuclear generating stations. Ontario Hydro Rep., May 1, 1993.
- Tullis, T.E., 1977. Stress measurements in shallow overcoring on the Palmdale uplift. *EOS Trans. Am. Geophys. Union*, 58: pp. 1122.
- Van Tyne, A.M., 1975. Subsurface investigation of the Clarendon-Linden structure, western New York. Geological Survey, New York State Museum and Science Service, Open-File Rep., May 15, 1975.
- White, O.L., Karrow, P.F. and MacDonald, J.R., 1973. Residual stress relief phenomena in southern Ontario. Proc. 9th Canadian Rock Mechanics Symposium, Montreal, pp. 323–348.

Direct ESR dating of fault gouge using clay minerals and the assessment of fault activity

TATSURO FUKUCHI

*Institute of Earth Sciences, Faculty of Liberal Arts, Yamaguchi University, 1677-1 Yoshida,
Yamaguchi 753, Japan*

Abstract

The ESR dating method has been applied to the fault gouge of the Nojima Fault, the outcrop of which arose due to the southern Hyogo Prefecture Earthquake on January 17th, 1995, and to the fault gouge of the Median Tectonic Line (MTL) which is a major active fault in Japan, without considering the resetting of ESR signals. The ESR ages obtained for clay minerals in the fault gouges are considered to indicate the age of the beginning of the fault movements at the outcrop. Assuming no radon loss and the general values of water content and α -ray efficiency, the ESR ages of the fault gouges of the Nojima Fault and MTL are estimated as 0.55–1.16 and 6.76–9.28 Ma, respectively. The ESR age of the Nojima Fault is consistent with the age of the beginning of the Rokko Movements in the Kinki districts estimated geologically. On the other hand, the ESR age obtained from the MTL is younger than the K-Ar age (about 11 Ma), which is presumably overestimated due to the existence of the source minerals in the K-Ar dating sample. Since it is geologically known that the MTL at the outcrop had moved until the Late Pleistocene-Holocene, the fault movement of the MTL at this outcrop probably began at 6.76–9.28 Ma B.P. after the intrusion of the felsitic dyke (12–16 Ma) which is the source rock of the fault gouge into the fault boundary. The ESR dating of clay minerals in the fault gouge may be effective for assessing fault activity if no Quaternary deposit exists at the outcrop. The younger the ESR age of the fault gouge is, the higher the fault activity is. If not indurated and the freshest clay gouge can be collected at the outcrop, the ESR age of the most recent fault movement may be obtained from the clay gouge.

1. Introduction

Electron spin resonance (ESR) dating has been applied to quartz grains from the fault gouge for assessing fault activity. The ESR method is originally based on the complete resetting of ESR signals in the quartz grains at the time of fault movement (Ikeya et al., 1982; Miki and Ikeya, 1982). In regard to the resetting of ESR signals, two mechanisms have been considered: one is mechanical crushing or sliding; the other is thermal annealing of defects by frictional heat.

Fukuchi (1992) determined the complete resetting condition by combining the thermal conduction equation on frictional heat (McKenzie and Brune, 1972) with decay curves of ESR signals, and indicated that ESR signals can never be completely reset under normal stresses less than 6.8 MPa at a displacement of 1 m. On the other hand, Ariyama (1985) and Tanaka (1990) formerly reported that ESR signals could be completely reset by shearing at a displacement of 1 m even under normal stresses less than 1.0 MPa, using a ring-type shearing apparatus. However, Tanaka's shearing apparatus made of stainless steel has some problems, and ESR signals in quartz grains are clarified to be minimally reset using a ceramics apparatus (Hataya and Tanaka, 1993). Thus, most of the resetting experiments indicate that ESR signals in quartz are partially or minimally reset by mechanical crushing, grinding or shearing (Miki and Ikeya, 1982; Sato et al., 1985; Fukuchi et al., 1986; Buhay et al., 1988; Lee and Schwarcz, 1993; Hataya and Tanaka, 1993). Therefore, in order to determine the ages of fault movements by ESR, fault gouge samples must be collected from deep underground, where the complete resetting of the ESR signals by frictional heat is expected, using a boring machine.

Recently, Fukuchi (1992, 1993) proposed a new ESR dating method of fault movements, by which ESR ages might be directly determined from lattice defect centres created freshly in quartz by fracturing or deformation. In this paper, I propose another direct ESR dating method using clay minerals in fault gouge.

2. Samples

Fault gouge samples were collected from the outcrops (Fig. 1) of the Nojima (Earthquake) Fault at Nojima-Hirabayashi on Awaji Island, which moved during the southern Hyogo Prefecture Earthquake on January 17th, 1995 (Lin et al., 1995), and from the Median Tectonic Line (MTL) at Urayama-kawa in Ehime Prefecture (Takahashi, 1992). Fig. 2 shows photographs of the outcrops of the Nojima Fault and MTL. The fault gouge of the Nojima Fault is derived from a body of the Older Ryoke granitoids produced in the Cretaceous period. The fault sample was collected as 1–2 cm thick sheets from the fault plane (Figs. 2A and 3A). This fault gouge was not indurated so much. The recent clay or soil attached on the fault gouge was removed and washed out with water. On the other hand, the fault gouge of the MTL is derived from both black schist (lower block) in the Sanbagawa Metamorphic zone and felsitic dyke (upper block) intruded into the fault boundary (the MTL boundary) between the Sanbagawa zone and the Izumi zone. For ESR measurements, the gouge of felsitic dyke was collected from the 2–3 cm thick layer contacting with the fault plane (Figs. 2B and 3B). This fault gouge is completely indurated and is considered to be older than the fault gouge of the Nojima Fault. The fault gouge samples collected were first screened into <38 µm and ≥38 µm by the wet method. Next, the samples screened to <38 µm were further sieved into <2, 2–8, 8–20 and 20–38 µm by (Millipore) filters using a vacuum pump.

Fig. 4 shows X-ray powder diffraction patterns of grains taken from the fault

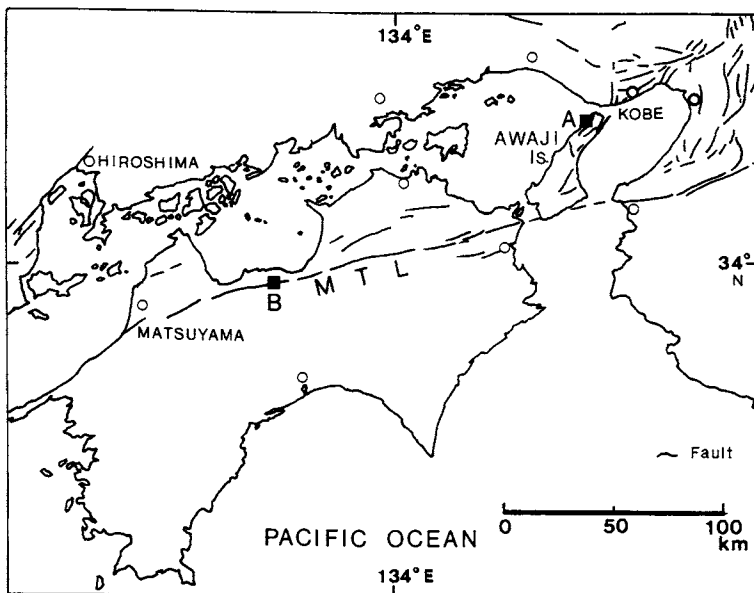


Fig. 1. Locality map of the Nojima Fault (A) and MTL (B).

gouge of the Nojima Fault. The fault gouge consists mainly of quartz, plagioclase, K-feldspars, montmorillonite, kaolinite and laumontite. The X-ray diffraction peaks of quartz and feldspars decrease with decreasing grain size, whereas the peaks of montmorillonite and kaolinite increase. Therefore, the montmorillonite and kaolinite were presumably produced by weathering of the feldspars. The outcrop of the Nojima Fault was exposed by faulting during the southern Hyogo Prefecture Earthquake. However, it has been found by a trenching survey that the displacement of the Nojima Fault occurred along the fault plane formed by its previous movements, which had occurred at least twice since the Holocene (Suzuki et al., 1995). At the outcrop of the Nojima Fault, the Cretaceous granitoid contacts with the Iwaya Formation of Middle-Late Miocene distributed below the recent deposits. Therefore, the age of fault plane formation is considered to be older than Holocene. Since the outcrop is located near the ground surface, and furthermore the fault gouge contains much water, the resetting of ESR signals is hardly expected.

Fig. 5 shows X-ray powder diffraction patterns of the fault gouge samples out of the MTL. The peaks of quartz and K-feldspars decrease with decreasing the grain size, whereas the peaks of illite and kaolinite increase. Therefore, these clay minerals are considered to have been produced from the feldspars. In the case of the fault gouge of the MTL, the crystal growth of clay minerals in the fault gouge proceeds with most of it consisting of illite and kaolinite of 8–20 µm grain size (Fig. 5). These clay minerals are usually prominent at grain sizes less than 2 µm. The larger grains in the MTL fault gouge indicate that the fault gouge is relatively old. Another

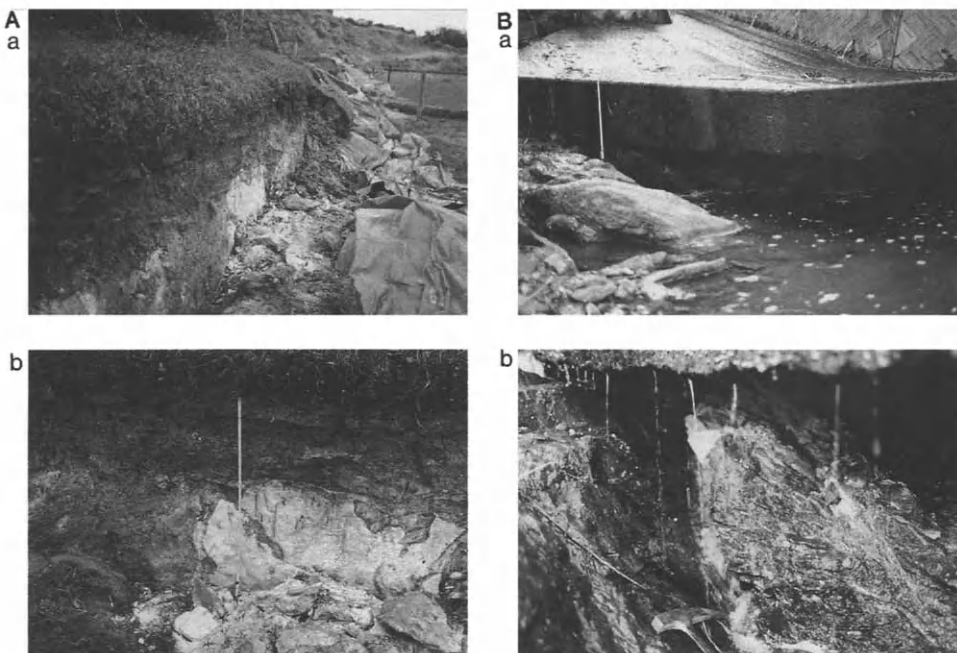


Fig. 2. Photographs of the outcrops of the Nojima Fault (A) and MTL (B). (A) Strike: N38°E; Dip: 80°W; Striations: 20°SW. (B) Strike: N81°E; Dip: 47°N.

felsitic fault gouge formed in the fracture zone of the MTL has been dated at about 11 Ma by K-Ar dating, furthermore the felsitic dyke which is the source rock of these fault gouges is also dated at 12–16 Ma (Takagi and Shibata, 1992). The grain size of clay minerals may be useful as a tentative indicator of fault activity and further studies on the grain size are expected.

3. Experimental

ESR measurements were conducted at room temperature using a JEOL FE1X ESR spectrometer with 100 kHz field modulation. The samples sieved were soaked in 10–36% HCl for 1 h to 2 days in order to remove impurities, and each sample of 100 mg was used for ESR measurements. The *g*-values of ESR signals were determined in comparison with those of the Mn²⁺ signals in MnO. Artificial irradiation for the determination of total doses (TD values) was carried out with characteristic X-rays from a Cu target tube (K_{α} : wavelength = 1.54 Å). The doses were calibrated by irradiating the same samples with γ -rays. The γ -ray irradiation was done with a ⁶⁰Co source. The concentrations of uranium, thorium and K₂O needed for the calculation of annual doses were determined by ICP-MS spectrometry

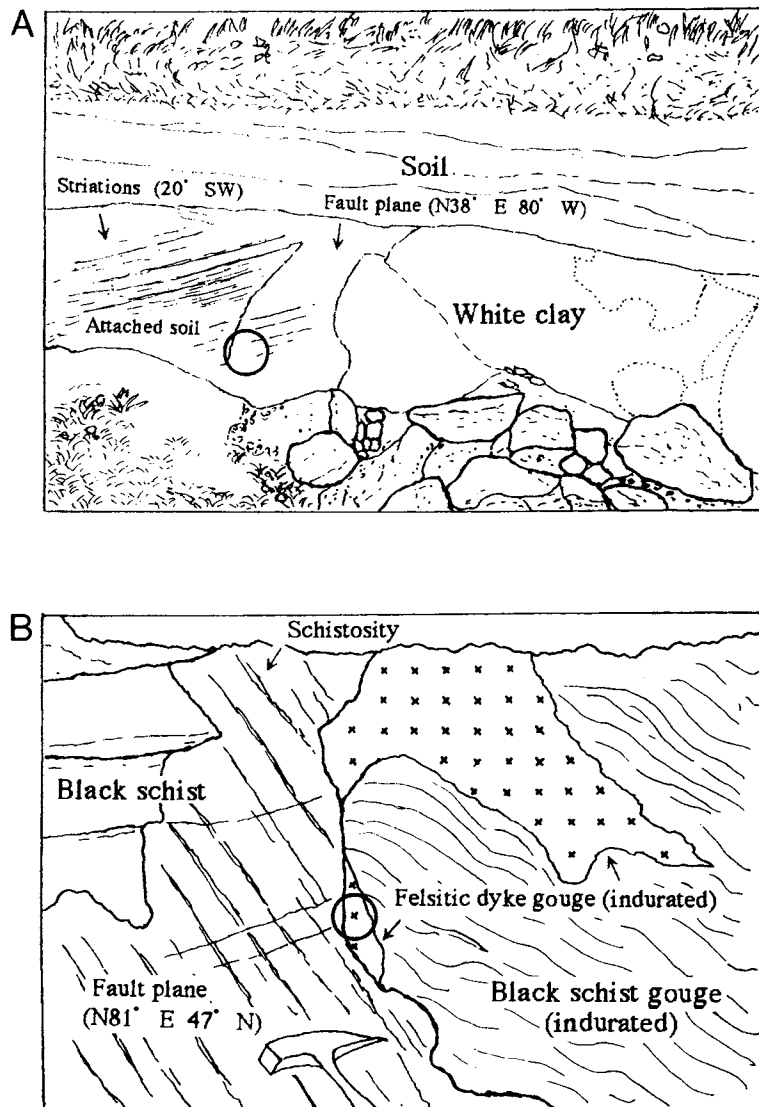


Fig. 3. Sketches showing the sampling points of the fault gouges of the Nojima Fault (A) and MTL (B). The fault gouge samples were collected from the circles in the figures. The sketches correspond to Figs. 2A(b) and 2B(b), respectively. (A) Recent soil is attached on the fault surface due to the movement during the southern Hyogo Prefecture Earthquake. The white clay was used for ESR dating. (B) The yellowish felsitic dyke gouge along the fault plane was used for ESR dating. The hammer is put on the fault plane.

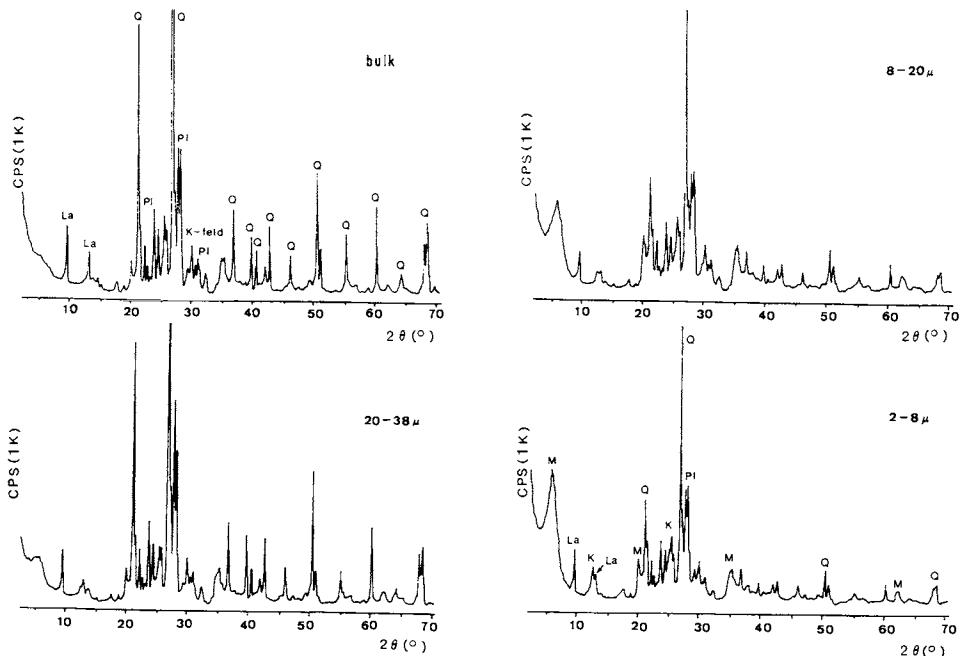


Fig. 4. X-ray powder diffraction patterns obtained from the fault gouge of the Nojima Fault. Q, quartz; Pl, plagioclase; K-feld, K-feldspars; La, laumontite; K, kaolinite; M, montmorillonite. Target: Cu, voltage and current, 40 kV 20 mA; response: 1 s; slits: DS 1 RS 0.15 SS 1; scan speed: 2°/min.

and atomic absorption spectrophotometry (Imai, 1990a, b). The annual doses were calculated using the conversion table of Nambi and Aitken (1986).

4. Results and discussion

Fig. 6 shows ESR spectra of clay minerals obtained from the fault gouges of the Nojima Fault and MTL. A quartet signal (Signals A–D), E' and peroxy centres are detected from the fault gouge sample of the Nojima Fault. The quartet is considered to be due to a hydroxyl radical (HOHC ; $\text{Si}-\text{O}^{\cdot}\text{H}$) binding with a H_2O^+ ion in montmorillonite. Three hydrogen atoms ($I=1/2$) in this radical splits a single line into quartet with the intensity ratio of 1:3:3:1 by hyperfine interaction (Fukuchi, 1995). Signal B is often overlapped by another ESR signal. These signals are considered to be applicable to dating of less than 10–20 Ma. The E' and peroxy centres are intrinsic ESR centres in quartz. The E' centre is ascribed to an electron trapped at an oxygen vacancy site (McMorris, 1967, 1969; Yip and Fowler, 1975) and is often used for ESR dating of fault movements. The E' centre was first used for the dating of faults by Ikeya et al. (1982). The peroxy centre is ascribed to a hole trapped at an interstitial oxygen in quartz ($\text{Si}-\text{O}-\text{O}^{\cdot}$) (Friebele et al., 1979;

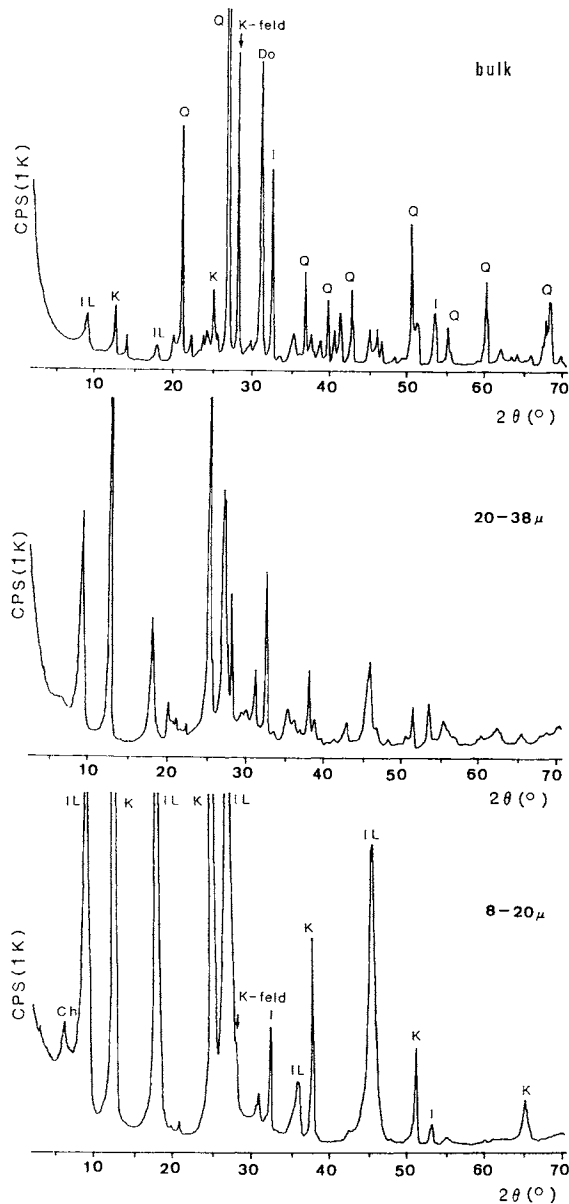


Fig. 5. X-ray powder diffraction patterns obtained from the fault gouges of the MTL. Q, quartz; K-feld, K-feldspars; K, kaolinite; IL, illite; I, ilmenite; Do, dolomite; Ch, chlorite. The conditions for measurement are the same as Fig. 4.

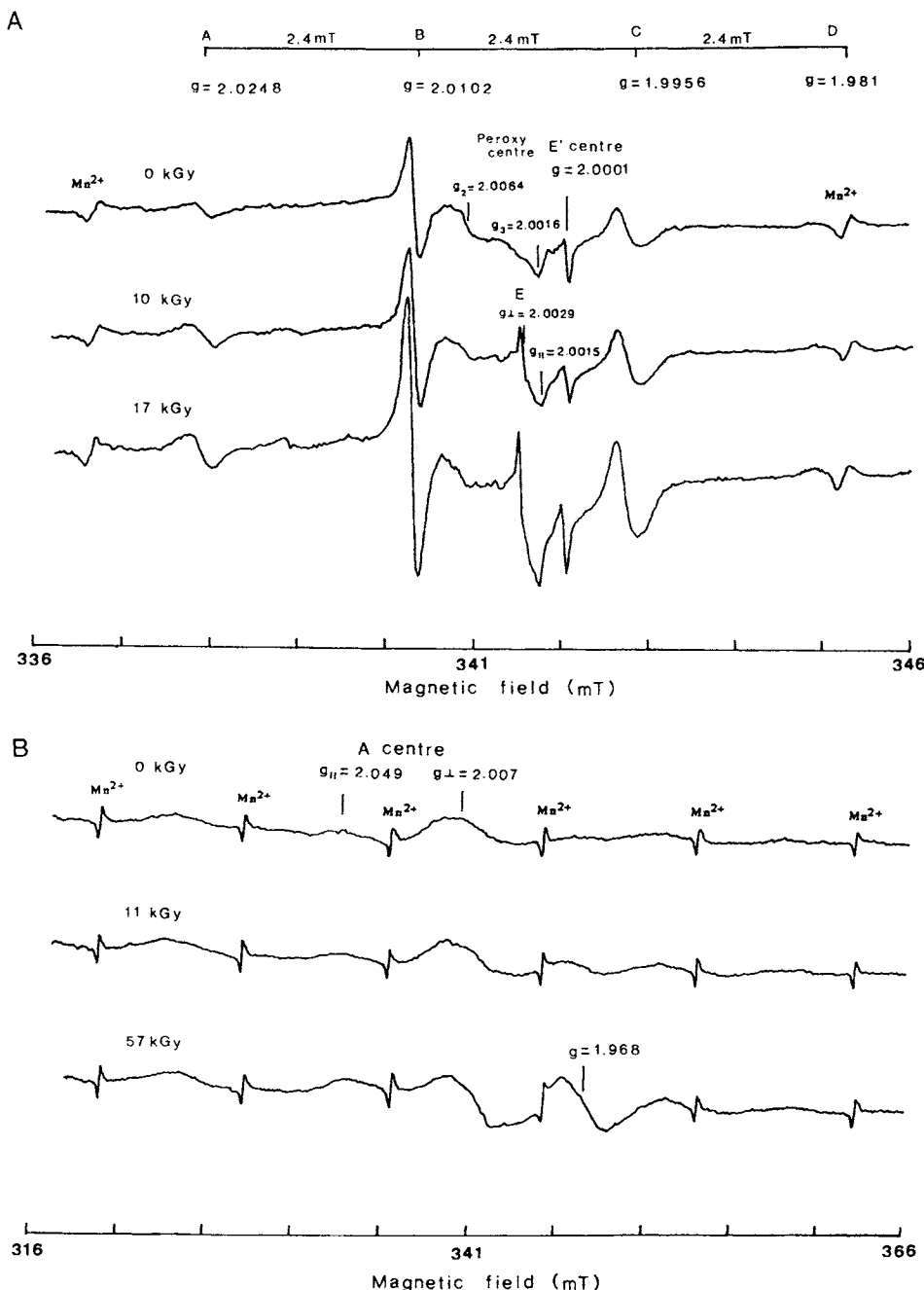


Fig. 6. ESR spectra obtained from the fault gouges of the Nojima Fault (A) and MTL (B). Microwave frequency: 9.44 GHz; temperature: RT; microwave power: 1 mW; modulation width: 100 kHz 0.05 mT; Response: 0.3 s; sweep time: 8 min.

Griscom, 1979; Stapelbroek et al., 1979). This centre hardly increases by natural γ -rays. A signal (Signal E) is detected only after artificial irradiation. This signal is considered to be due to CO_3^{3-} radicals, and may be usable as a dating signal although it has low thermal stability (Fukuchi, 1995).

On the other hand, some ESR signals are detected in the fault gouge samples of the MTL. The ESR signal at $g=2.007$ is identified as A centre ($g\parallel=2.049$, $g\perp=2.007$) which may be ascribed to a hole trapped at bridging oxygens stabilized by divalent cations in the silica layer of kaolinite (Angel et al., 1974; Muller and Calas, 1989; Ildefonse et al., 1990, 1991). The A centre is considered to be stable over a geological period of 1 Ga (Ildefonse et al., 1990, 1991). The signal at $g=1.968$ is an unidentified centre and is usually not detected in kaolinite.

Fig. 7 shows the intensity changes of Signals A–D and the E' centre obtained from the fault gouge of the Nojima Fault and the A centre from that of the MTL by artificial irradiation. The intensities of these signals increase with increasing radiation doses. The total doses (TD values) of natural radiation are determined by extrapolating the regression curves obtained from the data points using the least-square fitting method. The TD value obtained from Signals A–D from the Nojima Fault is estimated to be about 11.3–12.8 kGy and that from the E' centre to be 37.9 kGy using the fault gouge of 2–8 μm in grain size, whereas that from the A centre of the MTL is 24.7 kGy for grains of <20 μm . The TD values obtained for Signals A–D and the A centre are considered to give the total dose since the formation of the clay minerals. The TD value from the E' centre in quartz does not always give the total dose since the formation of the Older Ryoke granitoid which is the source rock of the fault gouge of the Nojima Fault. If the E' centre was completely reset at the time of a fault movement, the TD value may give the total dose which corresponds to the accumulated dose since the first movement of the Nojima Fault. As the TD value for the E' centre is much larger than those for Signals A–D, the E' centre seems to have been incompletely reset by the former fault movements before the southern Hyogo Prefecture Earthquake. Generally, older fault gouge samples tend to give larger TD values, as is suggested from the TD values for Signals A–D and the A centre, therefore the TD value obtained from the fault gouge may be useful as an indicator of fault activity in addition to the grain size of clay minerals.

ESR ages are obtained by dividing the TD value by the annual dose (D): ESR Age = TD/ D . The ESR method is almost established as a radiation dosimeter as well as a thermoluminescence dosimeter (TLD) (Ikeya, 1994). However, the accuracy of ESR ages strongly depends on the material used, and one of the most important issues in ESR dating is how to evaluate the annual dose.

The concentrations of uranium, thorium and K_2O estimated from the fault gouges of the Nojima Fault and MTL are shown in Table 1. In the case of the Nojima Fault, the concentrations of uranium and thorium increase with decreasing the grain size of the fault gouge constituents, whereas the concentration of K_2O is almost independent. On the other hand, the concentrations of radioactive elements decrease by treating the grains of 8–20 μm in 36% HCl for 2 days to about 1/10 of those

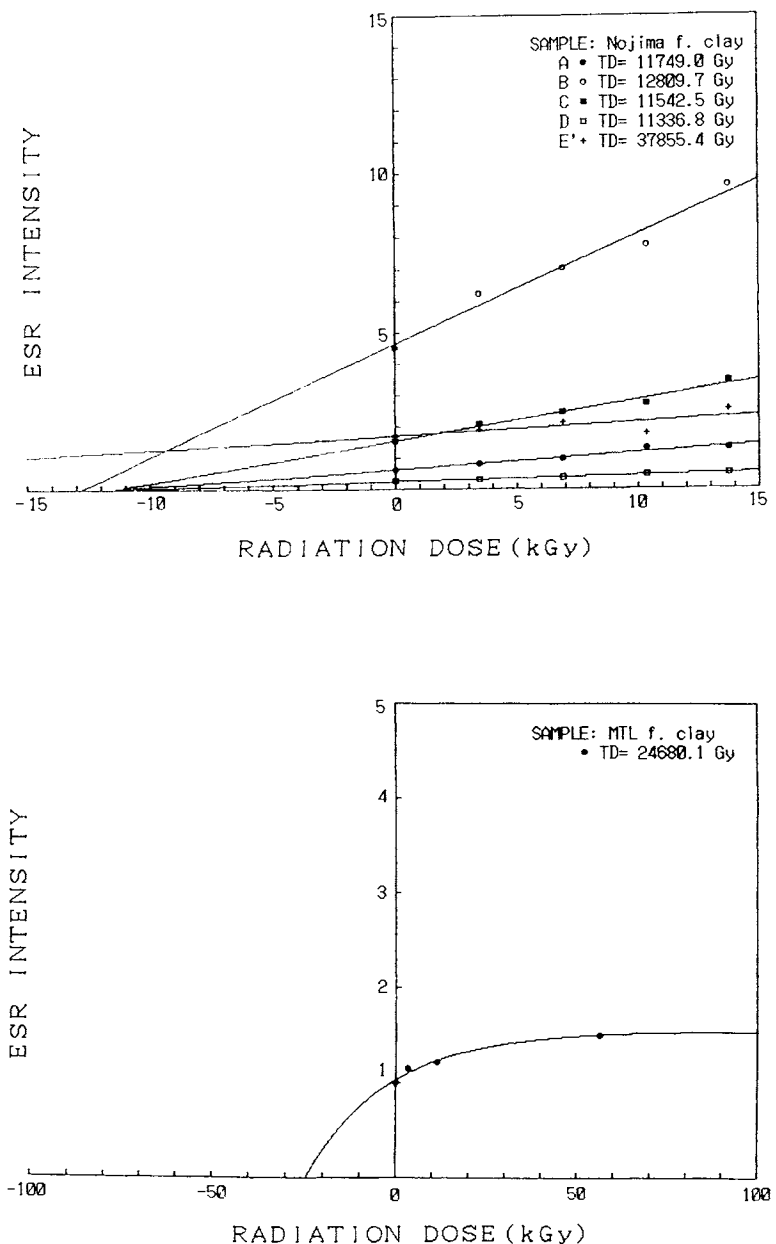


Fig. 7. Changes of the signal intensities of Signals A-D and the E' centre of the Nojima Fault (A) and the A centre of the MTL (B) by artificial irradiation, and the TD values obtained by extrapolating the regression curves.

TABLE I

Concentrations of uranium, thorium and K_2O obtained from the fault gouges of the Nojima Fault and MTL

Sample	Grain size (μm)	U (ppm)	Th (ppm)	K_2O (%)
Nojima Fault	<38	10.00	13.19	3.58
	8–20	15.94	22.57	3.39
	8–20 ^a	1.36	0.71	2.24
	<8	19.49	25.06	3.23
MTL	<38	0.16	0.10	3.63
	<20	0.12	0.06	4.05

^aSoaked in 36% HCl for 2 days.

before the treatment. This presumably indicates that most of uranium and thorium adhere around the clay minerals or quartz grains. The concentrations obtained from the fault gouge of the MTL do not change so much with decreasing the grain size.

When determining the annual dose from the concentrations of radioactive elements in the fault gouge, water content, defect creation efficiency by α -rays (k -value) and radioactive disequilibrium must be considered because these factors influence the annual dose evaluation. Table 2 shows annual doses calculated from the fault

TABLE II

Annual doses calculated from the radioactive elements in the fault gouges of the Nojima Fault and MTL

Sample	Grain size (μm)	Water content(%)							
		0		10		20		30	
		k	k	k	k	k	k	k	k
		0.05	0.15	0.05	0.15	0.05	0.15	0.05	0.15
Nojima Fault	<38	8.69	12.4	7.74	11.0	6.98	9.88	6.36	8.96
	8–20	12.0	18.1	10.7	16.0	9.63	14.3	8.77	13.0
	<8	13.6	20.8	12.1	18.4	10.9	16.5	9.92	14.9
MTL	<38	3.26	3.31	2.92	2.96	2.63	2.67	2.40	2.44
	<20	3.61	3.65	3.23	3.26	2.92	2.95	2.66	2.69
<i>No radon loss ($\times 10^{-3}$ Gy/year)</i>									
Nojima Fault	<38	5.04	6.71	4.49	5.94	4.04	5.33	3.68	4.84
	8–20	6.08	8.79	5.40	7.76	4.86	6.95	4.42	6.29
	<8	6.51	9.74	5.78	8.59	5.20	7.69	4.73	6.96
MTL	<38	3.21	3.24	2.87	2.89	2.59	2.61	2.37	2.38
	<20	3.57	3.59	3.19	3.21	2.89	2.90	2.63	2.65
<i>100% radon loss ($\times 10^{-3}$ Gy/year)</i>									
Nojima Fault	<38	5.04	6.71	4.49	5.94	4.04	5.33	3.68	4.84
	8–20	6.08	8.79	5.40	7.76	4.86	6.95	4.42	6.29
	<8	6.51	9.74	5.78	8.59	5.20	7.69	4.73	6.96
MTL	<38	3.21	3.24	2.87	2.89	2.59	2.61	2.37	2.38
	<20	3.57	3.59	3.19	3.21	2.89	2.90	2.63	2.65

k , the defect creation efficiency by α -rays (k -values).

gouges, assuming the general values of water content and k -value. Though the water contents of the fault gouges of the Nojima Fault and MTL were approximately estimated to be 10–20% by weighing, those may vary with the seasons. The k -value depends on the material. For example, the k -value of quartz is 0.07 and most silicate and carbonate minerals take values from 0.05 to 0.15 (Ikeya, 1994). Thus, in this paper, the annual doses were calculated using a water content of 0–30% and a k -value of 0.05–0.15. Generally, the higher the k -value or the lower water content is, the larger the annual dose becomes. When the water content is Δ and k -value is k , the annual dose (D) is expressed as follows (Hennig and Grün, 1983):

$$D = kD\alpha/(1 + 1.49\Delta) + D\beta/(1 + 1.25\Delta) + D\gamma/(1 + \Delta)$$

where $D\alpha$, $D\beta$ and $D\gamma$ are the annual doses by α , β and γ rays, respectively.

In regard to the disequilibrium of radioactive elements, we have no direct method of monitoring the migration of radioactive elements during the geological age. However, if uranium and thorium once adhere around the clay minerals, they may remain adhesive and unchanged during the Quaternary period. In addition, the evolution of radon gas from the fault zone also is well known. Radon gas is evolved when the minerals are crushed by faulting or weathered by alteration. Radon easily dissolves in water and excess radon may concentrate in the fault gouge. Thus, there still remain some problems on the disequilibrium of radioactive elements and these problems must be clarified in future by analyzing in detail radioactive elements in the fracture zone. In Table 2, annual doses assuming no (0%) and 100% radon losses are shown.

ESR ages of the Nojima Fault and MTL are obtained by dividing the TD values shown in Fig. 7 by the annual doses. Since the TD values of the Nojima Fault and MTL were determined from the fault gouges of 2–8 and 8–20 μm in grain size, respectively, the annual doses obtained from the fault gouges of <8 and <20 μm (Table 2) were used for the calculation of the ESR ages. In Table 3, the ESR ages at a water content of 0–10% and a k -value of 0.05 and 0.15 are shown. The ESR age of the fault gouge of the Nojima Fault is estimated as 0.55–1.16 Ma for Signals A, C and D, while that of the MTL as 6.7–9.28 Ma for the A centre. If 100% radon loss is assumed, the ages are 1.19–2.44 and 6.87–9.37 Ma, respectively. In the case of the MTL, since the concentrations of uranium and thorium in the fault gouge are low, there is only a small difference between the ESR ages of no radon loss and 100% radon loss or of $k=0.05$ and 0.15. This indicates that the lower the concentrations of uranium and thorium in the fault gouge is, the more exactly the ESR age can be determined.

As mentioned above, the ESR ages obtained from the fault gouges do not correspond to the most recent fault movements of the Nojima Fault and MTL, but to the formation of the fault gouges. The formation of the fault clay gouges is considered to have begun by fracturing of the source rocks. Generally, the formation of montmorillonite and kaolinite are mainly caused by hydrothermal alteration or weathering of feldspars or micas. According to experiments on hydrothermal synthesis (The Clay Science Society of Japan, 1987), these clay minerals grow by

TABLE III
Total doses and ESR ages obtained from the fault gouges of the Nojima Fault and MTL

Sample	ESR signal	TD (kGy)	Water content (%)							
			0		10		20		30	
			<i>k</i>	<i>k</i>	<i>k</i>	<i>k</i>	<i>k</i>	<i>k</i>	<i>k</i>	<i>k</i>
			0.05	0.15	0.05	0.15	0.05	0.15	0.05	0.15
Nojima Fault	<i>No radon loss</i> ($\times 10^4$ year)									
	A	11.7	86.6	56.4	97.2	63.8	107.9	71.2	118.5	78.6
	B	12.8	94.4	61.5	106.0	69.6	117.6	77.7	129.2	85.7
	C	11.5	85.0	55.4	95.5	62.7	106.0	70.0	116.4	77.3
	D	11.3	83.5	54.4	93.8	61.6	104.1	68.7	114.3	75.9
	E' center	37.9	278.9	181.6	313.3	205.6	347.6	229.5	381.8	253.4
MTL	A center	24.7	683.5	676.4	765.0	757.3	846.4	838.0	927.7	918.6
<i>100% radon loss</i> ($\times 10^4$ year)										
Nojima Fault	A	11.7	180.5	120.6	203.2	136.7	225.9	152.7	248.5	168.7
	B	12.8	196.8	131.5	221.6	149.0	246.3	166.5	271.0	184.0
	C	11.5	177.3	118.5	199.7	134.3	221.9	150.0	244.2	165.8
	D	11.3	174.2	116.4	196.1	131.9	218.0	147.4	239.8	162.8
	E' center	37.9	581.6	388.5	654.8	440.4	727.9	492.1	800.7	543.7
	MTL	A center	24.7	690.5	687.3	772.8	769.3	855.1	851.2	937.2

hydrothermal reaction in a short time (from a few months to a few years) relative to the geological age. Even though some thousands of years were spent for the synthesis of montmorillonite or kaolinite, it would be almost within the limits of error in dating. A more important fact is that the hydrothermal reaction does not continue eternally and terminate in time. Since the source minerals which react with hydrothermal water would be depleted, reaction rims formed around the source minerals may prevent further hydrothermal reactions. The source minerals in the fracture zone have larger reaction areas with water because they are downsized by faulting, therefore the clay mineralization may easily progress and terminate after a relatively short time. Thus, the ESR age for clay minerals in the fault gouge may show the beginning of fault movements at the outcrop.

According to Fujita (1995), the Rokko Movements around the Rokko mountains in the Kinki districts, including the fault movements of the Nojima Fault, are considered to have started in the middle Quaternary period and to have become more active after Middle Pleistocene. Therefore, the ESR age of the fault gouge of the Nojima Fault, 0.55–1.16 Ma, is consistent with the age of the beginning of the Rokko Movements estimated geologically. On the other hand, the felsitic fault gouge of the MTL at Urayama-kawa has been dated to be about 11 Ma by the K-Ar method (Takagi and Shibata, 1992). However, the gouge sample used for the K-Ar dating may contain the source minerals such as quartz and feldspars besides

kaolinite and illite, therefore the K-Ar age may be overestimated. The ESR age of the MTL is younger than the K-Ar age: 6.76–9.28 Ma. In the case of the ESR dating of clay minerals, the ESR signals coming from clay minerals are clearly distinguished from those in quartz or the other source minerals, and the age corresponds to the formation of clay minerals.

According to Takahashi (1992), the outcrop where the MTL cuts gravel beds of Late Pleistocene-Holocene was previously observed at Urayama-kawa and the MTL at Urayama-kawa had moved until Late Pleistocene-Holocene. Therefore, the fault movements of the MTL at Urayama-kawa may have again begun at 6.76–9.28 Ma B.P. after the intrusion of the felsitic dyke (12–16 Ma) into the fault boundary.

The direct ESR dating of fault gouge is effective for the assessment of fault activity if no Quaternary deposit exists at the outcrop. Then, the ESR age obtained from the fault gouge does not mean the most recent fault movement, but the beginning of the fault movements at the outcrop. When the age of the beginning is younger than 1–2 Ma, the fault is concluded to be an active fault. The younger the ESR age of the fault gouge is, the higher the fault activity is. Therefore, if not indurated and the freshest clay gouge can be collected at the outcrop, the age of the most recent fault movement may be obtained from the clay gouge.

5. Conclusions

The direct ESR dating of the fault gouges obtained from the Nojima Fault and MTL was carried out using ESR signals in montmorillonite and kaolinite. The ESR ages of the clay minerals in fault gouges of the Nojima Fault and MTL were estimated to be 0.55–1.16 and 6.76–9.28 Ma, respectively, assuming no radon loss and the general values of water content and α -ray efficiency (k -value). The ESR age from the Nojima Fault is consistent with the age of the beginning of the Rokko Movements in the Kinki districts estimated geologically, while the age from the MTL is younger than the K-Ar age (about 11 Ma) reported previously, which is presumably overestimated due to the existence of the source minerals besides clay minerals in the dating sample. The direct ESR dating of fault gouge may be effective for the assessment of fault activity if no Quaternary deposit exists at the outcrop. The age of the most recent fault movement may be obtained from not indurated and the freshest clay gouge.

Acknowledgements

I thank Professor H. Taniguchi for his support in using the ESR spectrometer, Dr. N. Imai for his help in chemical analysis of radioactive elements by ICP-MS and Dr. T. Kojima for his cooperation in γ -irradiation with a ^{60}Co source. I wish to thank Dr. A. Lin for his suggestions in collecting the fault samples, Professor T. Miki for his discussions and comments and Ms. N. Fukuchi for her assistance in

making the manuscript. The idea of direct ESR dating by using clay minerals in fault gouge came across my mind when I studied as a research student at Osaka University from October in 1993 to March in 1994. I am grateful to Professor M. Ikeya for his support and helpful discussions. This work was partly supported by a Grant-in-Aid for Scientific Research (No. 07238217) from the Ministry of Education, Science and Culture of Japan.

References

- Angel, B., Jones, J.P.E. and Hall, P.L., 1974. Electron spin resonance studies of doped synthetic kaolinite, *I. Clay Miner.*, 10: 247–255.
- Ariyama, T., 1985. Conditions of resetting the ESR clock during faulting. In: M. Ikeya and T. Miki (Editors), *ESR Dating and Dosimetry*. IONICS, Tokyo, pp. 251–258.
- Buhay, W.M., Schwarcz, H.P. and Grün, R., 1988. ESR dating of fault gouge: the effect of grain size. *Q. Sci. Rev.*, 7: 515–522.
- Friebel, E.J., Griscom, D.L. and Stapelbroek, M., 1979. Fundamental defect centers in glass: the peroxy radical in irradiated high-purity fused silica. *Phys. Rev. Lett.*, 42: 1346–1349.
- Fujita, K., 1995. Hyogoken-nanbu Earthquake from the view-point of the Quaternary Tectonic of Kinki – I saw the 'Rokko Movements' in the Earthquake of Kobe. *Chishitsu News*, 490: 7–13.
- Fukuchi, T., 1992. ESR studies for absolute dating of fault movements. *J. Geol. Soc. London*, 149: 265–272.
- Fukuchi, T., 1993. Vacancy-associated type ESR centers observed in natural silica and their application to geology. *Appl. Radiat. Isotopes*, 44: 179–184.
- Fukuchi, T., 1995. Quartet ESR signals detected from natural clay minerals and their applicability to radiation dosimetry and dating. *Jpn. J. Appl. Phys.*, submitted.
- Fukuchi, T., Imai, N. and Shimokawa, K., 1986. ESR dating of fault movement using various defect centres in quartz; the case in the western South Fossa Magna, Japan. *Earth Planet. Sci. Lett.*, 78: 121–128.
- Griscom, D.L., 1979. Point defects and radiation damage processes in α -quartz. *Proc. 33rd Frequency Control Symp.*, 98–109.
- Hataya, R. and Tanaka, K., 1993. Examination on applicability of ESR dating of fault movements – Re-examination on perfect annealing of ESR signals in quartz. *Abstracts of the 100th Annual Meeting of Geol. Soc. Jpn.*, p. 493.
- Hennig, G.J. and Grün, R., 1983. ESR dating in geology. *Q. Sci. Rev.*, 2: 157–238.
- Ikeya, M., 1994. *New Application of Electron Spin Resonance. Dating, Dosimetry and Microscopy*. World Scientific, Singapore, 500 pp.
- Ikeya, M., Miki, T. and Tanaka, K., 1982. Dating of a fault by ESR on intrafault materials. *Science*, 215: 1392–1393.
- Ildefonse, P., Muller, J.-P., Clozel, B. and Calas, G., 1990. Study of two alteration systems as natural analogues for radionuclide release and migration. *Eng. Geol.*, 29: 413–439.
- Ildefonse, P., Muller, J.-P., Clozel, B. and Calas, G., 1991. Records of past contact between altered rocks and radioactive solutions through radiation-induced defects in kaolinite. *Mater. Res. Soc.*, 212: 749–756.
- Imai, N., 1990a. Quantitative analysis of original and powdered rocks and mineral inclusions by laser ablation inductively coupled plasma mass spectrometry. *Analyt. Chim. Acta*, 235: 381–391.
- Imai, N., 1990b. Multielement analysis of rocks with the use of geological certified reference material by inductively coupled plasma mass spectrometry. *Analyt. Sci.*, 6: 389–395.
- Lee, H.K. and Schwarcz, H.P., 1993. An experimental study of shear-induced zeroing of ESR signals in quartz. *Appl. Radiat. Isot.*, 44: 191–195.

- Lin, A., Imiya, H., Uda, S., Iinuma, K., Misawa, T., Yoshida, T., Abematsu, Y., Wada, T. and Kawai, K., 1995. Investigation of the Nojima Earthquake Fault occurred on Awaji Island in the southern Hyogo Prefecture Earthquake. *J. Geogr.*, 104: 113–126.
- McKenzie, D. and Brune, J.N., 1972. Melting on fault planes during large earthquakes. *Geophys. J. R. Astron. Soc.*, 29: 65–78.
- McMorris, D.W., 1967. ESR detection of fossil alpha damage in quartz. *Nature*, 226: 146–148.
- McMorris, D.W., 1969. Trapped-electron dating: ESR studies. *Nature*, 222: 870–871.
- Miki, T. and Ikeya, M., 1982. Physical basis of a fault dating with ESR. *Naturwissenschaften*, 69: 390–391.
- Muller, P. and Calas, G., 1989. Tracing kaolinites through their defect centers: kaolinite paragenesis in a laterite (Cameroon). *Econ. Geol.*, 84: 694–707.
- Nambi, K.S.V. and Aitken, M.J., 1986. Annual dose conversion factors for TL and ESR. *Archaeometry*, 28: 202–205.
- Sato, T., Suito, K. and Ichikawa, Y., 1985. Characteristics of ESR and TL signals on quartz from fault regions. In: M. Ikeya and T. Miki (Editors), *ESR Dating and Dosimetry*. IONICS, Tokyo, pp. 267–273.
- Stapelbroek, M., Griscom, D.L., Friebele, E.J. and Sigel, G.H., Jr., 1979. Oxygen-associated trapped-hole centers in high-purity fused silicas. *J. Non-crystal. Solids*, 32: 313–326.
- Suzuki, Y., Matsuda, T., Nakata, T., Sakamoto, T., Odaka, J., Goto, H., Asahi, K., Chida, N., Takeuchi, A., Azuma, T., Okada, A. and Nakamura, T., 1995. Preliminary report on the paleoseismicity on the Nojima Fault, one of the earthquake source faults of the 1995 earthquake in the Hyogo Prefecture. In: I. Sueño, K. Endo and Y. Ikeda (Editors), *Southern Hyogo Prefecture Earthquake on 17 January, 1995*, p. 33.
- Takagi, H. and Shibata, K., 1992. K-Ar dating of fault gouge-examples along the Median Tectonic Line. *Mem. Geol. Soc. Jpn.*, 40: 31–38.
- Takahashi, J., 1992. Faulting history of the Median Tectonic Line in Ehime Prefecture. *Mem. Geol. Soc. Jpn.*, 40: 99–112.
- Tanaka, K., 1990. Dating of fault movement by ESR method – basis and application. Ph.D. Thesis, Kyushu University, 111 pp.
- The Clay Science Society of Japan, 1987. *Handbook of Clay*. Gihodo Publishing, Tokyo, 2nd ed., 1354 pp.
- Yip, K.L. and Fowler, W.B., 1975. Electronic structure of E' centers in SiO₂. *Phys. Rev. B*, 11: 2327–2338.

Injection veins of crushing-originated pseudotachylyte and fault gouge formed during seismic faulting

AIMING LIN¹

Earthquake Research Institute, University of Tokyo, Tokyo 113, Japan

Abstract

This paper describes the injection veins of crushing-originated pseudotachylyte and fault gouge formed along the Iida-Matsukawa fault in granitic cataclasite, southern Nagano Prefecture, central Japan. The pseudotachylyte, which shows a dense and aphanitic appearances, and fault gouge occur as simple veins (fault vein) along the main fault plane and as complex network veins (injection vein) in the neighboring cataclasite. Locally, the injection veins of pseudotachylyte and fault gouge can be traced back to the fault veins. Powder X-ray diffraction patterns and petrological analysis indicate that both of the pseudotachylytes and fault gouges consist entirely of fine-grained angular clasts and that the pseudotachylytes and fault gouges have a similar X-ray diffraction patterns with that of the host granite. The similarity of chemical compositions and distribution patterns of grain size also show that the injection veins of pseudotachylyte and fault gouge have the same source material as that of fault veins. Field occurrences and petrological characteristics strongly suggest that the injection veins of pseudotachylyte and fault gouge formed during seismic faulting by a rapid intrusion and fluidization of crushed fine-grained materials generated in the shear zone in a gas-solid-fluid system.

1. Introduction

The pseudotachylytes found as simple veins and injected networks in fault zones are widely known as *Earthquake faulting fossils*. These rocks generally have some of the aspects of an igneous rock that intruded into fractures and others of a sedimentary breccia cemented by fine-grained matrix. The melting origin of pseudotachylyte has been demonstrated by field and petrological studies (Sibson, 1975; Maddock, 1983; Lin, 1991, 1994a, b). The experimental results also show that the melting-originated pseudotachylyte can be generated by frictional heating at depths as shallow as several tens of meters (Lin, 1991; Lin and Shimamoto, 1994, 1996).

¹Present address: Department of Earth and Planetary Sciences, Faculty of Science, Kobe University, Nada-ku, Kobe, 657, Japan.

However, it has also been reported recently that there are some crushing-originated pseudotachylytes which are dark, aphanitic in appearance, and show the occurrence of simple veins and networks injected into the wallrocks (Lin et al., 1994). Furthermore, fault gouge veins injected into the fractures in the wallrocks have also been found (Lin et al., 1994), and injection veins composed of angular wallrock fragments have also been reported (Gretener, 1977; Sibson, 1986, 1987).

These crushing-originated pseudotachylyte and fault gouge veins have a general character which shows an occurrence of injection. The occurrences of injected pseudotachylyte and fault gouge veins along particular faults suggest that the associated fractures were related to dynamic rupture propagation and slip during incremental coseismic displacement. The process of earthquake rupture propagation within the seismogenic zone is inherently complex at all scales, but a lack of adequate geological data inhibits any detailed investigations into the actual process of rupture and slip (Scholz, 1990). The study of injection veins of pseudotachylyte and fault gouge-bearing fault structures, however, can provide, by direct observation, a unique view of the process of earthquake rupturing at shallow crust that cannot be obtained through indirect seismic studies.

This paper presents crushing-originated pseudotachylyte veins and some fault gouge veins associated with the injection and fluidization of fine-grained crushed-materials, based on field and petrological studies in the Iida-Matsukawa fault, southern Nagano Prefecture, central Japan, and discusses the process and mechanism of injection and fluidization of fine-grained materials.

2. Geological setting

The Iida-Matsukawa fault extends 12 km in NW-SE direction, with a steep dip in the southern part of the Kiso range, Nagano Prefecture, central Japan (Fig. 1). The bed rocks consist of granitic rocks of the Ryoke belt. It was inferred that the Iida-Matsukawa fault is an active B class fault (average slip rate of 0.1 mm/year) (Research Group for Active Faults of Japan, 1991). The deformational geomorphology, petrofabrics of fault rocks, and the ESR-TL ages of fault gouges indicate that this fault moved in the late Pleistocene (Lin, 1989).

The fractured zone of the Iida-Matsukawa fault generally ranges from a few meters to a few tens of meters in thickness and consists of fault rocks such as cataclasite, protocataclasite, fault gouge and fault breccia (Figs. 2–4) (using the fault-rock terminology of Sibson, 1977). Some cataclasites show foliated textures (Figs. 4 and 5d), which are characterized by the orientation of the biotite and some aggregates of quartz and feldspar clasts.

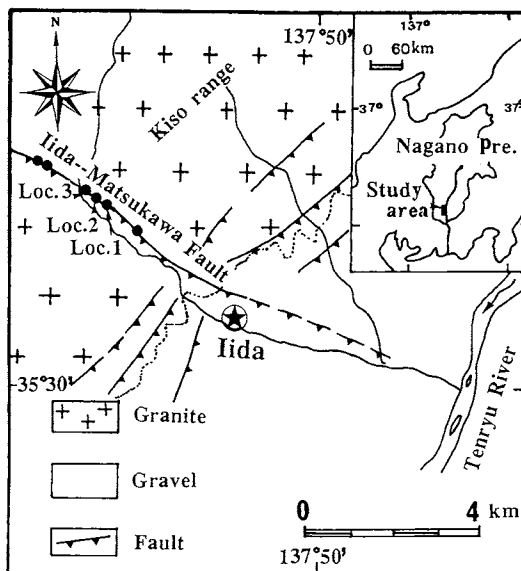


Fig. 1. Simplified geological map of the Iida region, southern Nagano Prefecture, central Japan. Solid circles show the locations of main outcrops along the Iida-Matsukaga fault.

3. Field occurrence of pseudotachylyte and fault gouge veins

3.1. Pseudotachylyte veins

The pseudotachylytes have been found at several locations along the Iida-Matsukawa fault; the main locations are shown in Fig. 1. They occur as simple veins along the fault plane (called the fault vein) and as a complex network of veins (called the injection vein) injected into the fractures in the cataclastic rocks (Figs. 2–5). Some pseudotachylyte veins have been offset by small fractures as shown in Fig. 5c. Some parts of the side face of pseudotachylyte veins have been introduced into new fault planes on which there are fault gouges ranging from a few millimeters to a few centimeters in thickness, and a lot of striations (Fig. 5a). Some pseudotachylyte veins occur in the fault breccia zone which has been consolidated later, and some pseudotachylyte fragments are involved in this fault breccia zone. Locally, injection veins can be traced back to the parent pseudotachylyte-generated fault plane by a continuity of veins. The contacts between the pseudotachylyte veins and the cataclastic rocks are generally sharp as shown in Fig. 5. The veins are commonly a few millimeters to a few centimeters in thickness, and individual veins can be followed up to a few meters along the fault zone (Figs. 2–5).

The pseudotachylyte veins are dark-brown to black in color, locally show a vitreous luster similar to that of glassy pseudotachylyte as described by Lin (1994a). The rocks are compact and aphanitic in appearance, consisting of fine-grained

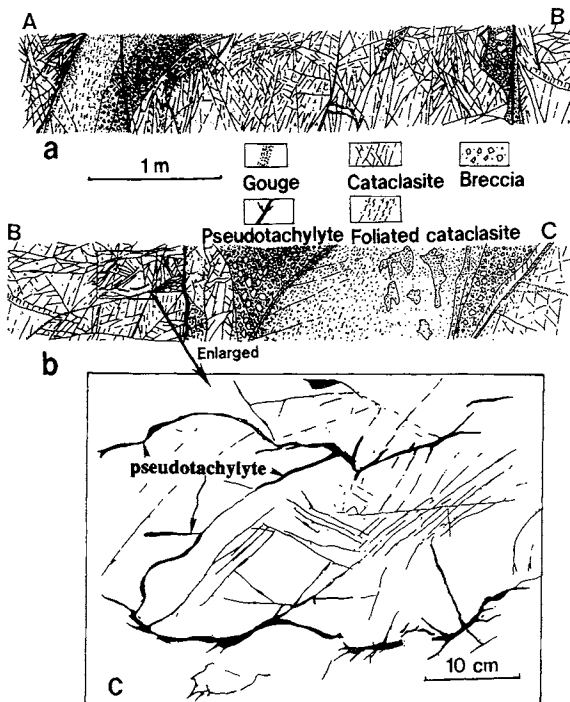


Fig. 2. Sketches of the fault outcrop at Loc. 1. Pseudotachylite veins occurring as simple veins along the fault plane and as injected network veins in the cataclasite zone. The right side of sketch (a) continues to the left side of (b), and (c) is an enlarged view of the upper-left portion of (b).

matrix and some fragments of the host rocks. In the matrix, no mineral particles can be recognized with the naked eye.

3.2. Fault gouge veins

The fault gouges have been found at many locations along the Iida-Matsukawa fault, and also can be divided into two types of occurrence similar to that of the pseudotachylite veins: fault veins occurring along the fault plane; and the veins injected into the country granitic rock. The injection veins are only found at Locs. 1 and 2 (Fig. 1); one of them is shown as a sketch in Fig. 4. The fault vein occurring along the fault plane generally ranges from a few millimeters to a few tens of centimeters in thickness, in which some foliations characterized by color layers (grayish-green, grayish-brown to gray) can be observed. The gouge veins injected into the country rocks occur as simple veins or complex networks in some fractured zones (Figs. 3, 4, 5d and 6), and can also be observed on the hand samples as shown in Fig. 6. Locally, the injection veins can be traced back to the parent gouge vein occurring along the fault plane similar to the occurrence of pseudotachylite

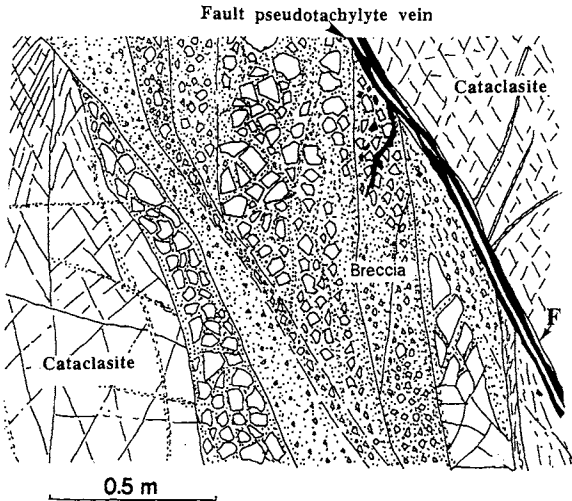


Fig. 3. A sketch of the fault outcrop at Loc. 3. Pseudotachylite veins occurring in the breccia zone. F, fault plane.

veins. The fault vein typically occurs as a thin layer ranging a few millimeters to a few centimeters in thickness, or locally as a lump on concave surfaces up to 10–20 cm in diameter. The injection gouge veins are variable: from a few millimeters to a few tens of centimeters, but generally from 4–6 to 10 mm in thickness. The contacts between the injected gouge veins and the country rock, as seen with the naked eye, are generally sharp.

4. Microscopy of pseudotachylites and fault gouges

4.1. Pseudotachylite veins

In thin section, microscopically, the pseudotachylites are generally pale-brown to dark-brown in plane polarized light and dark in crossed polarized light. The occurrences of injected pseudotachylite veins can also be observed microscopically, and the contacts between the veins and the host cataclastic rocks are generally sharp but, locally, less clear (Fig. 8). These veins consist of fine-grained matrix which exhibits the optical character of glass, with fragments of quartz and feldspar scattering in the matrix. Fragments of biotite included in the host granitic rocks cannot be observed. There are some fragments of saussuritized plagioclase, showing a plume-texture similar to that of microlites observed in melting-originated pseudotachylite as described by Lin (1994b). The pseudotachylite matrix consists dominantly of fine-grained angular fragments (Fig. 9). These fragments are generally larger than 2–3 μm , and are smaller than cataclasite in size (Fig. 9a).

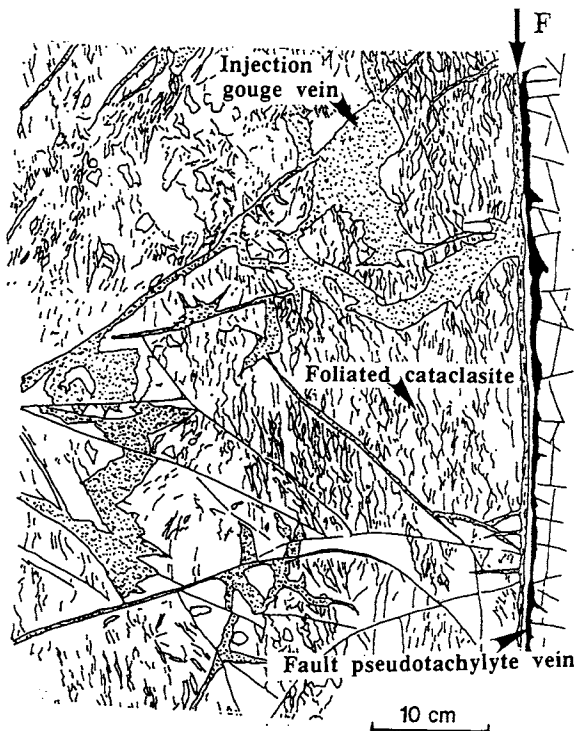
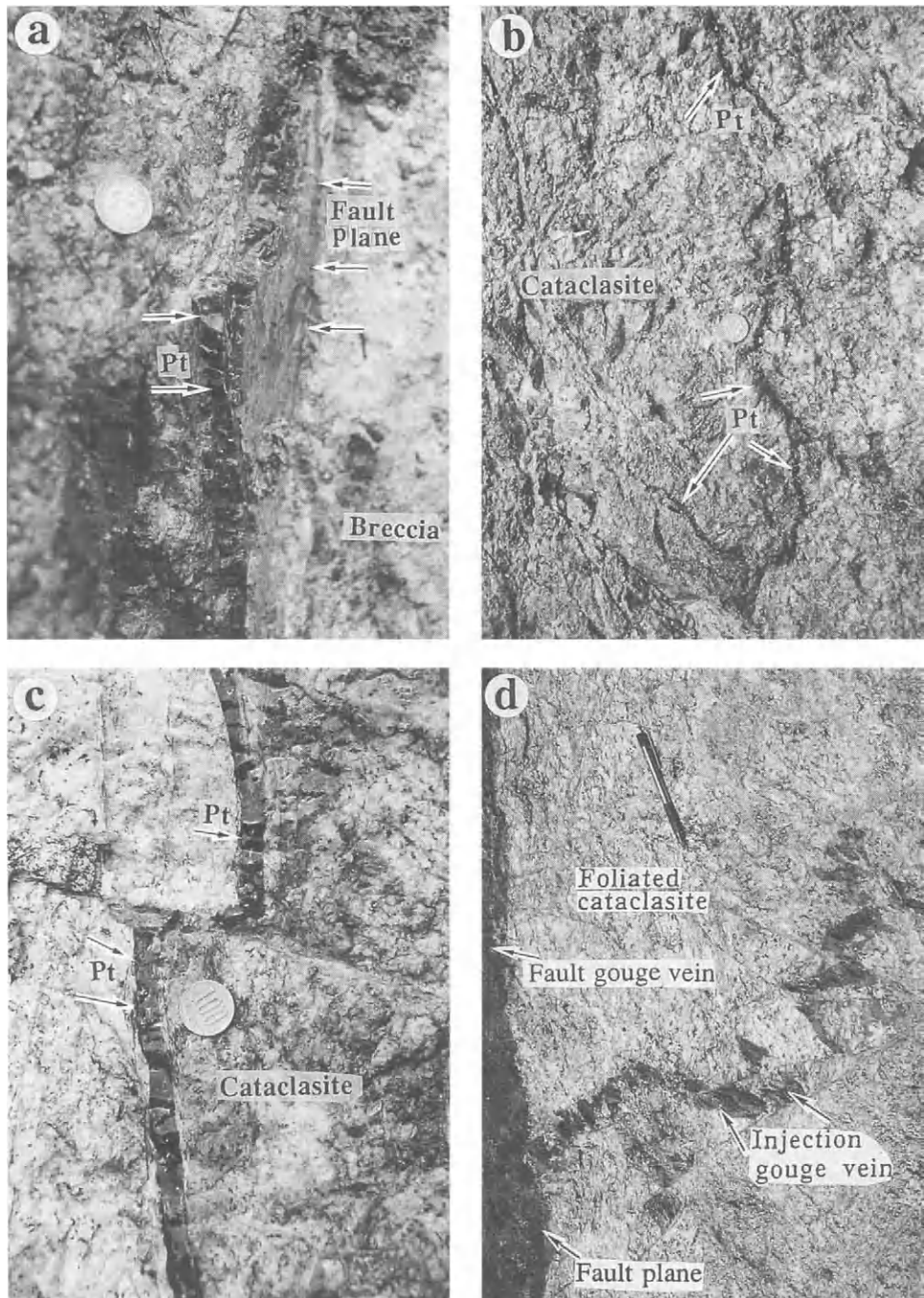


Fig. 4. A sketch of the fault outcrop at Loc. 2. Pseudotachylite veins occurring along the fault plane (F). Fault gouge occurring along the fault plane as simple vein and injected into the cataclasite as irregular network veins.

4.2. Fault gouge veins

The fault gouges, generally showing a character similar to that of pseudotachylite, are yellowish-brown to brown in plane polarized light and dark in crossed polarized light. It is hard to ascertain whether the fine-grained matrix materials are crystalline clasts or aphanitic cryptocrystalline. The contacts between the injection veins and the host cataclastic rocks are generally sharp (Fig. 7a,b) but, locally, is less sharp between the fault gouge occurring on the fault plane and the cataclastic rocks. The photomicrographs show that the fault gouge veins are composed of fine-grained fragments generally larger than 2–3 μm in size (Fig. 8c).

Fig. 5. Photographs showing the occurrence of pseudotachylite and fault gouge veins. (a) Pseudotachylite vein (Pt) occurring along the fault plane. (b), (c) Pseudotachylite veins (Pt) injected into the granitic cataclasite. The pseudotachylite vein was displaced a few centimeters by later slipping along the cracks shown in (c). (d) Fault gouge veins occurring along the fault plane and injected into the foliated cataclasite in the fractured zone.



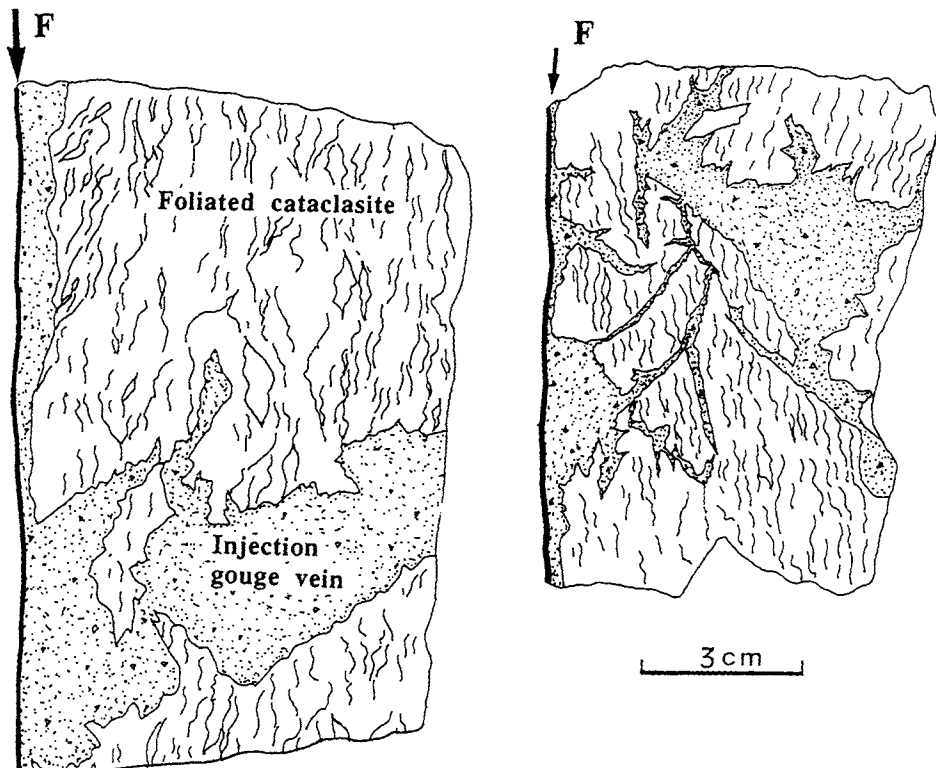


Fig. 6. Sketches of hand specimens showing the occurrences of the fault veins and injection veins of fault gouge taken from Loc. 2. F, fault plane.

5. Powder X-ray diffraction patterns of pseudotachylytes and fault gouges

A RINT 2200 X-Ray diffractometer was used to obtain the diffraction patterns for the Iida-Matsukawa pseudotachylytes and fault gouges. The experimental conditions were: filtered $\text{Cu}\alpha$ (1.54050 \AA) radiation, X-ray generator 18 kW, 60 kV, 300 mA, sampling width 0.02° , scanning speed $3.0^\circ/\text{min}$, divergence slit 1.0° , scattering slit 1.0° , receiving slit 0.15 mm , θ deposition 5.0° .

The X-ray diffraction spectra of the pseudotachylyte veins and fault gouge veins are shown in Figs. 10 and 11, respectively, and one spectrum of quartz is also shown as a standard sample for comparison. All these X-ray diffraction spectra show a diffraction pattern of crystalline materials. There is a similarity in diffraction patterns among the country granitic rock, pseudotachylyte, and fault gouge, in which the main crystalline peaks indicate that the presence of quartz and feldspar in all the samples (Figs. 10 and 11). Some mica peaks such as biotite and muscovite can only be recognized in the granitic country rocks, and a little clay mineral peaks such as chrolite and montmorillonite can be recognized only in the pseudotachylytes and

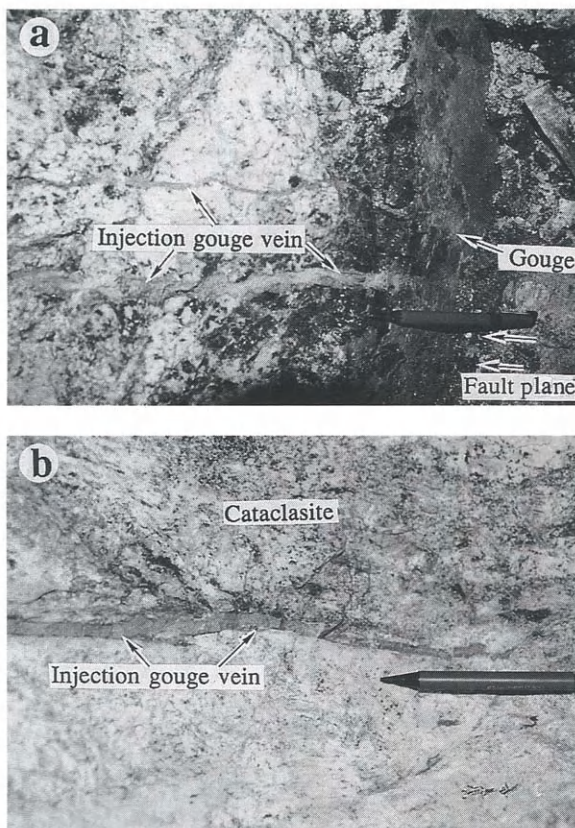


Fig. 7. Photographs showing the occurrences of the fault gouge veins. (a) Fault vein occurs along the fault plane (F) and injection veins of fault gouge. (b) Injection vein of fault gouge injected into the cataclasite.

fault gouges. It is possible that the clay minerals formed from micas by hydrothermal alteration of feldspars and micas. These diffraction patterns suggest that the rock-forming minerals of the granitic country rocks are almost the same as that of pseudotachylytes and fault gouges.

6. Chemical compositions

The average bulk chemical compositions of the pseudotachylytes, the gouges, and their associated country rock analyzed by XRF were displayed in Table 1. The average bulk compositions of the veins of pseudotachylyte and gouge are very similar to that of the country granitic rock in the Iida-Matsukawa fault. Thus, the veins of the pseudotachylyte and gouge are interpreted to have formed from the

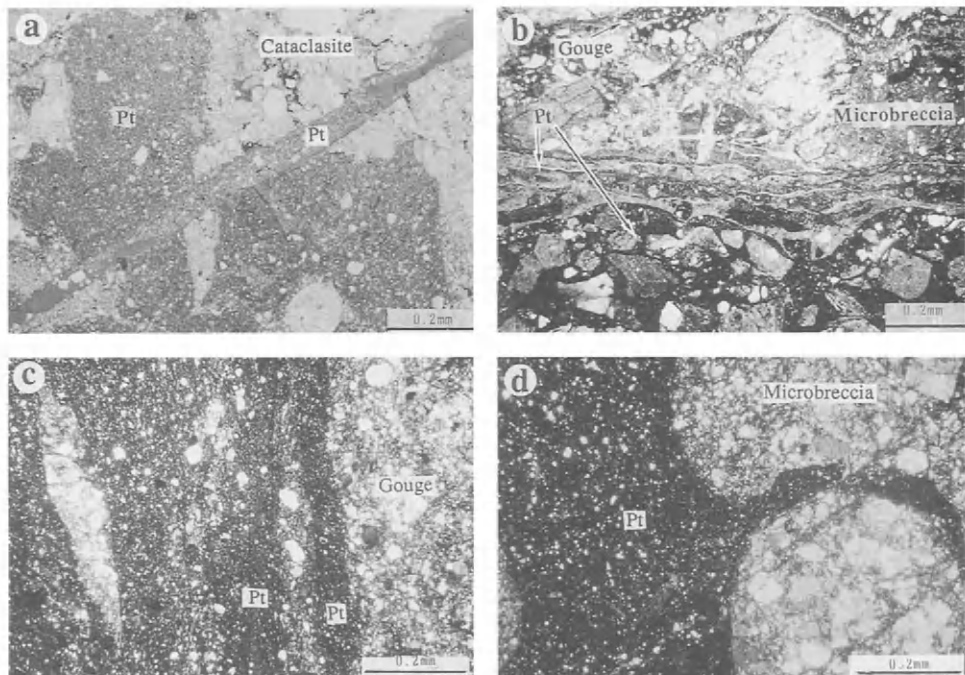


Fig. 8. Photomicrographs of the pseudotachylyte and gouge veins (Pt). (a) New pseudotachylyte vein injected into older pseudotachylyte vein and cataclasite. (b) Pseudotachylyte vein occurring along the fault microbreccia zone. Note that some pseudotachylyte clasts (Pt) can be observed in the fault microbreccia zone. (c) Pseudotachylyte and gouge veins occurring along the fault plane. The boundary between the pseudotachylyte and fault gouge is not so sharp. (d) Pseudotachylyte vein injected into the fault microbreccia zone. (a,b) Plane-polarized light; (c,d) crossed-polarized light.

rock in which they occur, based on the similarity between the chemical compositions of the veins of pseudotachylyte and gouge and the country granitic rock, the powder X-ray diffraction patterns, as well as the field occurrences.

7. Clast-size distribution

The purpose of measurement of clast-size distribution is to determine whether the size distributions of fragments in the injected veins of pseudotachylyte and fault gouge are the same as those of fault veins of pseudotachylyte and fault gouge occurring along the fault plane. If the injected veins have the same material source as that of fault vein, they would have a similar or same size distribution pattern. The measurements were performed on the SEM photomicrographs, as the matrix materials are too fine to observe under optical microscope, using the measuring method described by Shimamoto and Nagahama (1992).

The results of measurements were plotted as cumulative frequency diagrams for

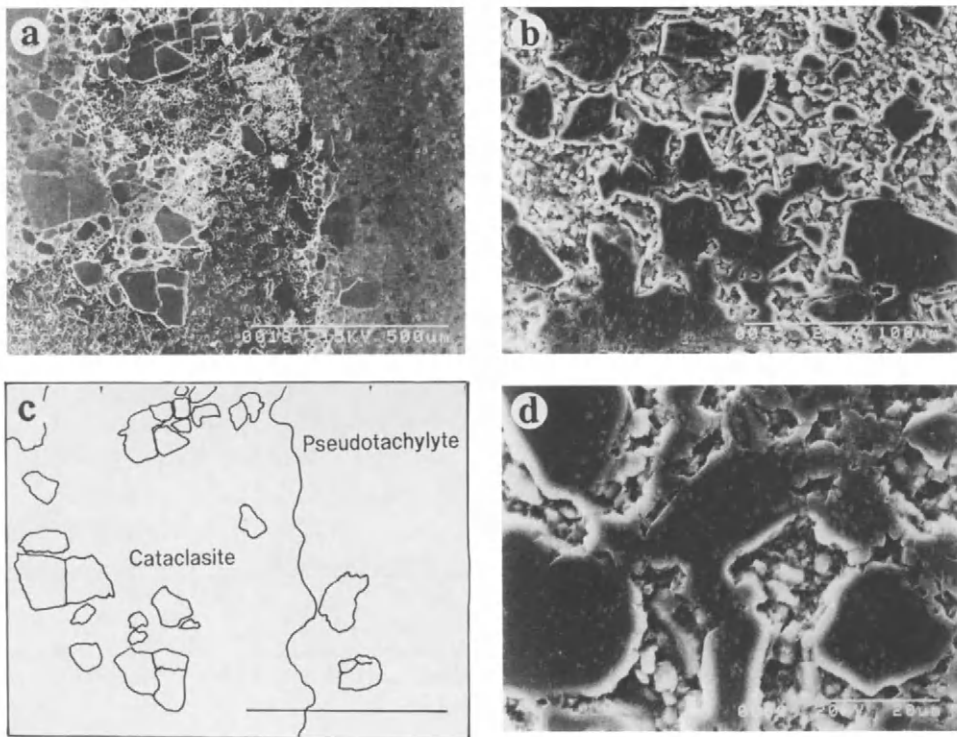


Fig. 9. SEM photomicrographs showing the textures of the pseudotachylite taken from Loc. 1. (a) The boundary between the pseudotachylite and cataclasite; (c) a sketch of (a). (b,d) The fine-grained matrix of pseudotachylite consists almost entirely of angular fine-grained clasts.

the major diameter (r) in transversal axis and the total numbers of measured grains (N) in the vertical axis, using logarithmic scales on both axes (Fig. 12). The results of grain-size analysis show that the matrices consist of 80–90 vol% fragments larger than 2–3 μm , and only 10–20 vol% fine-grained fragments smaller than 2–3 μm . It is clearly observed that there is a similar size-distribution pattern between that of the injection veins and fault veins, and a different pattern between the country granitic cataclasites and the veins of pseudotachylite and fault gouge.

8. Discussions

Most of the melting-originated pseudotachylites described in the literature have striking similarities: dense and aphanitic in appearance, occurring as irregular veins intruded into country rocks both as simple and complex networks, and generally a few millimeters to a few centimeters in thickness. It was Shand (1916) who first described and sketched the occurrence of irregular, branching pseudotachylite veins

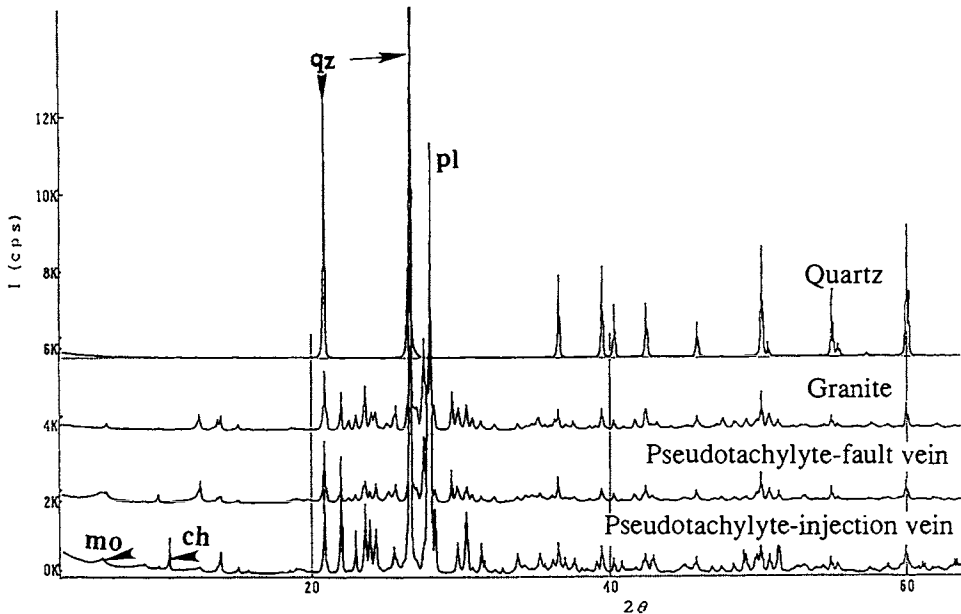


Fig. 10. Powder X-ray diffraction spectra of the pseudotachylite veins. Granite: country granite sample taken from Loc. 1. Quartz, standard sample of quartz; qz, quartz; ch, chlorite; mo, montmorillonite; pl, plagioclase.

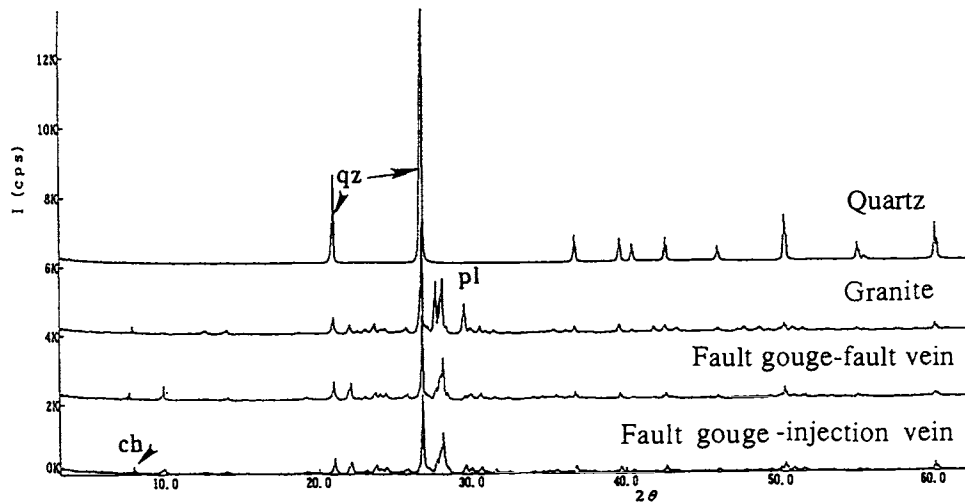


Fig. 11. Powder X-ray diffraction spectra of the fault gouge veins. Granite: country granite sample taken from Loc. 1. Quartz, standard sample of quartz; qz, quartz; ch, chlorite; pl, plagioclase.

TABLE I

Bulk composition of pseudotachylyte, gouge, and the country granitic rock analyzed by XRF

Wt%	Country granite	Pt veins		Gouge veins	
		Injection	Fault	Injection	Fault
SiO ₂	72.11	71.62	71.59	71.90	72.50
TiO ₂	0.27	0.43	0.33	0.32	0.19
Al ₂ O ₃	15.13	15.12	14.53	15.22	14.56
FeO	1.34	2.94	2.58	2.37	1.96
MnO	0.05	0.06	0.07	0.06	0.05
MgO	0.91	0.62	1.52	0.49	0.67
CaO	2.28	2.18	2.36	2.38	1.57
Na ₂ O	3.94	3.10	3.60	3.52	4.08
K ₂ O	3.24	3.99	2.89	3.14	3.91
P ₂ O ₅	0.08	0.09	0.05	0.07	0.05
Total	99.35	100.15	99.52	99.47	99.54

Pt, pseudotachylyte; FeO, total Fe calculated as FeO.

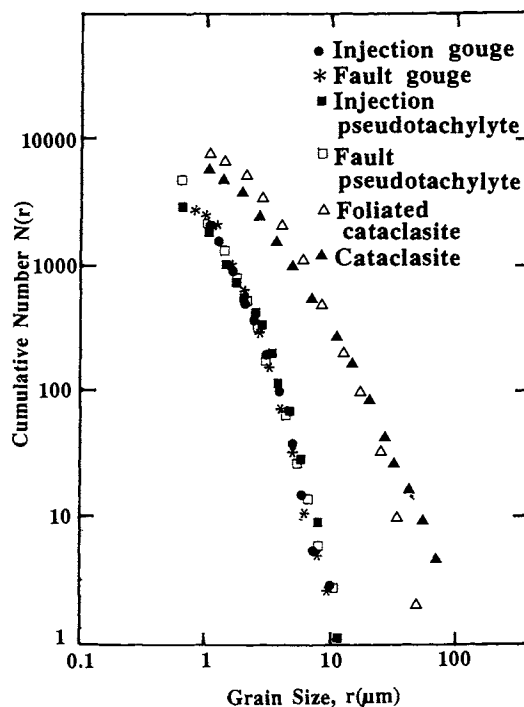


Fig. 12. Size distributions of clasts contained in the fault veins and injection veins of pseudotachylyte and fault gouge as well as cataclasite occurring along the Iida-Matsukawa fault.

in the Vredefort region, South Africa. Sibson (1975) classified the fault-generated pseudotachylyte veins into two fundamental classes of veins: (i) fault veins, laying along markedly planar shear fractures on which the pseudotachylyte has been generated, and (ii) injection veins, intruded into the country rocks and often appearing to be dilational veins along which there has been no lateral offset of markers.

As already stated above, the pseudotachylyte and fault gouge veins found in the Iida-Matsukawa fault also show a general character of intrusion, which occur as simple vein and complex networks, having a dense and aphanitic appearance; microscopically, no minerals can be observed in the fine-grained matrix. However, from SEM observations it is clear that the fine-grained matrix is composed of angular clasts, showing little evidence of frictional attrition such as rounded, embayed and other irregular outlines as described by Lin (1994a). This indicates clearly that this pseudotachylyte was mainly formed by crushing rather than melting. The boundaries between these pseudotachylyte and fault gouge veins and the country granitic rock are sharp, as seen both in the field and microscopically, where there is no lateral offset of markers and no striking shear textures. This shows that these veins formed at the shear zone and were intruded into the country granitic rock along the cracks.

The question is: did these pseudotachylyte and fault gouge veins form by rapid intruding of fine-grained clasts, like spraying during seismic faulting, or by the deposition of clay minerals transported by hydrothermal fluids along fractures? The powder X-ray diffraction patterns and the similarity of bulk chemical compositions between the veins of pseudotachylyte and gouge show that the rock-forming minerals in these injection veins are similar to those of fault veins and the country granitic rock. This suggests that the injection veins have the same source materials as those of the fault veins and the country granitic rock. If the injection veins were formed by the precipitation of clay minerals transported by the ground water along cracks, they would have a different composition compared to the fault veins and the country granitic rock. Furthermore, there is a similarity of size-distribution of clasts between the injection vein and fault vein. This also shows that there is the same source between the two type veins.

The field occurrences, powder X-ray diffraction patterns, the chemical compositions, and the results of the size-distribution of clasts show that the injection veins formed by the rapid injection of fine-grained clasts during seismic faulting. If the injection veins were formed by a slow flowing process after seismic faulting, it is impossible that the solid clasts, without water, intruded into the cracks a few meters beyond the source fault plane. If the injection veins were formed by water flow, there would be different compositions among the injection veins, the fault veins, and the country granitic rock, and the fine-grained matrix materials would be distributed differently. In this case, there would be more fine-grained matrix materials in the injection vein than in the fault vein. The size-distribution patterns, however, never show such a tendency.

Herein, it is suggested that the rapid injection formed by *fluidization* of fine-

grained clasts generated in the shear zone. The fluidization was defined as “the mixing process of gas and lose fine-grained material so that the whole flows like a liquid, e.g. the formation of an ash flow or nuée ardente during a volcanic eruption.” in the *Glossary of Geology* (Bates and Jackson, 1980), and was first introduced to explain the geological phenomenon by Reynolds (1954). Although the term fluidization is applied specifically to a gas–solid system, it is striking applicable to a suspension of solid particles in an upward flowing stream of liquid which has a lower density than that of the particles. The geological examples of intrusive fluidized systems are characterized by net veins of dike, by breccias in which many of the fragments derived from the adjacent wallrocks are rounded as if by sandblast, and by mechanical hybrids (Reynolds, 1954). The other geological examples of intrusive veins are associated with seismic faulting, such as melting-originated pseudotachylyte veins (Lin, 1991, 1994a), and liquefaction veins formed during large earthquakes, which also show characteristics of simple and network veins injected into the wallrocks. It has also been observed by the author that there are a lot of clasts over 60–70 vol% contained in the typical melting-originated pseudotachylytes such as those described by Sibson (1975), Lin (1991, 1994a) and Toyoshima (1990). This hints that the clasts mixed with the melt were injected into the cavity space generated during seismic slip by rapid intruding-like spraying in a gas–solid–liquid system, like a pyroclastic flow rather than slow flowing of liquid. The substantial cavity may accompany seismic slip in strong rocks at depths of several kilometers (Sibson, 1986). These cavities forming transitory low-pressure channels are particular sites for the rapid passage of fluidized particles. The rapid injection of the fluidized particles may be formed by the sudden fluid-pressure differentials generated in dilatational jogs during rupture arrest as described by Sibson (1986). It is important to realize that the bubble phase of gas–solid systems has no counterpart in liquid–solid systems, and that the turbulent expanded bed is, in consequence, specific to gas–solid systems. This is of importance to the geologist because – from recognition of turbulent expanded and rock fragments which have not been appreciably transported away from their source rock, together with a lack of sorting of the fragments concerned and possible presence of druses – it can be inferred that the field agent was gas and not liquid. Closely allied in mechanism to the process of fluidization of solid particles by gas is the method of painting by spraying (Reynolds, 1954). It is possible that the injection veins found in the Iida-Matsukawa fault were formed by such fluidization of fine-grained materials during seismic faulting.

9. Conclusions

As stated above, the following conclusions can be obtained: (1) the dark, dense and aphanitic pseudotachylyte found in the Iida-Matsukawa fault was formed mainly by crushing rather than melting; (2) the injection veins of pseudotachylyte and fault gouge were formed by rapid injection of fine-grained materials during seismic

faulting; (3) it is suggested that the injection veins were formed by the fluidization of fine-grained materials generated in fault zone.

Acknowledgements

I would like to express my sincere thanks to professor T. Matsuda of the University of Kumamoto and professor T. Shimamoto of the University of Tokyo for their advice and discussions during this study.

References

- Bates, R.L. and Jackson, J.A. (Editors), 1980. *Glossary of Geology*. Am. Geol. Inst., Falls Church, VA, 751 pp.
- Gretener, P.E., 1977. On the character of thrust sheets with particular reference to the basal tongues. *Bull. Can. Petrol. Geol.*, 25: 110–122.
- Lin, A., 1989. ESR and TL datings of active faults in the Iida area of the southern Ina valley (in Japanese). *Active Fault Res.*, 7: 49–62.
- Lin, A., 1991. Origin-of fault-generated pseudotachylytes. Ph.D. Thesis, Tokyo University, 108 pp.
- Lin, A., 1994a. Glassy pseudotachylytes from the Fuyun fault zone, northwest China. *J. Struct. Geol.*, 16: 71–83.
- Lin, A., 1994b. Microlite morphology and chemistry in pseudotachylyte, from the Fuyun fault zone. *J. Geol.*, 102: 317–329.
- Lin, A. and Shimamoto, T., 1994. Chemical composition of experimentally-generated pseudotachylytes. *Struct. Geol.*, 39: 85–101 (in Japanese, with English abstract).
- Lin, A. and Shimamoto, T., 1996. Experimentally-generated pseudotachylytes: a selective melting process. *Island Arc*, in review.
- Lin, A., Matsuda, T. and Shimamoto, T., 1994. Pseudotachylyte from the Iida-Matsukawa fault, Nagano Prefecture: Pseudotachylyte of crush origin? *Struct. Geol.*, 39: 44–51 (in Japanese, with English abstract).
- Maddock, R.H., 1983. Melt origin of fault-generated pseudotachylytes demonstrated by textures. *Geology*, 11: 105–108.
- Research Group for Active Faults of Japan, 1991. *Active faults in Japan-sheet maps and inventories*. University of Tokyo Press, Tokyo, pp. 186–191 (in Japanese, with English abstract).
- Reynolds, D.L., 1954. Fluidization as a geological process, and its bearing on the problem of intrusive granites. *Am. J. Sci.*, 252: 577–614.
- Scholz, C.H., 1990. *The Mechanics of Earthquakes and Faulting*. Cambridge University Press, Cambridge, 433 pp.
- Shand, S.J., 1916. The pseudotachylyte of Parijs (orange Free State), and its relation to “trap-shotten gneiss” and “flinty crush-rock”. *Quart. J. Geol. Soc. (London)*, 72: 198–221.
- Shimamoto, T. and Nagahama, H., 1992. An argument against the crush origin of pseudotachylytes based on the analysis of clast-size distribution. *J. Struct. Geol.*, 14: 999–1006.
- Sibson, R.H., 1975. Generation of pseudotachylyte by ancient seismic faulting. *Geophys. J. R. Astron. Soc.*, 43: 775–794.
- Sibson, R.H., 1977. Fault rocks and fault mechanisms. *J. Geol. Soc. London*, 133: 191–213.
- Sibson, R.H., 1986. Brecciation processes in fault zones: Inferences from earthquake rupturing. *Pure Appl. Geophys.*, 124: 159–176.

- Sibson, R.H., 1987. Earthquake rupturing as a mineralizing agent in hydrothermal systems. *Geology*, 15: 701–704.
- Toyoshima, T., 1990. Pseudodachylyte from the Main Zone of the Hitaka metamorphic belt, Hokkaido, northern Japan. *J. Metamorph. Geol.*, 8: 507–523.

Changes in Coulomb failure function due to the occurrence of the M7.2 Kobe Earthquake of January 17, 1995, as a possible measure of the change in seismicity

MANABU HASHIMOTO¹

Crustal Dynamics Department, Geographical Survey Institute, Kitasato 1, Tsukuba, Ibaraki 305, Japan

Abstract

We calculated changes in Coulomb failure function (CFF) for a geodetic fault model of the M7.2 Kobe Earthquake of January 17, 1995, to investigate the possible relationship between the occurrence of the main shock and the following increase in seismicity in the surrounding area.

The modeled fault, which was derived from geodetic data, consists of six nearly vertical planes trending in the NE-SW direction with dominant right-lateral strike-slip and some thrust components. We calculate CFF changes for several focal mechanisms which are usually seen in the Kinki district or are consistent with the type of active faults there, and compare its distribution with the seismicity observed after the main shock.

Calculated CFF for right-lateral slip on NE-SW trending vertical planes or left-lateral slip on NW-SE trending vertical planes, which are dominant focal mechanisms in this area, increases along the northeastern extension of the source region and around the Yamasaki fault, a conjugate fault located northwest of the source region. In the former region a drastic increase in number of earthquakes were observed after the main shock. The activation of seismicity was also observed near the Yamasaki fault. CFF decreases in the north of the source region, where the size of earthquakes became smaller than before the main shock. CFF may decrease a little in the Wakayama region, where no notable changes in seismicity were observed.

The Kobe Earthquake may have loaded stresses which might lead to right-lateral slip on the eastern half of the Arima-Takatsuki Tectonic Line and segments of the Median Tectonic Line in the Wakayama and Tokushima regions. Since these faults have no record of M7 or greater events during at least 400 years, we should be aware of the seismicity around these tectonic lines.

1. Introduction

We have often seen increase of seismicity including occurrence of earthquakes of moderate size in the surrounding regions of source area after some large events. We

¹Tel.: +81 298 645977; fax: +81 298 642655; e-mail: hasimoto@crust.gsi.go.jp.

consider that these succeeding events are the slip of faults, which are close to failure, induced by stress changes due to the main shock. There are several examples of induced activity, such as swarm activity in eastern Izu, Japan, after the M6.9 Izu-Hanto earthquake in 1974 (Yamashina, 1978), the sequence of M6.5 and M6.7 events in Superstition Hills, California, in 1987 (Hudnut et al., 1989; Larsen et al., 1992), the activation of seismicity in the surrounding region after the M7.1 Loma Prieta earthquake in California in 1989 (Reasenberg and Simpson, 1992), and an M6.6 event in Big Bear after the M7.5 Landers earthquake in California in 1992 (Harris and Simpson, 1992; Stein et al., 1992; King et al., 1994). The calculations of stress or strain for main shock in these studies show that succeeding events occurred in the zones of stress or strain increase.

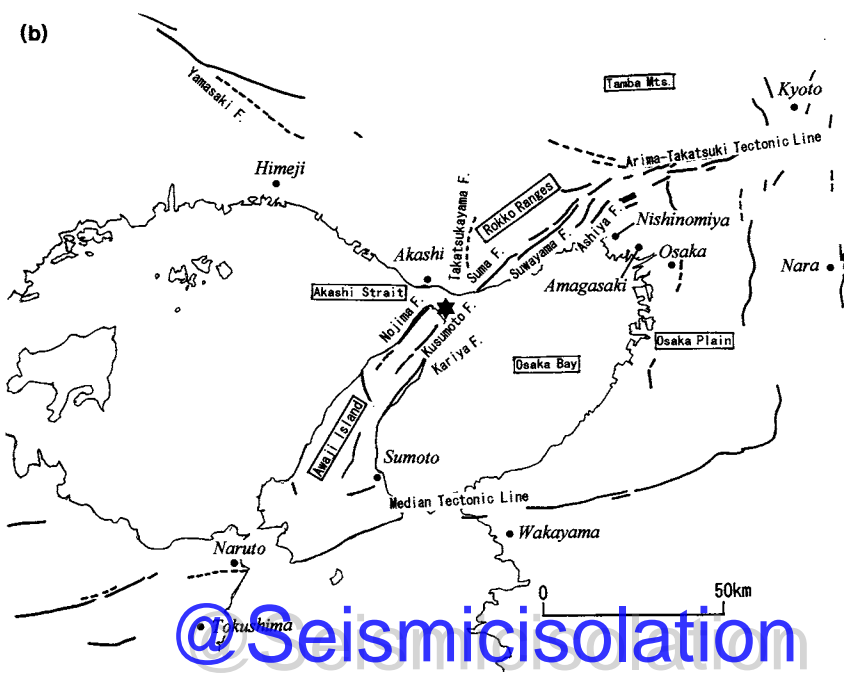
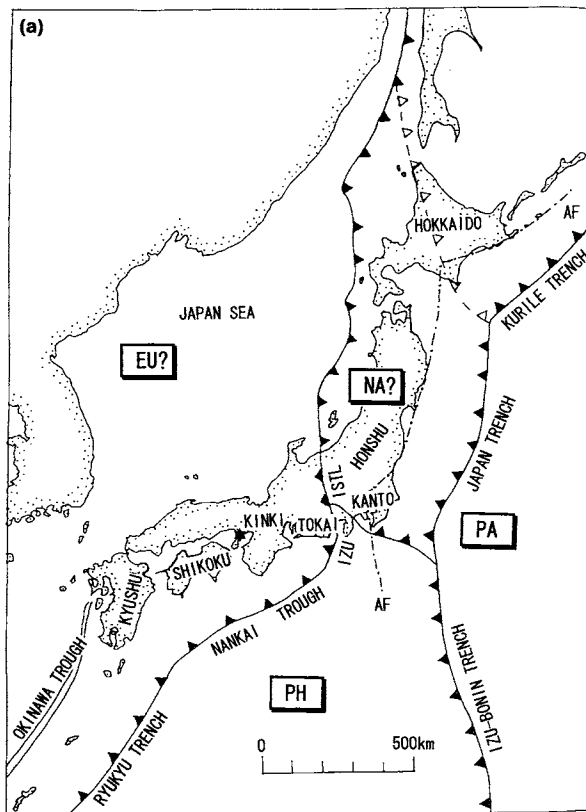
The Kobe earthquake occurred on January 17, 1995, in the Kinki district, southwestern Japan (Fig. 1), and claimed more than 6000 fatalities. This earthquake raised several problems, not only with regard to its nature but also for earthquake science itself. One of the remarkable phenomena is changes in seismicity in the surrounding regions of the source area after the occurrence of the main shock (Disaster Prevention Research Institute, Kyoto University; DPRI, 1995) (see also Ando, 1995; Mizoue et al., 1995; Katao, 1995; Nishigami et al., 1995; Earthquake Research Institute, University of Tokyo, 1995; Yoshikawa and Ito, 1995). It is essential to examine correlation between changes in seismicity and stress changes due to the main shock if we try to objectively evaluate the possibility of aftershock activity or induced seismicity for future large earthquakes. Furthermore, since active faults are densely distributed around the source region of the Kobe earthquake (Fig. 1(b)), it is important to evaluate the effects on these faults as quantitatively as possible for the purpose of seismic hazard analysis.

In this paper, we present some results of calculation of Coulomb failure function for a fault model derived from geodetic data, and discuss possible correlation between changes in seismicity and stress changes induced by the main shock.

2. Calculation of Coulomb failure function

According to the Coulomb-Mohr criterion, fracture occurs on an arbitrary plane when shear stress (τ) exceeds frictional strength. Frictional strength is assumed to be proportional to the difference between normal stress (σ_n) and pore pressure (P), and its proportional coefficient is the internal frictional coefficient (μ) (e.g. Scholz, 1990).

Fig. 1. Index map of the Kinki district, southwestern Japan: (a) Tectonic plates and major geological structures; AF, the aseismic front; ISTL, the Itoigawa-Shizuoka tectonic line; EU, Eurasian plate; NA, North American plate; PH, Philippine Sea plate; PA, Pacific plate. (b) Distribution of active faults modified after Geological Survey of Japan (1995). Asterisks in both maps indicate the epicenter of the Kobe earthquake.



For intact rock, when the following condition,

$$\tau = \tau_0 + \mu(\sigma_n - P), \quad (1)$$

is satisfied, shear fracture will occur, where τ_0 is cohesive strength and compressive stress is positive for σ_n . Since we discuss the stress in the Kinki district where microseismicity is high and active faults are densely distributed, the assumption of intact rock may be inappropriate. If we assume that cohesive strength on pre-existing faults is negligible (Seno, 1995), then

$$\tau = \mu(\sigma_n - P). \quad (2)$$

Next we consider the following function,

$$CFF = \tau - \mu(\sigma_n - P) \quad (3)$$

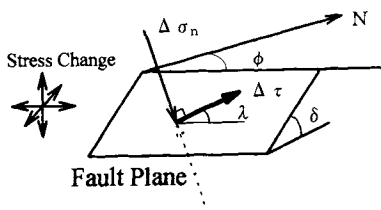
We can regard this function, the Coulomb Failure Function (hereafter CFF), as the measure of the possibility of shear fracture on an arbitrary preexisting fault plane. However, we cannot measure the absolute value of stress on a fault plane at present. Therefore it is reasonable to calculate its change due to earthquake or volcanism,

$$\Delta CFF = \Delta\tau - \mu - (\Delta\sigma_n - \Delta P), \quad (4)$$

and evaluate whether the fault under consideration may be accelerated or decelerated to fracture (Fig. 2). Furthermore, since the change in pore pressure is hard to be measured, it is practical to reduce internal frictional coefficient from the value estimated for dry rock (e.g., King et al., 1994). Assuming $B = \Delta P / \Delta\sigma_n$, we calculate

$$\Delta CFF = \Delta\tau - \mu(1 - B)\Delta\sigma_n = \Delta\tau - \mu'\Delta\sigma_n. \quad (5)$$

Byerlee (1978) estimated μ to be 0.65–0.85 for dry rock. However Reasenberg and Simpson (1992) concluded that μ' can be 0.1–0.3 on the basis of comparison of change in CFF with seismicity changes in central California. We adopt 0.4 for μ' after King et al. (1994).



$$\Delta CFF = \Delta\tau + \mu(\Delta\sigma_n - \Delta P)$$

(μ : Friction Coefficient)

Fig. 2. Coordinate system and stress components for a fault plane. ϕ , δ and λ are strike, dip and rake, respectively. $\Delta\tau$ and $\Delta\sigma_n$ are changes in shear stress in the direction of the assumed slip and normal stress, respectively. ΔP is change in pore pressure.

Okada (1992) gave a closed formula to calculate static displacements and strains in elastic half space for shear or tensile fracture of an arbitrary rectangular fault. We use Okada's formula to calculate stresses at an arbitrary point. Then we calculate shear, normal stresses and ΔCFF for some selected focal mechanisms and compare their distribution with observed seismicity changes.

3. Changes in seismicity around the source region of the Kobe earthquake

The Disaster Prevention Research Institute, Kyoto University (hereafter DPRI) (DPRI, 1995), Ando (1995) and Katao (1995) reported a drastic increase in seismicity in the Tamba region, northeastern extension of the source region, immediately after the Kobe earthquake (Fig. 3). Seismicity is usually high in the Tamba region, but the rate of cumulative number of events increased to 5–6 times more than before the main shock (DPRI, 1995; Katao, 1995). Furthermore seismicity became active along the Yamasaki Fault located northwest of the epicenter, which is a conjugate fault to the Rokko fault system (Fig. 4) (Ando, 1995; Nishigami et al., 1995). On Awaji Island, many aftershocks including a large one of M4.9 ((3) in Fig. 3) occurred along the southwestern extension of the Nojima Fault (Ando, 1995). This event has a nodal plane parallel to the aftershock distribution and a mechanism that is a dominantly right-lateral strike-slip with thrust component (Yoshikawa and Ito, 1995). Nishigami et al. (1995) also reported that the size of earthquakes became smaller in the Sasayama region, north of the epicenter, after the Kobe earthquake (Region C in Fig. 4). On the other hand, seismicity in the Wakayama region, which is one of the most active regions in Japan, showed no notable changes (Earthquake Research Institute, University of Tokyo, 1995). Thus changes in seismicity show variation from place to place.

It is interesting that the largest aftershock (M5.4 (JMA), 7:39 a.m., on January 17 (JST); (1) in Fig. 3) was located off the aftershock distribution (Yoshikawa and Ito, 1995). According to Yoshikawa and Ito (1995), this event has a strike slip type mechanism with *P* axis (maximum compressive axis) rotated clockwise from that of the main shock. There is an active fault trending in the ENE–WSW direction, which is concordant with the strike of one nodal plane of the focal mechanism of this event. It is interesting to assume the stress change due to the main shock induced the activity along this fault.

Since there is no delay between the main shock and these changes in seismicity, we can assume that stress changes due to the main shock induced these seismicity changes. In order to test this hypothesis we examined the stress field calculated for a published fault model.

4. Static stress changes calculated for the geodetic fault model

We use a fault model derived from geodetic data by Hashimoto et al. (1996) (Table 1 and Fig. 5). They assumed the geometry of six rectangular fault planes

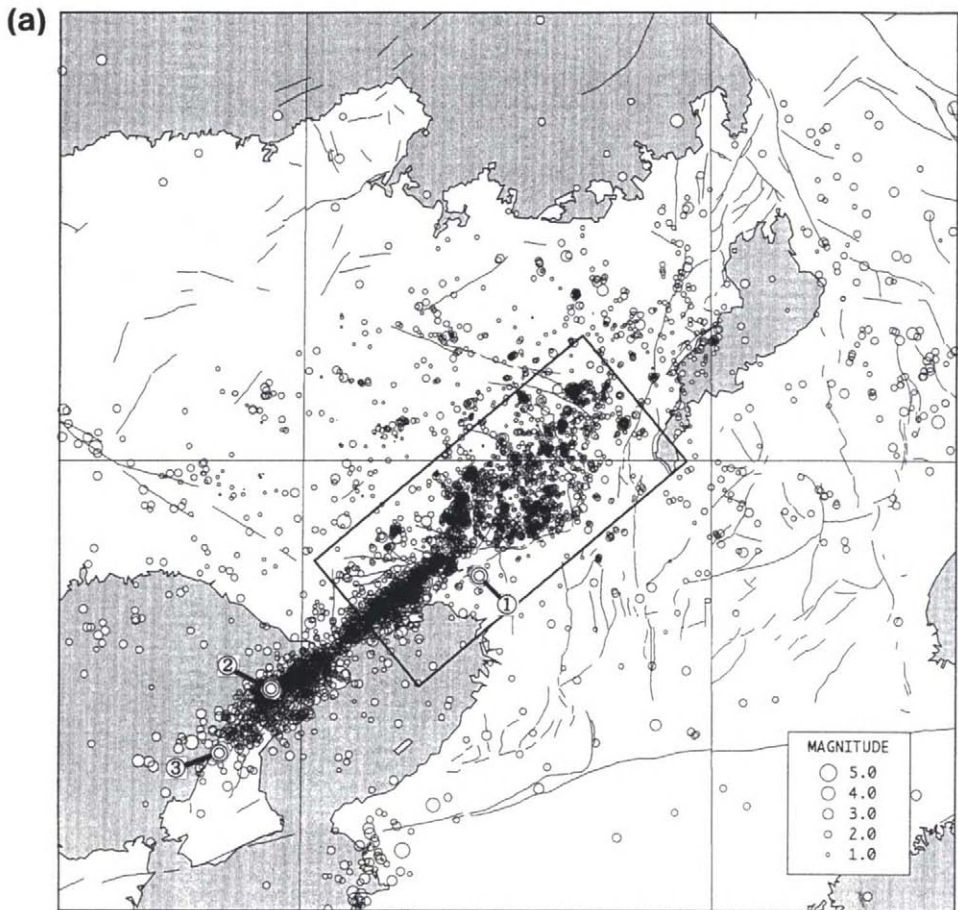
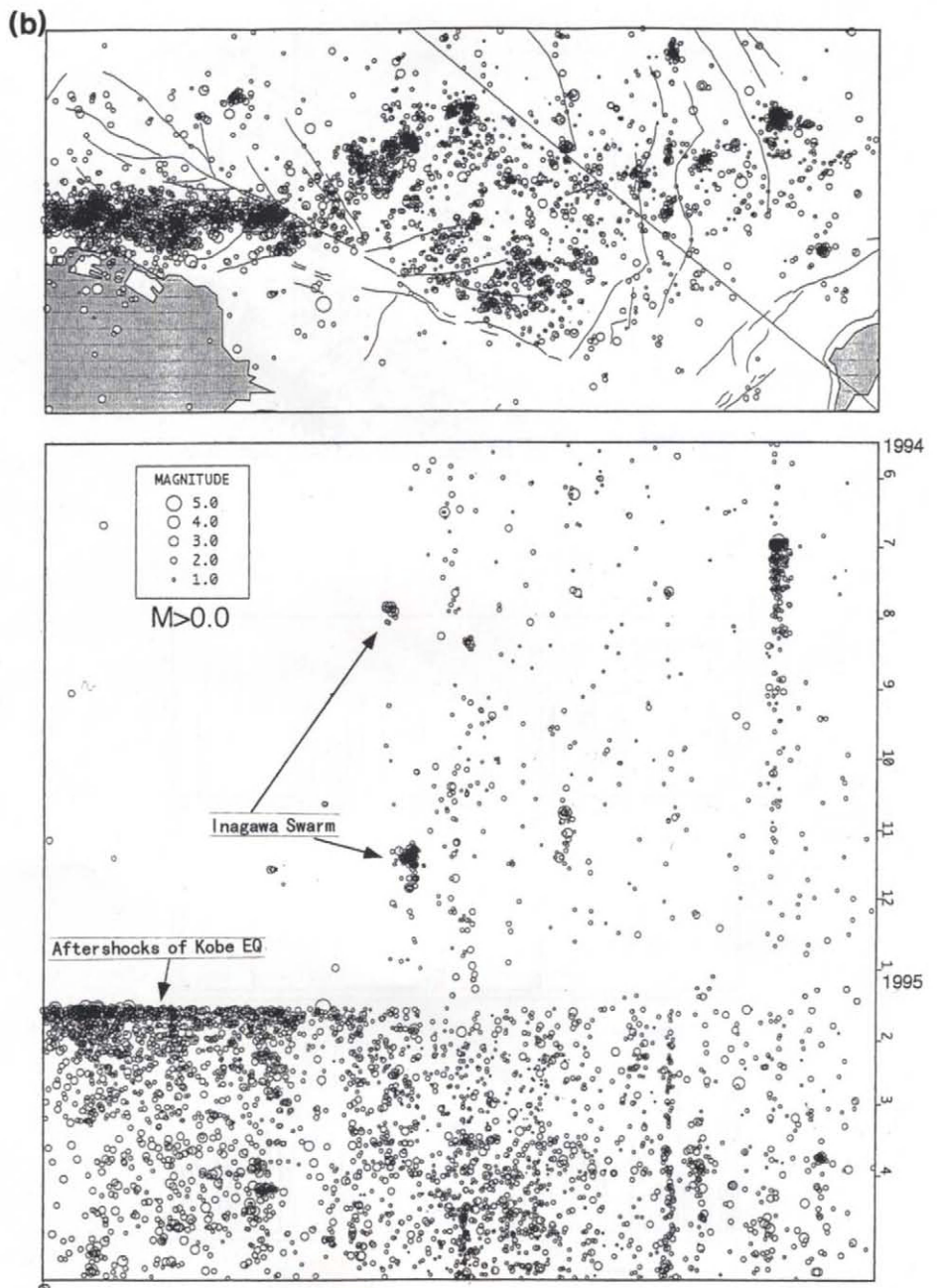


Fig. 3. Shallow seismicity (<30 km) in the northern and central Kinki district during the period from May 16, 1994 to May 15, 1995. (a) Epicentral distribution modified after Disaseter Prevention Research Institute, Kyoto University (DPRI, 1995): double circles with number show epicenters of three large aftershocks discussed in the text (after Yoshikawa and Ito, 1995): (1) 1/17 07:38 (M5.4), (2) 1/17 06:28 (M4.8) and (3) 2/18 21:37 (M4.9). (b) Space-time distribution for the events inside the rectangle in Fig. 3(a) (Disaseter Prevention Research Institute, Kyoto University, DPRI, 1995).

with uniform slip on the basis of distribution of active faults and aftershocks, and estimated the slip of each sub-fault by fitting displacements of continuous GPS sites, distance changes between control points by EDM and GPS surveys, and height changes of benchmarks by leveling in least-squares sense. According to this model, there are three segments of large slip, such as the Nojima fault in the Awaji Island, a segment beneath western Kobe and the Akashi Strait, and the northernmost segment. The former two segments have a slip larger than 2 m, while the last has only a 1-m slip. Some segments have significant thrust components. Comparing



@Seismicisolation

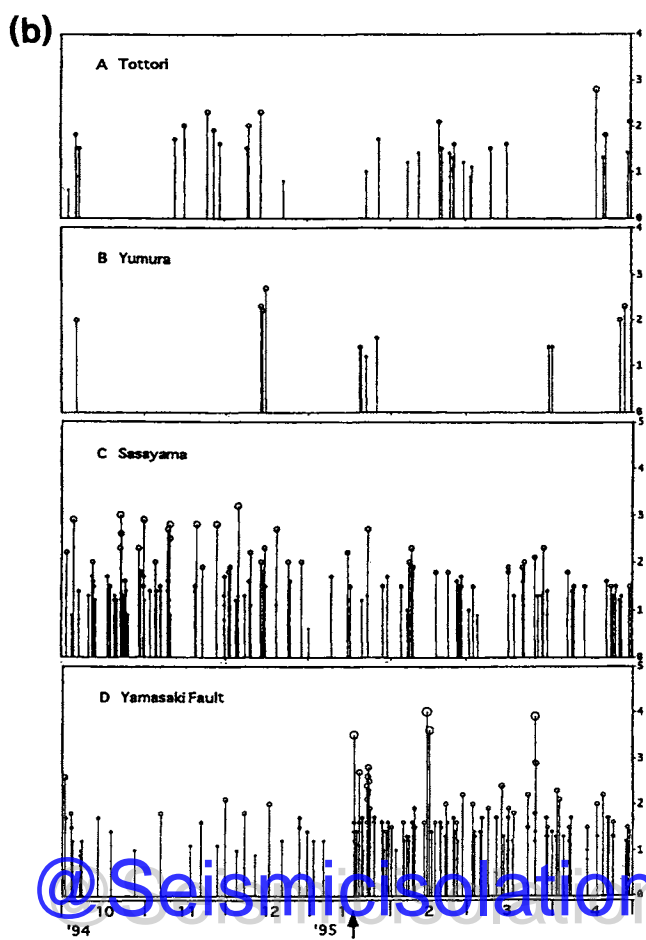
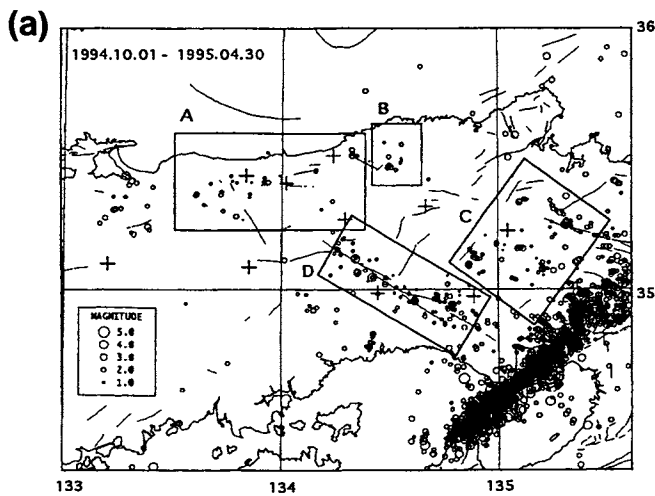


TABLE I

The fault parameters used for stress calculation

#	Lat.	Lon.	<i>L</i>	<i>W</i>	<i>H</i>	Strike	Dip	Rake	<i>U</i>
1	134.777	135.323	10.0	9.0	3.0	225	80	166	1.13
2	34.713	135.244	7.5	9.0	3.0	240	80	120	0.19
3	34.681	135.173	7.5	10.0	2.0	240	70	131	0.39
4	34.646	135.105	7.5	10.0	2.0	233	70	150	2.03
5	34.618	135.014	7.5	10.0	0.0	225	95	186	2.55
6	34.568	134.954	5.0	10.0	0.0	225	95	224	1.78

Legend: #, identification number of segments in Fig. 5; Lat. and Lon., latitude and longitude of the northeastern edge of each segment; *L*, *W* and *H*, length, width and depth of upper margin in km; Strike, strike of each segment measured clockwise from the north; Dip, dip angle from the horizon, positive in the northwest direction; Rake, slip angle measured counterclockwise from the horizon; *U*, slip in m (Hashimoto et al., 1996).

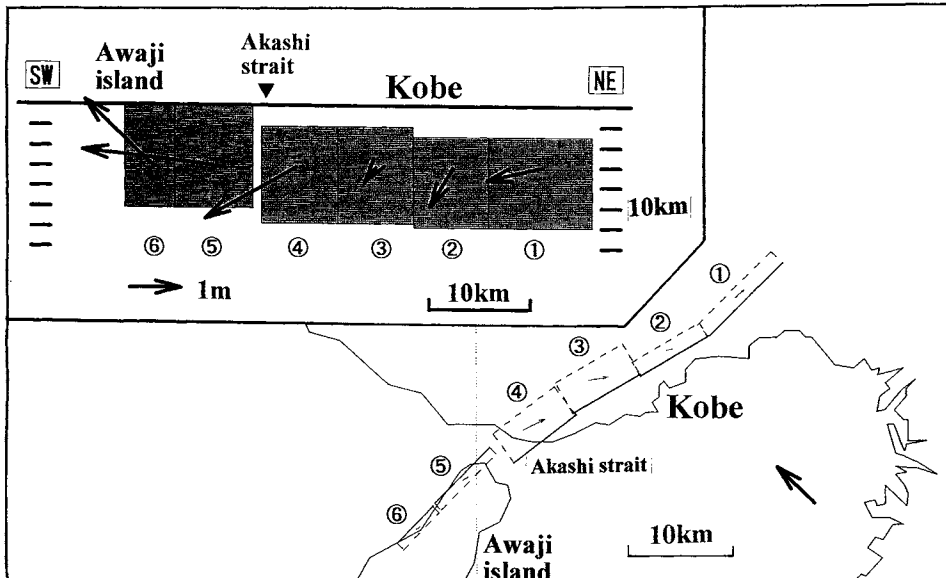


Fig. 5. Geometry and slip distribution of the fault model used for the calculation of stresses (Hashimoto et al., 1996).

Fig. 4. Shallow seismicity in the northwestern Kinki district during the period from October 1, 1994 to April 30, 1995. (a) Epicentral distribution. (b) Space-time distribution in each rectangle shown in (a) (Nishigami et al., 1995).

residuals for several models with different parameter sets for each fault plane, the top margin of segment in the Awaji Island is close to the surface, but those of the segments on the Kobe side become deeper towards the north.

In the Kinki district, many earthquakes have a mechanism of strike-slip type with the P axis in the nearly E–W direction (e.g., Ando, 1994). However the Arima-Takatsuki and median tectonic lines (hereafter ATTL and MTL, respectively) trend in the E–W to ENE–WSW directions, which is not necessarily consistent with the mechanism of earthquakes in this region. Furthermore there are several N–S trending faults which are suspected to be thrust ones (Research Group in Active Faults, 1991). Therefore we calculated Δ CFF for the following mechanisms: (1) right-lateral strike-slip on vertical planes parallel to the aftershock distribution, (2) left-lateral strike-slip on vertical planes parallel to the Yamasaki fault, (3) right-lateral strike-slip on vertical planes parallel to the ATTL and MTL, (4) pure thrust on N–S trending planes which dip 45° in the east and (5) the same mechanism as in (4) but dipping westward. Considering that the average depth of earthquakes in this region is 10 km (Ando, 1994), we adopted 10 km for the depth of calculated points.

Fig. 6(a) shows the distribution of Δ CFF for case (1). Distribution of Δ CFF for case (2), which is not shown, is very similar to that for case (1). There are four lobes of CFF increase which extend far away from the source fault. Three of them, the northeastern and southwestern extensions of modeled fault and the northwestern lobe, coincide with the zone where the seismicity became active. We can therefore conclude that the activation of seismicity in the Tamba region, around the Yamasaki fault and the southwestern extension of the Nojima fault, was due to the stress loading by the main shock. It may be controversial that the fourth lobe which extends southeastward from the middle of the modeled fault has no corresponding seismicity. In the north of the source region, CFF decreased by more than 0.04 MPa, which is concordant with reduced activity in the Sasayama region (C in Fig. 4). Depending on assumed focal mechanism, CFF decreases by less than 0.04 MPa or is close to zero in the Wakayama region, where no notable changes in seismicity were found.

Distribution of Δ CFF for case (3) is also similar to that for case (1), but all lobes are rotated clockwise (Fig. 6(b)). Therefore the eastern half of ATTL is in the region of increase of more than 0.08 MPa. The epicenter of the largest aftershock also is in the region of CFF increase. This result suggests that this aftershock was possibly an off-fault event induced by the main shock. However, because this area is close to the modeled faults, the result may strongly depend on the adopted model. We must check for other fault models derived from seismic data or joint inversion.

We calculated Δ CFF on the vertical cross-sections along the three tectonic lines, the ATTL and MTL and the Yamasaki fault in order to examine the effect of the main shock (Fig. 7). The focal mechanism is assumed to be pure right-lateral strike-slip for the ATTL and MTL, and left-lateral strike-slip for the Yamasaki fault on vertical fault planes. Along the ATTL, which is located very close to the northernmost edge of the modeled fault, large CFF increase and decrease are seen (Fig. 7), but

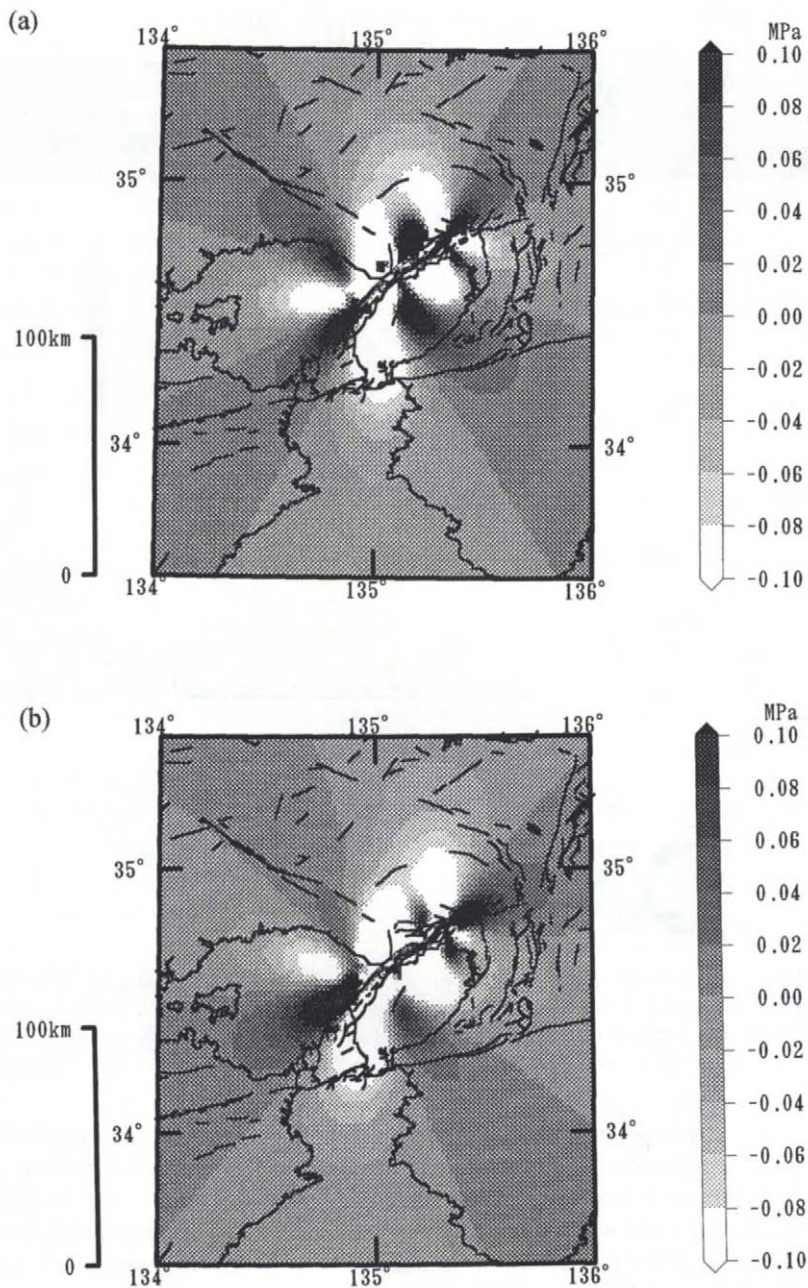


Fig. 6. Changes in Coulomb failure function for right lateral slip on vertical planes at the depth of 10 km. μ' and rigidity are 0.4 and 4×10^{10} GPa, respectively. (a) Case for assumed fault planes trending in N45°E (nearly parallel to the modeled fault). (b) Case for assumed fault planes trending in N78°E (nearly parallel to the Arima-Takatsuki and median tectonic lines).

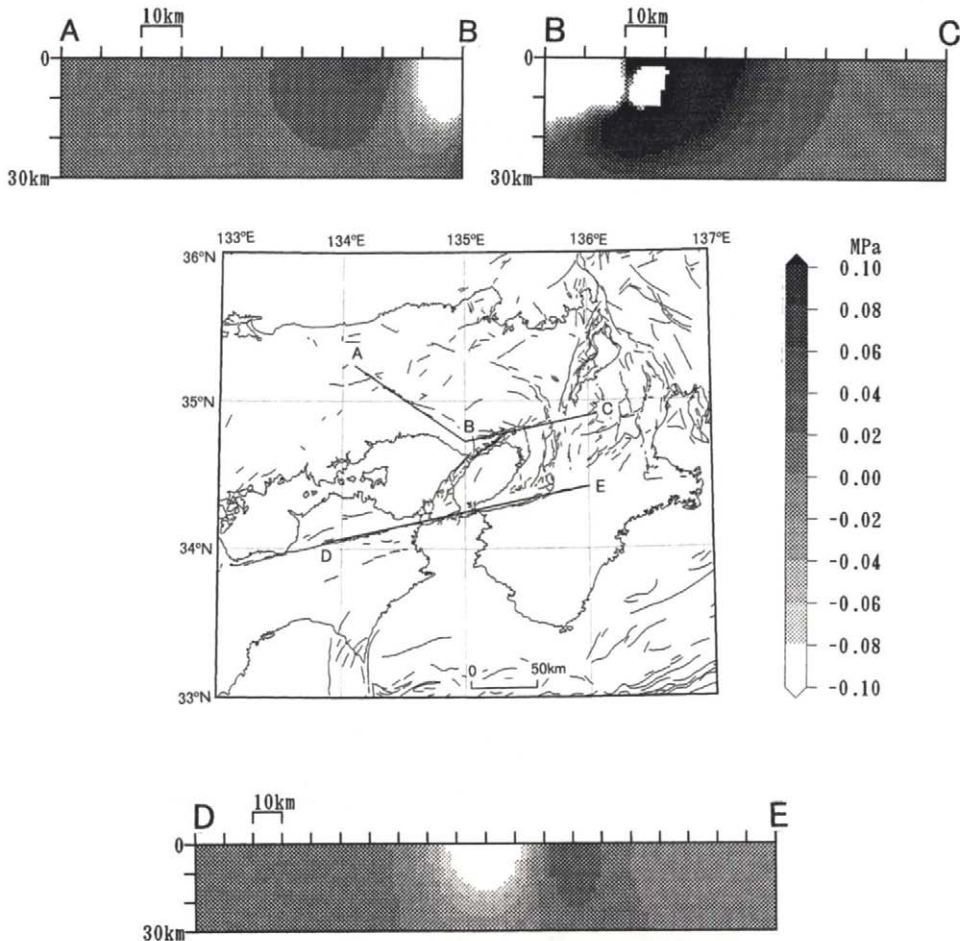


Fig. 7. Changes in Coulomb failure function on the vertical planes between 0 and 30 km along the Yamasaki fault (section A–B), the Arima-Takatsuki tectonic line (section B–C) and the median tectonic line (section D–E). Assumed mechanism is left-lateral strike-slip for the Yamasaki fault, while right-lateral for ATT and MTL. μ' and rigidity are 0.4 and 4×10^{10} GPa, respectively.

these may be attributed to the linear elasticity and model configuration. Even if we neglect these large stress changes near the meeting point with source fault (about 20 km from B), we still see significant increase east of this point. The shallow part of the Yamasaki fault was also loaded by ~ 0.06 MPa (Fig. 7). Along the MTL, we see the zone of CFF decrease by more than 0.1 MPa, sandwiched by zones of CFF increased up to 0.04 MPa (Fig. 7).

Fig. 8 shows the changes in CFF for the mechanisms of N–S trending thrust dipping east- and westward, respectively. Since N–S trending thrust faults are distributed in and around the Osaka plain, we focus our discussion on Δ CFF east

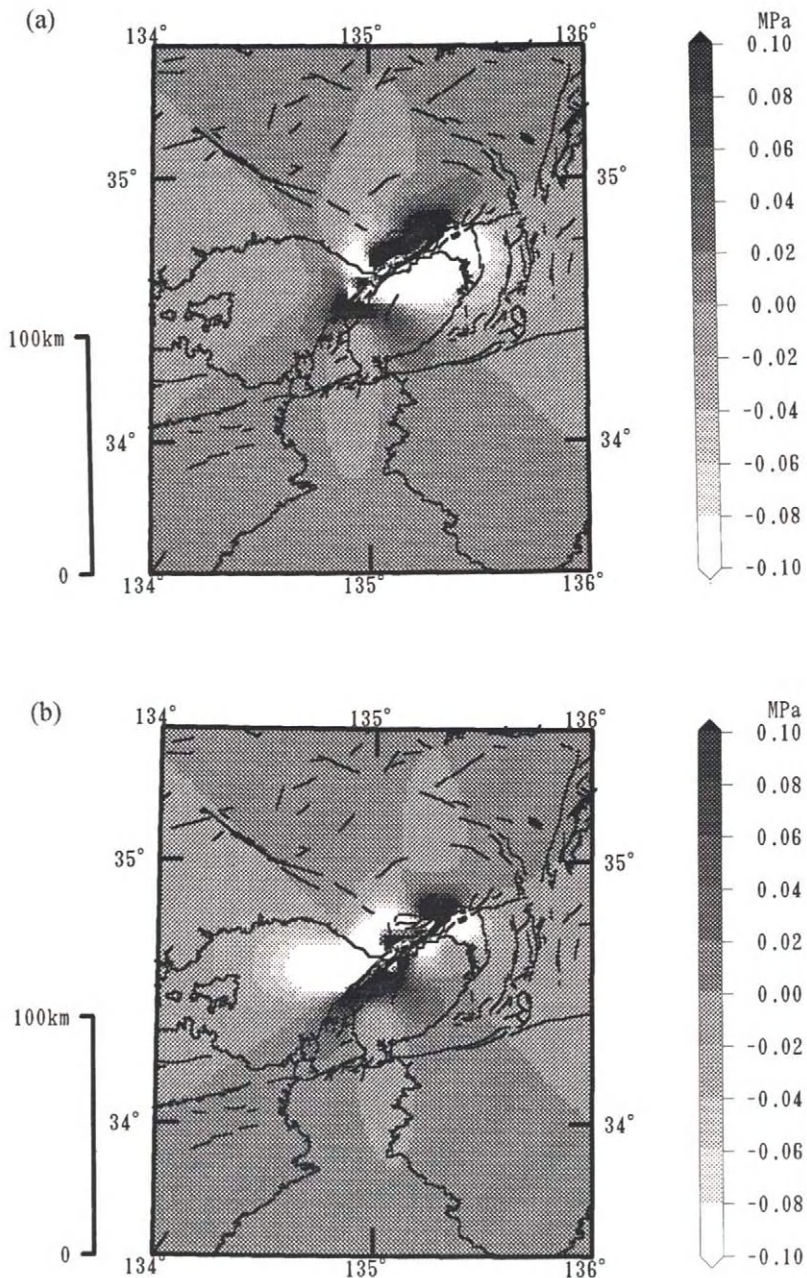


Fig. 8. Changes in Coulomb failure function for thrusting on planes trending NS at a depth of 10 km. (a) Case for fault planes dipping by 45° eastwards. (b) Case for fault planes dipping by 45° westwards. μ' and rigidity are 0.4 and 4×10^{10} GPa, respectively.

of the source region. For the eastward dipping thrust mechanism, CFF decreases by more than 0.1 MPa there (Fig. 8(a)). However decrease of CFF is as small as 0.02 MPa in the Osaka plain for westward dipping thrust faults (Fig. 8(b)). Because the assumed dip and rake are the same, 45° and 90°, respectively, changes in shear stresses are the same for both cases. This difference is due to the change in normal stress. The faulting of the main shock significantly increased normal stress for westward dipping planes east of the source region, while it decreased for eastward dipping faults.

CFF of thrust mechanisms significantly increased on Awaji island (Fig. 8(a)). A large aftershock of M4.8 ((2) in Fig. 3) occurred in this zone of CFF increase. This aftershock has a thrust type mechanism with an E-W trending *P* axis which is concordant with the calculated CFF changes, though it is not clear whether the fault plane dips east or west.

5. Implications for future seismic hazard assessment

We pointed out the possible correlation between changes in seismicity and those in Coulomb failure functions calculated for the geodetic fault model of the Kobe earthquake. In the north of the source region, theoretical stress changes show a satisfactorily good correlation with seismicity changes. Activation of seismicity in the Tamba and Yamasaki regions can be explained by the CFF increase due to the main shock. Decrease of the magnitude of earthquakes in the Sasayama region might also be correlated with the CFF decrease. The largest aftershock, which occurred off the main trend of aftershocks, might be an induced event. Thus theoretical stress changes can be a measure of the possibility of occurrence of events succeeding a large earthquake.

Recently several inversion techniques have been developed for the estimation of coseismic slip of large earthquakes (e.g., Yabuki and Matsuzura, 1992; Wald and Heaton, 1994). Seismic data can be collected in nearly real time through networks. Deployment of a continuous GPS observation system also enables us to rapidly detect coseismic deformations (e.g., Tsuji et al., 1995). Therefore it may not be impossible to obtain slip distributions of a large earthquake within a day or two after its occurrence. On the basis of this estimated slip distribution we can calculate CFF changes easily, and point out possible regions of seismicity increase or induced events.

Of course, there are some exceptions for which Δ CFF is inconsistent with seismicity changes, such as the predicted CFF increase in the Osaka Bay. There may be several reasons.

The first reason is the simplicity of the assumed model. The present geodetic model consists of six sub-faults, each of which has a uniform slip. Uniform slip faults causes infinite stress at their edges. Therefore we must suspect large stresses near the modeled faults; and it is necessary to calculate for more sophisticated fault models with smooth slip variations obtained by joint inversion.

The second reason is the effect of coefficient of internal frictional. We adopted a relatively low value of 0.4. Reasenberg and Simpson (1992) concluded that the optimal range is 0.1–0.3 for the Californian earthquake by computing Δ CFF for several values and comparing them with seismicity changes. It is controversial to incorporate the results in California directly because the condition of underground water in Japan might be different from that in California. It may be interesting to estimate the coefficient of internal friction in Japan using a similar method to Reasenberg and Simpson (1992). However it is essential to determine this parameter by integrating the information of underground water and crustal structure and the results of rock experiments.

The third reason is the effect of crustal structure itself. We assumed a homogeneous elastic half space. Actually there are crustal heterogeneities, such as difference in rocks, alluviums or faults, etc., in the Kinki district. These factors may strongly affect the stress field. However, it is hard to calculate stresses in heterogeneous material with thin weak zones or discontinuities like geological or seismic faults. We must develop a numerical method to deal with such complicated material.

There are other drawbacks in this calculation. Since we assume a purely elastic model, which enables us a fast and feasible calculation, the estimated stress changes are static and this method is unable to predict increase or decay of stress depending on elapsed time. As the next step, for more practical purpose, we must incorporate time-dependent responses, such as viscoelasticity and secular movements of plates.

The predicted CFF increase is quite a bit lower in the Tamba region than along the ATTL, but changes in seismicity are much more remarkable. We have not established any quantitative relationship between the amount of CFF changes and the seismicity changes or the size of induced events. This is because the occurrence of an earthquake depends not only on the stress increases, but also on the strength of faults and stress level immediately before the main shock. Therefore, it is essential to get repeated information on the stress level of faults, by geodetic work, in situ measurements, excavation of faults, etc., in order to evaluate the potential that faults would be activated in response to large earthquakes.

6. Conclusions

We calculated changes in Coulomb failure function for a geodetic fault model of the Kobe earthquake to compare them with seismicity changes in the surrounding regions, and derived the following conclusions.

- (1) Calculated CFF for right-lateral slip on NE–SW trending vertical planes or left-lateral slip on NW–SE trending vertical planes, which are dominant focal mechanisms in this area, are in good accordance with the observed seismicity changes. CFF increases in the northeastern extension of source region and around the Yamasaki fault, where the activation of seismicity was also observed after the main shock. CFF decreases in the north of the source region, where the size of earthquakes became smaller than before the main shock. CFF may

decrease a little in the Wakayama region, where no notable changes in seismicity were observed.

- (2) The Kobe Earthquake may have loaded stresses which might lead to right-lateral slip on the eastern half of the Arima-Takatsuki tectonic line and segments of the median tectonic line in the Wakayama and Tokushima regions. Since these faults have no record of M7 or greater events during at least 400 years, we should pay attention to the seismicity around these tectonic faults.

Acknowledgment

I would like to thank Drs. Takashi Tada, Takeshi Sagiya and Prof. Tetsuzo Seno for their helpful comments. I also thank Dr. Yoshimitsu Okada who kindly permitted me to use his program of dislocation model.

References

- Ando, M., 1994. Microearthquakes. In: Summery of Observations for Earthquake Prediction in Japan (Part 3) – Kinki, Chugoku, Shikoku, Kyushu and Okinawa Areas, Special Report of the Regional Subcommittee for Earthquake Prediction, Vol. 6, pp. 32–84 (in Japanese).
- Ando, M., 1995. Foreshocks, main shock, aftershocks and induced earthquakes. Earth Monthly (Supplement 13): 18–29 (in Japanese).
- Byerlee, J.D., 1978. Friction in rocks. Pure Appl. Geophys., 116: 615–626.
- Disaster Prevention Research Institute, Kyoto University, 1995. Activation of seismicity in the northern Kinki district. Report of Coordinating Committee for Earthquake Prediction, 54: 517–521 (in Japanese).
- Earthquake Research Institute, University of Tokyo, 1995. Seismic activity in and around the Kii Peninsula (January–March, 1995). Rep. Coordinating Committee for Earthquake Prediction, 54: 527–542 (in Japanese).
- Geological Survey of Japan, 1995. presented at the 111th Meeting of the Coordinating Committee for Earthquake Prediction on January 18, 1995.
- Harris, R.A. and Simpson, R.W., 1992. Changes in static stress on southern California faults after the 1992 Landers earthquake. Nature, 360: 251–254.
- Hashimoto, M., Sagiya, T., Tsuji, H., Hatanaka, Y. and Tada, T., 1996. Coseismic displacements of the 1995 Hyogo-Ken Nanbu earthquake. J. Phys. Earth, in press.
- Hudnut, K.W., Seeber, L. and Pacheco, J., 1989. Cross-fault triggering in the November 1987 Superstition Hills earthquake sequence, southern California. Geophys. Res. Lett., 16: 199–202.
- Katao, H., 1995. Seismicity in Hokusetsu-Tamba region before/after the Hyogoken-Nanbu earthquake. Prog. Abstr. of the 1995 Fall Meeting of Seismol. Soc. Japan, A49 (in Japanese).
- King, G.C.P., Stein, R.S. and Lin, J., 1994. Static stress changes and triggering of earthquakes. Bull. Seismol. Soc. Am., 84: 935–953.
- Larsen, S., Reilinger, R., Neugebauer, H. and Strange, W. 1992. Global positioning system measurements of deformations associated with the 1987 Superstition Hills earthquake: Evidence for conjugate faulting. J. Geophys. Res., 97: 4885–4902.
- Mizoue, M., Nakamura, M. and Seto, N., 1995. Fault systems accompanied by induced seismicity around the source region of the 1995 Kobe earthquake. Earth Monthly (Supplement 13): 38–46 (in Japanese).
- Nishigami, K., Nakao, S., Yabe, S., Watanabe, K. and Matsumura, K., 1995. Change in seismicity in the

- eastern Chugoku region after the 1995 Hyogoken-Nanbu earthquake. *Prog. Abstr. Of the 1995 Fall Meeting of Seismol. Soc. Japan*, A50 (in Japanese).
- Okada, Y., 1992. Internal deformation due to shear and tensile faults in a half-space. *Bull. Seismol. Soc. Am.*, 82: 1018–1040.
- Reasenberg, P.A. and Simpson, R.W., 1992. Response of regional seismicity to the static stress change produced by the Loma Prieta earthquake. *Science*, 255, 1687–1690.
- Research Group for Active Faults in Japan, 1991. *Active Faults in Japan (Revised) – Map and Data*, University of Tokyo Press, 437 pp. (in Japanese).
- Scholz, C.H., 1990. *The Mechanics of Earthquakes and Faulting*. Cambridge Univ. Press, 439 pp.
- Seno, T., 1995. *Fundamentals in Plate Tectonics*. Asakura Shoten, 190 pp. (in Japanese).
- Stein, R.S., King, G.C.P. and Lin, J., 1992. Change in failure stress on the southern San Andreas fault system caused by the 1992 magnitude=7.4 Landers earthquake. *Science*, 258: 1328–1332.
- Tsuji, H., Hatanaka, Y., Sagiya, T. and Hashimoto, M., 1995. Coseismic crustal deformation from the 1994 Hokkaido-Toho-Oki earthquake monitored by a nation-wide continuous GPS array in Japan. *Geophys. Res. Lett.*, 22: 1669–1672.
- Wald, D.J. and Heaton, T.H., 1994. Spatial and temporal distribution of slip for the Landers, California, earthquake. *Bull. Seismol. Soc. Am.*, 84: 668–691.
- Yabuki, T. and Matsu'ura, M., 1992. Geodetic data inversion using a Bayesian information criterion for spatial distribution of fault slip. *Geophys. J. Int.*, 109: 363–375.
- Yamashina, K., 1978. Induced earthquakes in the Izu peninsula by the Izu-Hanto-Oki earthquake of 1974, Japan. *Tectonophysics*, 51: 139–154.
- Yoshikawa, S. and Ito, H., 1995. Outline of the 1995 Kobe earthquake. *Earth Monthly (Supplement 13)*: 30–38 (in Japanese).

Bedrock structure around faults and its relation to earthquake disaster

JUNPEI AKAMATSU^{a,*}, KEIICHI NISHIMURA^b, HITOSHI MORIKAWA^c, SUMIO SAWADA^c, KENSUKE ONOUE^a, HIDEO SAITO^a, MITSURU JIDO^a, TAKAO KAGAWA^d, KAZUO KAMURA^e, KENJI SATO^e, KUNIO FURUNO^e and MASAI KOMAZAWA^f

^a*Disaster Prevention Research Institute, Kyoto University, Gokasho, Uji, Kyoto 611, Japan*, ^b*Geophysical Institute, Graduate School of Science, Kyoto University, Sakyo, Kyoto 606-01, Japan*, ^c*Civil Engineering, Graduate School of Engineering, Kyoto University, Sakyo, Kyoto 606-01, Japan*, ^d*Geo-Research Institute, 3-1-23, Nishi-honmachi, Nishi-ku, Osaka 550, Japan*, ^e*Research Institute of Environment Geology Chiba, 3-5-1 Inage-kaigan, Mihamachi, Chiba 261, Japan* and ^f*Geological Survey of Japan, 1-1-3, Higashi, Tsukuba 305, Japan*

Abstract

The frequency-wavenumber and horizontal-to-vertical ratio spectral analyses of microseisms (long-period microtremors), and the bandpass filtering of Bouguer gravity anomalies, were conducted to elucidate the subsurface structure around the eastern end of the severely damaged belt-like zone in the Kobe-Hanshin area which appeared during the 1995 Hyogoken-nanbu (Kobe) earthquake. A close relationship was found between the fault-related bedrock configuration thus obtained and the distribution of earthquake damage: a narrow zone of severe damage was located 1.5–2 km apart from the basin edge where the depth to bedrock changes abruptly by several hundreds to a thousand meters. The relationship was attributed to the amplification of ground motions due to the specific configuration of bedrock, that is, focusing of seismic waves and/or interference between incident S-waves and surface-waves secondarily generated at the basin edge. It is pointed out, as a lesson learned from the Hyogoken-nanbu earthquake disaster, that the investigation of fault-related 3-D bedrock configuration is an urgent issue for hazard mapping of an urban area on a sedimentary basin.

1. Introduction

The Hyogoken-nanbu (Kobe) Earthquake of January 17, 1995 ($M7.2$), brought destructive earthquake damage to the Kobe-Hanshin area on the northern margin of Osaka basin, west Japan. The extremely severe damage of JMA (Japan

* Corresponding author.

Meteorological Agency) Intensity 7 is distributed in an E-W to ENE-WSW oriented belt-like zone running through the narrow urban area between the Rokko mountains to the north and the Osaka bay to the south. There are different opinions concerning the cause of damage distribution: the movement of unknown buried active faults or the amplification of ground motions by thin Alluvial deposits and/or by deeper sedimentary layers. For example, Shimamoto et al. (1996) considered the belt-like distribution of severe damage as a surface manifestation of displacements along a buried fault just below the damage zone. Hirano and Hada (1996) suggested that surface faulting and failures appeared not only along several pre-existing Quaternary faults, but also along their extensions within the damaged zone. On the other hand, according to the seismological studies, the seismogenic faults were located not under the belt-like zone, but 1–2 km northwest of the zone (e.g., Sekiguchi et al., 1996). Pitarka et al. (1996) suggested a possibility that earthquake ground motions were amplified largely in the damaged zone by the step-like configuration of bedrock on the basin edge. Similar effects of bedrock configuration have been also suggested for the damage distribution in a wide area far from the source region, including the Osaka plain (Nakagawa et al., 1996) and the Kyoto basin (Study Group of Geology of Higashiyama High School and Yasumatsu, 1995).

The study area of this paper is located in the eastern part of the severely damaged zone. In this area, the damaged zone turns northward along a narrow zone in a sedimentary basin located about 1.5 km from the eastern end of the Rokko mountains. An active fault called the Koyo fault runs across the study area in a NE-SW direction. According to the aftershock observations with a linear array, the depth to bedrock changes abruptly from northwest to southeast across the Koyo fault (Nishimura et al., 1996; Waga et al., 1996). It should be noted that the study area, including the Koyo fault, is situated about 6 km east of the northeastern edge of the seismologically determined seismogenic fault. This suggests that the damage distribution in the area was controlled by the bedrock configuration and, therefore, that it is important to study the subsurface structure to clarify the cause of earthquake damage. This is the main purpose of this study.

In the following we use geophysical data, such as microseisms (long-period microtremors) and gravity anomaly, to elucidate the 3-D bedrock configuration. As we have already shown (Akamatsu et al., 1994a,b, 1996a,b), the comparative analysis of microseisms and gravity data is useful to study 3-D subsurface structure aiming at the microzonation of the sedimentary region.

2. Geological setting

Fig. 1 is a map of the northern part of the Osaka basin, showing the location of study area and the severely damaged zone of JMA Intensity 7. The basin is bounded on the north by the Rokko mountains (mainly Late Cretaceous granitic rocks) and the Tamba mountains (Mesozoic and Pleistocene). Along the boundary, there are many active faults forming the Rokko fault system and the Arima-Takatsuki tectonic line. The Kobe-Hanshin area is located between the Rokko mountains and

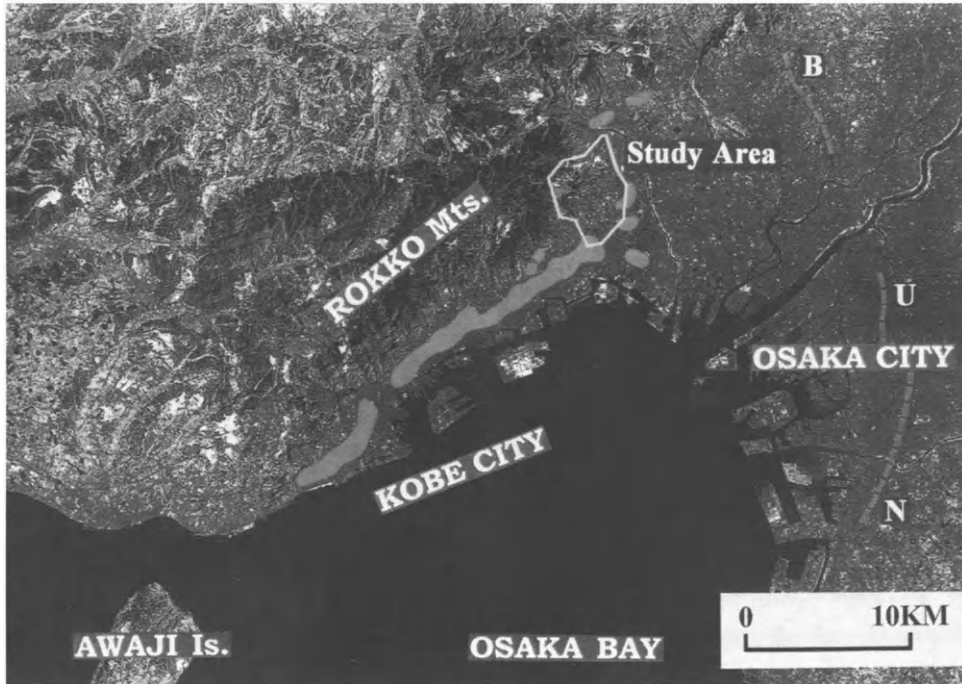


Fig. 1. Map of the northern part of the Osaka basin. The severely damaged belt-like zone of JMA Intensity 7 is colored red, and the study area yellow. The green broken lines show the faults in the Osaka plain: B, Butsunenji-yama; U, Uemachi; and N, Nagai faults.

the Osaka bay. The depth to bedrock in the area is estimated to be several hundreds to 1000 m or more (Endo et al., 1995; Iwata et al., 1996; Nakagawa et al., 1996).

The study area, northern Nishinomiya City and southern Takarazuka City, is located around the eastern end of the Rokko mountains. Fig. 2 shows the geological map and the active faults belonging to the Rokko fault system, the Koyo fault and the Ashiya fault. Between the two faults, stands Mt. Kabuto-yama comprised mainly of granitic rocks (309 m high), which is surrounded by the Lower Subgroup of Osaka Group (Early Pleistocene) with terraces formed by Late Pleistocene deposits. To the southeast of the Koyo fault, the same terraces are formed on the Upper Subgroup of Osaka Group (Middle Pleistocene). The elevation of the ground surface above sea level is about 150–200 m around Mt. Kabuto-yama, and about 50–80 m to the southeast of the Koyo fault.

3. Subsurface structure inferred from analyses of microseisms

3.1. Observations

We conducted extensive observations of microseisms to obtain suitable data for studying 3-D subsurface structure. The employed method of investigation is fre-

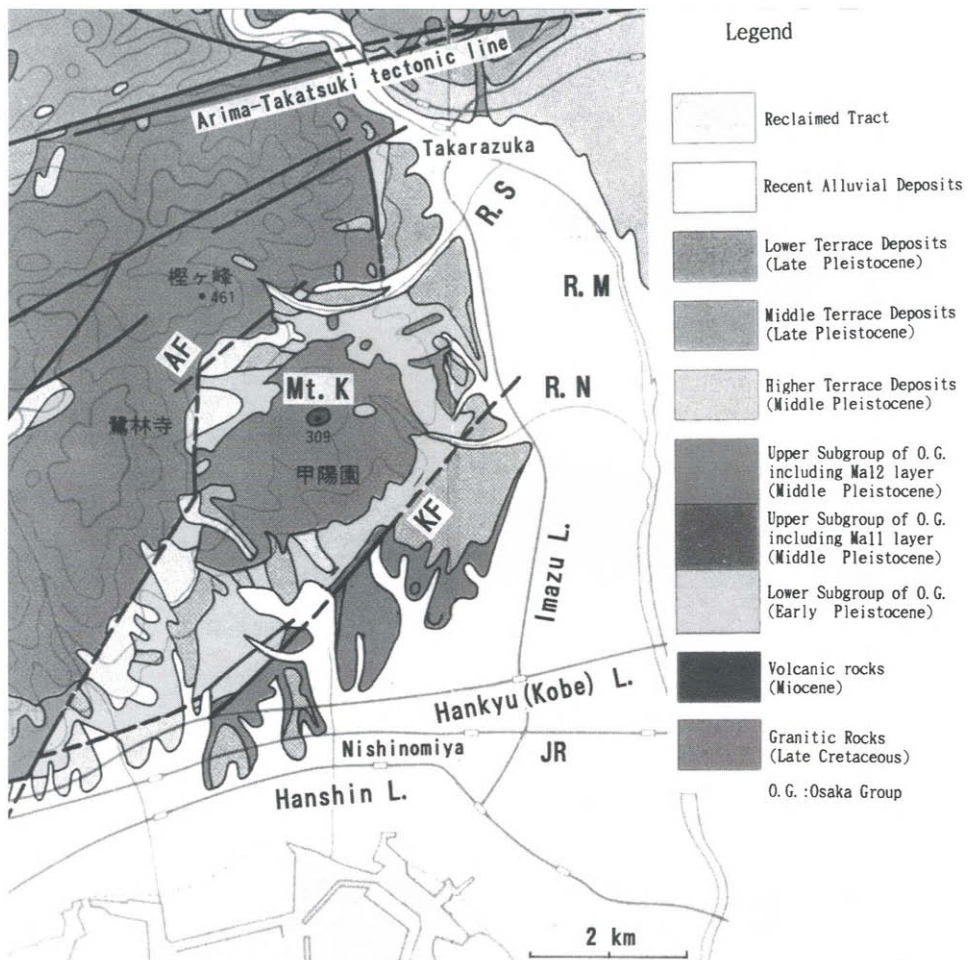


Fig. 2. Geological map in and around the study area with fault traces: KF, Koyo fault; and AF, Ashiya fault. Mt.K indicates Mt. Kabuto-yama. R.M, R.S and R.N indicate the rivers: Mukogawa, Sakasegawa and Nigawa, respectively. Railway lines are shown. The map is reproduced from Itihara et al. (1991).

quency-wavenumber ($f\text{-}k$) spectral analysis of vertical components of microseisms, which gives the dispersion of phase velocities of Rayleigh-waves used for determining subsurface velocity structure. We also examine spectral ratio of microseisms between the horizontal and vertical components (H/V) to obtain the characteristic frequency of soil ground, which in turn provides the information about the depth to bedrock. For this, array observations were carried out using seven sets from a three-component seismometer with a natural period of 10 s. Two sets were fixed on reference sites to monitor the temporal variation of microseisms: one on a rock site, OHK, and the other on an Alluvial site, NHS. Five other sets were moved from

site to site to form seismic arrays of various sizes and shapes for simultaneous observations. The distance between the sites ranged from 250 to 500 m. All 75 observation sites are shown in Fig. 6. Observations were made at night to avoid local traffic noise. Digital records (20 min) were obtained at all sites. Data were sampled every 0.01 s after passing through 10-Hz anti-alias (lowpass) filters. The accuracy of timing was 0.01 s. As a result, a total of 15 array datasets were obtained.

3.2. Velocity structure from f - k spectral analysis and H/V analysis

The f - k spectral analysis was performed to obtain the phase velocity and the direction of propagation of Rayleigh-wave components of microseisms. The analysis is based on the maximum likelihood method (MLM) (Capon, 1969; Horike, 1980). Before applying the method, we corrected a seismogram for instrumental characteristics to obtain ground velocity, and selected proper portions of the seismogram which were uncontaminated by local traffic noise. The length of the selected portions was 50–80 s for each dataset, which was sufficient for spectral analysis, judging from the frequency components of the microseisms. Four or five portions were selected for each array.

Among 15 array datasets, six were obtained from linear array observations and nine were from 2-D arrays. We present the results of analysis for the four 2-D arrays, shown in Fig. 3, which are considered most suitable to investigate the difference in the bedrock configuration between both sides of the Koyo fault. The

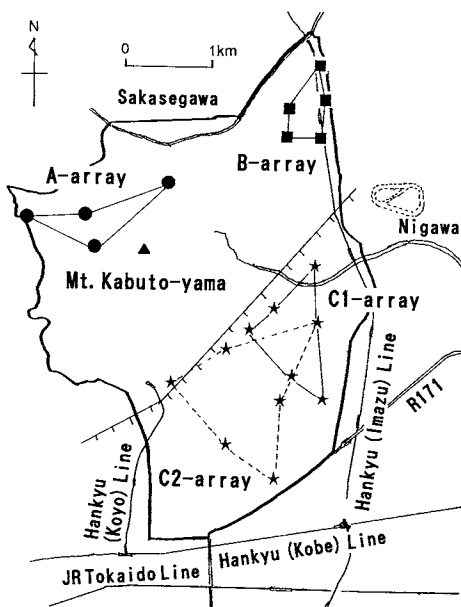


Fig. 3. Location of the arrays for f - k spectral analysis of microseisms.

A- and B-arrays are located on the northwest side of the Koyo fault, and the C1- and C2-arrays on the southeast side. The results of analysis for C1- and C2-arrays were combined to obtain a single dispersion curve of phase velocities. Fig. 4 shows the dispersion curves of phase velocities from each array. As seen from the figure, the phase velocities for all the arrays show normal dispersion, and those from the A- and B-arrays are remarkably higher than the C1- and C2-arrays. The difference in the frequency range between A- and B-arrays and C1- and C2-arrays is due to the difference in the degree of resolution which depends on the ratio of array size to wavelength.

From the dispersion curves obtained above, we estimated the subsurface velocity structures of three regions using the inversion method. The initial structural model was composed of three layers overlying on a half space, with the layer parameters as defined in the Kagawa et al. (1992) model for the Osaka plain. The inversion was performed by changing the thickness value of the layers with the velocities and densities being fixed. The optimal thickness of layers was determined in the sense of the least-squares method, that is, by minimizing the power of the difference between the observed and theoretical phase velocities. Fig. 5 shows the structural models obtained for three regions, and the corresponding theoretical dispersion curves are drawn in Fig. 4. The total thickness of sediments is estimated at 300 m for the A-array, and at 400 m for the B-array in the northwest of the Koyo fault. On the other hand, the thickness is as much as 850 m for C-arrays to the southeast of the Koyo fault.

In the next step, we examined the spatial distribution of the peak period of H/V to obtain additional information about the depth to bedrock in the whole study area. This investigation is based on the fact that there is an empirical relation between peak period of H/V and the depth to bedrock for an area on thick soil-sediments, as long as there is a sharp velocity contrast between soil-sediments and

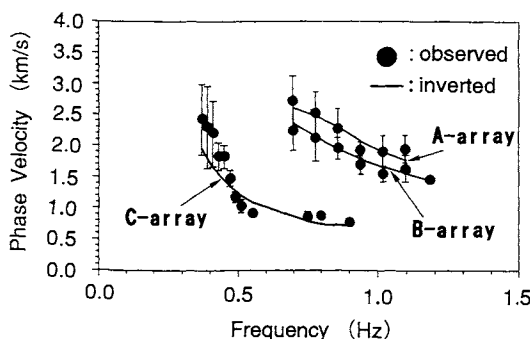


Fig. 4. Observed phase velocities of microseisms and theoretical dispersion curves of Rayleigh waves for each array. The observed phase velocities from C1- and C2-arrays are combined to obtain a single dispersion curve (C-array). Theoretical dispersion curves are calculated for the optimal models shown in Fig. 5. Note the large difference in dispersion characteristics between the A- and B-array regions and the C-array region.

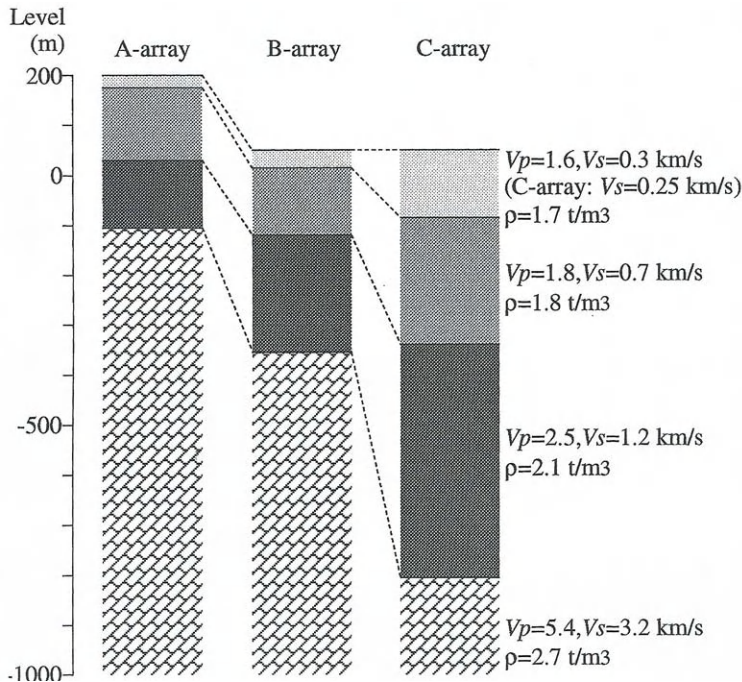


Fig. 5. Subsurface structural models for each array region. Note that bedrock subsides from -100 m (A-array) to -800 m (C-array) across the Koyo fault.

bedrock (Akamatsu et al., 1994b). Hereafter we call this “ H/V analysis”. H/V analysis for the investigation of subsurface structures was originally proposed by Nogoshi and Igarashi (1971), who examined the relationship between the H/V of short-period microtremors and the shallow structure of sedimentary basins. Recently, Nakamura (1989) applied the H/V method to the study of site response to short-period earthquake ground motions. We are applying H/V analysis to the investigation of bedrock configuration by extending the period range to those of microseisms.

Fig. 6 shows the distribution of peak period T_p of H/V around the Koyo fault. In the figure, the squares indicate the sites where a sharp peak of H/V was observed, and the triangles indicate the sites without remarkable peaks. The size of the square represents the period range of T_p . It is clear that there is a sharp contrast in appearance of peaks and distribution of T_p between both sides of the Koyo fault: (1) on the northwest side of the Koyo fault, remarkable peaks are not observed at many sites, except for the sites around Mt. Kabuto-yama where T_p is less than 1.5 s; (2) on the southeast side of the Koyo fault, T_p is larger than about 2.5 s, increasing gradually toward the southeast to 4.0 s or more; and (3) in the northernmost part of the study area T_p is about 2.0 s, although the sites are located on the north side of the fault.

These features observed from the distribution of T_p are in general accord with

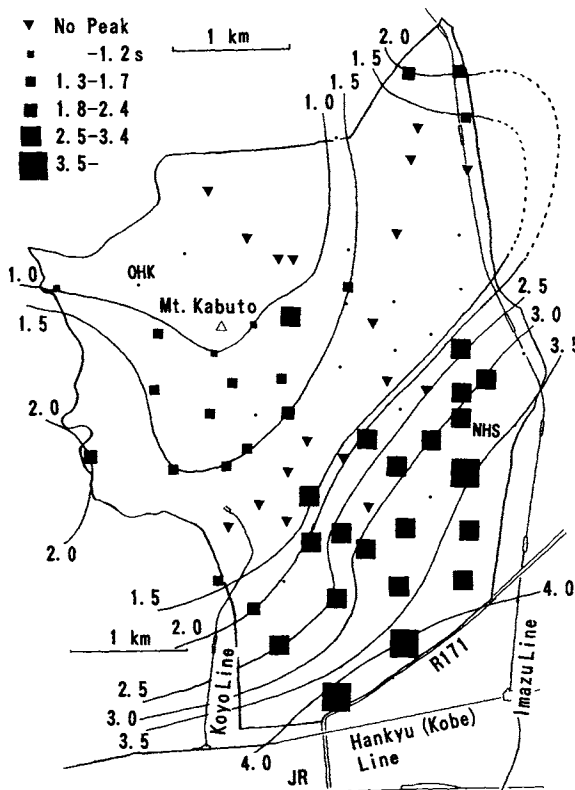


Fig. 6. Distribution of peak period T_p for H/V of microseisms. Squares indicate the site where a sharp H/V peak was observed, and its size represents the period range of T_p . Triangles indicate the sites without remarkable peaks. Dots indicate the sites for which data analysis is under way. Note a sharp contrast in the appearance of peaks and the distribution of T_p between both sides of the Koyo fault. It is also notable that sharp peaks with large T_p values were observed in the northernmost sites, although these sites are located on the north side of the Koyo fault.

the results obtained by f - k spectral analysis mentioned above. In the region of the A-array where the thickness of sediments is estimated about 300 m, no remarkable peaks of H/V were observed; in the region of the B-array with 400-m thick sediments, we found fairly remarkable peaks with a period of 1.5–2.0 s; and in the region of the C-array, remarkable peaks of H/V with a period range of 2.5–4.0 s correspond to the large thickness of sediments reaching up to 850 m.

4. Configuration of bedrock from bandpass-filtered Bouguer gravity anomaly

To discuss 3-D configuration of bedrock, we analyzed the gravity data compiled by the Geological Survey of Japan. The procedure of analysis is as follows: (1)

calculation of the Bouguer gravity anomaly as mesh data with a 500 m grid interval, using a reduction density of 2.45 g cm^{-3} which is regarded to be the most appropriate to the region around the Osaka basin (Shichi et al., 1996); (2) removal from the gravity anomaly of the regional component with a large wavelength and so-called noise with an extremely small wavelength, with the combined use of an upward-continuation filter (Gupta and Ramani, 1980). The residual component of gravity anomaly, obtained as the difference between two anomalies, upward-continued to heights of 50 and 2000 m, respectively, considered to be bandpass-filtered anomalies, is characterized by wavelengths smaller than about 6 km. According to Komazawa (1984), the bandpass-filtered anomalies thus obtained are due to the density distribution down to a depth of about 2 km. In this depth range the difference in density is largest between the soil-sediments and the bedrock. Therefore, it is highly probable that the bandpass-filtered anomaly reflects the configuration of bedrock.

Fig. 7 shows the map of the bandpass-filtered Bouguer gravity anomaly. The contour intervals are 0.5 mGal. The white and dotted areas show negative and positive anomalies, respectively. The anomaly changes rapidly from positive to negative values in the NW-SE direction near across the Koyo fault. Fig. 8 shows the gravity profiles for microseisms along the various directions from the observation site, OHK. Profiles, nos. 4–7, cross the known surface-trace of the Koyo fault, while on profiles 1–3, no surface-traces of faults are observed. The location of the Koyo fault is indicated with a bold arrow. It is apparent from simple numerical modeling that the positive to negative change in anomalies, and their spatial distribution on profiles 4–7, indicate the existence of a dip fault and its location. It should be noted that the spatial patterns of anomalies in profiles 1–3 are very similar to those in 4–7. This suggests that there exists a step-like subsidence of bedrock across profiles 1–3, although its location is not on the extension of the Koyo fault.

5. Discussion

5.1. Subsurface structure and depth to bedrock

The results of f - k and H/V analyses of microseisms show that the bedrock configuration in the study area is rather complicated. The depth to bedrock is quite different on both sides of the NE-SW-oriented Koyo fault: –100 m from sea level in the northwest region and –800 m in the southwest region, if we take into account the elevation of the observation sites. The change in depth to bedrock across the Koyo fault is also suggested by bandpass-filtered Bouguer gravity anomalies on profiles 4–7 shown in Fig. 8. The positive anomalies on the northwest side of the fault imply elevated bedrocks, and the negative anomalies on the southeast side the subsidence of bedrocks.

In the study area, Nishimura et al. (1996) and Waga et al. (1996) made aftershock observations with a linear array crossing the Koyo fault at right angles. They found

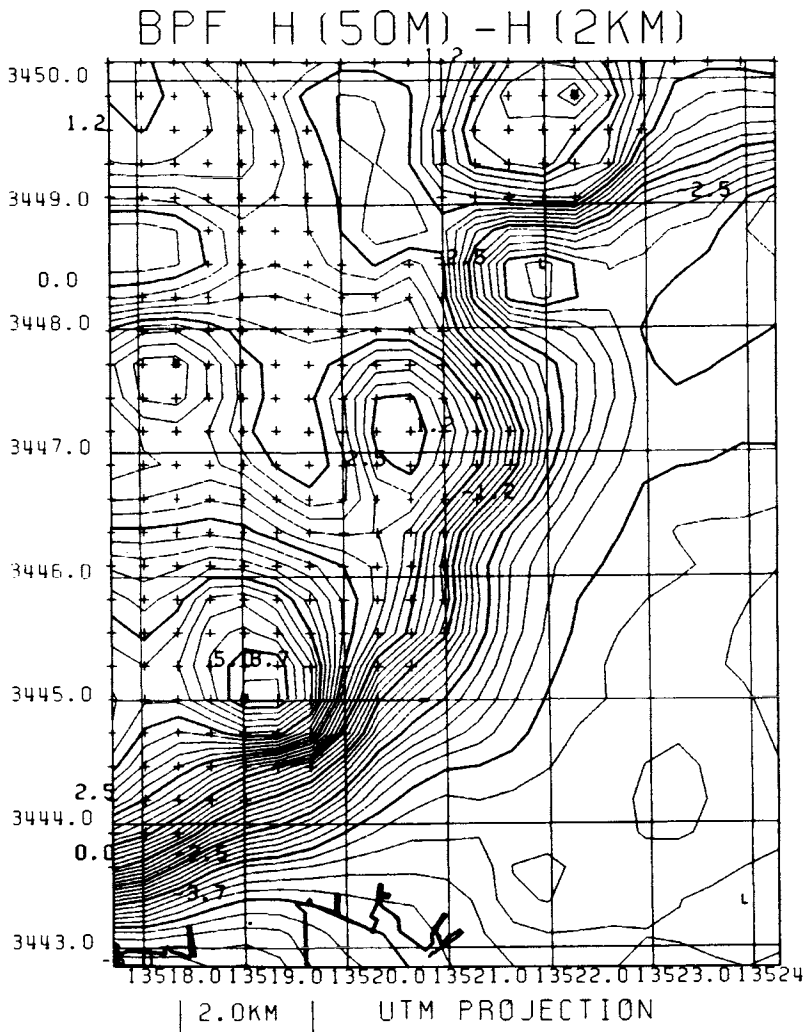
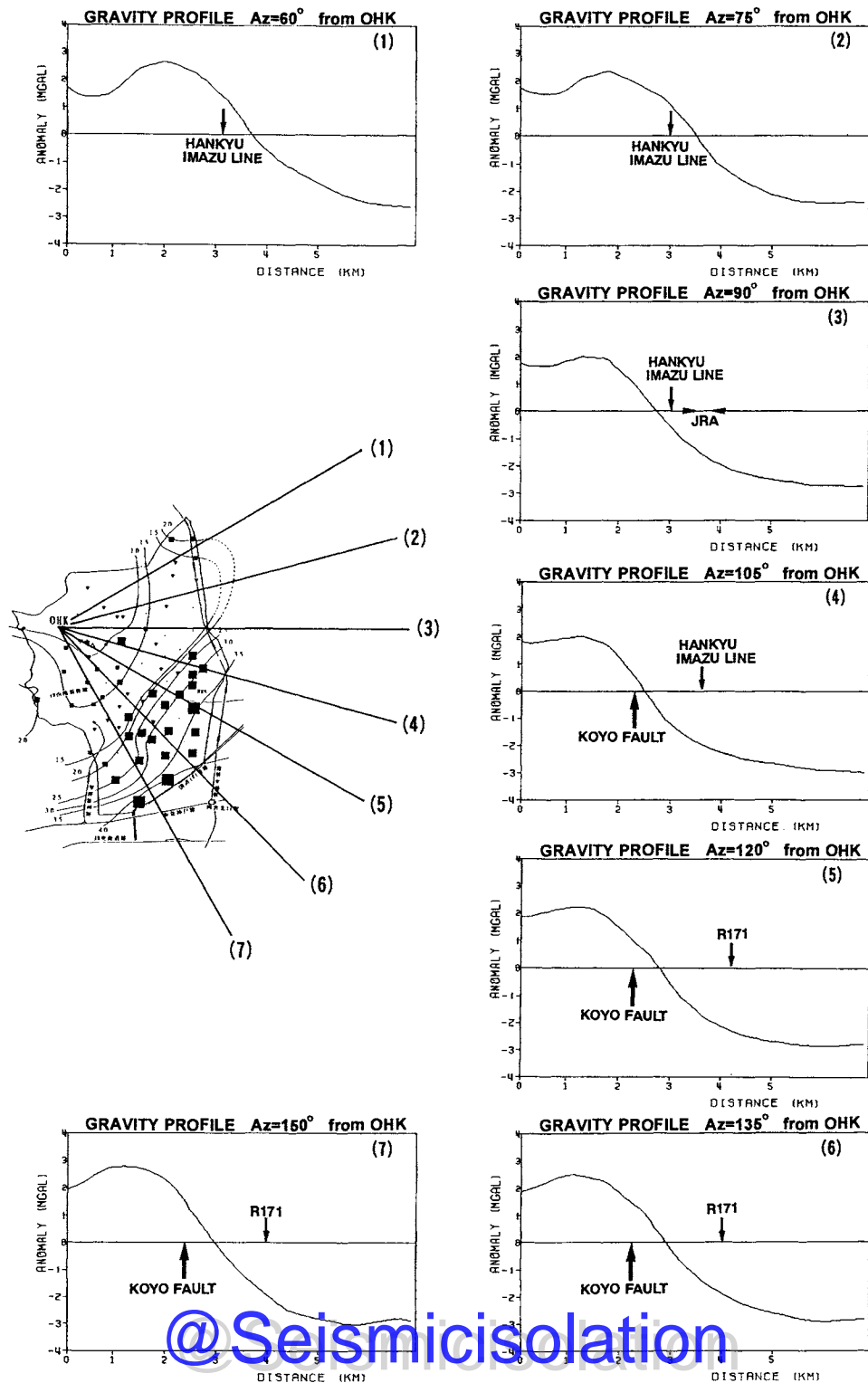


Fig. 7. Contour map of bandpass-filtered Bouguer gravity anomaly. Reduction density is 2.45 g cm^{-3} . Bandpass filtering is achieved by combined use of two upward-continuation filters, one continued to a height of 50 m, and the other to a height of 2000 m. Contour interval is 0.5 mGal. The white and dotted areas show negative and positive anomalies. Note that positive to negative change in anomalies occurs nearby along the Koyo fault.

Fig. 8. Gravity profiles along various directions from observation site, OHK, for microseisms. Bold and thin arrows indicate the location of the surface-trace of the Koyo fault, and Root 171 or Hankyu Imazu Line, respectively. Profiles 4–7 cross the Koyo fault, while no surface-traces of faults are observed on profiles 1–3. Note that spatial patterns of anomalies in profiles 1–3 are very similar to those in profiles 4–6.



a systematic gap in the arrival time of P waves between both sides of the fault, and attributed the gap to the change in depth to bedrock: the depth change is estimated to be 0.7–1.0 km depending on the assumed velocity ($V_p = 2.0\text{--}2.5 \text{ km s}^{-1}$) for the soil sediments. Their result is in good agreement with our results.

It is interesting to note that the results of f - k spectral analysis for the B-array shows fairly thick sediments in the northernmost part of the study area, as shown in Fig. 5. Moreover, we can see remarkable H/V peaks with a period of about 2.0 s in the same area (see Fig. 6). These features from the results of analysis of microseisms correspond to the positive to negative change in the bandpass-filtered gravity anomalies on profile 1. This suggests that there is a considerable change in the depth to bedrock in the northernmost part of the study area located 1.5–2 km from the Koyo fault and its NE extension. In this connection, it is noticeable that the positive to negative changes, similar to that on profile 1, are also observed on profiles 2 and 3 (see Fig. 8). Therefore, it seems reasonable to consider that the bedrock gap in the northernmost part continues southward to the Koyo fault. The amount of gap is considered to be a little smaller than that across the Koyo fault, because the difference between positive and negative anomalies on profiles 1–3 (4.7–5.2 mGal), are less than those on profiles 4–7 (5.0–5.8 mGal). We suggest the possibility that the Rokko mountains are bounded on the eastern end by the NE–SW-oriented Koyo fault and the bedrock gap with an NS strike, although the latter has not been recognized generally as a fault.

An abrupt change in the depth to bedrock across an active fault has been also suggested in the other parts of the Kobe-Hanshin area located west of the present study area. Iwata et al. (1996) discussed the subsurface structure of the sedimentary basin in eastern Kobe City by analyzing records of aftershocks of the Hyogoken-nanbu earthquake, and concluded that there is a step-like change in depth to bedrock from 200 m or less to around 1000 m at the foot of the Rokko mountains near the southwest end of the Ashiya fault. Seismic reflection surveys conducted in the central parts of Kobe City revealed that more than 1000-m thick horizontally layered sediments could be detected to continue to the edge of the basin where the bedrock is elevated abruptly in the form of a reverse fault (see Iwata et al., 1996). Such a feature of bedrock configuration was also suggested from the results of comparative analysis of microseisms and gravity anomaly (Akamatsu et al., 1996b). All these results show that the abrupt change in the depth to bedrock across active faults is a characteristic feature commonly observed in the wide region between the Rokko mountains and Osaka bay, including the present study area.

5.2. Relation between distribution of damage and bedrock configuration

A relation between the distribution of damage and bedrock configuration has been reported in many parts of the severely damaged belt-like zone of JMA Intensity 7. A damage survey of buildings and houses made by Akamatsu et al. (1995a) showed that there was a region in eastern Kobe City, within which 61–77% of wooden houses were collapsed or heavily damaged, while the amount was reduced to 27–48%

outside the region. This region is located from 800 to 1700 m away from the Suwayama fault at the foot of the Rokko mountains. As reported by Architectural Institute of Japan (1995), not only wooden houses but also reinforced concrete buildings or steel buildings were most severely damaged within the whole belt-like zone of JMA Intensity 7, which runs through the urban area 1–2 km south from the foot of the Rokko mountains.

The severely damaged belt-like zone was first recognized by Shimamoto et al. (1996). They related the appearance of the zone to the movement of an unknown buried fault just below the zone, which they named “the Kobe-Nishinomiya fault”. A similar interpretation, that buried faults played a role of a seismogenic fault, was proposed by Hirano and Hada (1996), who emphasized that the surface faulting or failures appeared not only along several pre-existing Quaternary faults but also along their southwest extensions within the belt-like zone.

These and similar interpretations, however, could not be supported by the results of seismological and geodetic studies. The location of the seismogenic fault determined by seismological methods is not below the belt-like zone: according to Kikuchi (1995), the fault rupture started below the Akashi strait and propagated bilaterally southwestward and northeastward. The northeastern part of the fault was located under the Rokko mountains, and the rupture along this part of fault is considered to have stopped near or below Mt. Rokko. A more precise location of the seismogenic fault was given by Sekiguchi et al. (1996), who examined the ground particle motions using the strong motion seismograms recorded in the source area and obtained almost the same result as Kikuchi (1995). These results are strongly supported by a geodetic survey of coseismic displacement (Hashimoto et al., 1996). According to Hashimoto et al. (1996), the theoretical coseismic displacement calculated with a fault model located below the belt-like zone could not explain the geodetic data obtained in and around the Kobe-Hanshin area.

The cause of the belt-like zone that appeared 1.5–2 km distant from the seismogenic fault was examined by Pitarka et al. (1996) by means of numerical modeling of ground motions from aftershocks. They suggested that the step-like configuration of bedrock at the basin edge is responsible for the amplification of ground motion in the belt-like zone: the most important role was played by the interference between incident S-waves and surface-waves secondarily generated at the basin edge. This argument, concerned with eastern Kobe City, is highly suggestive for examination of the distribution of damage in the present study, because the relationship between the damage distribution and the bedrock configuration is very similar.

Reconnaissances of damage distribution around the Koyo fault were made by Iwai (1996), Iwai et al. (1996) and Tachibana et al. (1995) among others. In the southern part of study area, the severe damage is distributed in a narrow region oriented close to the NE–SW direction, parallel to the strike of the Koyo fault. For example, Iwai (1996) mapped the distribution of damage to wooden houses and found that more than 70% of houses were collapsed in the NE–SW oriented narrow region as shown in Fig. 9. It is important to note that the belt-like zone turns to the north in the northern part of the study area (Tachibana et al., 1995; JIT and

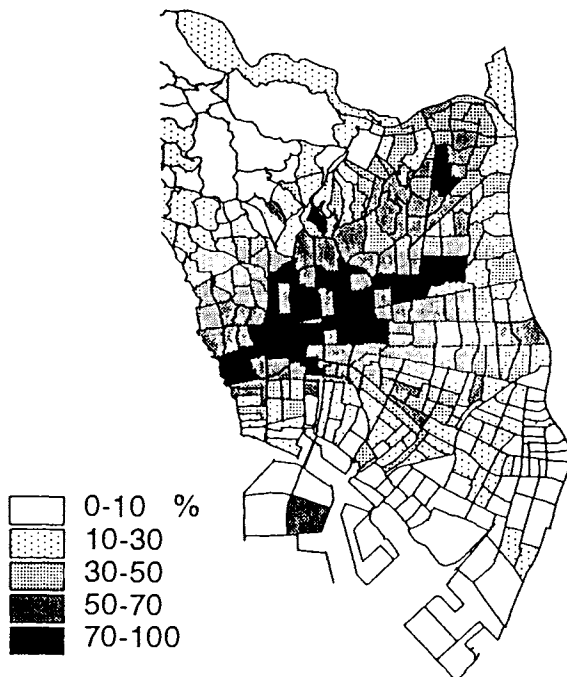


Fig. 9. Distribution of damage to wooden houses in Nishinomiya City (Iwai, 1996). The rate of the number of collapsed houses to the total number in small areas are shown. Note that severe damage concentrated in a narrow belt-like zone oriented nearly in a NE-SW direction, parallel to the strike of the Koyo fault.

Kashiwai, 1996), that is, to the direction parallel to the strike of the bedrock gap discussed above. It must be pointed out here that the most severe damage was concentrated within a narrow zone located about 1.5 km distant from the Koyo fault in the southern part, and from the bedrock gap in the northern part.

All these features enable us to speculate that the basin edge geometry around the Koyo fault was responsible for the damage distribution. It is supposed that the interference took place between the incident S-waves coming from below the sediments, and the surface-waves secondarily generated at the Koyo fault and the bedrock gap. This brought amplification of ground motions in the narrow belt-like zone. In addition, the azimuthal dependence of radiation of seismic waves should be taken into account. According to Ejiri et al. (1996), seismic waves radiated most strongly in the northeast direction from the seismogenic fault, because of the northeastward propagation of rupture. The study area is located in this direction.

The effect of bedrock configuration has been also invoked for damage distribution in the regions far from the seismogenic fault, such as the Osaka plain and the Kyoto basin. On the Osaka plain, severe damage to buildings and houses was distributed

in the N–S direction from Toyonaka City to Sakai City through Osaka City, parallel to the Butsunenji-yama, Uemachi and Nagai faults (Nakagawa et al., 1996). Across the Uemachi fault, for example, the bedrock subsides stepwise from about 700 to 1500 m in depth (Nakagawa et al., 1996). The damage was concentrated on the subsiding side a few kilometers from the fault traces. Nakagawa et al. (1996) attributed the damage distribution to focusing and defocusing of seismic waves due to refraction at the irregular bedrock surface: the focusing occurring on the subsiding side and the defocusing on the elevated side. Similarly, in the Kyoto basin more than 60 km from the source region, damage to roofing tiles of wooden houses concentrated near the Hanaore fault on the eastern edge of the basin and the Katagihara fault on the western edge (Study Group of Geology of Higashiyama High School and Yasumatsu, 1995). This is also interpreted by the focusing of seismic waves due to the bedrock configuration. The effect of focusing on damage distribution has been pointed out in other earthquake disasters, such as the 1963 Skopje earthquake in Yugoslavia (Poceski, 1969) and the 1923 Kanto earthquake in Japan (Tsunoda, 1994).

All the above discussions lead us to conclude that the belt-like zones of severe damage, not only in the present study area but also in the wider area, were caused, at least partly, by the amplification of ground motions due to the step-like configuration of bedrock, such as focusing of seismic waves and/or interference between the incident S-waves and the secondarily generated surface-waves.

Up to now, the ground vibration characteristics on thick soil-sediments have been studied mainly to resolve earthquake-proofing problems of high and large urban facilities, focusing on the long natural period. With respect to short-period range, earthquake engineering and engineering seismology have paid attention only to the effects of shallow subsurface structure on seismic ground motions. However, the earthquake damage caused by the Hyogoken-nanbu earthquake demonstrates the importance of the effects of deep structure in the short period range as well: most of the severe damage was to low buildings and residential houses at a short natural period, e.g., less than about 0.5 s. Thus, from the viewpoint of hazard mapping of an urban area on a sedimentary basin, it is an urgent issue to investigate the fault-related 3-D bedrock configuration. For this purpose, comparative analysis of microseisms and Bouguer gravity anomaly is highly prospective, because we can obtain more reliable structural models estimated using different kinds of parameters: seismic impedance and density distribution.

6. Summary and conclusion

The subsurface structure around the Koyo fault in northern Nishinomiya City and southern Takarazuka city in the Hanshin area, west Japan, was studied by means of $f-k$ and H/V spectral analyses of microseisms and bandpass filtering of Bouguer gravity anomalies, and the obtained results were compared with the distribution of damage caused by the Hyogoken-nanbu earthquake.

The main results concerning the subsurface structure are as follows: (1) in the region northwest of the Koyo fault, the thickness of terraces formed by Late Pleistocene sediments and Lower Subgroup of Osaka Group of Early Pleistocene reaches up to 300 m; (2) the bedrock subsides abruptly from northwest to southeast across the Koyo fault by about 700 m; and (3) there may be a considerable gap in the depth to bedrock along the N-S trending boundary between the terraces to the west and the Alluvial plain to the east.

The relation between the damaged zone and the configuration of bedrock is as follows: the most severe damage to wooden houses was distributed in narrow belt-like zones oriented parallel to the Koyo fault (NE-SW) and to the strike of the bedrock gap (N-S). These zones were located about 1.5 km apart from the Koyo fault or the bedrock gap.

In conclusion, it is suggested that the belt-like zone of severe damage was caused, at least partly, by amplification of ground motions due to the step-like configuration of bedrock, such as focusing of seismic waves and/or interference between the incident S-waves and the surface-waves secondarily generated at the basin edge.

Finally it is pointed out that the deep subsurface structure is responsible for amplification of ground motion in the short-period range as well as in the long-period range, and therefore that the investigation of fault-related 3-D bedrock configuration is an urgent issue of hazard mapping of an urban area on a sedimentary basin.

Acknowledgment

The authors wish to thank Daisuke Nakajima, Graduate School of Engineering, Kyoto University, for his help with f - k spectra and inversion analysis.

References

- Akamatsu, J., Nishimura, K., Komazawa, M., Onoue, K., Kitahara, A. and Morikawa, H., 1994a. Earthquake disaster on thick soil sediments. Proc. 4th Symp. Geo-environments and Geo-technics, pp. 375–380 (in Japanese, with English abstract).
- Akamatsu, J., Li, W., Morikawa, H., Saito, H., Lu, Q., Tao, N., Kameda, H., Zhang, Z. and Fujiwara, T., 1994b. Vibrational characteristics of soil sediments in the Shanghai plain inferred from microseisms – on relationship between peak frequency of spectral ratio, H/V, and depth to bedrock. Annu. Disast. Prev. Res. Inst., Kyoto Univ. 37B-1: 119–126 (in Japanese, with English abstract).
- Akamatsu, J., Morikawa, H., Saito, H. and Jido, M., 1995a. Relation between the distribution of damage caused by the 1995 Hyogoken-nambu earthquake and ground vibration characteristics inferred from microseisms. J. Natural Disast. Sci., 16: 63–70.
- Akamatsu, J., Nishimura, K. and Komazawa, M., 1995b. Microzoning of a sedimentary region based on comparative analysis of microseisms and gravity data. Proc. 5th Int. Conf. Seismic Zonation, II: 933–940.
- Akamatsu, J., Yasui, H., Nishimura, K. and Komazawa, M., 1996a. Application of microseisms to

- microzoning of an urban area in a sedimentary basin. In: V. Schenk (Editor), *Earthquake Hazard and Risk*. Kluwer Academic Publ., Dordrecht, pp. 267–279.
- Akamatsu, J., Saito, H., Jido, M., Morikawa H., Nishimura, K. and Komazawa, M., 1996b. Effects of irregular bedrock configuration in a sedimentary basin on ground vibration characteristics – Possible cause of damage distribution of the 1995 Hanshin-Awaji great earthquake disaster. Proc. 11th World Conf. on Earthq. Eng.: Paper No. 1655.
- Architectural Institute of Japan, 1995. Preliminary Reconnaissance Report of the Hyogoken-Nanbu Earthquake, pp. 51–186 (in Japanese).
- Capon, J., 1969. High-resolution frequency-wave number spectrum analysis. Proc. IEEE, 57: 1408–1418.
- Ejiri, J., Sawada, Goto, Y. and Toki, K., 1996. Peak ground motion characteristics. In: Japanese Geotechnical Society (Editor), Special Issue on Geotechnical Aspects of the January 17, 1995, Hyogoken-Nambu Earthquake. Soil and Foundations, pp. 7–13.
- Endo, H., Watanabe, S., Makino, M., Murata, Y., Watanabe, K. and Urabe, A, 1995. Subsurface geology and disaster caused by the 1995 South Hyogo Earthquake. In: The Committee of Environmental Geology, Geological Society Japan (Editor), Proc. Symp. on the Great Hanshin-Awaji Earthquake and Its Geo-environments, pp. 219–224 (in Japanese, with English abstract).
- Gupta, V.K. and Ramani, N., 1980. Some aspects of regional-residual separation of gravity anomalies in a Precambrian terrain. *Geophysics*, 45: 1412–1426.
- Hashimoto, M., Sagiya, H., Tsuji, H., Hatanaka, Y. and Tada, T., 1996. Coseismic displacements of the 1995 Hyogo-ken nanbu earthquake. *J. Phys. Earth*, 44 (in press).
- Hirano, M. and Hada, S., 1996. Faults in the northeastern part of the Rokko mountains and surface faulting. In: Committee of Environmental Geology, Geological Society of Japan (Editor): Hanshin-Awaji Great Earthquake Disaster. Tokai Univ. Press, Tokyo, pp. 101–121 (in Japanese).
- Horiike, M., 1980. Estimation of phase velocity and transfer-function of microtremor. *J. Seism. Soc. Jap.*, 33: 425–442 (in Japanese, with English abstract).
- Itihara, M., Yoshikawa, S., Mitamura, M., Mizuno, K. and Hayashi, T., 1991. 1:125 000 Quaternary geological map of Osaka and adjacent areas, Kinki, Japan. Urban Kubota, 30.
- Iwai, S., 1996. Application of geographic information system (GIS) for damage data management on buildings. In: H. Nirei and J. Akamatsu (Editors), *Geo-environmental Change and Prediction of Earthquake Ground Motions*, UEHR Rep., Disast. Prev. Res. Inst., Kyoto Univ., E18: 213–234 (in Japanese, with English abstract).
- Iwai, S., Kameda, H., Suzuki, Y. and Kakumoto, S., 1996. GIS application to damage data management on buildings and urban facilities in the January 17, 1995, Hyogoken-nambu earthquake. Proc. 11th World Conf. on Earthq. Eng.: Paper No. 851.
- Iwata, T., Irikura, K., Toki, K., Sasatani, T., Kudo, K., Seo, K. and Yokoi, T., 1996. Prospecting of subsurface structure in and around Kobe City. In: T. Fujiwara (Editor), *Inspection of disaster caused by the 1995 Hyogoken-nambu Earthquake by means of analyses of damage survey*, supported by the Japanese Ministry of Education, Science, Sport and Culture (Grant No. 0730005), pp. 21–49 (in Japanese).
- Joint Investigation Team of Geological Survey Consultant Society in Kansai to Hanshin Great Earthquake Disaster and Kashiwai Y., 1996. Damage in and around the eastern part of the Rokko mountains. In: Committee of Environmental Geology, Geological Society of Japan (Editor), *Hanshin-Awaji Great Earthquake Disaster*. Tokai Univ. Press, Tokyo, pp. 181–185 (in Japanese).
- Kagawa, T., Sawada, S., Iwasaki, T. and Nanjoh, A., 1992. Deep soil structure beneath Osaka plain derived from array observation of microtremor. Proc. Symp. on Recent Geologic Structure and the State-of-the-Arts on Soil Characteristics of the Kansai Ground, pp. 127–134 (in Japanese).
- Kikuchi, M., 1995. Source mechanism of Hyogoken-nambu earthquake, January 17, 1995. In: Geological Society of Japan (Editor), *Preliminary Report on the 1995 South Hyogo Prefecture Earthquake*, pp. 117–122 (in Japanese).
- Komazawa, M., 1984. On the quantitative gravimetric analysis in the Hokuroku district. *Geophys. Explor.*, 37: 123–134 (in Japanese, with English abstract).
- Nakagawa, K., Shiono, K., Inoue, N. and Sano, M., 1996. Geological characteristics and problems in

- and around Osaka basin as a basis for assessment of seismic hazards. In: Japanese Geotechnical Society (Editor), Special Issue on Geotechnical Aspects of the January 17 1995 Hyogoken-Nambu Earthquake. Soil and Foundations, pp. 18–28.
- Nakamura, Y., 1989. A method for dynamic characteristics estimation of subsurface using microtremors on the ground surface. QR RTRI, 30: 25–33.
- Nishimura, K., Kawasaki, S. and Waga, S., 1996. Observations of aftershocks with small arrays in Nishinomiya and Takarazuka, and northern Awaji Island. In: Disast. Prev. Res. Inst., Kyoto Univ. (Editor), Hanshin-Awaji Great Earthquake Disaster, pp. 151–161 (in Japanese).
- Nogoshi, M. and Igarashi, T., 1971. On the amplitude characteristics of microtremor (Part 2). J. Seism. Soc. Jap., 24: 26–40 (in Japanese, with English abstract).
- Pitarka, A., Irikura, K., Iwata, T., and Kagawa, T., 1996. Was the basin edge geometry responsible for the damage concentration in Higashinada-ku during the 1995 Hyogoken-nanbu (Kobe) earthquake. J. Phys. Earth, 44 (in press).
- Poceski, A., 1969. The ground effects of the Skopje July 26, 1963 earthquake. Bull. Seism. Soc. Am., 59: 1–22.
- Sekiguchi, H., Irikura, K., Iwata, T., Kakehi, Y., Hoshiba, M., 1996. Determination of the location of faulting beneath Kobe during the 1995 Hyogo-ken Nanbu, Japan, earthquake from near-source particle motion. Geophys. Res. Lett., 23: 387–390.
- Shichi, R., Nakamura, K., Jido, M., Akamatsu, J., Nishimura, K. and Komazawa, M., 1996. A dense gravity survey in the northern periphery of the focal area of the 1995 Southern Hyogo Earthquake. Abstracts 1996 Japan Earth and Planetary Science Joint Meeting, p. 630 (in Japanese).
- Shimamoto, T., Kawamoto, H., Tsutsumi, A. and Ootomo, S., 1996. Belt of earthquake disaster and active faults. In: Committee of Environmental Geology, Geological Society of Japan (Editor), Hanshin-Awaji Great Earthquake Disaster. Tokai Univ. Press, Tokyo, pp. 122–134 (in Japanese).
- Study Group of Geology of Higashiyama High School and Yasumatsu, Y., 1995. Why damage to living houses concentrated in near the Hanaore and Katagihara faults? Bull. Res. Higashiyama Sch., 40: 133–152 (in Japanese).
- Tachibana, E., Inoue, K., Inoue, Y., Oono, Y., Saka, T., Suzuki, S., Natani, S. and Baba, K., 1995. Damage to buildings in Nishinomiya, Amagasaaki, Itami and Takarazuka Cities. In: Architectural Institute of Japan (Editor), Preliminary Reconnaissance Report of the Hyogoken-Nanbu Earthquake. AJJ, Tokyo, pp. 51–69 (in Japanese).
- Tsunoda, F., 1994. The quake of the 1923 Kanto earthquake in the southwestern of the Saitama plain. J. Coll. Liberal Arts, Saitama Univ., 29: 161–186 (in Japanese, with English abstract).
- Waga, S., Kawasaki, S. and Nishimura, K., 1996. Bedrock structure around the Koyo fault inferred from array observation of aftershocks. In: H. Nirei and J. Akamatsu (Editors), Geo-environmental Change and Prediction of Earthquake Ground Motions, UEHR Rep., Disast. Prev. Res. Inst., Kyoto Univ., E18: 107–114 (in Japanese).

Risk assessment for destructive inland earthquakes: application to fault systems in central Japan

YUJI KANAORI^{a,*} and SHIN-ICHI KAWAKAMI^b

^aDepartment of Geological Sciences, Faculty of General Education, Gifu University, 1-1 Yanagido, Gifu City 501-11, Japan and ^bDepartment of Earth and Planetary Sciences, Faculty of Education, Gifu University, 1-1 Yanagido, Gifu City 501-11, Japan

Abstract

The seismic risk of an active fault has been previously evaluated independently by its length or the slip rate averaged over the Quaternary Period; the magnitude of an earthquake was estimated from the fault length, while the recurrence interval was obtained from the ratio of the seismic slip to the average slip rate. The occurrence of the magnitude $M=7.2$ Kobe earthquake in 1995 revealed that the respective fault length and average slip rate were insufficient to evaluate the seismic risk. This earthquake was caused by the movement of the fault system, which consisted of a number of active faults. This means that an inland earthquake is produced by the movement of a fault system, not by an independent active fault.

Seismic moments released by the fault movement are a function of the length, width, and slip of the fault. The average rate of seismic moment-release for a given fault system is calculated by averaging the total moments released in a given period. The total moment is given by the sum of individual events in the fault system. The average rate r is an important parameter in evaluating the seismic risk of a fault system. With the use of this parameter, the magnitude M of the next earthquake which should occur along the fault system can be estimated from the duration of the interseismic period T between the latest events by the equation: $\log T = 1.3M + 17.0 - \log r$.

Alternatively, if we can specify the magnitude of the next earthquake by identifying the length of the seismic gap along the fault system, the interseismic period T can be obtained from the magnitude M and the average rate r .

When the interseismic period T is substituted for the elapsed time t in the above equation, the potential magnitude M_p can be estimated from the average rate r and the elapsed time t for a fault or fault system. This parameter gives the maximum magnitudes which would occur at present by the accumulation of seismic moments since the latest event. The durability of a large structure is no more than 100 years. The potential magnitude M_{p+100} of 100 years after the present can also be calculated. It is proposed that the potential magnitudes at present (1995) or 100 years later can be used as basic data for the assessment of earthquake-proof designs of large structures.

Based on the different dimensions between the interseismic period T and the elapsed time

* Corresponding author.

t for each seismic gap along fault systems in central Japan, the seismic gap can be categorized into the following three risk classes, ranked in the order of most dangerous to least dangerous:

Risk rank A elapsed time $t \geq$ interseismic period T

Risk rank B elapsed time $t <$ interseismic period T

Risk rank C elapsed time $t <$ interseismic period T .

1. Introduction

Koto (1893) was the first to demonstrate that “a fault moves to create an inland earthquake”, by investigating damages caused by the 1891 $M8.0$ Nobi earthquake. The Nobi earthquake was one of the greatest inland earthquakes in Japan’s history. Surface displacements accompanying this event sporadically appeared along the Neodani fault, some of which are now preserved (Matsuda, 1974). After the Nobi earthquake, the 1909 $M6.8$ Anegawa, 1945 $M6.8$ Mikawa, and 1948 Fukui $M7.1$ inland earthquakes occurred, and induced serious disasters in the western part of central Japan (Kanaori et al., 1994b). These inland earthquakes have also confirmed the causal relationship between fault movements and inland earthquake generation.

Lineaments which displace surface topography have been found since the 1960s, mainly by the method of geomorphological reading of aerial photographs. Some of the lineaments are identified as active faults (Research Group for Active Faults in Japan, 1980). Since then, most Japanese researchers on active faults have believed that “an active fault moves to create a large inland earthquake” (e.g., Matsuda, 1992). They have also accepted the “characteristic earthquake model”, in which each active fault moves repeatedly with a constant interval to produce earthquakes having the same magnitude (Schwartz and Coppersmith, 1984).

Following the seismic quiescence of approximately 50 years after the 1948 $M7.1$ Fukui earthquake generation, the $M7.2$ Kobe earthquake hit the coastal cities of Kobe and Osaka on 17 January 1995. This inland earthquake induced serious damage to buildings and houses, and loss of life was greater than 6300 fatalities according to the latest statistics. Discussions have recently been focused on what caused the Kobe earthquake and which faults moved (Hashimoto et al., 1995; Shimamoto, 1995; Kanaori and Kawakami, 1996a). At any rate, from the generation of this earthquake, the following can be ascertained:

- (1) The Kobe earthquake was probably generated by the movement of the fault system which was denoted as the Arima-Takatsuki tectonic line (ATTL) (Kanaori et al., 1992d, 1993a). The fault system was defined as the line linking a number of active faults from the northern margin of the Osaka plane through the Rokko Mountains and Awaji Island to the median tectonic line. The activity of this fault system is inconsistent with the characteristic earthquake model, since the model assumes that each fault moves independently.
- (2) A 9-km rupture having a 1.7-m right-lateral slip was found to appear on the

ground surface along the pre-existing Nojima fault in the northern part of Awaji Island after the Kobe earthquake (Awata et al., 1996), whereas small cracks of less than several tens of centimeters with right-lateral slips were located sporadically along the pre-existing active faults in the Rokko Mountains (see Kanaori and Kawakami, 1996b). Aftershocks of the Kobe earthquake were distributed in a 40-km-long, 20-km wide zone along the central segment of the ATTL. It is pointed out from these surface features and aftershock distributions that a large inland earthquake was caused by the displacement of the earth's crust along the fault system. An active fault is only a surface rupture which is reflected in the seismogenic fault in the Earth's crust (Kanaori et al., 1991).

- (3) The set of active faults creating the Kobe earthquake was misunderstood to be a dangerous fault set which had produced no movement during past 1000 years (Matsuda, 1981), because no historical earthquake was known to occur along the fault set. However, from the investigation of a trench which was excavated at a site along the Nojima fault after the Kobe earthquake, Suzuki et al. (1995) discovered evidence that this fault moved approximately 400 years ago.
- (4) The 400-year-ago event discovered by the trench excavation can be correlated with that of the 1596 $M7.5$ Keicho-Fushimi earthquake. The magnitude of the Keicho-Fushimi earthquake is estimated as 7.5 from the extent of damaged areas (Usami, 1987). This magnitude is 0.3-times larger than that of the Kobe earthquake, although both earthquakes were probably created by movement of the same fault system. This suggests that a ruptured region or a segment of a fault system changed in each earthquake event, resulting in different magnitudes.
- (5) Active faults within the Japanese Islands have been previously assumed to move one at time in a recurrence interval of more than 1000 years with some deviation (Matsuda, 1981). The Kobe earthquake, however, occurred at a shorter interval of approximately 400 years. Thus, the concept and duration of the recurrence interval should be re-examined.

In the future, inland earthquakes will continue to occur and, unfortunately, serious disasters will be induced in the Japanese islands. The occurrence of an inland earthquake is inevitable because of the tectonic setting of the Japanese Islands, which are located around plate boundaries. In order to lessen the natural disasters induced by an inland earthquake, the implications of the generation of the Kobe earthquake should be seriously considered in further research of fault activity and inland earthquake generation.

In this paper, a study of the Kobe earthquake generation, points out problems of previous methods for evaluating the seismic risk using the length and average slip rate of active faults independently (e.g., Kakimi, 1983). An alternative to the previous methods is proposed. The proposed method uses the average rate of seismic moment-release as a parameter for the seismic risk of a fault system (Kanaori et al., 1992b,d; Kanaori and Kawakami, 1996b). Finally, the method is applied to evaluating the seismic risk of fault systems in central Japan as an example, and further problems about its applicability and improvement are discussed.

2. Fault length and slip rate

In the case of assessing the risk of an earthquake caused by the fault movement, the length and the slip or slip rate of a fault have been treated independently (Research Group for Active Faults in Japan, 1980, 1991). Namely, the fault length was used to estimate the magnitude of an earthquake which is created by the fault movement, while a recurrence interval is obtained from the ratio of the slip of the seismic fault to the average slip rate. The previous method using two parameters for seismic risk evaluation of the fault is briefly reviewed, and its problems are pointed out and discussed below.

2.1. Fault length and earthquake magnitude

Fig. 1 shows the relationship between the length L of surface ruptures or seismogenic faults and the magnitude M of inland earthquakes in Japan. Based on this relationship, the following empirical equation is obtained by Matsuda (1975) as,

$$\log L (\text{km}) = 0.6M - 2.9 \quad (1)$$

From this equation, the magnitude M of an earthquake can be estimated, when the length L of the fault is given. This equation means that a longer fault creates an earthquake of greater magnitude. Since the fault which can be identified on the ground surface is expressed as the line of the intersection of the ground surface and the seismogenic fault plane in the earth's crust, the fault length L is equal to or shorter than that of the seismogenic fault plane.

For example, the surface rupture accompanying the Kobe earthquake is 9 km-long along the pre-existing Nojima fault (Awata et al., 1996), while the seismogenic

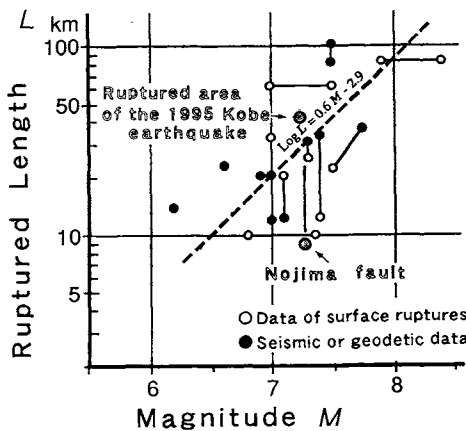


Fig. 1. Relationship between length L of ruptured planes (fault) and magnitude M (after Matsuda, 1975). The lengths of the seismogenic fault and the Nojima fault accompanying the 1995 $M7.2$ Kobe earthquake are plotted.

fault is estimated as 40 km-long from the aftershock distribution and surface ruptures (Kanaori and Kawakami, 1996a,b). This difference verifies that the length of the surface rupture is shorter than the seismogenic fault in the crust (cf. Fig. 1).

From the magnitude 7.2 of the Kobe earthquake, the fault length L is estimated as 26 km by use of Eq. (1). This length falls between the lengths of the surface rupture along the Nojima fault and the seismogenic fault. In contrast, from the 40-km length L of the seismogenic fault, the magnitude M is calculated as 7.5. This magnitude is greater than the actual magnitude of the Kobe earthquake. Thus, when the magnitude of an earthquake is estimated from the $M-L$ relation, it must be regarded as a rough estimate. When faults align in an *en echelon* arrangement or constitute a major fault system, it is difficult to determine the length of the fault or segment which moves in a single earthquake.

In the same manner as the $M-L$ relation, an empirical equation is also obtained between a fault slip and the magnitude of an earthquake (Matsuda, 1975). The value of the fault slip of a single event is variable along the fault trace, as identified along the Neodani fault which created the 1891 Nobi earthquake (Muramatu, 1976). After the Kobe earthquake, a displacement of only several tens of centimeters was found along active faults in the Rokko Mountains, whereas the displacement along the Nojima fault reached 170 cm at the maximum (Kanaori and Kawakami, 1996a,b). This slip variation along the fault system suggests that the relationship between the slip and the magnitude of an earthquake event is not always valid.

2.2. Average slip rate of active fault

Displacements of strata and tectonic relief along an active fault result from the accumulation of slips which were caused by multiple movements since the formation of the fault. The average slip rate S is obtained by dividing the total displacement D by the period t during the slip accumulation. The average slip rate S is commonly expressed as the value of displacement (m) per 1000 years. Because the average slip rate is estimated from the displacement of the strata or tectonic relief, the value is averaged over a long period, ranging from several hundred thousand years to one million years. The average slip rate S is not always reflected in a single slip of the fault, as demonstrated by the Kobe earthquake and mentioned above.

The Nojima fault was categorized as a Class B active fault from the average slip rate (Research Group for Active Faults in Japan, 1980,1991). Active faults in the Japanese Islands are ad hoc classified into three categories using the dimension of the average slip rate S ($m/10^3$ years) as a parameter (Research Group for Active Faults in Japan, 1980,1991):

- Class A active fault $1 \leq S < 10$;
- Class B active fault $0.1 \leq S < 1$;
- Class C active fault $0.01 \leq S < 0.1$.

The Arima-Takatsuki tectonic line including the Nojima fault was presumed to move at the time of the 1596 Keicho-Fushimi earthquake. A 2-m right-lateral slip was found on the ground surface along the pre-existing Nojima fault after the 1995 Kobe earthquake. This means that the average slip rate is 2 m/400 years. This rate is converted to 5 m/ 10^3 years. Accordingly, the Nojima fault must be categorized as a Class A active fault. This indicates that the slip of the Kobe event was one order greater than the slip estimated from the slip rate averaged over the Quaternary.

2.3. Average slip rate and active interval

Wallace (1970) introduced the recurrence interval R (years), expressed as $R = d/(S - C)$, where d (m) and C (m) are the fault slip produced by the earthquake, and the creep component of the fault, respectively. In the case of active faults on the Japanese Islands, no creep component has been detected. The equation was modified as $R = d/S$ (Matsuda, 1975). As shown in Fig. 2, the recurrence interval R is calculated from the seismic slip d divided by the average slip rate S .

Using the $d-S$ relationship, a recurrence interval R has been estimated for each active fault in the Japanese Islands. For example, the 1930 $M7.3$ Kita-Izu earthquake produced a 2-m right-lateral slip on the Tanna fault. Since the Tanna fault has 2 m/ 10^3 years average slip rate, it is categorized as a Class A active fault. The recurrence interval of the Tanna fault is estimated as 1000 years by dividing 2 m by 2 m/ 10^3 years (Matsuda, 1994). The Fukozu fault, a Class C active fault, slipped vertically by 1 m at the time of the 1945 $M6.8$ Mikawa earthquake. The average slip rate of the Fukozu fault is estimated as 0.08 m/ 10^3 years, so the recurrence interval is around 10 000 years, which is obtained in the same way as the Tanna fault. Thereby, it has long been accepted among Japanese researchers that Class A and C active faults regularly move at recurrence intervals of 1000 and 10 000 years,

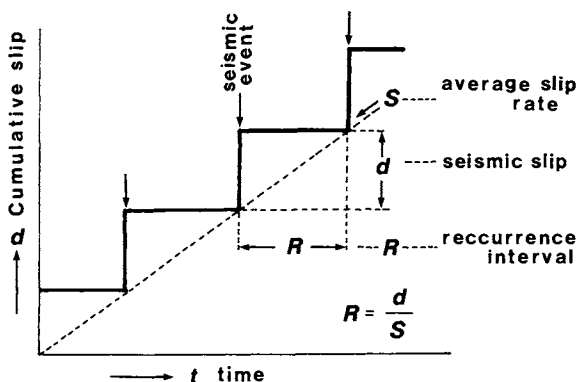


Fig. 2. Previous method of the seismic risk evaluation for active faults using the seismic slip and the average slip rate as parameters (after Matsuda, 1976). The recurrence interval R is calculated from the seismic slip d divided by the average slip rate S .

respectively. Also, class B active faults are believed to move at an interval between these durations.

However, it has not been clarified why the recurrence interval is different for each active fault class, and the physical implications have not been understood sufficiently (Kawakami et al., 1992). Asada (1991) posed a question about the different recurrence intervals among active fault classes. He pointed out that the number of Class C active faults might be two-orders more than that of Class A active faults, because the number of active faults which have created earthquakes during the past 100 years is nearly equal, independent of the active fault class. However, the actual number of Class C active faults is nearly equal to that of Class A. This paradox is pointed out by Asada (1991).

The average slip rate of the Nojima fault during relatively long periods was not reflected in the seismic slip accompanying the Kobe earthquake, as mentioned above. The surface displacement in the Rokko Mountains was significantly smaller than that along the Nojima fault. No surface displacement was detected in the 1984 $M6.8$ Western Nagano-ken earthquake (Yamashina et al., 1985). This suggests that the seismic risk and probability of the next earthquake occurrence are underestimated from the recurrence interval obtained from the ratio of seismic slip d to average slip rate S (Wallace, 1987).

The average right-lateral slip rate of the ATTL is geomorphologically estimated as $0.5\text{--}1.5\text{ m}/10^3\text{ years}$ (Sangawa, 1978). Since the Nojima fault constitutes the ATTL, the fault has a value similar to the ATTL. The recurrence interval of the Nojima fault is estimated as 1100–3400 years from the 1.7-m slip of the Kobe earthquake divided by the average slip rate of $0.5\text{--}1.5\text{ m}/10^3\text{ years}$. This recurrence interval is 3–9 times larger than the actual interval of approximately 400 years between the 1995 Kobe and the 1596 Keicho-Fushimi earthquakes.

Matsuda (1983) believed that the recurrence interval obtained from the slip and the average slip rate had a deviation period ranging from one-half to 2 times the actual interval. If the recurrence interval of a fault is 1000 years, it ranges from 500 to 2000 years. This wide range does not indicate whether or not a given fault moves in the relatively short duration of a human lifetime, or the structure durability. The 400-year recurrence interval must be excluded in the above deviation range, indicating that the fault system does not move regularly at a recurrence interval.

2.4. Problems with the previous method

Matsuda (1978) defined an index P for the seismic risk of an active fault. The index P is expressed as the ratio of time t elapsed since the latest event to the recurrence interval R . According to Matsuda's example, a type A fault having a high P value and a type B fault which has no movement during the historical age are regarded as dangerous faults, as shown in Fig. 3. On the other hand, a type C fault has a low P , since the fault has already moved in the near past. Matsuda (1992) selected two faults as examples of low-risk faults: the Neodani fault generating the 1891 Nobi earthquake, and the Tanna fault causing the 1930 Kita-Izu earthquake.

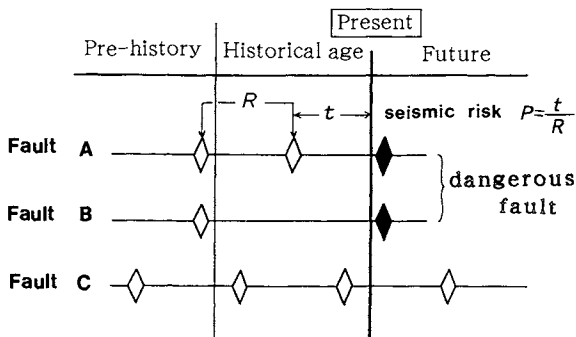


Fig. 3. The seismic risk evaluation for active faults, based on the recurrence interval R and the elapsed time t since the latest event (Matsuda, 1978). The seismic risk P is expressed as the ratio of t/R .

The seismic risk index P defined above is higher when it is closer to 1, whereas it is lower when closer to 0. However, when two faults have the same P value, the order of the generation period of earthquakes depends on the duration of the recurrence interval R . Assuming that an active fault has $P=0.9$, a fault which moves at a recurrence interval of 1000 years could produce an earthquake in the next 100 years. In contrast, in the case of a fault having a recurrence interval R of 10 000 years, the fault has the potential of producing in the next 1000 years. More precise methods should be introduced to evaluate the seismic risk of faults in the earthquake-proof design of structures, because the durable period is no more than 100 years.

In the past two decades, the seismic risk of an active fault has been evaluated from the slip of a single event and the slip rate averaged over the Quaternary, assuming that an active fault moves regularly at the characteristic interval. However, Wallace (1987) pointed out the danger of underestimating the seismic risk from the recurrence interval, because fault activity is clustered in an active period which alternates with a quiet period. Scholz (1990a,b) claimed that the characteristic earthquake model is too simple to evaluate the seismic risk, and that the model should be revised.

Since no records of historical earthquakes contain information on active faults along the Rokko Mountains, those active faults were categorized into the type B fault in Fig. 3 (Matsuda, 1981). In contrast, archaeological studies of paleoliquefaction and flowage at excavation sites revealed that these active faults probably moved at the time of the 1596 Keicho-Fushimi earthquake (Sangawa, 1992; Kanaori et al., 1993b). A number of trenches were excavated along the eastern ATTL and the Nojima fault after the Kobe earthquake to examine their activity. The excavation exposed evidence of an event which occurred 400 years ago. The 400-year interval rejects the hypothesis that Class A active faults have a recurrence interval of approximately 1000 years, as well as the hypothesis that the active faults in the Rokko Mountains had a high risk index P . If a trench-excavation study had been conducted at the site of active faults which constitute the ATTL, the fault system

producing the 1995 Kobe earthquake might be misunderstood to have a low seismic risk due to the discovery of the 400-year-ago event.

The previous method of evaluating the seismic risk is too inaccurate to give input data for earthquake-proof design of large structures. An alternative method should be developed for more precise evaluation.

3. Average rate of moment-release and seismic risk

An average rate r of moment-release of a fault system is obtained from the total moments which are released divided by the movement in a given period. The seismic moment is a function of the length, width, and slip of the fault (e.g., Brune, 1968). The method of evaluating the seismic risk of a fault system using the average rate, which is described in this section, would be better than that of the previous method, which uses the length and slip rate independently.

3.1. An average rate of moment-release

When a fault having the length L creates a seismic slip d , the released moment m_o is given by μLWD , where μ is the rigidity, and W is the width of the fault (Fig. 4). Total seismic-released moments during a given period t is also expressed as μLDd . Since d is equal to the accumulation slip D , the average rate r is given as:

$$r = \mu LD/t, \quad (2)$$

where D/t is equal to the average slip rate S .

On the other hand, the relationship between the seismic moment m_o and the magnitude M of earthquakes which have occurred in and around the Japanese

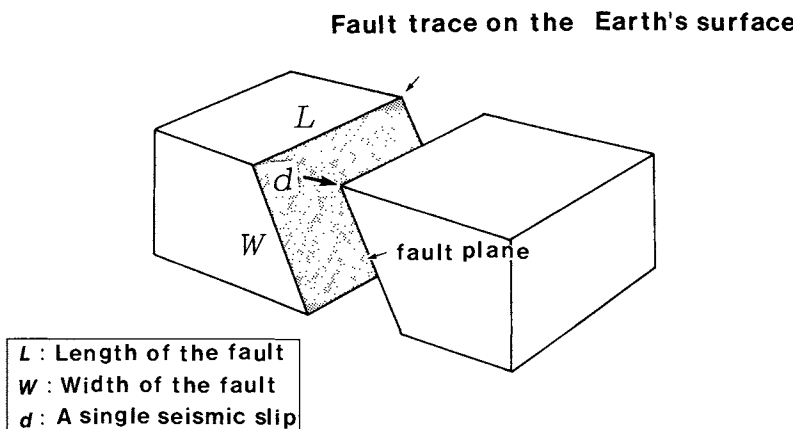


Fig. 4. A schematic diagram of a surface fault, fault plane, and the slip.

Islands is empirically expressed as (Wesnousky et al., 1982),

$$\log m_o = 17.0 + 1.3M. \quad (3)$$

Using this empirical equation, the moment m_o can be estimated from its magnitude M . Fig. 5 shows the relationship between the moment m_o and the magnitude M of earthquakes in and around central Japan. In particular, the m_o - M relationship of Eq. (3) is established among inland earthquakes. The total released moment by the 1995 Kobe earthquake was calculated as 2.49×10^{26} dyne cm/year (Kikuchi, 1995). This value is plotted directly on the straight line in Fig. 5, indicating the validity of Eq. (3). An average rate r is also given from the total moments of all earthquakes along a fault or fault system divided by a given period (Kanaori et al., 1992b,d).

The average rate r of seismic moment-release on a given fault system is calculated by dividing the total of the released moments, which is the sum of all destructive earthquakes along the fault system, by the temporal length of the historical period. The average rates can also be estimated from the average Quaternary slip rates of the major active faults which constitute the fault system. The average rate of moment-release calculated from the summation of moments released by historical earthquakes along the fault systems in central Japan over the approximate period of the last 1000 years is in good agreement with the estimate from slip rates of

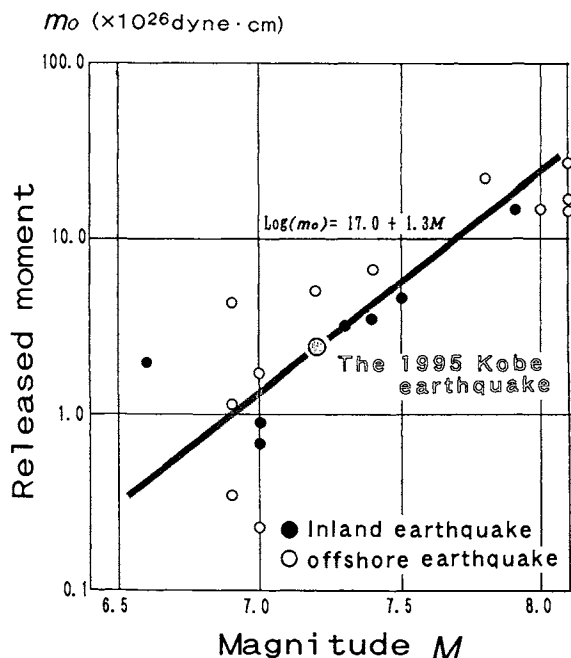


Fig. 5. Relationship between the magnitude M and moment release m_o of earthquakes in and around central Japan. The straight line is empirically drawn (Wesnousky et al., 1982).

constituent active faults over the Quaternary period (Fig. 6) (Kanaori et al., 1992b,d).

Although the averaging periods are different in two orders of magnitudes between the two average-rate calculations, the good correlation implies that the movement of a fault or segment of a fault system is responsible for the generation of a large inland earthquake. It is pointed out that the average rate of moment-release is a good parameter for evaluating the seismic risk of the fault or fault system.

Fig. 7 shows an example of an accumulation curve of moments which have been released by large inland earthquakes along the Hanaore-Kongo fault line (HKFL) (Kanaori et al., 1992c, 1994a). The moment m_o of each earthquake is estimated from the magnitude M by using Eq. (3). This figure shows an irregular pattern of moment-release along the fault system, implying a seismic cycle of alternating active and quiet periods. The average rate r is given by the slope of the straight line linking the left corners of the step-like curve in Fig. 7.

3.2. The average rate and interseismic period

Seismic moments are accumulated along the fault or fault system during an interseismic period T . If the moments are released constantly at an average rate, the moments m_o are given as the product of T and the average rate r , i.e., $m_o = rT$. Taking the logarithm of the both sides of this equation, and replacing the moment m_o by using Eq. (3), the following equation is obtained:

$$\log T = 1.3M + 17.0 - \log r. \quad (4)$$

Fig. 8 shows the relationship between the interseismic period T and the magnitude

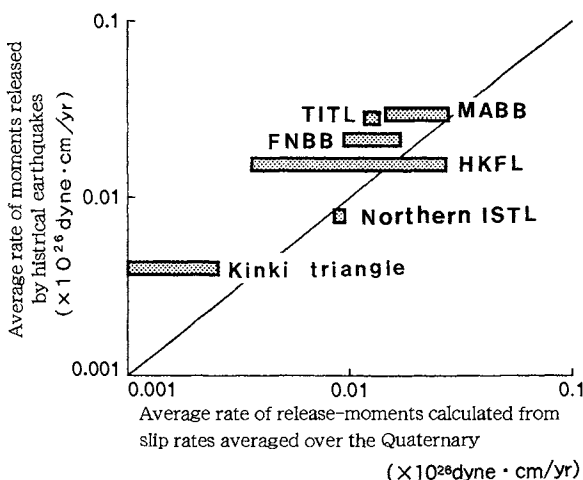


Fig. 6. Relationship between average rates of moment-release obtained from the average slip rate and fault dimensions, and the magnitude of historical earthquakes (Kanaori et al., 1992b).

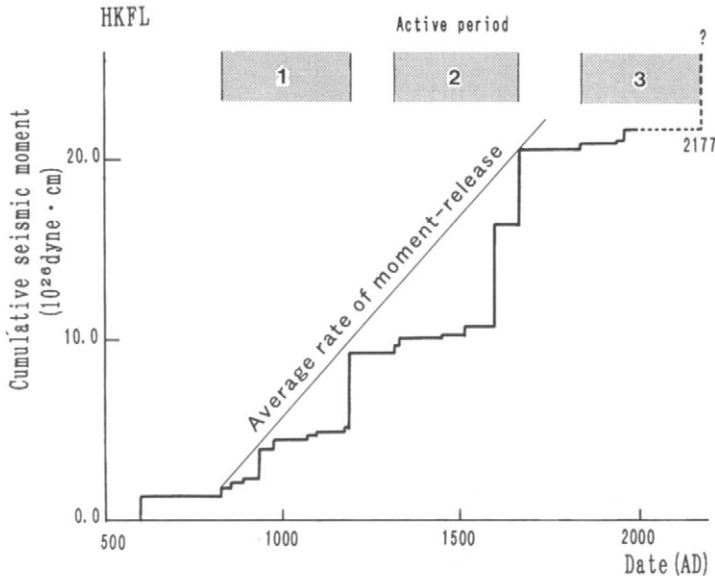


Fig. 7. Accumulative curve of seismic released moments along the Hanaore-Kongo fault line (Kanaori et al., 1992c). The moment released by each earthquake is estimated from the magnitude, using Eq. (3).

M of the expected earthquake with seven lines showing the average rate r . When the average rate r is obtained for an objective fault or fault system, the interseismic period T is estimated by using Eq. (4). In contrast, the magnitude M of an earthquake which is predicted to occur can be estimated from Eq. (4), when the interseismic period T is given.

Whether or not Eq. (4) is applicable to the 1995 Kobe earthquake is checked below, as an example. The distribution of the aftershocks and surface ruptures indicate that the length L and the width W of the ruptured plane of the earthquake are 40 and 20 km, respectively. The average right-lateral and dip-slip rate S of the ATTL is geomorphologically estimated from the displacement of river terraces to range from 0.5 to 1.5 m/10³ years, and from 0.1 to 0.9 m/10³ years, respectively (Sangawa, 1978). By substituting these values into Eq. (2), the average rate r is calculated as 0.0017 to 0.0063 × 10²⁶ dyne cm/year (Table 1). On the other hand, the interseismic period T is approximately 400 years, since the 1596 Keicho-Fushimi earthquake is considered to have occurred before the 1995 Kobe earthquake along the ATTL (Kanaori et al., 1993b). The estimated r and T give a magnitude ranging from 6.8 to 7.2, as shown in Fig. 8. The upper value of the estimate is consistent with the actual magnitude of the Kobe earthquake, indicating that this method is valid.

3.3. Fault length and interseismic period

By deleting the magnitude M from Eqs. (1) and (4), the following relation can be established among the fault length L , the interseismic period T , and the average

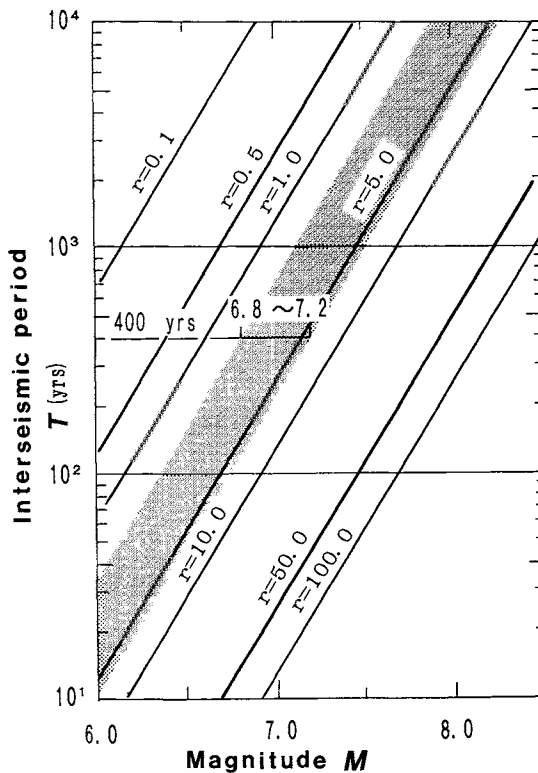


Fig. 8. Relationship between the magnitude M of a possible earthquake and the interseismic period T . Seven lines for different average rates r ($\times 10^{26}$ dyne cm/year) are shown. The shaded zone is the range of the average moment-release rate of the ATTL, estimated from the average slip rates of the constituent faults (Kanaori and Kawakami, 1996a,b).

TABLE I

The average rate of moment-release of the ruptured surface which created the 1995 $M7.2$ Kobe earthquake (Kanaori and Kawakami, 1996b)

Slip sense	Average slip rate ^a S (mm/year)	moment-release	Average rate of $r(\times 10^{26}$ dyne cm/year)
Right-lateral	0.5–1.5		0.0014–0.0041
Dip-slip	0.1–0.8		0.0003–0.0022
Total			0.0017–0.0063

$L=40$ km, $W=20$ km, $\mu=3.4 \times 10^{11}$ dynes/cm².

^aBased on Sangawa (1978).

rate r :

$$\log T = 23.3 + 2.17 \log L - \log r. \quad (5)$$

Fig. 9 shows the relationship between the fault length L and the interseismic period

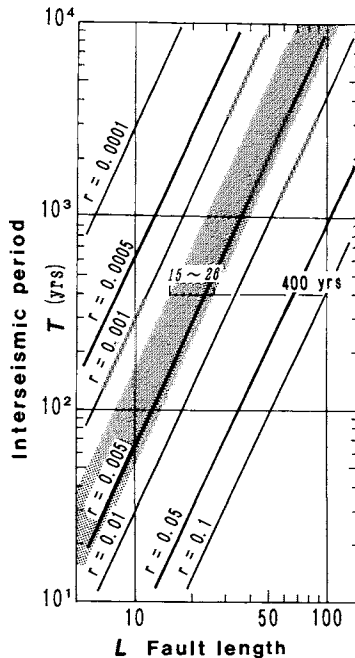


Fig. 9. Relationship between the ruptured length L of a possible earthquake and the interseismic period T . Seven lines for different average rates r ($\times 10^{26}$ dyne cm/year) are shown. The shaded zone is the range of the average moment-release rate of the ATTL, estimated from the average slip rates of the constituent faults.

T with seven lines of different average rates. The fault length L of an earthquake event or an interseismic period T can be estimated from this relationship, when the average rate r is known for the fault system.

Taking the Kobe earthquake as an example, the fault length L can be estimated in the same manner as the magnitude M (cf. Fig. 8). Since the interseismic period T is approximately 400 years, the fault length L is estimated to range from 15 to 26 km, as shown in Fig. 9. This estimated length is shorter than the seismogenic fault length of 40 km. This is consistent with the view that only part of the seismogenic fault appears on the ground surface.

3.4. Potential magnitude and seismic risk

Assuming that a fault or fault system, moves to release all moments which have been accumulated, previously, the magnitude M_p of the earthquake generated is defined here as the potential magnitude of the fault. The potential magnitude M_p can be estimated as follows.

First, the elapsed time t is calculated as the period between the date of the latest earthquake and the present (1995) for a fault or fault system. When the interseismic

period T is replaced by the elapsed time t in Eq. (5) and Fig. 8, the potential magnitude M_p can be estimated from the average rate r and the elapsed time t of a fault or fault system. Because a large structure is durable during no more than 100 years, the potential magnitude M_{p+100} of 100 years after the present can be also calculated using the same relationship.

The precision of the present method for seismic risk evaluation using the average rate of moment-release depends on an accurate estimate of the following two parameters: (1) the dimension of the fault rupture, and (2) the average slip rate of the fault or magnitude of historical earthquakes. When the seismic risk of a fault or fault system is evaluated by this method, the two parameters should be obtained as precisely as possible.

4. Seismic risk re-evaluation of fault systems in central Japan

Central Japan can be divided into several blocks of major fault systems (tectonic lines or block boundaries), which are composed of large-scale active faults on the ground surface (Fig. 10). It has been pointed out, from temporal and spatial distributions of historical earthquakes which have caused damage in central Japan, that most destructive earthquakes are probably created by movements of fault systems (Kanaori et al., 1991). This suggests that the seismic risk of inland earthquakes is larger along a fault system than in the blocks. Kanaori et al. (1992b,d) evaluated the seismic risk along fault systems and along the blocks in central Japan separately, using the average rate of moment-release. However, it appears that the seismic risk evaluation for central Japan is insufficient, when implications of the Kobe earthquake occurrence are taken into account.

4.1. Fault system forming a block boundary

Most historical earthquakes which have damaged central Japan occur along fault systems forming block boundaries, as shown in Fig. 11. The main shock of the 1995 Kobe earthquake was located at the mid-point of the Arima-Takatsuki tectonic line (ATTL), which is composed of a number of active faults, while the regions of aftershock occurrence were along the central 40-km-long segment of the ATTL. This means that the seismic risk should be more strongly assessed for a fault system, rather than for each active fault.

4.1.1. Active and quiet periods

Fig. 12(a) shows migrations of ruptured regions with time along the Hanaore-Kongo fault line (HKFL). The length of the ruptured regions is estimated from the magnitude of the earthquake using Eq. (1). A seismic cycle of alternating active and quiet periods can be found in the spatial and temporal distribution (Fig. 12(b)). Quiet periods are intercalated with three active periods. When an active period begins, part of the fault system starts to rupture. The active period terminates after

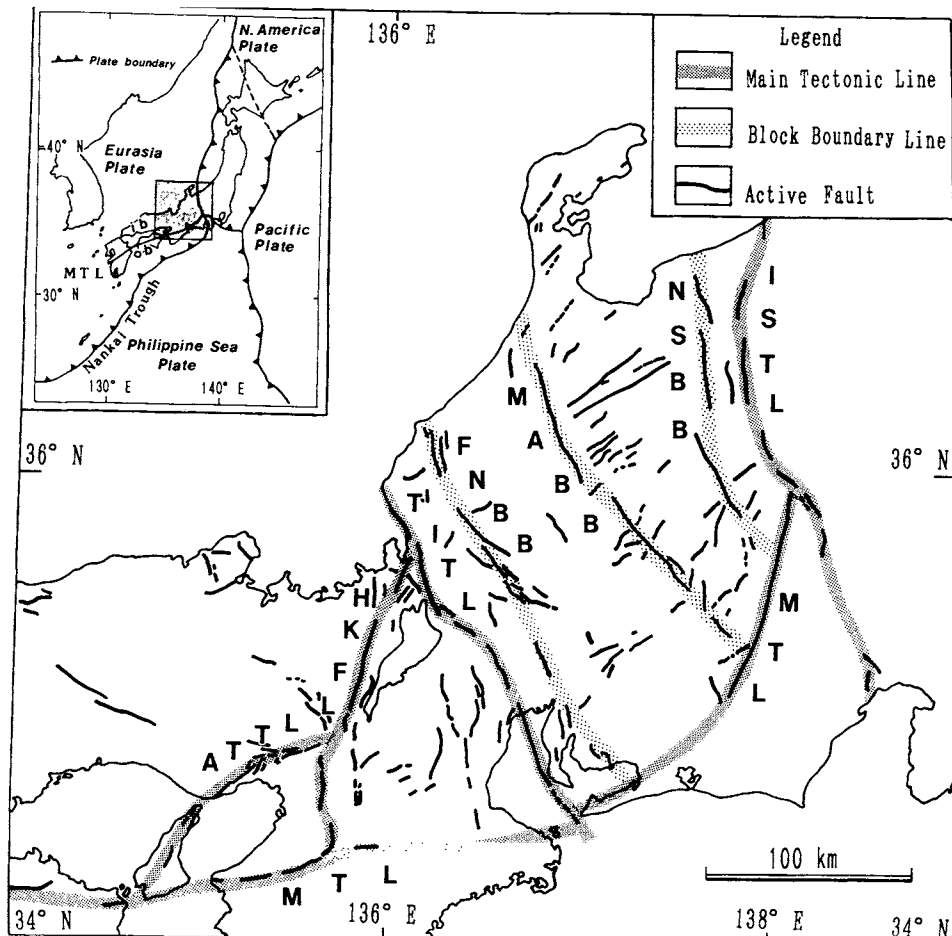


Fig. 10. Map showing the major fault systems in central Japan (based on Kanaori et al., 1992a, 1993a). The fault systems are defined as lines linking large-scale active faults. The inset shows the plate boundaries in and around the Japanese Islands and the location of central Japan. The fault systems are: ATTL, the Arima-Takatsuki tectonic line; HKFL, the Hanaore-Kongo fault line; ISTL, the Itoigawa-Shizuoka tectonic line; MTL, the Median Tectonic Line; and TITL, the Tsurugawan-Isewan tectonic line. The block boundary lines are: FNBB, the Fukui-Neodani block boundary; MABB, the Miboro-Atera block boundary; and NSBB, the Nekomata-Sakaitoge block boundary. The zones are: ib, the inner belt, and ob, the outer belt.

the entire length of the fault system is ruptured without overlapping. A fault or segment which constitutes the fault system produces one earthquake during the active period. During an active period, each fault segment moves to create an earthquake in the period between the minimum and maximum intervals shown in Fig. 12(b). This also implies that each fault or segment does not move at a regular interval.

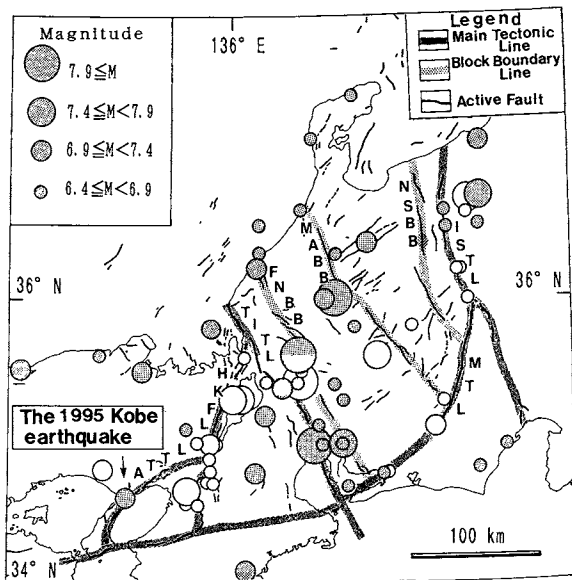


Fig. 11. Epicenters of destructive inland earthquakes in the Kinki district that have occurred since 599 A.D. Magnitudes are represented by the circle size according to the legend. Earthquake data are based on Usami (1987). The epicenter of the 1995 Kobe earthquake is located at the Akashi strait between Kobe City and Awaji Island.

4.1.2. Estimate of average moment-release rate

Fig. 13 shows average rates of moment-release along fault systems and in regions inside the blocks of central Japan. This figure also indicates that the average rate is commonly higher along the fault systems than in regions inside the blocks. Kanaori et al. (1992b) detected unruptured regions in the current active period. An unruptured region is regarded as a seismic gap having a high risk of producing the next large, inland earthquake. They evaluated the seismic risk of each seismic gap using the method of the average rate of moment-release.

Kanaori et al. (1992b,d) estimated the time when the next earthquake will occur along each block boundary in central Japan. In their calculation, the magnitude of the earthquake is estimated from the identified seismic gaps. The time is calculated from the moment divided by the average moment-release rate of the entire block boundary. Although the seismic gap is identified, adoption of the average rate for the entire block boundary means that the expected event does not necessarily occur at the seismic gap.

In the case of the Kobe earthquake, the actual magnitude is consistent with the magnitude estimated from seismic moments accumulated along the 40-km-long ruptured areas since the 1596 Keicho-Fushimi earthquake (Kanaori and Kawakami, 1996a,b). This consistency indicates that the seismic risk of a part or segment of a

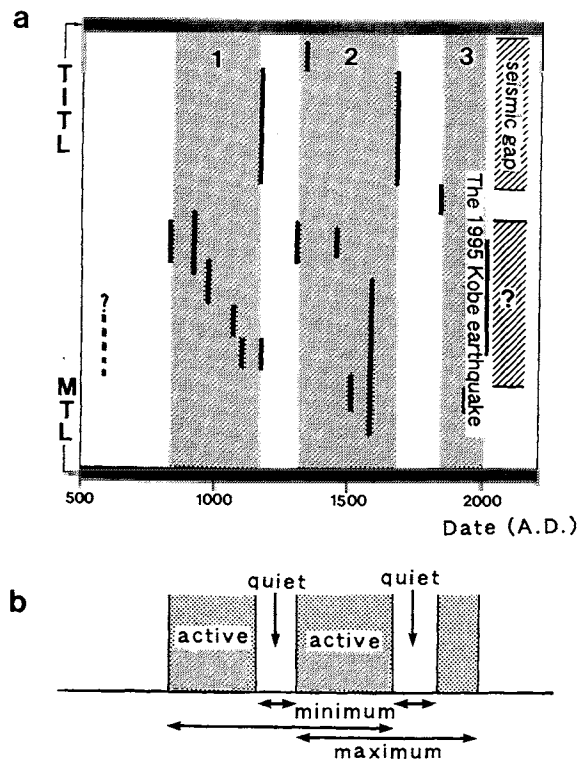


Fig. 12. (a) Spatial and temporal distribution of destructive earthquakes along the Hanaore-Kongo fault line (Kanaori et al., 1992c). The ruptured length L is calculated from the magnitude M using Eq. (1). The calculated length is drawn at the center of each epicenter. Two seismic gaps are detected in the current active period (denoted as 3). The southern gap may be correlated with the ruptured region of the 1995 Kobe earthquake. (b) A schematic diagram of a seismic cycle with alternating active and quiet periods. A fault or segment which constitutes the fault system moves only once during an active period.

fault system should be evaluated by using the average rate which is allocated into the seismic gap or segment.

Accordingly, the seismic risk of the seismic gaps in central Japan is re-calculated in this study, assuming that the total average rate of a fault system is uniformly distributed along its length, and that the average rate which is shared into the seismic gap is obtained from the average rate of the entire fault system multiplied by the ratio of the length of the seismic gap to the total length of the fault system. Table 2 shows the interseismic period in each seismic gap from the result of the re-calculation. The moments were accumulated along the fault system during the interseismic period.

4.1.3. Seismic risk of seismic gaps

The elapsed time t of a seismic gap is given as the period between the present (1995) and the year of the latest earthquake generation. Fig. 14 shows the interseismic

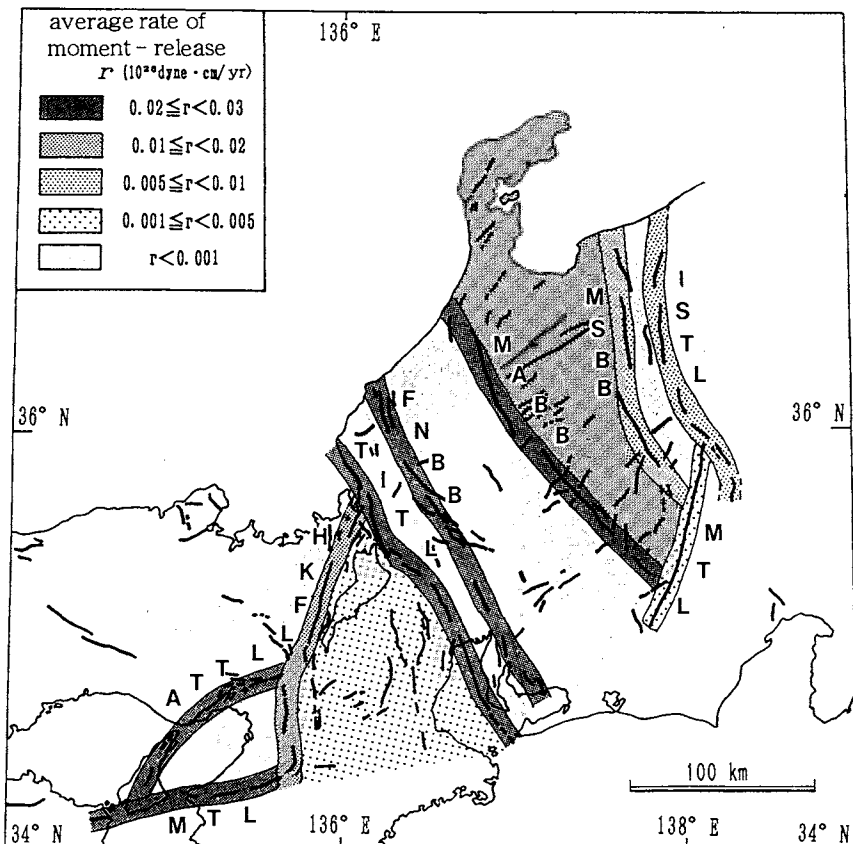


Fig. 13. Average rates of moment-release along block boundaries and inside blocks of central Japan (Kanaori et al., 1992d). The values of the Arima-Takatsuki tectonic line and the Median Tectonic Line are changed from the values obtained previously. The abbreviations are the same as those in Fig. 10.

period T derived from Eq. (4), and the elapsed time t for seismic gaps in central Japan. When the elapsed time t of the seismic gap for the latest earthquake is unknown, it is considered as 1000 years, taking into account the duration of the historical age of Japan.

The first record in historical documents of an earthquake which caused damage appeared in 599 A.D. In the 600s, few records are available. After the late 800s, records of destructive earthquakes are substantial. In Fig. 14, the elapsed time t and the interseismic period T of the ATT_L creating the 1995 Kobe earthquake are also shown. The elapsed time t is given as the period between the 1596 Keicho-Fushimi and the 1995 Kobe earthquakes, while the interseismic period T shown by the white bar in Fig. 14 is estimated from the magnitude $M7.2$ of the Kobe earthquake, using Eq. (3).

The relationship between the interseismic period T and the elapsed time t is

TABLE II

Interseismic period T and elapsed time t of seismic gaps along fault systems forming block boundaries in central Japan

Seismic gap	Length, L (km)	M	Average rate of moment-release ^a , r ($\times 10^{26}$ dyne cm/year)	Interseismic period, T (years)	Latest earthquake (A.D.)	Elapsed time, t (years)
ISTL ($L=125$ km, $r=0.0087-0.0093$)						
A	20	7.0	0.00139-0.00149	905-848	unknown	
MABB ($L=200$ km, $r=0.0148-0.0284$)						
B	40 (20+20)	7.5 7.0	0.00296-0.00568 0.00148-0.00284	1919-1000 851-444	unknown unknown	
C	30	7.3	0.00222-0.00426	1378-718	unknown	
TITL ($L=185$ km, $r=0.0122-0.0138$)						
D	30	+7.3	0.00198-0.00224	1537-1358	unknown	
E	30	7.3	0.00198-0.00224	1537-1358	1325?	670
HKFL ($L=160$ km, $r=0.0037-0.0276$)						
F	40	7.5	0.00069-0.00518	4396-589	1662	333
G	20	7.0	0.00046-0.00345	2739-365	1510	385
Kongo f.	15	6.8	0.00029-0.00216	2708-363	1510	385
ATTI ($L=100$ km, $r=0.0043-0.0157$)						
H	30	7.3	0.00129-0.00471	2364-648	1596	399
I	30	7.3	0.00129-0.00471	2364-648	1596	399

^aAverage rate of moment-release of the tectonic line and block boundary is based on Kanaori et al. (1992d).

classified as: (1) t is equal to or larger than T , (2) t is within the range of T , and (3) t is smaller than T . The fault system can be categorized into the following three risk ranks, in order from the most dangerous to less dangerous faults;

Risk rank A elapsed time $t \geq$ interseismic period T

Risk rank B elapsed time $t \subset$ interseismic period T

Risk rank C elapsed time $t <$ interseismic period T .

It is founded that the central 40-km-long segment of the ATTl which produced the 1995 Kobe earthquake is categorized into Risk rank B (Fig. 14). The seismic gaps A and C' in Fig. 15 are categorized into Risk rank A. These two gaps have the highest seismic risk, because the elapsed time exceeds the interseismic period. The seismic gap belonging to Risk rank B has a high probability of earthquake generation, the same as the fault system before generating the Kobe earthquake.

Fig. 15 shows the location and seismic risk of seismic gaps in central Japan. The seismic gaps include those previously detected by Kanaori et al. (1992b,d). The eastern and western regions of the ATTl are regarded as seismic gaps, because

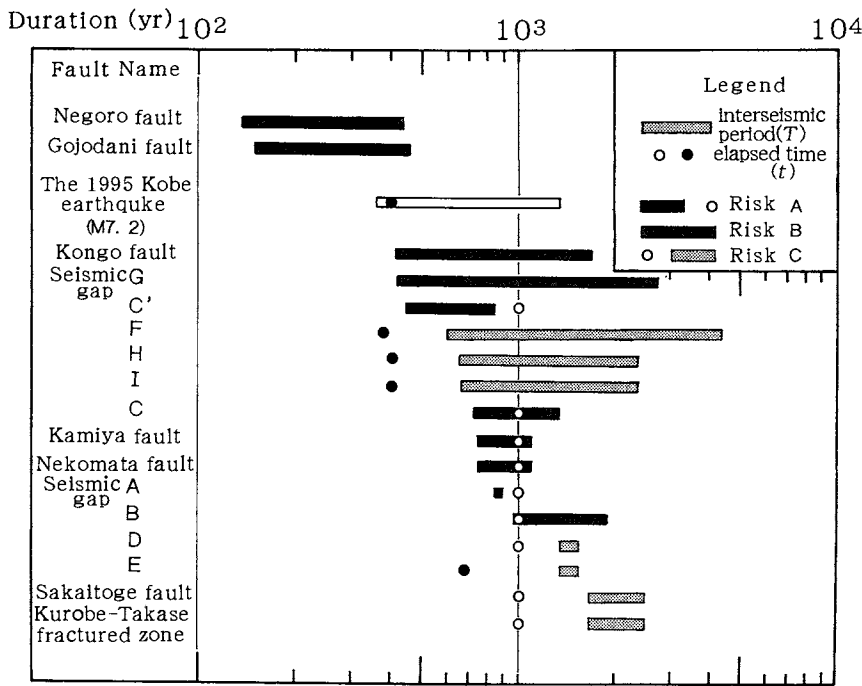


Fig. 14. Relationship between interseismic period T and elapsed time t since the latest event at seismic gaps and dangerous faults. Solid circles show seismic gaps and active faults whose latest earthquakes are known. Open circles are those whose historical earthquakes are unknown. Abbreviations of the seismic gaps correspond to those in Fig. 15.

these regions were unruptured at the time the Kobe earthquake. The two regions are denoted as seismic gaps H and I, respectively.

4.1.4. seismic risk with no historical earthquakes

Kanaori et al. (1991) discussed whether the block boundary fault systems are in an active or a quiet period. Since historical earthquakes are unknown along the MTL and the NSBB, it is impossible to determine whether those fault system are presently in an active or a quiet period. In these fault systems, seismic gaps also cannot be detected. Assuming that the next rupture region occurs at the active fault which constitutes the fault system, the seismic risk along the two fault systems can be evaluated at each active fault.

Table 3 shows the moment which is accumulated during the interseismic period of each active fault. The Gojodani fault and the Negoro fault along the MTL, and the Nekomata fault and Kamiya fault along the NSBB belong to Risk rank B.

4.1.5. Estimate of potential magnitude

Table 4 shows a calculation of the potential magnitude of faults which constitute the TITL, as an example of the method described in Section 3.4. In this calculation,

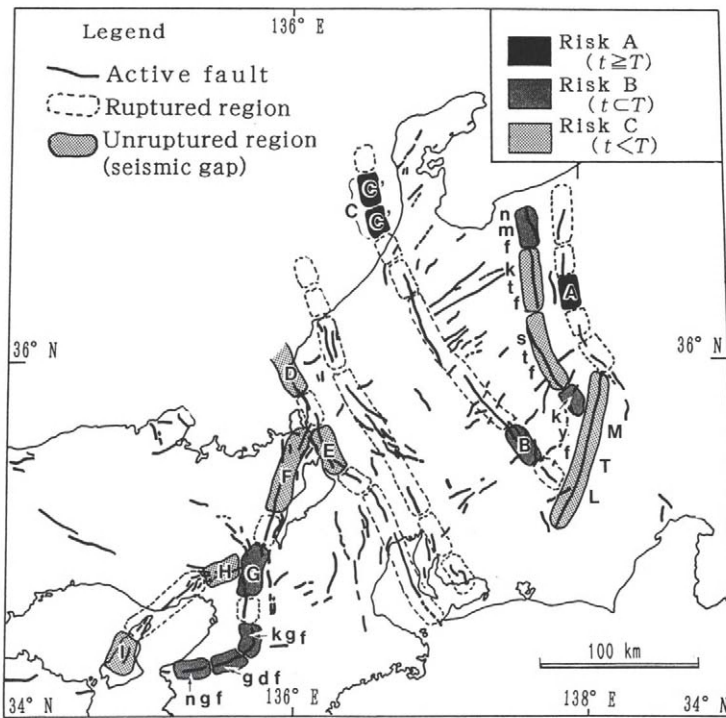


Fig. 15. Seismic risk rank of seismic gaps along fault systems with historical earthquakes, and faults along fault systems whose earthquakes are historically unknown (Kanaori et al., 1992b,d). The seismic gaps H and I were detected along the Arima-Takatsuki tectonic line after the 1995 Kobe earthquake. Abbreviations of the faults are: gdf, the Gojodani fault; kgf, the Kongo fault; ktf, the Kurobe-Takase fractured zone; kf, the Kamiya fault; ngf, the Negoro fault; nmf, the Nekomata fault; and stf, the Sakaitoge fault.

it is assumed that ruptured areas of the next earthquake are the same as the latest ruptured areas or the seismic gaps, and the ratio of seismic total moments stored along the fault system to the moments accumulated since the latest event are calculated at the present (1995). The potential magnitudes M_p and M_{p+100} indicate the maximum magnitude of an earthquake which the fault or seismic gap would produce for an earthquake in 1995 and 100 years after, respectively. It is proposed that the potential magnitude in 1995 or 100 years after should be used as basic data of seismic input for earthquake-proof designs of large structures.

4.2. Seismic risk of active faults within blocks

Although large inland earthquakes mostly occur along the fault systems forming block boundaries, some of them are exceptions, and located in the region inside the blocks. For example, the 1819 $M7.2$ Omi earthquake, the 1854 $M7.2$ Iga-Ueno

TABLE III

Interseismic period T and elapsed time t along the fault systems forming block boundaries whose historical earthquakes are unknown

Fault name	Length, L (km)	M	Average rate of moment-release, r ($\times 10^{26}$ dyne cm/year) ^b	Interseismic period, T (years)	Latest earthquake, T (years)	Elapsed time, t (years)
NSBB ($L = 180$ km, $r = 0.0073\text{--}0.0109 \times 10^{26}$ dyne cm/year ^a)						
Nekomata fault	15	6.8	0.00061–0.00091	1101–738	unknown	
Kurobe-Takase fractured zone	30	7.3	0.00122–0.00182	2499–1673	unknown	
Sakaitoge fault	30	7.3	0.00122–0.00182	2499–1673	unknown	
Kamiya fault	15	6.8	0.00061–0.00091	1101–738	unknown	
MTL						
Western Kii Peninsula						
Gojodani fault	15	7.1	0.00337–0.01047	463–149	1596	399
Negoro fault	20	7.0	0.00306–0.00952	415–133	1596	399
Eastern Chubu district	100	8.2	0.00015–0.00048	100 000 <	unknown	

^aBased on Kanaori et al. (1992d).

^b $\mu = 3.4 \times 10^{11}$ dyne/cm², $W = 15\text{--}20$ km.

S is based on Research Group for Active Faults in Japan (1991).

TABLE IV

Examples of calculations of potential magnitude for the Tsugawana-Isewan tectonic line (TITL)

Ruptured region	Length, L (km)	Average rate allocated, r ($\times 10^{26}$ dyne cm/year)	Elapsed time ^a , t (years)	M_p (%)	M_{p+100}
Seismic gap D	30 +	0.00198–0.00224	1000	7.2	7.2
Seismic gap E	30	0.00198–0.00224	670	7.0	7.1
1909 Anegawa earthquake (Sekigahara fault)	15	0.00099–0.00112	86	6.1	6.4
1586 Tensho earthquake (Yoro fault and Isewan fault)	80	0.0053–0.0060	409	7.2	7.4

^aIn 1995.

earthquake, and the 1859 $M7.0$ Hietsu earthquake can be listed as historical earthquakes which occurred inside blocks in central Japan. Recently, the 1961 $M7.1$ Kita-Nimo earthquake and the 1984 $M6.8$ earthquake occurred there. On the other hand, a few large-scale active faults which have an equivalent length to that of block boundary faults exist in the region inside the block (Kanaori et al., 1992a).

It is generally difficult to detect a dangerous active fault inside the crustal blocks. A procedure for detection of active faults with high risk inside blocks in central Japan is proposed below.

Using the relationship between the fault length L and interseismic period T at a given average rate of moment-release (cf. Fig. 9), the fault length L or the

interseismic period T can be estimated. Table 5 shows the relation among active fault class, average slip rate S , fault length L , average moment-release rate r , magnitude M , moment m_o , and interseismic period T . A range of average slip rates is first specified, including the median value of each active fault class A, B, or C. The average rate r is calculated at a given fault length L , using Eq. (2). The interseismic period T can be estimated from the average rate r and the fault length L , using Eq. (5) and Fig. 9.

Table 5 shows that the interseismic interval is independent of the active fault class, and that the shorter active faults, which are categorized into the same class, have shorter interseismic intervals. This is inconsistent with the previous hypothesis in which Class A faults move in a shorter interval than that of the lower-class active fault.

It is concluded that the interseismic interval of the active fault depends on both the length L and the average slip rate S . When an interseismic interval is estimated for an active fault, both the fault length L and the average rate r should be taken into account for the estimation.

Since destructive earthquakes which are generated inside the blocks are not understood yet in the context of the tectonic settings, it is difficult to determine the activity pattern of faults in the blocks. However, average slip rate S and length L of those active faults have been determined (Research Group for Active Faults in Japan, 1991). Table 5 can be used to evaluate the seismic risk of active faults inside blocks.

Based on the relationship between the average rate r and fault length L , examples of dangerous faults in the blocks of central Japan for the duration of a few hundred years are listed in Table 6. Further investigations should concentrate on these dangerous faults to detect the slip rate and the latest earthquake.

TABLE V
The average slip rate S and interseismic period T

Active fault class	Average slip rate, S (mm/year)	Length, L (km)	Average rate of moment-release*, r ($\times 10^{26}$ dyne cm/year)	M	m_o	Interseismic period, T (years)
A	3.0–7.0	10	0.00153–0.00476	6.5	0.28	183–59
		20	0.00306–0.00952	7.0	1.27	415–133
		40	0.00612–0.01904	7.5	5.68	928–298
		60	0.00918–0.02856	7.8	13.7	1492–480
		80	0.01224–0.03808	8.0	25.5	2083–670
B	0.3–0.7	10	0.00015–0.00048	6.5	0.28	1830–588
		20	0.00031–0.00095	7.0	1.27	4097–1334
		30	0.00046–0.00143	7.3	3.05	6645–2136
		40	0.00061–0.00190	7.5	5.68	9281–2983
C	0.03–0.07	10	0.00002–0.00005	6.5	0.28	18300–5880
		20	0.00003–0.00010	7.0	1.27	40970–13340

* $\mu = 3.4 \times 10^{11}$ dyne/cm², $W = 15\text{--}20$ km.

TABLE VI

Examples of dangerous active faults in blocks^a

Fault name	Length, <i>L</i> (km)	Average slip rate, <i>S</i> (mm/year)	Latest earthquake (A.D.)
The Block between the NSBB and the MABB			
Ushikubi fault	79	Class A–B	unknown
Ina fault	16	2.1–3.2	unknown
Kiso Mountain faults	35	0.5–1.0	unknown
The Block between the MABB and the FNBB			
Hatiman fault	24	Class B	unknown
Akagawa fault	24	Class B	unknown

^aSelected from Research Group for Active Faults in Japan (1991).

Since active faults are only ruptures which appear on the ground surface as a result of earthquakes, all active faults which exist in the blocks do not move in the coming several hundred years. It is necessary to distinguish the dangerous active faults from the other faults in the blocks.

5. Further problems

The present method of evaluating the seismic risk of a fault or a fault system by use of the average rate of moment-release, with an application to central Japan, is described above. When the method is applied to actual fault systems, some problems still remain to be solved for a precise evaluation of the seismic risk. The problems and precautions for using the method are stated below.

5.1. Block boundary faults and ruptured regions

Based on the assumption that large inland earthquakes are generated along fault systems forming block boundaries in central Japan, the seismic risk of the block boundary and regions inside the blocks are evaluated separately. The main shock of the 1995 Kobe earthquake occurred at the mid-point of the Arima-Takatsuki tectonic line (ATT) defined by Kanaori et al. (1993a). Its aftershocks were also distributed along the central 40-km-long segment of the ATT (Kanaori and Kawakami, 1996a).

However, it is impossible to predict where the seismic rupture started along the ATT before the Kobe earthquake. This earthquake was not created by the movement of a single active fault, but by the fault system which was composed of a number of active faults. An active fault is not the cause of an earthquake, but is only a surface manifestation as a result of an earthquake. When the seismic risk is evaluated for a single fault which constitutes a fault system independently, the magnitude of the earthquake will be underestimated.

Matsuzaki et al. (1996) simulated seismic activity along the fault systems of Southwest Japan using a theological model. The result of their simulation reveals that ruptured regions do not drastically change during a period of few thousand years. Further studies should be focused on identifying fault systems forming a block boundary and the regions ruptured by a single earthquake, by examining data for outcrops and fractured zones accompanying faults, together with their correlation to seismic data.

The seismic risk of the Japanese Islands has been evaluated previously by the density of active faults, and the maximum magnitude expected in each seismic region (Kakimi, 1983; Matsuda, 1990). In this evaluation, fault systems except for the MTL, are regarded as boundaries of respective seismic regions. Characteristics of each region were also emphasized. On the other hand, for the San Andreas fault in the western US, the seismic risk is evaluated along the fault trace and seismic gaps, and the probability of earthquake generation during a specific period is calculated for each segment of the fault (Working Group of California Earthquake Probability, 1988). As demonstrated by the generation of the Kobe earthquake, large inland earthquakes which cause serious damage are generated by the movement of fault systems forming block boundaries. Large-scale active faults which constitute the fault system must be energetically investigated. Results of the investigation will be useful to improve the risk evaluation method for the fault system.

5.2. Estimates of the average rate

The average rate of moments which are released by the movement of a fault is an important parameter in evaluating its seismic risk, as mentioned above. By evaluating the seismic risk more precisely, useful data will be obtained for the long-term prediction of such earthquakes, and then natural disasters induced by the next inland earthquake of a fault system can be reduced. The seismic risk evaluation uses the following three parameters: (1) the average slip rate of an active fault which constitutes a fault system forming a block boundary, (2) the length and width of the fault or ruptured plane, and (3) the date of the latest earthquake due to the fault movement. Actually, the three parameters should be determined precisely for each fault or fault system, in order to improve the precision of the estimate.

- (1) The average slip rate has been geomorphologically estimated as the value averaged over a period ranging from several hundred thousand years to one million years. However, the slip rate averaged over a relatively long period is not reflected in a single seismic slip of the active fault. This difference in the slip rates between long and short periods will be clarified in the future by using geodetic data of leveling and GPS (Global Positioning System).
- (2) In order to determine the length and width of a fault or ruptured plane precisely, it is necessary to get seismic data of micro-earthquakes, and aftershock distributions of small to large earthquakes. The lower limit of the micro-

earthquakes which occur in central Japan (Mikumo et al., 1988) and the aftershocks of the Kobe earthquake (Hirata, 1995) is 15–20 km deep. This depth gives the width of the earth's crust, which behaves in a brittle manner. On the other hand, the length of a rupture due to a single earthquake can be identified from damaged areas of historical earthquakes and aftershock distributions of recent destructive earthquakes.

- (3) The date of the latest earthquake along a fault or fault system can be identified sometimes by a trench excavation of the fault, or descriptions in historical documents. Since a trench excavation is performed in limited areas, the latest earthquake cannot be detected for all active faults. On the other hand, only a few active faults have been correlated with historical earthquakes. This correlation will be continued for historical earthquakes and active faults.

6. Conclusion

The generation of the 1995 Kobe earthquake requires reconsideration of previous models concerning the relationship between faults and earthquakes, or methods for evaluating the seismic risk of an active fault proposed in Japan. These models and methods are inconsistent with the knowledge obtained from the generation of the Kobe earthquake. Much important information has been obtained from the earthquake. In order to lessen natural disasters caused by inland earthquakes, it is necessary to develop a new method for the risk assessment taking into account the observations. Recognition of the importance of studying active faults has been greatly increased. It is essential to place active faults in the tectonic setting of the Japanese Islands.

Since a large number of excavation studies have been planned and conducted, and new data will be published in the near future, it is very important to interpret the data appropriately. The Kobe earthquake has required that we create new models for fault activity and methods for seismic risk assessment. The method presented in this paper should give a new insight into seismic risk assessment and earthquake-proof designs of large structures in seismically unstable areas.

Acknowledgment

The authors wish to thank Prof. K. Yairi of Gifu University for useful discussions. They also express appreciation to Ms Y. Ando for drafting the figures in this paper. A portion of this work was supported by a Grant-in-Aid from the Ministry of Education, Science, and Culture of Japan (No. 08680482).

References

- Asada, T., 1991. Some questions on active faults. *Active Fault Res.*, 9: 1–3 (in Japanese).
- Awata, Y., Mizuno, K., Sugiyama, Y., Imura, R., Shimokawa, K., Okumura, K., Tsukuda, E. and Kimura, K., 1996. Surface fault ruptures on the Northwest coast of Awaji Island associated with the Hyogo-ken Nanbu Earthquake of 1995, Japan. *Zisin*, 49: 113–124 (in Japanese with English Abstract).
- Brune, J.N., 1968. Seismic moment, seismicity, and rate of slip along major fault zones. *J. Geophys. Res.*, 73: 774–784.
- Hashimoto, M., Sagiya, T., Tsuji, H., Hatanaka, Y. and Tada, T., 1995. Coseismic displacement of the 1995 Kobe earthquake. *J. Phys. Earth*, in press.
- Hirata, S., 1995. Aftershock activity accompanying the 1995 Kobe earthquake. Kagaku, Iwanami Publishing Co., Tokyo, 65: 199 (in Japanese).
- Kakimi, T., 1983. Regional interrelation between active faults and destructive earthquakes on land in Japan. *Bull. Geol. Surv. Japan*, 34: 295–309 (in Japanese with English Abstract).
- Kakimi, T., 1995. Pacing of paleo-earthquake research: predicting earthquake recurrence from paleo-earthquakes. In: Y. Ohta and K. Shimazaki (Editors), *Exploring Paleo-earthquakes*, Kokon-shoin Publishing Co., Tokyo, pp. 2–26 (in Japanese).
- Kanaori, Y., Kawakami, S. and Yairi, K., 1991. Space-time distribution patterns of destructive earthquakes in the inner belt of central Japan: activity intervals and locations of earthquakes. *Eng. Geol.*, 31: 209–230.
- Kanaori, Y., Kawakami, S. and Yairi, K., 1992a. The block structure and Quaternary strike-slip block rotation of central Japan. *Tectonics*, 11: 47–56.
- Kanaori, Y., Kawakami, S. and Yairi, K., 1992b. Space-time distribution patterns of destructive earthquakes in the inner belt of central Japan (part 2): moment-release rates and earthquake prediction. *Eng. Geol.*, 32: 113–122.
- Kanaori, Y., Kawakami, S. and Yairi, K., 1992c. Space-time distribution patterns of destructive earthquakes in the Kinki district, central Japan: implications of the Hanaore-Kongo fault and Tsurugawani-Isewan tectonic lines. *J. Jpn. Soc. Eng. Geol.*, 33: 187–201 (in Japanese with English Abstract).
- Kanaori, Y., Kawakami, S. and Yairi, K., 1992d. Space-time distribution patterns of destructive earthquakes in the inner belt of central Japan (part 3): seismic hazard assessment. *Eng. Geol.*, 33: 99–110.
- Kanaori, Y., Kawakami, S. and Yairi, K., 1993a. Space-time correlations between inland earthquakes in central Japan and great offshore earthquakes along the Nankai trough. *Eng. Geol.*, 33: 289–303.
- Kanaori, Y., Kawakami, S., Yairi, K. and Hattori, T., 1993b. Liquefaction and flowage at archaeological sites in the inner belt of central Japan: tectonic and hazard implications. *Eng. Geol.*, 35: 65–80.
- Kanaori, Y., Kawakami, S. and Yairi, K., 1994a. Seismotectonics of the Median Tectonic Line in southwest Japan: implications for coupling among major fault systems. *Pure Appl. Geophys.*, 142: 589–607.
- Kanaori, Y., Kawakami, S., Yairi, K. and Niwa, S., 1994b. A sequence of destructive earthquakes and the coupling of fault systems in central Japan. *Eng. Geol.*, 37: 167–180.
- Kanaori, Y. and Kawakami, S., 1996a. Microplate model and large inland earthquakes of southwest Japan: Implications for generation of the 1995 M 7.2 Hyogo-ken-nanbu Earthquake. *Zisin*, 49: 125–139 (in Japanese with English Abstract).
- Kanaori, Y., and Kawakami, S., 1996b. The 1995 7.2 magnitude Kobe earthquake and the Arima-Takatsuki tectonic line: implications of the seismic risk for central Japan. *Eng. Geol.* 43, 135–150.
- Kawakami, S., Kanaori, Y. and Yairi, K., 1992. The C-class active faults problems and a future direction of active faults study: a comment to the questions by T. Asada. *Active Fault Res.*, 10: 1–7 (in Japanese).
- Kikuchi, M., 1995. Focal mechanisms from far-field bodily waves. *Monthly Earth*, (Suppl. 13): 47–53 (in Japanese).
- Koto, B., 1893. On the cause of the great earthquake in Central Japan, 1891. *J. Coll. Sci. Imp. Univ. Japan*, 5: 196–353.
- Matsuda, T., 1974. Surface faults associated with Nobi (Mino-Owari) earthquake of 1891. *Spec. Bull. Earthquake Res. Inst.*, Univ. Tokyo, 13: 85–126 (in Japanese with English Abstract).

- Matsuda, T., 1975. Magnitude and recurrence interval of earthquakes from a fault. *Zisin* 2, 28: 169–283 (in Japanese with English Abstract).
- Matsuda, T., 1976. Active faults and earthquakes – the geological aspect. *Memoirs Geol. Soc. Japan*, 12: 15–32 (in Japanese with English Abstract).
- Matsuda, T., 1978. Earthquake traces. In: T. Asada (Editor), *Method for Earthquake Prediction*, Tokyo Univ. Press, Tokyo, pp. 29–54 (in Japanese).
- Matsuda, T., 1981. Active faults and damaging earthquakes in Japan — macroscopic zoning and precaution fault zones. In: D.W. Simpson and P.G. Richard (Editors), *Earthquake Prediction; an International review*. Am. Geophys. Union, pp. 279–289.
- Matsuda, T., 1983. Magnitude and Frequency of Crustal Movements. *Trans. Jpn. Geomor. Union*, 4: 151–165 (in Japanese with English Abstract).
- Matsuda, T., 1990. Seismic zoning map of Japanese Islands, with maximum magnitudes derived from active fault data. *Earthquake Res. Inst. Univ. Tokyo*, 65: 289–319.
- Matsuda, T., 1992. Estimation activity of the active fault. *J. Geogr.* 101: 442–452 (in Japanese with English Abstract).
- Matsuda, T., 1994. Watching active faults. In: *Earthquake and Fault*, Shimazaki, T. and Matsuda, T. (eds.), Tokyo Univ. Press, Tokyo, pp. 24–44 (in Japanese).
- Matsuzaki, M., Kawakami, S., Kanaori, Y. and Yairi, Y., 1996. Modeling of the interaction between destructive earthquakes and large off coast earthquakes in central Japan. *Eng. Geol.* 42, in press.
- Mikumo, T., Wada, H. and Koizumi, M., 1988. Seismotectonics of the Hida region. *Tectonophysics*, 14: 95–119.
- Muramatu, I., 1976. Neodani fault and Nobi earthquake. *Memoirs Geol. Soc. Japan*, 12: 117–127.
- Research Group for Active Faults in Japan, 1980. Active faults in Japan, sheet maps and inventories. Tokyo Univ. Press, Tokyo, 363 pp. (in Japanese with English Abstract).
- Research Group for Active Faults in Japan, 1991. Active faults in Japan, sheet maps and inventories, revised edition. Tokyo Univ. Press, Tokyo, 437 pp. (in Japanese with English Abstract).
- Sangawa, A., 1978. Fault topography and Quaternary faulting along the middle and eastern parts of the Arima-Takatsuki tectonic line, Kinki district, central Japan. *Geogr. Rev. Japan*, 51: 760–775 (in Japanese with English Abstract).
- Sangawa, A., 1992. Traces of paleoearthquakes observed in many archaeological sites. *Jpn. Soc. Soil Mech. Funda. Eng.*, 40: 13–18 (in Japanese).
- Scholz, C.H., 1990a. Earthquake as a chaos. *Nature*, 348: 197–198.
- Scholz, C.H., 1990b. *The Mechanics of Earthquakes and Faulting*, Cambridge Univ. Press, 439 pp.
- Schwartz, D.P. and Coppersmith, K.J., 1984. Fault behavior and characteristic earthquakes: examples from the Wasatch and San Andreas faults. *J. Geophys. Res.*, 89: 5681–5698.
- Shimamoto, T., 1995. Mystery of “belt of seismic disasters”. Kagaku, Iwanami Publishing Co., Tokyo, 65: 195–198 (in Japanese).
- Suzuki, Y., Watanabe, M., Nakata, T., Okada, H., Sawa, H., Imaizumi, T., Hirano, S., Maemoku, H., and the Research group for the paleoseismicity of the Nojima Fault, 1995. Excavation study of the Nojima Fault — second report. *Abstract Fall conven. of Japan Seismol. Soc.*, 1995, A70 (in Japanese).
- Usami, T., 1987. *Descriptive Catalogue of Disastrous Earthquakes in Japan*, new edition. Tokyo Univ. Press, Tokyo, 434 pp. (in Japanese).
- Utsu, T., 1974. Space-time pattern of large earthquakes occurring off the Pacific coast of the Japanese Islands. *J. Phys. Earth*, 22: 325–342.
- Wallace, R.E., 1970. Earthquake recurrence intervals on the San Andreas fault. *Geol. Soc. Am. Bull.*, 82: 2875–2890.
- Wallace, R.E., 1987. Grouping and migration of surface faulting and variations in slip rates on faults in the Great Basin Province. *Bull. Seismol. Soc. Am.*, 81: 2875–2890.
- Wesnousky, S.G., Scholz, C.H. and Shimazaki, K., 1982. Deformation of an island arc: rates of moment release and crustal shortening in intraplate Japan determined from seismicity and Quaternary fault data. *J. Geophys. Res.*, 87: 6829–6852.

Working Group of California Earthquake Probability, 1988. Probabilities of large earthquake occurring in California on the San Andreas fault, US Geol. Surv. Open-file Rept. 88-398, 61 pp.

Yamashina, K., Matsuda, T. and Ariyama, T., 1985. Ground breaks associated with the 1984 Western Nagano prefecture earthquake. Bull. Earthquake Res. Inst. Univ. Tokyo, 60: 249–279 (in Japanese with English Abstract).

Channel network modelling of the fractured granite in the Hinachi area, Japan

KUNIO WATANABE^{a,*}, YOKITO SUGIMURA^b, YUTAKA MORITA^c
and TATSUYA TANAKA^d

^a*Faculty of Engineering, Saitama University, 255 Shimo-Okubo, Urawa, Saitama 338, Japan,* ^b*Dam Structure Division, Research Institute of Water Resources Development Public Corporation, 936 Jinde, Urawa, Saitama 338, Japan,* ^c*Design Division, IDOWR Engineering Co. Ltd., 1-7-7 Umesato, Sugimami, Tokyo 166, Japan* and ^d*Civil Engineering Technical Division, Obayashi Corporation, 2-2-9 Hongo, Bunkyo, Tokyo 113, Japan*

Abstract

A hydrogeological model of the fractured granite that has developed in the Hinachi area of Japan was constructed, taking into account the geological structure of the fracture system. The major objective of this study focussed on the proper modelling of the highly permeable channel network that has developed in the fractured granite. The distribution of highly weathered areas, thought to be an indication of highly permeable channels, was investigated. It was found that the locations of the areas mostly coincided with several geological features, such as the step structure, the end points of a single fracture and the intersections between fractures. The sizes of the highly weathered areas were studied. It was found that the size distribution of the highly weathered areas could be approximated by a log-normal distribution curve. The relation between the porosity and hydraulic conductivity of granite was also examined. An empirical equation that can well approximate the relation was derived. Using this equation, the hydraulic conductivity of weathered granite can be estimated from the porosity of a small specimen. The average hydraulic conductivity of highly weathered areas, estimated from porosity, is 10^4 to 10^5 times larger than fresh granite. It was concluded that these highly weathered areas act as channels. The channel network existing in a rock mass must be properly modelled for the analysis of groundwater flow. On the basis of the results obtained in the present study, a process for channel network modelling was proposed.

1. Introduction

The proper analysis of groundwater flow in a fractured rock mass is very important in many geotechnical fields such as dam construction, tunnel excavation, water resources development within the rock mass, and deep underground waste disposal.

* Corresponding author. Tel.: +81 48 8583571; fax: +81 48 8559361.

The proper hydrogeological modelling of a fractured rock mass is indispensable for the analysis of groundwater flow. It has been pointed out in many previous studies that a large amount of groundwater flows through several selected seepage paths called channels that have developed in a fractured rock mass (Bear et al., 1993). It is important to properly evaluate the channel network in an actual rock mass and to construct a reliable hydrogeological model of the rock mass before any groundwater analysis is performed. The estimation of the locations and the hydraulic conductivities of those channels in an actual rock mass, however, is very difficult, so that the general technique of how to construct a hydrogeological model has not yet been established.

The channels might have been created during a long history of geotectonic movement that includes the creation, the propagation, and the reactivation of fractures, and may be closely related to the geological features of the fracture system. Basic study of the relation between the geological structure and the channel is important in creating the proper technique for hydrogeological modelling.

Bossart and Mazurek (1991) studied, in detail, the geometry and hydraulic features of fractures that developed in the Grimsel Test Site constructed in the Alpine region of Switzerland. It was found that the fractures created or reactivated during the brittle deformation stage were the major conduits of groundwater flow. Munier (1993) examined the fracture system that developed in the vicinity of the Äspö Hard Rock Laboratory in Sweden, and concluded that groundwater mainly flows through selected fractures that have been generated or reactivated within geologically recent time. These studies have clearly shown that the geological history of a fractured rock mass must be taken into consideration when a hydrogeological model is constructed. Tanaka et al. (1994) and Watanabe et al. (1994) studied the hydrogeological features in fractured granite found in the Kamaishi Mine, Japan, and concluded that the intersections between conjugate fractures tend to be the highly permeable channels.

Mazurek et al. (1995) reported on the hydrogeological features of the rock mass around the Äspö Hard Rock Laboratory. It was concluded that the fractures running parallel to the maximum stress axis formed the hydraulically active fractures and can act as channels for groundwater flow. The importance of the splay fractures on the behavior of groundwater flow was also pointed out, with reference to the concept discussed in Martel and Pollard (1989). These studies have clearly pointed out that the hydraulic nature of a rock mass is closely related to the geological features and the earth pressure conditions.

Despite these studies, there remain many problems in the modelling of a channel network. Among these problems, how to construct a hydrogeological model, how to quantitatively evaluate the hydraulic properties of channels, and how to analyze the flow on the basis of geological informations are important.

As a basic study for creating the proper hydrogeological modelling technique, the present authors have examined the relation between the geological features and the indication of channels in the fractured granite that developed in the Hinachi area of Japan.



Fig. 1. The locations of the Hinachi and Kusaki areas in Japan.

2. Fractures in the Hinachi area

Fig. 1 shows two locations, Hinachi and Kusaki areas (solid circles) in Japan, that are mentioned in the present paper. Granite of the late Cretaceous age has commonly developed in these two areas. A wide sloped surface in the Hinachi area has been excavated for dam construction, and the fractures that have developed in the granite body can be well observed.

Fig. 2(a) presents a map of the fractures found over the excavated area. The

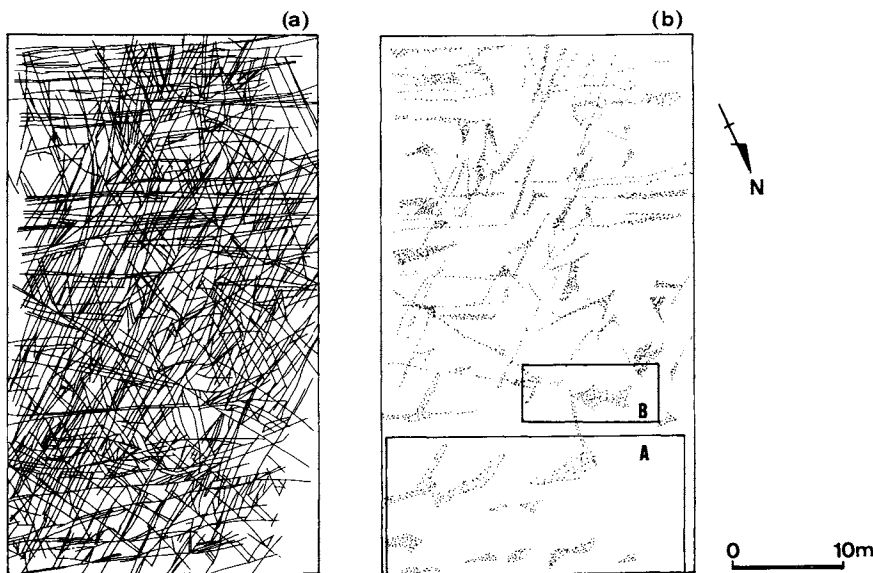


Fig. 2. (a) Fracture map of the excavated slope in the Hinachi area. (b) Distribution of highly weathered parts indicated by shaded areas. Sub-areas A and B indicated by the rectangles denote areas studied in greater detail.

highly weathered areas are shown as shaded regions in Fig. 2(b). The highly weathered rock is decomposed and brown in color due to oxidation. In Fig. 2(b), it is found that the highly weathered areas are mostly located along several fractures.

There are several chemical and physical reasons for the occurrence of partial weathering. In the usual case, the infiltration of rainwater and the oxidation are needed in the process of weathering. The highly weathered areas are thought to coincide with the high permeable regions (Davis and De Wiest, 1966). These areas can be thought of as an indication of channels. The geological structures of these highly weathered zones in sub-areas A and B in Fig. 2(b) were studied in detail.

Fig. 3 shows a stereographic projection of the directional distribution of the fractures. From this figure, it is found that the fractures are oriented in three dominant directions. One represents horizontal fractures while the other two dip vertically and are oriented approximately in the E-W and NE-SW directions. The extension of the horizontal fractures, however, are narrow and mostly cut by the vertical fractures, so that horizontal fractures are not thought to be important. There are other important fractures, although they are not numerous and are not clearly found in Fig. 3. These fractures dip vertically and strike roughly NW-SE. The fractures can be observed in Fig. 2(a), and displacements along these fractures are clearly observed at several locations. For this reason, it was decided that there are three important orientations of fractures, i.e., being almost vertical and E-W, NE-SW, and NW-SE in strike. Fractures having these orientations are referred to as E-W, NE-SW and NW-SE fractures in the present paper.

3. Geological structure of highly weathered areas

Fig. 4(a) shows the fracture map over sub-area A indicated in Fig. 2(b); three types of fractures, E-W, NE-SW and NW-SE oriented, are observed in this figure. Fig. 4(b) presents the distribution of highly weathered areas. The highly weathered

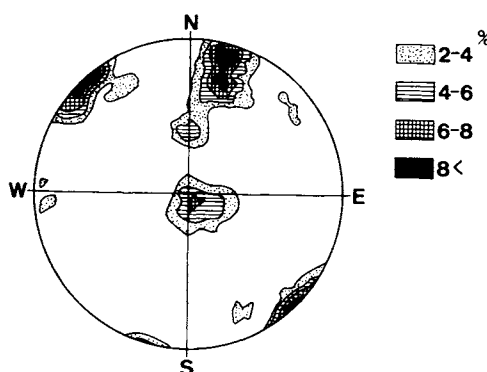


Fig. 3. Stereographic projection of fracture orientations as indicated in the legend (lower hemisphere).

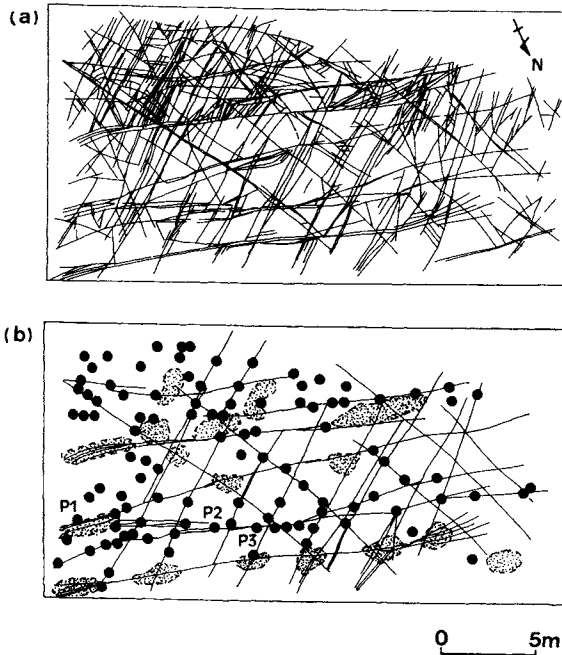


Fig. 4. (a) Fracture map of sub-area A shown in Fig. 2(b). (b) Distribution of highly weathered regions in sub-area A. Shaded areas indicate the wide zones of highly weathered rock. Solid circles are smaller areas of highly weathered rock.

regions are shown by the shaded areas and solid circles. Several major fractures in Fig. 4(a) are also shown in Fig. 4(b). The shaded areas are the wide weathered zones having areas of greater than 2 m^2 . The solid circles represent smaller regions of weathered rock, the areas being less than 2 m^2 . The small areas are mostly located at the intersections of NE-SW and NW-SE fractures.

Figs. 5(a), (b) and (c) show examples of these small areas of weathered rock located at points P1, P2 and P3 in Fig. 4(b). The shaded area in each figure represents the highly weathered region. Displacement directions observed along some of the fractures in the vicinity of highly weathered regions are also shown. As can be seen, the shapes of the highly weathered regions are complicated. The shape of each small weathered rock region was approximated by a circle, as shown in these figures, to roughly evaluate the size of the regions. Fig. 6 displays the distribution of the diameters of the circles. This distribution can be roughly approximated by the log-normal distribution curve shown in the figure.

The structure of the system of fractures shown in Fig. 4(a) can be interpreted as a combination of the two different fracture patterns presented in Figs. 7(a) and (b). The pattern shown in Fig. 7(a) is mainly composed of a number of E-W fractures and many splay fractures that branch from the E-W fractures. Arrows along the E-W fractures indicate the observed displacement directions. Splay fractures are

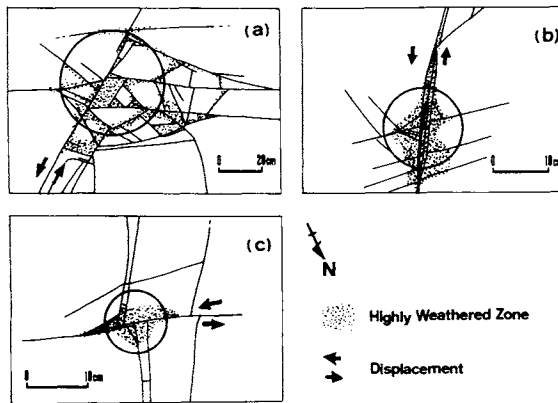


Fig. 5. Three examples of highly weathered regions. Figures (a), (b) and (c) correspond to points P1, P2 and P3 in Fig. 4(b). Circles in these figures approximate the area of the highly weathered zone. The size of each weathered zone is defined by the diameter of the circle.

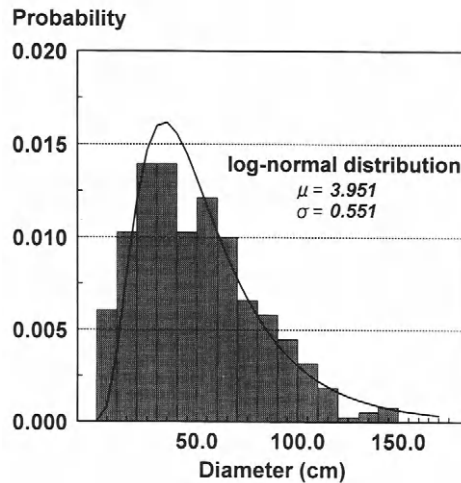


Fig. 6. Size distribution of the highly weathered zones. The solid line represents the log-normal distribution curve fit to the size distribution. Here, μ and σ are the average and standard deviation, respectively.

thought to be created by a left-lateral displacement along E–W fractures. Several step structures in which many small splay fractures connect two or three E–W fractures are observed. Splay fractures are also concentrated in the vicinity of the end points of E–W fractures.

Fig. 7(b) shows the other pattern composed of NE–SW and NW–SE fractures. Displacements along a number of these fractures are also indicated by short arrows. It was interpreted that these NE–SW and NW–SE fractures constitute conjugate fracture sets.

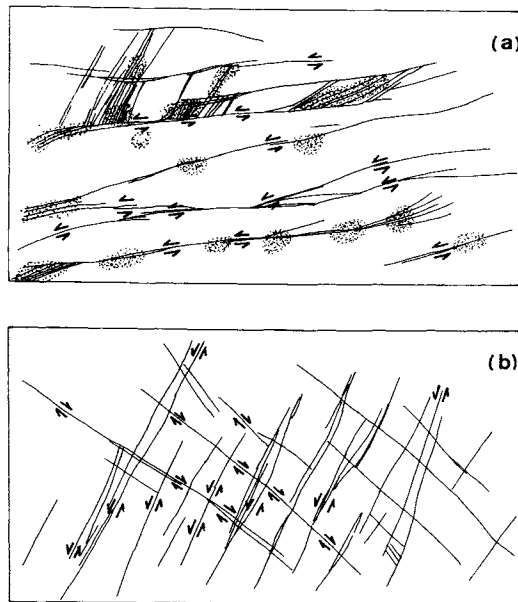


Fig. 7. Two major structures observed in sub-area A. Short arrows indicate the direction of the displacements.

The locations of weathered regions or zones corresponding to the shaded areas in Fig. 4(b) are also plotted in Fig. 7(a). It is found that these weathered zones exist along several E-W fractures. By comparing the locations of the wide weathered zones in Figs. 4(b) and 7(a), the zones can be essentially classified into two types. The first type consists of zones created at the step structures or at the end points of fractures where many splay fractures are concentrated. The zones in the second type are located at the points of intersection between E-W fractures and NE-SW or NW-SE fractures. On the other hand, small areas of weathered rock are mostly located at the intersections between NE-SW and NW-SE fractures that constitute conjugate sets.

Fig. 8 schematically illustrates the process that might have created the fracture patterns in sub-area A. The counter-clockwise rotation of the principal stress axes is essentially thought to be the mechanism that created this fracture pattern. Fig. 8(a) illustrates the creation of E-W fractures under stress conditions shown in the figure. The labelled arrows σ_1 and σ_3 are the maximum and the minimum stress directions, respectively. Many splay fractures were then created by the rotation of the maximum stress axis accompanied by shear displacement along the E-W fractures (Fig. 8(b)). Finally, many conjugate sets composed of NE-SW and NW-SE fractures were formed by the further rotation of the stress axis (Fig. 8(c)). The fracture structure in this area is thought to be essentially formed by this mechanism. The actual fracturing process, however, may be more complicated. It is observed at some

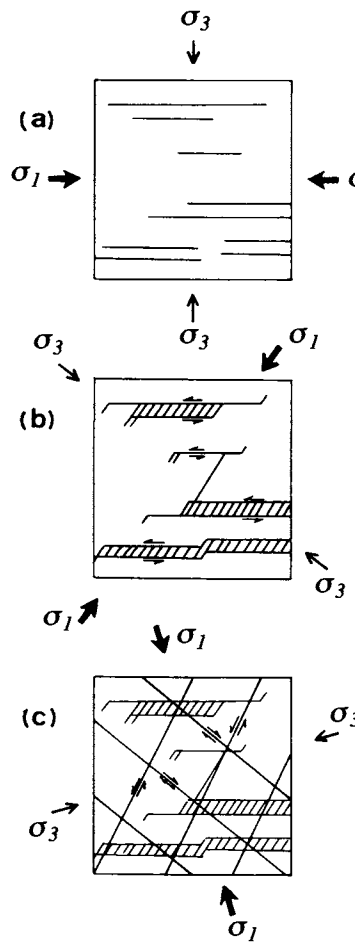


Fig. 8. Processes that could be responsible for the creation of the structures in sub-area A. The directions σ_1 and σ_3 are the maximum and the minimum principal stress directions, respectively. The creations of E-W fractures (a), splay fractures (b), and conjugate sets composed of NE-SW and NW-SE fractures (c) are schematically illustrated.

locations that E-W fractures slightly displace NE-SW and NW-SE fractures. This fact implies the reactivation of a number of E-W fractures after the creation of the NE-SW and NW-SE fractures. Although there remain some problems on the clarification of the fracturing process, the general mechanisms that have formed this overall structure can be interpreted as shown in Fig. 8.

Many small fractures are concentrated at the step structure, at the end points of fractures, and the intersections. From the fact that highly weathered regions are mostly located at these features, it is thought that these features produce the highly permeable zones. The concentration and deformation of these small fractures may

create open spaces within these features. The open spaces allow for large hydraulic conductivity. This is the possible reason that the highly weathered regions are located at the features.

4. Estimation of hydraulic conductivity

The hydraulic conductivity of highly weathered regions as well as the fresh areas of granite must be properly evaluated for constructing the hydrogeological model. Core specimens of fresh or slightly weathered rock having porosity of less than 2.0% can be easily sampled and the hydraulic conductivities can be easily measured. The hydraulic conductivities of the fresh and slightly weathered specimens sampled from the Hinachi area are less than $1.0 \times 10^{-9} \text{ cm s}^{-1}$. Samples of two specimens from the bored core had approximately 3.5% porosity. It was found that the hydraulic conductivities of these specimen were around $1.0 \times 10^{-7} \text{ cm s}^{-1}$. The hydraulic conductivity measurements in the highly weathered regions having porosity of greater than 4.0%, is very difficult due to the problems in the formation of the core specimen.

One possible way to estimate the hydraulic conductivity of highly weathered rock is an approximation from other values such as porosity. For the present purpose, the relation between hydraulic conductivity and porosity was studied. A total of 42 specimens of granite were collected from the Kusaki and the Hinachi areas, and the hydraulic conductivity and porosity of these specimen were measured. Fig. 9 displays the relation between the hydraulic conductivity and porosity of these specimens. The open and solid circles in this figure correspond to the specimens sampled from the Kusaki and the Hinachi districts, respectively. Two specimens of highly decomposed granite soil having about 30% porosity were also used in the measurements. The hydraulic conductivity of Hinachi granite is somewhat less than Kusaki granite when compared at the same porosity line. Although slight differences can be found, the general trends of the relations can be thought of as being almost identical.

There were no data in the porosity region between about 4 and 30% due to the difficulties in sampling and coring. In order to obtain data in this region, specimens having larger values of porosity were artificially made by heating core specimens of fresh rock in an electric oven. The specimens were repeatedly heated for about 2 h at several temperatures between 200 and 700°C. The heated specimens were then rapidly cooled in water. The porosity of these specimens gradually increased by the repetition of the heating and cooling processes. The change in hydraulic conductivity due to the increase in the porosity could be then examined. Three specimens of fresh rock were used in this test. The open circles in Fig. 10 represent the heated specimens and solid circles identify all the data in Fig. 9. The hydraulic conductivities of heated specimens are slightly greater than the other specimen values. Although some differences exist, the general trend of the relation between hydraulic conductiv-

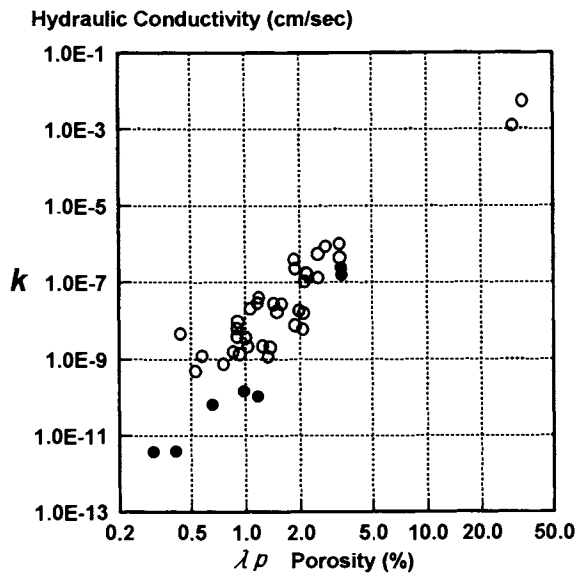


Fig. 9. Relation between hydraulic conductivity and porosity for granite. Open and solid circles indicate Kusaki and Hinachi granite, respectively.

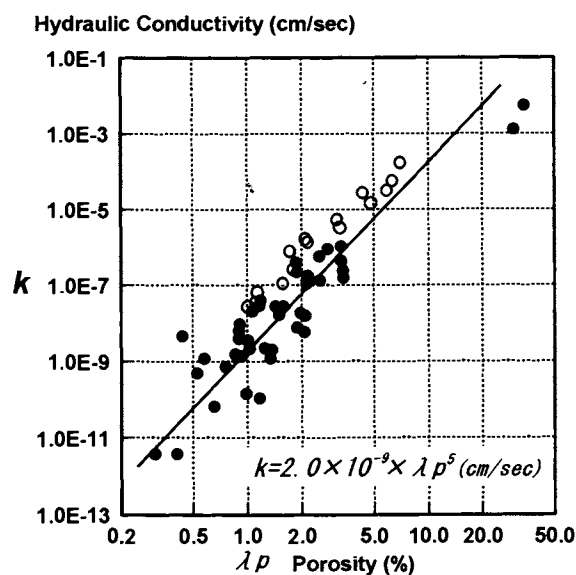


Fig. 10. Relation between hydraulic conductivity and porosity. Solid circles identify all the data in Fig. 9. Open circles denote the heated specimens. The solid line approximates the relation.

ity and porosity can be approximated by;

$$k = 2.0 \times 10^{-9} \times \lambda_p^5 \quad (1)$$

where, k is the hydraulic conductivity and λ_p is the porosity in %. Eq. (1) is indicated in Fig. 10 by the solid line and can now be used for estimating the hydraulic conductivity from values of porosity.

Fig. 11(a) shows the fracture map and distribution of the highly weathered zones in sub-area B (see Fig. 2(b)). Fig. 11(b) shows the fractures and highly weathered zones along the line drawn in Fig. 11(a). A total of 15 specimens were sampled from locations 1–15 indicated in this figure by the solid circles. Locations 2, 3, 4, 5, 11, 12, 13, 14, and 15 are highly weathered zones. The porosity and estimated hydraulic conductivity by use of Eq. (1) are summarized in Table 1. The sample numbers in this table correspond to the location numbers in Fig. 11(b); the highly weathered granite specimens are indicated in the footnote. The arithmetic mean of the hydraulic conductivities of highly weathered zones is about $6.4 \times 10^{-5} \text{ cm s}^{-1}$. This value is about 4–5 orders of magnitude larger than the fresh and slightly weathered rock in this area. From this result, it is concluded that a large amount of groundwater can flow through those highly weathered zones which act as channels. Of course, fractures are also good conduits of groundwater flow. Except for some large fractures, however, as the widths of fractures are not very wide, the discharge of groundwater through small fractures may not be large.

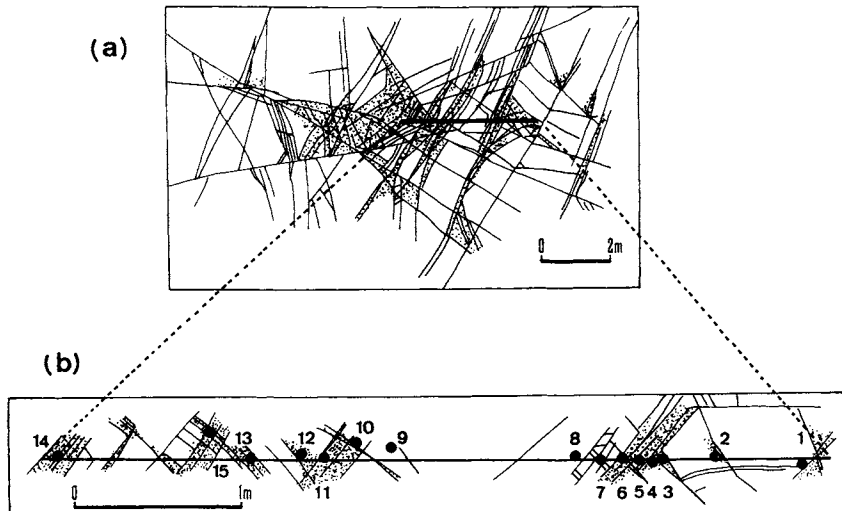


Fig. 11. (a) Fracture map and highly weathered zones in sub-area B shown in Fig. 2(b). (b) Sampling locations along the line shown in (a). Shaded areas indicate the highly weathered zones.

TABLE I
Porosity and the corresponding estimated hydraulic conductivity

Sample no.	Porosity, λ_p (%)	Hydraulic conductivity, k (cm s^{-1})
1	3.46	9.9E-07
2 ^a	5.53	1.0E-05
3 ^a	3.77	1.5E-06
4 ^a	5.92	1.5E-05
5 ^a	4.13	2.4E-06
6	3.00	4.9E-07
7	1.47	1.4E-08
8	1.96	5.8E-08
9	2.28	1.2E-07
10	2.53	2.1E-07
11 ^a	4.83	5.3E-06
12 ^a	7.17	3.8E-05
13 ^a	11.59	4.2E-04
14 ^a	7.80	5.8E-05
15 ^a	6.66	2.6E-05

^aThe specimen was sampled from a highly weathered region.

5. Process of channel network modelling

The hydrogeological model of this area can be constructed on the basis of the above-mentioned information concerning the geological structure of the area. Fig. 12 schematically illustrates the concept of the modelling process. Fig. 12(a) represents a rock mass having four fractures. A step structure is assumed in a fracture displayed in this figure. The intersection lines I and step structure S are taken as the channels as illustrated in Fig. 12(b). Groundwater can also flow through the fractures. To account for the flow through these fractures, a regular network of small channels is assumed to be located on every fracture, as shown in Fig. 12(c). In Fig. 12(c), it is assumed that the orientation of an individual channel on each fracture is either horizontal or vertical. When the hydraulic conductivity of each fracture is anisotropic, the channel directions are selected by the principal directions of the permeability tensor of the fracture. When combining all channels illustrated in Figs. 12(b) and (c), the final channel network can be constructed.

Fig. 13(b) illustrates an example of the channel network constructed around an intersection line between two fractures A and B in Fig. 13(a). This network is composed of one intersection line and the channels assumed on each fracture. Solid circles indicate the crossing points between these channels. Fig. 13(c) represents the connections between a crossing point P_0 in Fig. 13(b) and surrounding points P_1 , P_2 , P_3 , and P_4 . These points are connected by channels. The broken lines indicate channels on fracture B. Fig. 13(d) illustrates the flow conditions in these channels. H_0 , H_1 , H_2 , H_3 and H_4 are the piezometric heads on points P_0 , P_1 , P_2 , P_3 and P_4 ,

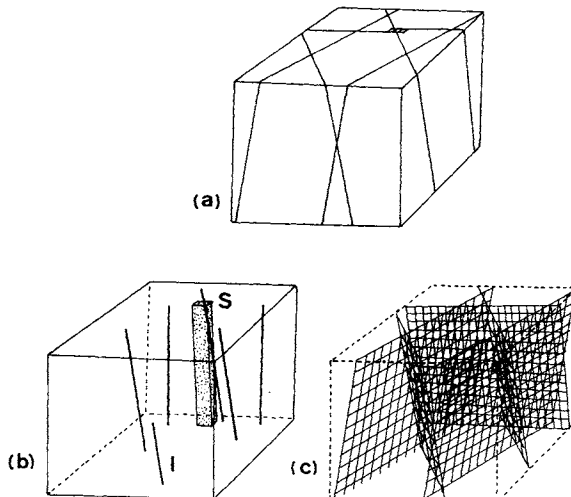


Fig. 12. Schematic illustration of the process for constructing a channel network model. (a) Fractures assumed in a block of granite. (b) The channels representing the step structure S and intersections I. (c) The regular networks assumed on the fractures.

respectively. Q_1 , Q_2 , Q_3 and Q_4 represent the discharge of groundwater flowing into point P_0 from P_1 , P_2 , P_3 and P_4 , respectively. Under steady-state conditions, the sum of Q_1 , Q_2 , Q_3 and Q_4 must be zero. That is,

$$Q_1 + Q_2 + Q_3 + Q_4 = 0 \quad (2)$$

The discharge for a given point Q_i ($i=1,4$) can be written as

$$Q_i = T_i \times (H_i - H_0) / l_i \quad (3)$$

where, l_i is the distance between P_0 and P_i ($i=1,4$), and T_i the transmissivity of the channel connecting P_0 and P_i .

Similar equations can be constructed for every crossing point in the similar manner. By solving all equations under given boundary conditions, the piezometric head distribution can be calculated.

The estimation of the transmissivity T_i of every channel is also important. Fig. 14 schematically illustrates a method to estimate the transmissivity. For a channel presenting an intersection line or a step structure, T_i can be simply estimated by the following equation as shown in Fig. 14(a);

$$T_i = A \cdot k_i \quad (4)$$

where, k_i is the hydraulic conductivity of the channel and A the cross-sectional area of the channel. The hydraulic conductivity k_i can be roughly estimated from the porosity using Eq. (1). For the assumed channel on a fracture, the transmissivity

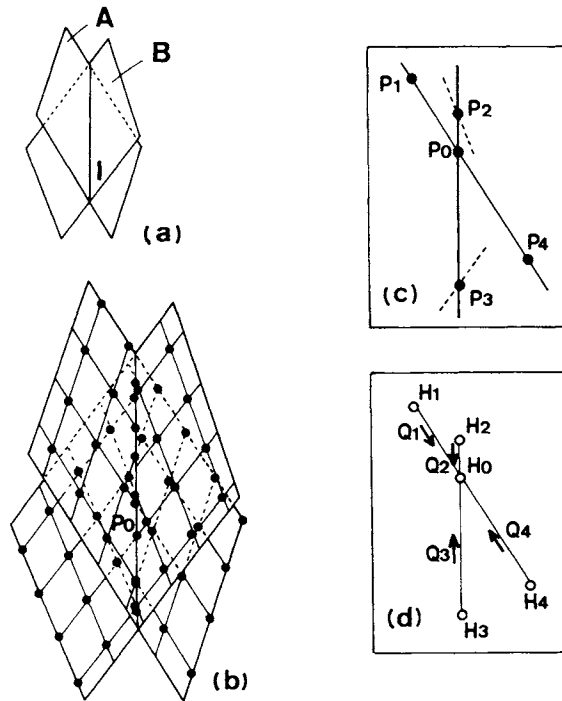


Fig. 13. Schematic illustration of an example of a channel network constructed on fractures A and B shown in (a). (b) Illustration of the network of channels. (c) Illustration of the connecting channels and water flow around P_0 point in (b). (d) The flow conditions in the channels where H_0 , H_1 , H_2 , H_3 , and H_4 are the piezometric heads on points P_0 , P_1 , P_2 , P_3 , and P_4 , respectively. The letters Q_1 , Q_2 , Q_3 , and Q_4 indicate the discharge of groundwater flow. Solid circles are the crossing points between channels.

T_i can be estimated as

$$T_{xi} = w \times \Delta z \times k \quad (5)$$

and

$$T_{zi} = w \times \Delta x \times k \quad (6)$$

where Δx and Δz are the spacings of the channels in the x and z directions as shown in Fig. 14(b), w is the fracture width and k the hydraulic conductivity of the fracture. Transmissivities T_{xi} and T_{zi} are for the channels that are assumed in the x and y directions, respectively. Hydraulic conductivity k can be estimated from the porosity of the filling material in the fracture, or from the opening width of the fracture.

The channel network model can be constructed by this process. This is a viable model for the weathered rock mass in the Hinachi area since it is constructed on the basis of a great deal of geological as well as hydraulic information.

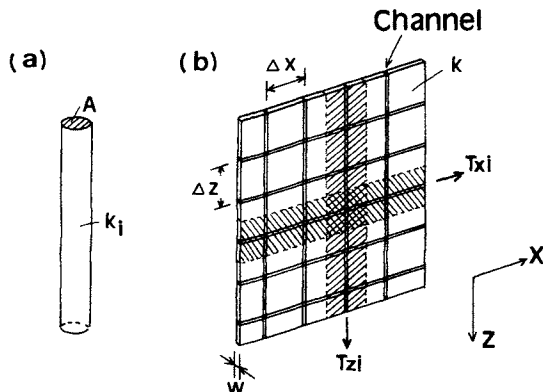


Fig. 14. Schematic illustration for the estimation of transmissivity T . (a) Typical channels along an intersection line, step structure or an end point of a fracture. Here, k_i is the hydraulic conductivity of the channel and A the area of the channel. (b) Assumed channels on a fracture, oriented in the x and z directions, having the respective transmissivities T_{xi} and T_{zi} . The x and z spacings of the channels are given by Δx and Δz , respectively. w is the width of the fracture and k the hydraulic conductivity.

6. Conclusions

The channel network model of the weathered granite that has developed in the Hinachi area was constructed on the basis of the geological structure of the area. The results obtained are as follows:

- (1) Highly weathered zones have developed at the locations of several geological features, i.e., the step structure, end points of fractures and intersections between fractures.
- (2) The size distribution of the area of highly weathered regions located at the intersections of fractures can be approximated by a log-normal distribution.
- (3) The empirical equation describing the relation between hydraulic conductivity and porosity of granite has been formulated.
- (4) Hydraulic conductivity of highly weathered granite can be estimated from porosity.
- (5) The estimated hydraulic conductivity of a highly weathered zone is at least 4 orders of magnitude greater than fresh granite.
- (6) The process of how to construct the channel network model has been proposed.

References

- Bossart, P. and Mazurek, M., 1991. Grimsel Test Site — Structural geology and water flow-path in the migration shear zone. NAGRA Technical Report, NTB 91-12, NAGRA, Switzerland, 55 pp.
- Bear, J., Tsang, C.F. and de Marsily, G. (Editors), 1993. Flow and contaminant transport in fractured rock, Academic Press, 560 pp.
- Davis, S.N. and De Wiest, R.J.M., 1966. Hydrogeology, John Wiley and Sons, 463 pp.

- Martel, S.J. and Pollard, D.D., 1989. Mechanics of slip and fracture along small faults and simple strike-slip fault zones in granitic rock. *J. Geophys. Res.*, 94(B7): 9417–9428.
- Mazurek, M., Bossart, P. and Eliasson, T., 1995. Classification and characterization of waterconducting features at Äspö. Progress Report 25-95-03, Äspö Laboratory, SKB, 76 pp.
- Munier, R., 1993. Four dimensional analysis of fractures at Äspö hard rock laboratory. *Eng. Geol.*, 33: 159–175.
- Tanaka, T., Watanabe, K., Maekawa, K. and Nakamura, N., 1994. Fracture network analysis based on the geologic model of channels. Part-1 Ideas and computer code. *J. Jpn. Soc. Eng. Geol.*, 35: 104–115 (in Japanese with English abstract).
- Watanabe, K., Tanaka, T., Uchida, M. and Iwasaki, H., 1994. Fracture network analysis based on the geological model of channels. Part-2 Analysis of the tracer migration test carried out in the Kamaishi mine. *Jpn. J. Jpn. Soc. Eng. Geol.*, 33: 132–142 (in Japanese with English abstract).

Keyword index

- Acceleration record, 5
 Acceleration response, 31
 Accumulation slip, 225
 Active fault, 64, 87, 107, 140, 144, 184, 186, 201, 221, 240, 241
 Active fault class, 223
 Active fault segment, 49
 Active faults, 110
 Active period, 231
 Active strike-slip fault, 59
 Activity of fault, 1
 Aftershock, 67, 88, 185
 Akashi strait, 64
 Amplification function, 19
 Amuria plate, 78
 Anegawa earthquake, 127
 Archaeological estimation, 69
 Archaeological excavation, 75
 Arima-Takatsuki, 190
 Arima-Takatsuki tectonic line, 67, 98, 196, 200, 222
 Arima-Takatsuki tectonic line (ATTL), 64, 87, 112, 241
 Array station, 8
 Arrival time, 210
 Ashiya fault, 201
 ATTL, 68, 74, 76, 79, 99, 223
 Average moment-release, 74
 Average moment-release rate, 73
 Average slip rate, 99, 221, 223, 225, 240
 Bandpass-filtered anomalies, 207
 Bedrock configuration, 203, 207, 210, 211, 212
 Blind fault, 63
 Block boundaries, 110
 Block boundary fault, 239
 Block rotation, 110
 Block structure, 64
 Borehole array, 9, 25
 Bouguer gravity anomaly, 207
 Brackish water, 122
 Brawley and Imperial, 56
 Brawley and Imperial fault system, 44
 Bulk density, 121
 Buried accelerograph, 10
 Buried fault, 211
 Buried seismometer, 9
 Calculated peak acceleration, 18
 Caterpillar model, 114
 Central Metasedimentary Belt Boundary Zone (CMBBZ), 139
 CFF, 190, 195
 Channel network, 258
 Channel network modelling, 258
 Characteristic earthquake model, 79, 86
 Chemical composition, 171, 176
 Clarendon-Linden Fault System, 138, 139, 142, 143, 144
 Clast-size distribution, 172
 Clay mineral, 149
 Clay minerals, 158
 Cohesive strength, 184
 Compressive stress, 184
 Core density variations, 125
 Cornwall-Massena earthquake, 134
 Coseismic displacement, 211
 Coseismic slip, 194
 Coseismic variation, 33
 Coulomb failure function, 194, 195
 Coulomb Failure Function (hereafter CFF), 184
 Coulomb-Mohr criterion, 182
 Coyote Creek fault system, 56
 Coyote Creek strike-slip fault, 44
 Creeping, 109
 Crustal deformation, 134

- Crustal movement, 120
 Crustal strain, 36
 Crust-fluid medium approach, 49
 Cumulative slip, 72
 Cyclic elasto-plastic, 20
- Damage distribution, 211
 Damaged belt-like zone, 210
 Darlington Nuclear Generating Station, 136
 Darlington project, 142
 De-amplification, 16
 Deformed zone, 47
 Depression zone, 46
 Design Earthquake, 140, 143
 Disaster belt, 91
 Displacement, 143
 Displacement orbit, 10
 Double couple mechanism, 5
- E' centre, 152
 Earthquake fault, 90
 Earthquake-proof design, 79, 224, 243
Earthquake-proof designs, 1
 Eastern Canadian earthquake, 136
 EDM, 186
 Elapsed time, 235
 Elapsed times, 236
 Electrical conductivity, 30, 37, 41
 Electron spin resonance (ESR), 147
en echelon, 67
 Engineering structure, 47
 Epicentral distance, 8, 36, 143
 Equi-linearized technique, 12
 ESR age, 158, 159, 160
 ESR dating, 152
 ESR measurement, 148, 150
 ESR signal, 149, 150, 155
 ESR spectra, 152
 Eurasia plate, 79
 Eurasian plate, 87
 Excess pore water pressure ratio, 24
- Fault, 185
 Fault gouge, 148, 149, 155, 158, 159, 164, 166, 172
 Fault gouge vein, 168, 170
 Fault length, 96, 220, 228, 239
- Fault plane, 190
 Fault segment, 53
 Fault segmentation, 44
 Fault slip, 222
 Fault system, 1, 64
 Fault vein, 176
 Fault zone, 4
f-k spectral analysis, 203, 210
 Filtered accelerogram, 9
 Finite element-finite difference (FEM-FDM), 21
 Flowage, 66
 Fluidization, 176
 Focal depth, 143
 Fourier amplitude, 15
 Fourier analysis, 33, 36
 Fourier spectrum, 15
 Fracture, 249, 250, 257
 Fracture map, 250
 Fracture pattern, 251
 Fracture structure, 253
 Fracture zone, 159
 Fracturing process, 254
 Frequency-dependent equivalent strain, 15
 Frequency-wavenumber (*f-k*) spectral analysis, 202
 Frictional boxes, 108
 Frictional shear stress, 49
 Frictional strength, 182
 Fukozu fault, 222
 Fukui earthquake, 76, 127
 Fukui-Neodani block boundary, 74, 76, 88
- γ -ray irradiation, 150
 Ganidake igneous complex, 28
 Geodetic data, 185
 Geodetic fault model, 195
 Geomorphological lineament, 64
 Glacio-isostatic uplift, 145
 Gojodani fault, 237
 Gouge vein, 166
 GPS, 186
 GPS (Global Positioning System), 242
 GPS observation, 194
 Grain density, 121, 125
 Gravity (Bouguer) anomalies, 64

- Gravity anomaly, 210
 Ground acceleration, 92
 Ground deformation, 44, 47, 49, 56, 59
 Ground displacement, 44, 49, 55
 Ground motion, 143
 Ground-structure interaction analysis, 49
 Groundwater, 29, 257
- Hanaore fault, 213
 Hanaore-Kongo fault line (HKFL), 64
 Hanaore-Kongo Fault Line (HKFL), 112, 120, 227
 Hanaore-Kongo fault line (HKFL), 227
 Hg pycnometer, 121
 Hietsu earthquake, 239
 High-density anomaly, 129
 Highly weathered area, 250
 Highly weathered zone, 257
 Hinachi granite, 255
 Historical earthquake, 73, 87
 HKFL, 109
 HKFL (Hanaore-Kongo Fault Line), 111
 Hoei earthquake, 128
 Horizontal acceleration, 5, 24
 Horizontal and vertical components (H/V), 202
 Horizontal compression, 135
 Horizontal displacement orbit, 25
 Horizontal stress, 140
 H/V , 204
 H/V analysis, 205
 H/V peak, 210
 Hydraulic, 40
 Hydraulic conductivity, 138, 140, 255, 257, 259
 Hydraulic piston coring, 120
 Hydrofracturing, 138, 140
 Hydrogeological model, 255
 Hydrothermal alteration, 171
 Hyogoken-nanbu (Kobe) Earthquake, 199
 Hyogo-ken-nanbu (Southern Hyogo Prefecture) earthquake, 1
 Hyogoken-nanbu earthquake, 213
- Iida-Matsukawa, 165
 Iida-Matsukawa fault, 164, 176
- Inflow, 30, 36
 Injection vein, 166, 168, 176
 Inland earthquake, 64, 67, 76, 128, 220, 231
 In-situ stress, 138
 Internal frictional coefficient, 182, 184
 Interseismic interval, 240
 Interseismic period, 227, 228, 234, 239
 Intraplate earthquake, 134
 Intraplate environment, 134
 Intraplate seismicity, 136
 Iron sulfides, 121
 Isewan-Tsurugawa Tectonic Line (ISTL), 120
- Kamaishi Mine, 28
 Kamiya fault, 237
 Kanbun earthquake, 120, 122
 Kanto earthquake, 213
 K-Ar age, 160
 K-Ar method, 159
 Katagihara fault, 213
 Keicho earthquake, 98, 99
 Keicho-Fushimi, 235
 Keicho-Fushimi earthquake, 68, 74, 113, 223, 233
 Kemaishi Mine, 40
 Kinematic hardening, 20
 Kinki district, 184
 Kinki triangle active fault zone, 87
 Kinki-Outer, 78
 Kita-Izu earthquake, 223
 Kita-Nimo earthquake, 239
 Kitatango earthquake, 127
 Kobe earthquake, 1, 64, 67, 74, 75, 76, 78, 79, 87, 88, 97, 99, 113, 185, 194, 196, 220, 226, 228, 235, 243
 Kobe-Nishinomiya fault, 211
 Koyo fault, 201, 203, 207, 210
 Kurihashi granodiorite, 28
 Kusaki granite, 255
 k -value, 157, 158
- Lacustrine sediment, 129
 Lake County uplift zone, 56
 Lake Mikatagoko, 120, 129
 Lake Suigetsu, 120
 Laurentide ice sheet, 136

- Left-lateral displacement, 252
 Linear elastic fracture mechanics, 44, 59
 Liquefaction, 66
 Liquefaction and flowage, 68, 89
 Liquefaction and flowage, 90
 Liquefaction-induced damping, 24
 Log-normal distribution, 251
- Magnitude, 36
 Maximum acceleration, 31
 Maximum displacement, 93, 97
 Maximum likelihood method (MLM), 203
 Maximum magnitude, 238, 242
 Maximum shear strain, 15
 Median tectonic line, 190, 196
 Median Tectonic Line (MTL), 64, 112, 148
 Melting-originated pseudotachylite, 173, 177
 Microplate, 77, 79
 Microplate model, 79
 Microseism, 201, 205, 207
 Microseismicity, 88
 Mikata fault, 120
 Mikawa, 76
 Mikawa earthquake, 88
 Modeled fault, 190
 Moment-release rate, 74, 233
 MTL, 76, 149, 155, 158
- Nankai, 87
 Nankai trough, 78, 111, 113, 129
 Nankai trough (NT), 76
 Nankai trough event, 77
 Negoro fault, 237
 Nekomata fault, 237
 Neodani, 94
 Neodani fault, 128, 221, 223
 Newmark's β -method, 21
 Niagara Escarpment, 137
 Niagara Region seismological zone, 143
 Nobi earthquake, 76, 94, 128, 223
 Nojima, 185
 Nojima (Earthquake) Fault, 148
 Nojima fault, 64, 88, 91, 93, 97, 149, 152, 155, 158, 159, 190, 220
 Non-linear kinetic hardening, 20
- Non-linear time domain analysis, 12
 Normal stress, 182
 North American Plate, 87, 134, 136
 Nukumi faults, 94
- Off-Echizenmisaki earthquake, 127
 Offshore earthquake, 76
 Older Ryoke granitoid, 155
 Orientation error, 9, 11
 Osaka microplate, 79
 Oscillator, 108
 Overlapping strike-slip fault, 45
- P* axis, 185, 190, 194
P wave, 210
 Pacific and Philippine Sea plates, 87
 Pacific plate, 78
 Paleo-environmental, 129
 Paleoliquefaction, 68
 Paleo-liquefaction and flowage, 224
 Paleoseismic evidence, 99
 Paleoseismicity, 99
 Peak acceleration, 143
 Peak ground motion, 12
 Peak period, 204, 205
 Penultimate earthquake, 99
 Permeability tensor, 258
 Peroxy centre, 152
 Phase velocity, 203, 204
 Philippine Sea plate, 79
 Piezometric head, 258
 Planar crack, 49
 Plane stress condition, 56
 Plasticity, 20
 Plate motion, 87
 Plate-margin earthquake, 136
 Plate-margin seismicity, 134
 Poisson's ratio, 55
 Pore pressure, 182, 184
 Porosity, 255, 257
 Potential magnitude, 220, 237, 238
 Powder X-ray diffraction, 176
 Power spectrum, 4
 Predominant frequency, 19
 Pre-existing active fault, 66
 Principal stress, 53
 Principle stress axes, 253
 Pseudotachylite, 165, 172

- Pseudotachylite vein, 165, 167, 170, 176
 P-wave velocity, 21
- Quasi-periodic, 99
 Quaternary fault, 97, 211
 Quaternary slip rate, 226
 Quiet period, 231
- Radial distance, 52
 Rainfall, 33, 41
 Rayleigh-wave, 202
 Recurrence interval, 222, 224
 Released moment, 72
 Response frequency spectra, 92
 Response spectrum, 143
 Richter magnitude, 143
 Right-stepping, 46, 56
 Rikuu earthquake, 94
 Rokko fault system, 87, 97, 185, 200, 201
 Rupture length, 97
 Rupture propagation, 93
 Rupture zone, 109
 Ruptured length, 96
 Rupturing fault, 136
 Ryukyu Trench, 87
- Sakurajima explosion, 127
 San Andreas Fault, 135
 San Andreas fault system, 44
 Seasonal variation, 36
 Sedimentation rate, 127
 Seismic activity, 31
 Seismic coupling, 110, 111
 Seismic cycle, 99, 231
 Seismic design, 140
 Seismic fault, 220
 Seismic gap, 97, 233, 234, 238
 Seismic hazard assessment, 94, 194
 Seismic moment, 97, 98, 225, 227
 Seismic moment-release, 69
 Seismic response, 25
 Seismic risk, 73, 224, 231, 237, 240
 Seismic risk assessment, 243
 Seismic risk evaluation, 242
 Seismic risk index, 224
 Seismic sequence, 76
 Seismic slip, 177, 223, 225
- Seismicity change, 185, 195
 Seismic-released moment, 225
 Seismogenic fault, 96, 134, 136, 144, 145, 211, 221
 Seismogeochemical, 40
 Seismograph, 29
 Seismological observation, 29
 Seismological zone, 140
 Seismotectonic environment, 145
 SEM, 172
 SEM observations, 176
 Sequential occurrence, 78
 SHAKE, 13
 SHAKE program, 16
 Shear displacement, 253
 Shear fracture, 184
 Shear modulus, 12
 Shear stress, 56, 182
 Single column ground model, 21
 Size distribution, 172, 176
 Slip accumulation, 221
 Slip distribution, 194
 Slip rate, 97, 164
 Soil liquefaction, 8, 16
 Southern Hyogo Earthquake, 8, 25
 Southern Hyogo Prefecture
 Earthquake, 148, 149, 155
 Space-time pattern, 112
 Spectral intensity, 5
 Splay fracture, 251
 Step structure, 253
 Step-like subsidence, 207
 Stick-slip model, 107
 Stress accumulation theory, 98
 Stress change, 194
 Stress intensity factor, 52
 Strick-slip model, 109
 Strike-slip, 190
 Strike-slip fault segment, 48, 55, 56, 58, 59
 Strong ground motion, 4
 Subsidence, 44
 Subsurface structure, 207
 Surface rupture, 66, 88, 220
 Surface-wave, 212
 Suwayama fault, 211
 S-wave, 212
 S-wave phase, 11

- S-wave refraction theory (SHAKE code), 31
- Tanna fault, 222, 223
- 3-D subsurface structure, 201
- TD value, 158
- Tectonic shear stress, 44, 49
- Tectonic surface faulting, 90
- Temporal cluster, 99
- Tensho earthquake, 128
- Three-dimensional liquefaction analysis, 20, 25
- Tonghai strike-slip fault segment, 59
- Total doses (TD values), 155
- Transmissivity, 259, 260
- Trapezoidal digital filter, 10
- Trench excavation, 243
- Tri-dimensional analysis, 49
- Tsurugawan-Isewan tectonic line, 74
- Turbidite, 121, 122
- Turbidite event, 125
- Uniaxial compressive strength, 139
- Uniform displacement, 93
- Uniform slip, 186, 194
- Uplift, 44
- Velocity response, 4
- Velocity structure, 202
- Velocity structure model, 16
- Viscoelastic deformation, 145
- Volcanic ash, 127
- Water chemistry, 40
- Water pressure, 30, 33, 40
- Western Quebec Zone (WQZ), 140
- Wisconian Glaciation, 136
- X-ray diffraction spectra, 170
- X-ray powder diffraction, 148
- Yamasaki Fault, 185, 190
- Yanger Drias period, 127
- Young's modulus, 55